Experimental Modelling of Debris Dynamics in Tsunami-Like Flow Conditions

Jacob Stolle

Thesis submitted to the
Faculty of Graduate and Postdoctoral Studies
in partial fulfillment of the requirements for the degree of

Master of Applied Science in Civil Engineering

Under the auspices of the Ottawa-Carleton Institute for Civil Engineering

Academic advisor: Prof. Ioan Nistor

University of Ottawa
Ottawa, Ontario, Canada
April 2016

Abstract

Tsunamis are among the most devastating and complex natural disasters, affecting coastal regions worldwide. Tsunami waves are generated through many natural phenomena, such as earthquakes, landslides, and volcanic eruptions. The waves travel at high speeds away from the source, potentially affecting multiple countries with very little warning. Over the past several decades, tsunamis such as the 2004 Indian Ocean, the 2010 Chilean, and the 2011 Tohoku Tsunami served as reminders of the potential devastation of these natural disasters, resulting in tragic loss of life and billions of dollars in damages. Forensic engineering field investigations and subsequent analysis of these events have demonstrated that infrastructure in these tsunami-prone regions was not adequately prepared for the extreme forces associated with a tsunami. As a result, there has been an increased research emphasis worldwide on the planning and design of infrastructure located in tsunami-prone areas to be better prepared for such future events.

The present study aims to experimentally investigate and analyze the motion of debris carried by an inundating tsunami flood. One of the previous challenges involved in the evaluation of debris motion during such events was a lack of experimental methods that could non-invasively, quickly and accurately track the motion of debris at high velocities. This study introduces two innovative methods of tracking the debris. The first one used a novel camera-based tracking algorithm, while the second used Bluetooth and Inertial Measurement Unit sensors to track the debris within the inundating tsunami flood. The study outlines, for the first time, the technology and methods involved in the two tracking methods as it used both dry-test and wet-test experiments to evaluate the applicability of these methods in coastal and hydraulic engineering.

This study used these two methods to evaluate the motion of debris from experiments conducted in a new Tsunami Wave Basin commissioned recently at Waseda University (Tokyo, Japan). The study examined the effect of the initial positioning of the debris, particularly focusing on the spreading area of the debris (determining thus their maximum displacement and the spreading angle of the debris). The results showed that an increase in the number of the debris resulted in an increase in the spreading angle of the debris and a decrease in the displacement of the debris. The increased number of debris also added significantly more variation in the final resting position of the debris due to the increased debris-debris collisions. The initial orientation of the debris also affected debris motion, particularly influencing the peak velocity of the debris and the distance from the initial debris resting position to where the peak velocity was observed.

Acknowledgements

First, I would like to express my deepest thanks to my academic advisor, Prof. Ioan Nistor. Throughout my time at the University of Ottawa, he provided me with countless opportunities for improvement of not only within the framework of my Masters but many other projects. Due to his kindness, I have been given many opportunities to travel and further my studies in hydraulic engineering. He provided me, without fail, any advice, help, or resources needed for the progression and completion of any project I was working on. His hard work and attention to detail has greatly improved not only the quality of this thesis but the quality of my work as a whole.

I would like to additionally express my gratitude to my informal academic advisor, Dr. Nils Goseberg. It was his tireless work on the ImpLOADis European Union project and throughout my Masters has made this project successful. In particular, his open-door policy and experience in experimental work was extraordinarily helpful and, again, his hard work and attention to detail has greatly improved my work as a whole. I was very lucky to have two excellent advisors throughout my time at the University of Ottawa.

I would also like to recognize the personnel at Waseda University (Tokyo, Japan). Prof. Tomoya Shibayama and Dr. Takahito Mikami, who provided their new experimental facilities and lent their vast expertise of hydraulic and coastal engineering. I would also like to acknowledge Mr. Ryota Nakamura and Mr. Shunya Matsuba for their help in aiding Dr. Nistor and Dr. Goseberg in the setup and running of the experiments.

Last but not least, I would like to thank my family and friends for their unending support. Through the most difficult parts of my academic career, they have kept me grounded and upbeat while also pushing me to be my best. Without them, none of the work I have done to this point would have been possible.

Table of Contents

List of Figures

List of Tables

List of Symbols

Roman Numerals

A_d	Cross-sectional area of the debris (m^2)
b_i	Body force (N)
B	Input matrix
c_j	ALE convective velocity (m/s)
C	Measurement matrix
C_b	Blue-Difference Chroma
C_r	Red-Difference Chroma
C_D	Drag coefficient
C_M	Mass coefficient
d	Length of the short axis of debris (m)
d_{eu}	Euclidian distance (m)
D	Displacement of the structure (m)
DRMS	*R*oot mean squared distance
D_{x_0,y_0}	Translation Matrix
e	Eccentricity of debris impact
E	Young's modulus (N/m^2)
k	Contact stiffness (N/m)
k_d	Equivalent stiffness of a 1D bar (N/m)
k_r	Ratio between the long axis and short axis of the boulder
K_t	Kalman gain
K_y	Probability distribution of the driftwood location
L	Luminance
L_d	Length of the debris (m)
m_d	Mass of the debris (kg)
m_f	Mass of fluid (kg)

$MRSE$	Mean radial spherical error
n	Number of tags
${}^{f}p_j$	Pixel coordinates in the flume plane
${}^{i}p_j$	Pixel coordinates in both the image plane
P_x^f	Measure of the error
P_x^c	Error covariance
P_x^c	Corrected error covariance
r_0	Radius of the debris (m)
R_θ	Rotation Matrix
r_i	Radius of gyration of the debris (m)
s	Scale Factor
S_s	Scaling Matrix
SE	Squared Error
t_d	Impulse duration (s)
Δt	Sampling interval (s)
u	Velocity of the debris (m/s)
u_t	Acceleration input vector
u'	Acceleration of the boulder (m/s^2)
U	Current velocity (m/s)
U_t	Fluid velocity field (m/s)
w_k	Normally distributed process noise
X	Lagrangian based coordinate system
x_0	X-coordinates of translation (m)
$\dot{x}$	Velocity in the x-direction (m/s)
$\ddot{x}$	Acceleration in the x-direction (m/s^2)
$\overline{x}_t$	Predicted state vector at time t

x_t^f System state

x_t^c Current prediction

x_{t-1} State vector at time $t-1$

y_0 Y-coordinates of translation (m)

$\overline{z_t}$ Measured state vector at time t

Greek Letter Symbols

β Obliqueness of debris impact (^{o})

ε_0 Distance from the center of gravity of the debris to the point of impact (m)

θ Angle of slope (^{o})

θ Angle of rotation

ρ_s Density of the debris (kg/m^3)

ρ_f Density of the fluid (kg/m^3)

μ Coefficient of friction

$\overline{\delta_y}$ Variance

χ ALE coordinate systems

φ Angle of debris impact relative to the debris surface (^{o})

ϕ State transition matrix

Mathematical Operators

$\partial/\partial a$ Partial derivative with respect to a variable a

Chapter 1. Introduction

1.1 Objectives

Tsunamis are among the most devastating natural disasters and, as a result of the relative rarity of these catastrophic events, the study of their loads and effects is difficult. Tsunamis can be triggered by various natural phenomena: subduction earthquakes, volcanic eruptions, and submerged or aerial landslides (Esteban et al., 2015). Primarily however, tsunamis are a result of subduction earthquakes, when a seismic event occurs along the boundary of tectonic plates. The movement of the plates result in the displacement of massive volumes of water, generating tsunami waves, propagating at several hundred kilometers per hour in the open ocean, with relatively small amplitudes (~1 m). As the wave begins to approach shallower coastal waters, the wave shoals, resulting in the deceleration of the wave, a decrease in its wavelength, and increase in its wave height (Esteban et al., 2015). As the shoaling develops, the wave will ultimately break and, depending on the nearshore bathymetry, travels over the coastal area as a turbulent bore or as a rapidly surging flood which propagates further inland, depending on the topography of the coastal area (Figure 1.1).

Figure 1.1: Inundating tsunami surge induced by the 2011 Tohoku Tsunami, Iwanuma, Japan (adopted from St-Germain et al. (2014))

Over the past decade, several major tsunamis have resulted in enormous economic loss, catastrophic loss of life and extensive damage to coastal communities. In December 2004, a M_w 9.1 subduction earthquake occurred off Indonesia and triggered a tsunami that resulted in over US $319 billion dollars in damages and the loss of over 220 000 lives throughout coastal states in the Indian Ocean (Ioualalen et al., 2007). In March 2011, a M_w 9.0 subduction earthquake triggered the Tohoku tsunami resulting in over US $209.8 billion with the loss of over 15,500 lives in Japan, despite extensive coastal structures in place for tsunami attacks (Fujii et al., 2011, Kazama and Noda, 2012).

The Canadian coasts have experienced many tsunamis, though rarely large enough to cause extreme damage (Clague et al., 2003). In November 1929, a M_w 7.2 earthquake triggered a large submarine slump (along the Laurentian slope), which in turn triggered a tsunami that struck the Burin Peninsula in Newfoundland, resulting in 28 deaths. In March 1964, a M_w 9.2 earthquake near Alaska resulted in over CDN $10 million in damages to Port Alberni, British Columbia (Clague et al., 1994, 2003). The West Coast of Canada, in particular, is vulnerable to tsunamis as it is located along the seismically active Pacific "Ring of Fire" as well as from tsunamis generated from further afield in the Pacific Ocean (Figure 1.2).

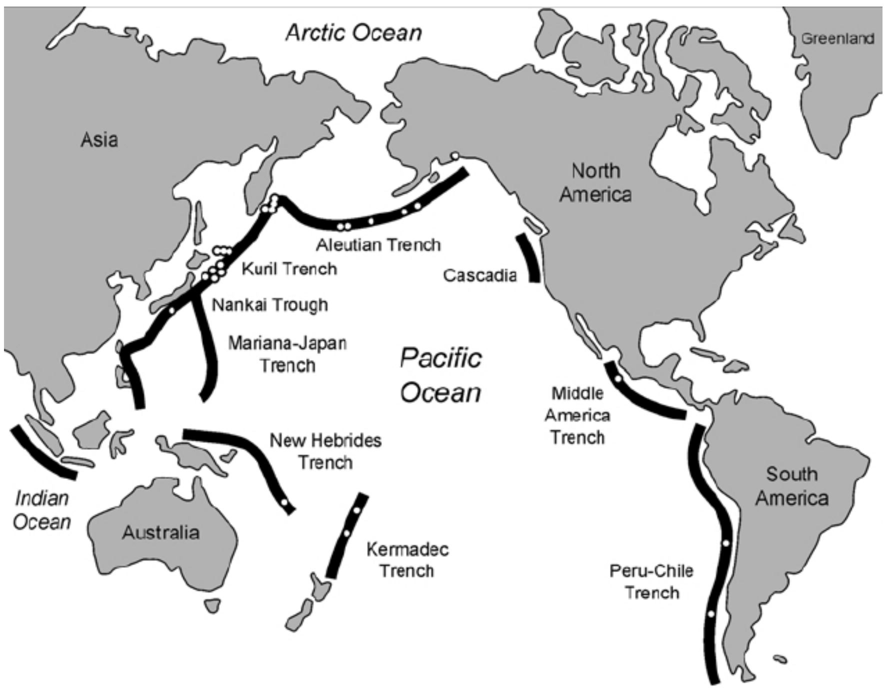

Figure 1.2: Some of the subduction earthquake zones throughout the Pacific and Indian Oceans (adopted from Clague et al. (2003)).

Due to the disproportionate gap between the scale of tsunamis and their return period, there has been difficulty in developing design standards for these catastrophic events. As a result, the focus of most research and policy worldwide has been the development of early warning systems (Esteban et al., 2015), such as the Pacific Tsunami Warning Network (Darienzo et al., 2005) that Canada is a part of and the German-Indonesian Tsunami Early Warning System (Spahn et al., 2010), to evacuate the local community as quickly as possible to limit loss of life. However, as was noted in many post-tsunami field surveys of the 2004 Indian Ocean and 2011 Tohoku tsunamis, critical infrastructure thought to have been resistant to tsunami attacks failed as a result of the extreme loads exerted on the structure (Yeh et al., 2013) and an incomplete understanding of the transfer of off-shore tsunami wave heights to onshore loading conditions (Goseberg et al., 2009, Chock et al., 2013, Taubenböck et al., 2013) (Figure 1.3). The loss of this critical infrastructure is not only dangerous throughout the tsunami event but additionally harms the disaster mitigation efforts and makes the reparation process to tsunami-stricken areas after the disaster more difficult.

Based on these recent findings, a concerted international research effort has been made to create guidelines and standards to properly design critical infrastructure (such as vertical evacuation structures, bridges, and hospitals) to withstand tsunamis loads. The Federal Emergency Management Agency (FEMA) in the United States has developed two sets of guidelines related to tsunamis: FEMA P55 (Fourth Edition, 2011) provides instruction on the design and construction of coastal structures to damage from natural disasters (such as hurricanes, earthquakes, and floods), and FEMA P646 (Second Edition, 2012) which provides formulations for specifically calculating tsunami loads on vertical evacuation structures. The Building Center of Japan has developed a code for the formulation of loads to inland structures as a result of tsunami flooding (Okada et al., 2005). The American Society of Civil Engineers (ASCE) is also in the process of developing a standard (in legal language), ASCE 7 Chapter 6 Tsunami Loads and Effects, for incorporating tsunami-resistant design for structures in at-risk states (Alaska, Washington, Oregon, California, and Hawaii).

Figure 1.3: Tsunami damaged structures. (a) Building in Phuket Island, Thailand; (b) Breakwater in Natori, Japan (adapted from Esteban et al. (2015)).

The University of Ottawa has initiated an international comprehensive interdisciplinary hydraulic-structural engineering research program (Saatcioglu et al., 2005, Palermo et al., 2009, Nistor et al., 2011, Al-Faesly et al., 2012) in collaboration with the National Research Council (NRC), Waseda University (Japan), and the University of Hannover (Germany) in response to the extreme damage observed after the 2004 Indian Ocean and 2011 Tohoku tsunamis. The ultimate goal of this research program was to develop new recommendations and guidelines for tsunami-resistant design in coastal areas. Up to this point, the focus of this research program has been on the identification of building failure mechanisms through field surveys of tsunami-stricken areas (Saatcioglu et al., 2005, Palermo et al., 2009, 2013), as well as numerical and experimental evaluation of debris impact and hydrodynamic loads on free-standing structures (Nouri et al., 2010, Nistor et al., 2011, Al-Faesly et al., 2012, St-Germain et al., 2013).

In the context of tsunami-resistant design of infrastructure, the determination of the potential loading conditions are important in the safe and cost-effective design of these structures.

Tsunami inundation mapping has been used to evaluate the potential hydrodynamic loads (Titov and Synolakis, 1998, Borrero et al., 2006); however methods for the evaluation of the potential debris impact loads have been limited to the conservative estimation that debris impact loads will always occur (Takahashi et al., 2011, *FEMA P646*, 2012). The difficulty in evaluating potential debris impact loads is due to the random nature of debris motion (Matsutomi, 2009) and a wide range of variables that will influence the debris motion (Naito et al., 2014). Detailed and rigorous experimental programs are hence needed to evaluate the entrainment and motion of debris while evaluating the effects of variables such as hydraulic conditions, debris geometry and the surrounding environment. The long-term objectives of this research study are:

- Develop benchmark experimental data of debris motion to be used in the validation of solid-fluid coupled numerical models.
- Evaluate the loads and effects of multiple debris impact and debris accumulation on structures.
- Provide guidelines for the safe design of structures in tsunami-prone areas for debris impact in tsunami flow conditions.

Considering the long-term objectives, the present study focuses on:

- Development of non-invasive tracking methods to quickly and accurately track the motion of the debris in high-velocity flow conditions.
- Evaluate debris entrainment and motion to provide high-quality information on the maximum spreading area of debris.
- Provide preliminary benchmark data concerning debris motion for validation of future numerical simulations.

1.2 Scope

The primary objective of the present study was to evaluate debris entrainment mechanisms and determine the effect of various test conditions on the overall motion of the debris in tsunami-like flow conditions. The focus of the study was to determine the area of propagation of the debris (longitudinal displacement and spreading angle) to evaluate the potential for debris impact. The experiments evaluated the effects of debris configuration and the number of debris on the trajectory and velocity of debris. The experiments were performed at the innovative new Tsunami Wave Basin (TWB) at Waseda University (Tokyo, Japan).

The motion of the debris was evaluated using two novel non-invasive tracking systems to track the motion of the debris as it propagated within the surge. From a literature review of current variables necessary to determine debris impact force (Chapter 2), the systems were developed to track the trajectory, orientation, velocity, and acceleration of the debris. The secondary objective of this study was to evaluate the effectiveness of these systems in the context of this study but also the wider fields of coastal and hydraulic engineering.

The study focused on the experimental modelling of debris motion and the entrainment of debris in tsunami-like flow conditions. Due to time constraints and physical constraints of the experimental environment, the study has multiple limitations regarding the evaluation of debris transport:

- Only one scale (1:40 geometric scaling) was examined throughout this study. The flow conditions were scaled using Froude scaling as a results the effects of turbulence on the debris motion was not examined, as turbulence scales with the Reynolds number (She and Leveque, 1994). The geometric scale was chosen to be a large as possible while maintaining reasonable prototype scaled flow conditions.
- The debris configurations were limited to a maximum of 18 debris as the debris tracking methods could not track more debris. The stacking of the debris was limited to two debris high. The number of debris was limited by the sampling rate of the sensor-based tracking system.
- One topography, a horizontal bottom, was evaluated; therefore the effect of slope, friction and fixed obstacles on debris transport was not evaluated. The horizontal bottom was chosen as the worst-case scenario for debris transport, with no slope restricting the debris motion.
- Throughout all of the experiments, the hydrodynamic conditions were kept consistent; the effect of different wave conditions on debris transport were not examine.
- As discussed further in Chapter 2 and 5, there are multiple methods of modelling tsunami waves, for this study only a broken elongated solitary wave was examined.

Due to the random nature of debris-fluid interactions, a comprehensive study of the motion and entrainment are needed to properly evaluate the variables that would affect these processes. The study presented here will provide a baseline for future comprehensive experimental studies using the two tracking methods to derive high-quality data to be derived from the experimental program to be provided for future numerical simulations. Moreover, the conclusions from this study will provide a deeper understanding of debris motion and help in the evaluation of debris impact forces and debris accumulation in future experimental studies.

1.3 Contributions and Novelty of the Study

The novelty of the present study lies in the comprehensive approach to the evaluation of debris entrainment and overall debris motion in tsunami-like flow conditions. The study examines the motion of multiple debris whereas the primary focus of the research community to this point has been on single debris, with an emphasis on impact forces. While some studies have evaluated multiple debris motion, the focus of this research has largely been on determining the effects of hydrodynamic conditions on the final resting position of the debris. The work presented herein examined the simultaneous motion of multiple debris and evaluated the intermediate variables important in determining debris impact force (their orientation, velocity, and acceleration). The comprehensive approach also allowed for the analysis of other variables, such as the effect of obstacles and debris configuration on debris motion, on the overall debris motion.

The study also presents two innovative non-invasive tracking systems for evaluating debris motion. One of the primary reasons that the intermediate variables have not been evaluated in the research community is due to a lack of non-invasive, cost-effective tracking systems that could accurately track the motion of multiple debris simultaneously. The study presents two novel methods that reliably track debris but which can also be applied to other applications fields of coastal and hydraulic engineering.

1.4 Publications

Journal Articles

1) Goseberg, N., Nistor, I., Mikami, T., Shibayama, T., and Stolle, J. (2016). "Non-Invasive Spatio-temporal "smart" debris Tracking in Turbulent Flows with Application to debris-laden Tsunami Inundation." *Journal of Hydraulic Engineering, ASCE, accepted.*
2) Nistor, I., Goseberg, N., Mikami, T., Shibayama, T., Stolle, J., Nakamura, R., and Matsuba, S. (2016). "Experimental Investigations of Debris Dynamics over a Horizontal Plane." *Journal of Waterway, Port, Coastal and Ocean Engineering, ASCE, accepted.*
3) Stolle, J., Nistor, I., and Goseberg, N. (2016). "Optical Tracking of Floating Debris in a Wave Basin." *Coastal Engineering Journal, JSCE, accepted.*

Other Refereed Contributions:

4) Goseberg, N.*, Nistor, I., and Stolle, J. (2015). ""Smart" debris Dynamics over a Horizontal Apron." *Coastal Structures & Solutions to Coastal Disasters Joint Conference, Boston, MA., USA.* (Oral presentation, accepted to conference proceedings)
5) Stolle, J.*, Nistor, I., and Goseberg, N. (2015). "Flood-Induced Debris Dynamics over a Horizontal Apron." *Coastal Structures & Solutions to Coastal Disasters Conference, Boston, MA., USA.* (Oral presentation, accepted to conference proceedings)
6) Stolle, J.*, Nistor, I., and Goseberg, N. (2016). "Optical Tracking of Water-Borne Debris in Laboratory Conditions." *Coastlab 2016, Ottawa, ON, Canada.* (Accepted for oral presentation, submitted to conference proceedings)
7) Goseberg, N.*, Nistor, I., and Stolle, J. (2016). "Inertial Forces on Shipping Containers from a Broken Tsunami Bore." *Coastlab 2016, Ottawa, ON, Canada.* (Accepted for oral presentation, accepted to conference proceedings)
8) Stolle, J*, Nistor, I., and Goseberg, N. (2016). "Optical Tracking of Debris in Extreme Hydrodynamic Conditions" *Canadian Society of Civil Engineering 5th International Natural Disaster Mitigation Specialty Conference, London, ON, Canada.* (Accepted for oral presentation, accepted to conference proceedings)
9) Nistor, I.*, Goseberg, N., Stolle, J., Matsuba, S., Nakamura, R., Mikami, T., and Shibayama, T. (2016). "Flood-Induced Debris Motion within a Built-in Environment." *International Conference on Coastal Engineering, Istanbul, Turkey.* (Accepted for oral presentation)

(*) – Indicates presenter of oral presentation.

1.5 Outline of the Thesis

Chapter 1 provides an introduction to the study outlining the objectives, scope, contributions and publications by the author related to his field of research.

Chapter 2 presents an in-depth literature review of debris motion and tsunami hydrodynamic conditions. First, the literature review reviews results of the forensic engineering investigations of tsunamis and different physical modelling techniques for modelling tsunami flow conditions. Secondly, physical modelling of debris motion is examined looking at debris motion and debris loads. This section outlines the various intermediate variables that need to be considered when evaluating debris motion. Finally, an assessment of the numerical models for debris motion examines the current methods used in numerical modelling to simulate solid-fluid interactions.

Chapter 3 introduces a novel debris tracking system that utilizes BLE and IMU sensors to track the debris with 6DOF. The accuracy of the sensor-based tracking system was evaluated using an experimental program at both the University of Ottawa and Waseda University. The results from this work are presented in this section which was accepted as an article to the Journal of Hydraulic Engineering (ASCE), titled "Non-Invasive Spatio-temporal "smart" debris Tracking in Turbulent Flows with Application to debris-laden Tsunami Inundation." The author performed the experiments for the validation of the "smart" debris tracking along with the analysis. Dr. Nils Goseberg performed the research and acquisition for the design of the "smart" debris system along with the analysis of the Inertial Measurement Unit (IMU) accuracy experiments.

Chapter 4 presents a novel camera-based object tracking algorithm and the various image processing techniques are explained. The accuracy of the system was thoroughly evaluated using an experimental program performed at Waseda University and recommendation for future improvements are discussed. The article was accepted to Coastal Engineering Journal (JSCE, Japan), titled "Optical Tracking of Floating Debris in a Wave Basin." The author designed and implemented the MATLAB code presented within the paper. Dr. Nils Goseberg and Dr. Ioan Nistor performed the experiments at Waseda University used in the validation of the code.

Chapter 5 examines the results of the physical modelling performed in the TWB at Waseda University. The section examines the hydrodynamics conditions in the framework of tsunami modelling. The debris motion is examined from the perspective of determining maximum area of spreading of the debris and the effect of multiple debris on the spreading distance. The article was accepted to Journal of Waterway, Port, Ocean, and Coastal Engineering (ASCE), titled "Hydraulic Experiments on Debris Dynamics over a Horizontal Plane." The author performed the analysis of the experiments presented in the paper. Dr. Nils Goseberg and Dr. Ioan Nistor performed the experiments at Waseda University.

Chapter 6 examines the results of the physical modelling at Waseda University. The article focused on the entrainment processes of the debris and the effect of the entrainment on debris motion. The article was submitted to the proceedings for the Coastal Structures and Solutions to Coastal Disasters Conference (ASCE, 2015), titled "Flood-Induced Debris Dynamics over a

Horizontal Apron.” The author performed the analysis of the experiments presented in the paper. Dr. Nils Goseberg and Dr. Ioan Nistor performed the experiments at Waseda University.

Chapter 7 examines the effect of the debris configurations and the initial orientation of debris on the debris motion, focusing particularly on the velocity as it is the most important variable in determining debris impact. The article was submitted to the proceedings for the Canadian Society of Civil Engineering Conference (CSCE, 2016), titled “Tracking of Debris in High-Velocity and High Volume Flows.” The author performed the analysis of the experiments presented in the paper. Dr. Nils Goseberg and Dr. Ioan Nistor performed the experiments at Waseda University.

Chapter 8 outlines the conclusions of this study and provides recommendations for future work.

Chapter 2. Literature Review

The literature review presented in this chapter focuses on past research contributions as well as the state-of-the-art research related to the evaluation of debris motion and debris impact forces within tsunami-like flow conditions. First, this review will examine the approaches for physical modelling tsunamis in an experimental setting. Secondly, this review will focus on experimental modelling of debris motion and impact forces. Finally, this review will examine current numerical techniques that have been used in the evaluation of debris motion. The main objectives of the review are to: (i) provide a background on the unique hydraulic conditions related to tsunami engineering; (ii) indicate a starting point for which the evaluation of debris motion has currently been evaluated within coastal engineering; and (iii) outline the current state and research needs for debris motion studies in relation to tsunami engineering.

2.1 Physical Modelling of Tsunami Flow Conditions

Modelling of tsunami flow conditions has consistently been one of the most complicated aspects of tsunami engineering. Tsunamis propagate over a wide variety of complicated bed and coastal topography making the generalization of the flow problematic. The variation in the environmental conditions result in a large variation in the wave period and wave shapes (Sriram et al., 2016). Takahashi et al. (2011) identified differences in tsunami inland inundation from the 2011 Tohoku tsunami based on coastline configurations (Figure 2.1):

a) Breaking wave type: tsunami wave breaks near the shoreline of a mild-sloping beach, runs up the sand dune and propagates over the low-lying land behind the dunes.
b) High runup type: tsunami wave breaks on a relatively steep slope and rapidly reaches high runup heights.
c) Slowly-varying type: Steep cliffs facing relatively deep sea fronts resulting in the tsunami wave not breaking and moving relatively smoothly up and down.
d) Overtopping type: Relatively deep sea fronts with relatively flat land results in the tsunami wave rapid overtopping and inundation.

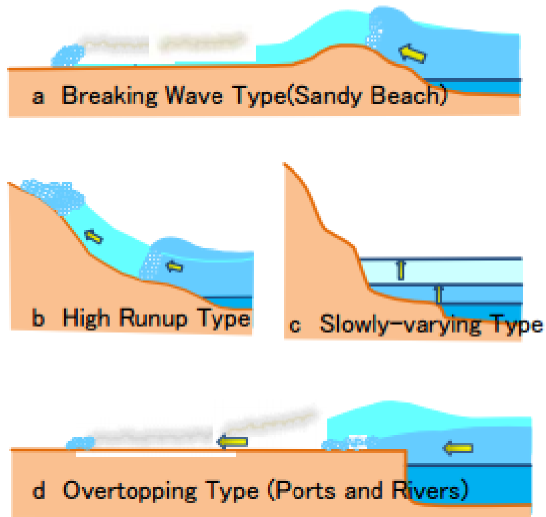

Figure 2.1: Potential tsunami inundation profiles (adopted from Takahashi et al. (2011)).

The modelling of tsunami flow conditions has developed through many iterations as researchers have attempted to model asymmetry of the long waves in the shoaling process and the large space- and time-scales associated with the tsunami wave (Madsen, 2010). Carrier and Greenspan (1958) derived an analytical solution of fully non-linear non-breaking waves on a uniformly sloping beach and later used the solution to model maximum tsunami inundation (Carrier et al., 2003). Based on the Carrier and Greenspan (1958) solution, cnoidal waves (Synolakis et al., 1988) and N-waves (Tadepalli and Synolakis, 1994) have been used in the modelling of tsunami waves however the use of these models has predominantly been for maximum wave runup (Synolakis et al., 1988, Tadepalli and Synolakis, 1994, Madsen and Schaeffer, 2010).

A study by Hammack and Segur (1974) experimentally examined the propagation of tsunamis caused by the impulsively raised or lowered sea floor and found that initial surface disturbance eventually led to the formation of solitary waves. Since that time, solitary waves have been among the most popular solutions to model important features of the tsunami wave in both numerical and physical modelling (Madsen et al., 2008). Arikawa (2011) investigated impulsive loading of a breaking tsunami wave on a wall, Wu and Murashige (2011) examined the maximum inundation of tsunami waves, Yao et al. (2014) examined debris motion, and Chen et al. (2015) evaluated tsunami-induced scour at off-shore breakwaters, along with many others, have made solitary waves among the standard of tsunami physical modelling. However, Madsen et al. (2008) noted that many of the solitary wave studies failed to establish any correlation to geophysical tsunamis and showed that the traditional solitary wave had relative time- and space-scales on the order of several orders of magnitudes smaller than field surveys of the 2004 Indian Ocean tsunami.

Recently, elongated solitary waves have been successfully generated in laboratory conditions and have shown more reasonable length and time-scales (Goseberg et al., 2013). Combining the solitary wave front, that has been extensively used as a reasonable estimation of the hydrodynamic loads for near-shore and debris motion studies (Arikawa, 2011, Chinnarasri et al., 2013, Seiffert et al., 2014, Yao et al., 2014), with the elongated tail give a much better representation of near-shore tsunami flow conditions. Sriram et al. (2016) showed that the runup time-series of the elongated solitary wave had a similar profile to forensic engineering results from the 2009 Samoa tsunami. However, the elongated solitary waves tend to require large-scale facilities, which can often be limiting.

Another approach to the physical modelling of a tsunami wave has been the dam break wave, where an impounded volume of water is released from an upstream reservoir into a straight channel. Chanson (2006) analyzed video footage of the 2004 Indian Ocean tsunami and demonstrated that the flow characteristics of a dam break wave are similar to that of a tsunami wave traveling over a coastal plain area (Figure 2.1: Breaking wave type). Imamura et al. (2008) used a dam break wave to model the motion of entrained boulders, Arnason et al. (2009) examined the interaction of bores with free-standing structures, and Al-Faesly et al. (2012) evaluated mitigation walls and their effectiveness at limiting tsunami impacts forces. Dam break waves have been particularly prevalent in numerical modelling due to the relative simplicity of developing the wave as opposed to the generation of other wave maker mechanisms (Canelas et al., 2013, Amicarelli et al., 2015).

The modelling of tsunami flow conditions has been a contentious issue in the field of coastal engineering. The wide range of flow conditions have led to a variation of modelling techniques that have different strengths and weaknesses. The choice of modelling technique must be carefully weighed against the phenomenon that are being studied and the facilities available. In the present study, the effectiveness of the solitary wave at modelling near-shore flow conditions and the use of a new wave basin at Waseda University has led to the decision to use an elongated solitary wave to model the near-shore transport of debris.

2.2 Physical Modelling of Debris Motion

In forensic engineering surveys of tsunami-stricken communities, the focus of the studies has primarily been on the evaluation of the hydraulic conditions throughout the region. From these surveys, maximum inundation heights, runup height and flow velocity can be determined (Saatcioglu et al., 2005, Borrero et al., 2006, Fritz et al., 2006). In many of these studies, debris impacts were noted as potential cause of structural failure (Yeh et al., 2013, 2014). However, information from the impact sites cannot easily be discerned aside from the fact that debris impact occurred as the flow conditions, debris velocity, and debris orientation at the time of impact is difficult to determine (Charvet et al., 2014). Without a direct video or image of the impact occurring very little can be done to evaluate the debris impact force from field investigations.

Debris motion has been equally challenging to evaluate, primarily since debris can vary from anything from construction materials to vehicles to shipping vessels and often have multiple sources (Naito et al., 2014). This makes difficult the matching of the debris found in a survey to a source. Naito et al. (2014) examined the position of displaced shipping vessels after the 2011 Tohoku tsunami as they had a very clear source (the port) and substantial documentation of their exact position before the tsunami occurred. From a forensic engineering survey, Naito et al. (2014) was able to develop a conservative estimation of the maximum spreading angle of the shipping vessels in relation to their source.

Through analysis of Google Earth images from before the event, Naito et al. (2014) identified the potential sources of debris. Based on these sources and subsequent field investigations, the method proposed by Naito et al. (2014) considered the origin of the debris as the geometric center of the source (in this case the port) (Figure 2.2). The debris was considered to propagate in a shore normal direction (solid red line). Naito et al. (2014) conservatively estimated that the debris would end up within a ±22.5^{o} cone (white solid line). Based on the observations from the field data, the majority of the debris fell within the proposed spreading angle.

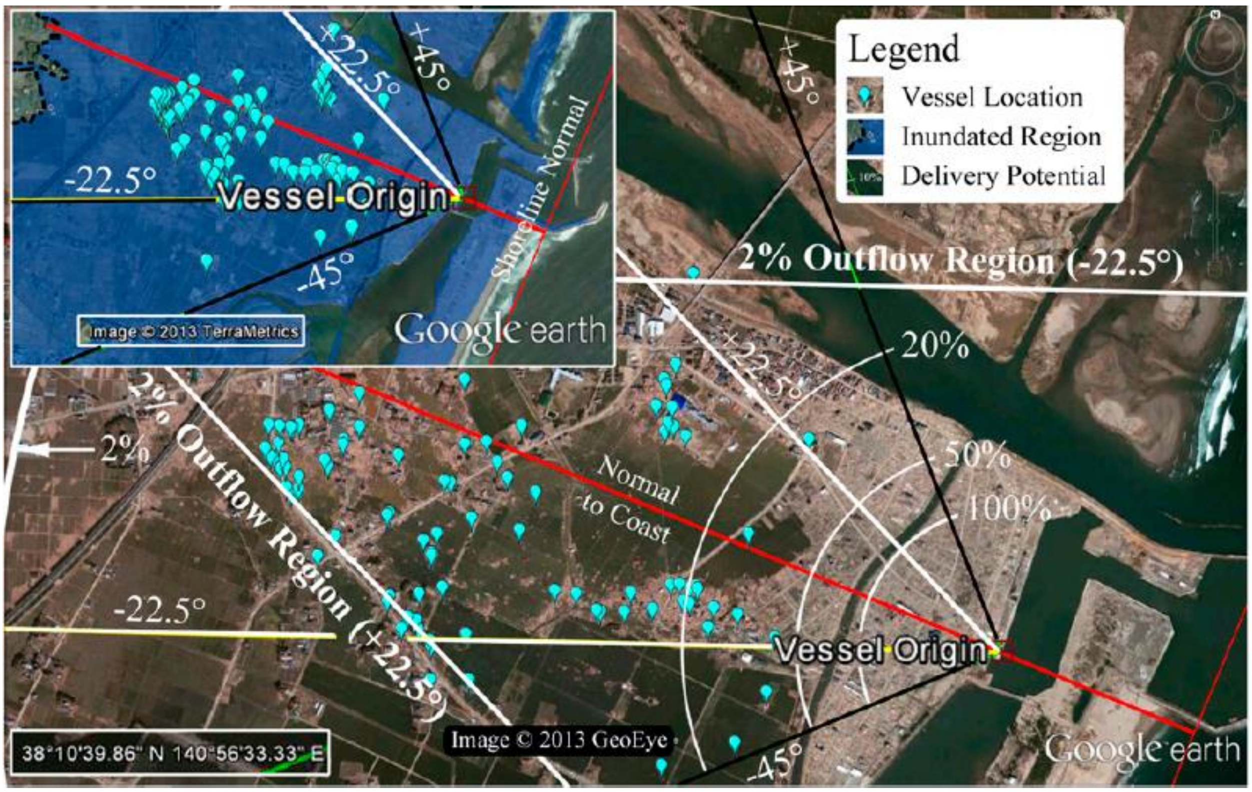

Figure 2.2: Estimation of debris spreading area (adopted from Naito et al. (2014)).

The maximum displacement of the debris was calculated based on the debris concentration, which was defined as the plan area of the debris divided by the spreading area of the debris. Again a conservative estimate was made to establish a debris concentration of 2% would contain the majority of the debris. Therefore the debris limits are defined by the ±22.5^{o} cone containing a spreading area that gave a debris concentration of 2%. Therefore, the area enclosed within the proposed maximum spreading angle would be equal to 50 times the plan area of the debris (Figure 2.2). However, if the spreading area encroached on an area where the inundation depth is less than 0.91 m, this area is not considered as it was expected the debris would ground and no longer propagate forward, as a result this would be the maximum inundation limit of the debris (Figure 2.3). Additionally, from the center of the inundation limit, a spreading area can be again determined using the ±22.5º cone from the inundation limit to the shoreline. The second area represents the potential spreading as a result of the outflow. Therefore, any critical buildings within the two spreading areas (shaded area in Figure 2.3) should be designed for a potential debris impact.

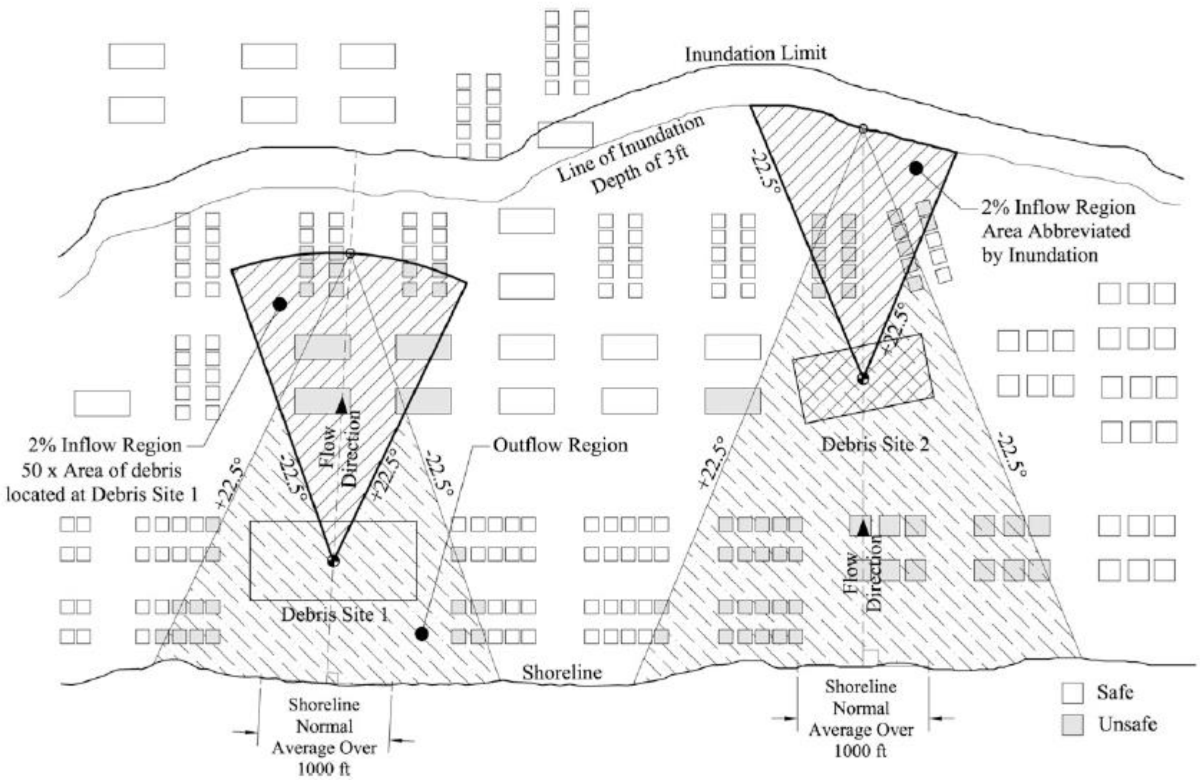

Figure 2.3. Identification of area for potential debris impact (Naito et al., 2014).

While the method by Naito et al. (2014) provided a conservative approach to evaluating debris impact potential, there is a lot of assumptions associated with the method. The topography of the spreading area would have a substantial influence on the flow conditions and therefore the debris motion. Naito et al. (2016) indicated in cases with large topographical features that would divert flow, the spreading area should be shifted to account for these anomalies. Naito et al. (2014) also indicated that buildings could be obstacles in the path of debris motion depending on the design of the structure. In cases of industrial areas, large reinforced concrete buildings would act as a barrier to debris motion as long as the inundation depths were less than 0.91 m (the draft of the debris) greater than the building height. However, in cases where the inundation depths area greater than 0.91 m above the height of the building or the surrounding buildings are likely to be destroyed by the inundating flow (wooden structures), the buildings should not be considered as an obstacle to the debris. Additionally, the method only examined one type of debris whereas other types have a wide variety of sizes and buoyancies that would influence propagation distance.

Due to the various challenges in evaluating debris motion in the field and the relative rarity of tsunami events, the primary research methods evolved around experimental modelling. However, there are still multiple challenges that must be overcome to properly model debris motion in an experimental setting. The foremost issue is the scaling issue related to modelling the tsunami flow conditions, which are outlined in Section 2.1. Related to the debris, the motion of debris is a highly random process (Bocchiola et al., 2006, Matsutomi, 2009) therefore extensive information is needed to establish meaningful results. To retrieve the necessary information, tracking of the debris' transient motion requires experimental methods that will not influence the debris motion while providing high-quality data regarding the debris position, orientation and velocity.

Braudrick and Grant (2000) examined the entrainment of individual large woody debris (LWD) in steady flow conditions. Experiments were performed to test a simple entrainment model of a single piece of LWD based on a balance of forces. The model considers the LWD as a smooth cylinder lying on a smooth bed. The initial movement of the LWD is by sliding, though the authors noted that the initial movement tends to be more complex with significant pivoting involved. Figure 2.4 outlines the basic force balance used in the model. The gravity force is the effective weight ($W_{eff} = W_{LWD} - F_{Buoyant}$). The friction force ($F_{friction}$) acts in the upstream direction and is a function of the normal force and the friction coefficient between the bed and the LWD. The drag force (F_{drag}) is a function of the water velocity, flow depth, drag coefficient, and the angle the log is traveling in relation to the flow. The model performed reasonably well under experimental scrutiny though the pivoting, which was not captured by the model, was an important aspect of the LWD motion. The perpendicular and parallel directions of the debris were chosen to represent the most common modes of debris transport, since debris propagating at an angle would pivot into the perpendicular and parallel directions.

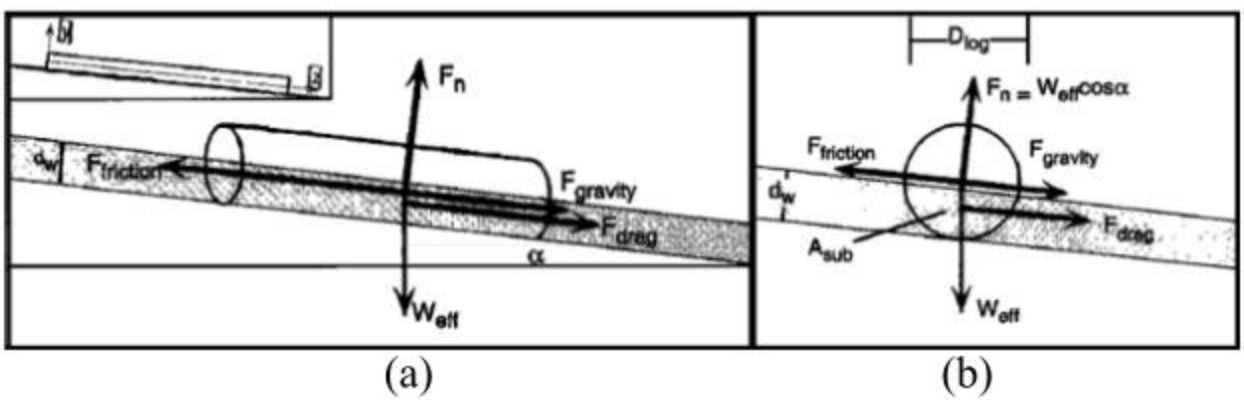

Figure 2.4: Debris entrainment force balance. (a) Debris parallel to flow direction; (b) Debris perpendicular to flow direction (adopted from Braudrick and Grant (2000)).

Imamura et al. (2008) experimentally evaluated the transport of boulders in a dam break flow and developed a simple model for estimating the motion. Imamura et al. (2008) determined that the boulders tended to be transported by saltation or rolling initially (within the higher velocity flow) and when the flow velocity began to decrease, as the bore reached the point of maximum inundation and as the bore receded, the boulders would be transported by sliding. The study also found that the orientation would affect the maximum inundation of the boulder. The boulder would always pivot to have the long axis perpendicular to the flow direction, using some of the available energy, resulting in the boulder initially placed perpendicular to the flow requiring less energy to pivot and therefore having a further inundation distance.

The model developed by Imamura et al. (2008) was based on a force balance of the boulder in contact with the ground. The forces to be consider for the boulder transport are the hydraulic force, the frictional force, and the component of the gravitational force on the slope. The balance of these forces resulted in:

$$\rho_s k_r d^3 X'' = \frac{1}{2} C_D \rho_f (U - v)|U - u|(k_r d^2) + C_M \rho_f U'(kd^3) - (C_M - 1)\rho_f u'(k_r d^3) - k_r F_b - k_r F_g \tag{2.1}$$

$$F_b = \frac{\mu(\rho_s - \rho_f) k_r d^3 g cos\theta\, X'}{|X'|} \tag{2.2}$$

$$F_g = (\rho_s - \rho_f) k d^3 g sin\theta \tag{2.3}$$

Where ρ_s is the density of the boulder, k_r is the ratio between the long axis and short axis of the boulder, d is the length of the short axis, u' is the acceleration of the boulder, C_D is the drag coefficient, ρ_f is the density of the fluid, U is the current velocity, u is the velocity of the boulder, θ is the angle of slope, μ is the coefficient of friction and C_M is the mass coefficient. This model tends to underestimate the propagation of the boulders, likely because the friction was always considered (even if saltation or rolling occurred) and the model does not consider the initial pivoting of the boulder.

Matsutomi et al. (2008) examined the effect of debris concentration on debris velocity as well as the hydrodynamic conditions in a dam break flow. Debris concentration was expressed as the void ratio (1 – plan area of debris/area of flume bed). An increase in the debris concentration resulted in increased flow resistance in the bore front. The flow resistance in turn increased bore depth as well as decreased moving velocity and bore front propagation. The debris velocity was found to be always less than or equal to the bore front velocity.

Matsutomi (2009) evaluated the motion of driftwood pieces in steady-state high velocity flow to determine the probability of the driftwood colliding with a structure. Based on a number of tests, the probability of impact was determined based on the lateral diffusion (y-direction) of the driftwood as the driftwood propagated downstream, therefore assuming that the structure would be in the center of the flume. The probability distribution of the driftwood location (K_y) in x and y was expressed as:

$$K_y(x, y) = \frac{1}{\sqrt{2\pi\overline{\delta_y}}} \exp\left(-\frac{(y - \bar{y})^2}{2\overline{\delta_y}^2}\right) \tag{2.4}$$

Where $\overline{\delta_y}$ is the variance as a function of x (flow direction), roughly expressed as:

$$\frac{\overline{\delta_y}^2(x)}{L_w^2} = \frac{\frac{1}{n}\sum_{i=1}^{n}(y-\bar{y})}{L_w^2} = a\left(\frac{x}{L_w}\right)^b \tag{2.5}$$

Where L_w is the length of the driftwood, a and b are a function of the debris properties and geometry. Extensive work is still needed in the classification of the a and b coefficients due to the variety of debris that are potentially present during a tsunami (Naito et al., 2014).

As a preliminary investigation of debris motion in tsunami-like flow conditions, Yao et al. (2014) evaluated the motion of scaled-down coastal houses in flow conditions developed by the shoaling and subsequent breaking of a solitary wave over a sloped bed (Figure 2.5). The study examined the maximum debris inundation compared to the maximum flow inundation. The debris initially propagated within the overflow of the bore due to high flow velocities and water depths. As the overflow approached maximum inundation, the flow velocity and flow depth decreased resulting in the debris contacting the bed and slowing down, falling behind the bore front. In the case of smaller waves, the debris fell behind the bore front earlier due to contact with the bed. For the most part, the debris was unaffected by the receding flow, except when the debris had grounded significantly earlier and were much closer to the coastline. Figure 2.5 shows snapshots of the bore front propagation (lines) in relation to the debris position (markers). The receding wave, in this case, would pull the debris further seaward than the initial position of the debris.

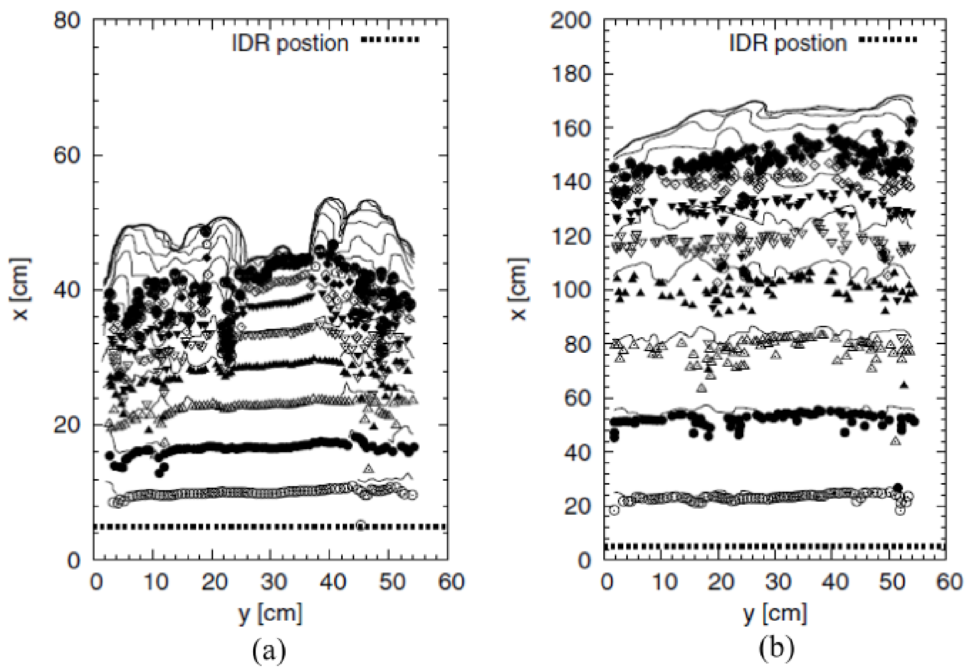

Figure 2.5: Debris motion compared to bore front. (a) Smaller wave height (0.02 m) for 0.167 s time interval; (b) Larger wave height (0.04 m) for 0.33 s time interval (adopted from Yao et al. (2014)).

Rueben et al. (2014) used a novel camera-based tracking algorithm to evaluate the repeatability of the motion of square boxes on a sloped bed. The camera-based tracking algorithm was developed to identify a pattern of dots on the top of each box. The number of dots present on the top of each box was the identifier of each box as well as the orientation. The algorithm performed well for experiments at a larger scale, however for smaller scale experiments the algorithm would struggle to identify the pattern on the top of each box.

Figure 2.6 outlines the results of the repeatability of one box for both the trajectory (Figure 2.6(a)) and the velocity (Figure 2.6(b)) for six experiments. The motion of the debris was generally one-dimensional and repeatable in the flow direction (positive x-direction). Once the debris reached its maximum inundation, the debris would ground and then be washed seaward by the receding wave. The receding direction was significantly more random, potentially due to persistent eddies produced by the grounded debris during the return flow.

Rueben et al. (2014) also examined the effect of multiple debris and a fixed obstacles on the debris motion. For multiple debris, the motion remained qualitatively similar to the single debris case. However, as a result of more debris, the grounding point was significantly closer to the shore and the peak onshore velocity occurred later. Alternatively, in the offshore direction, the peak velocities were similar to the single debris experiments. This is likely due to less disturbance in the local flow fields from debris as the debris had already dispersed. To examine the effect of obstacles, a fixed box was placed in front of the debris to initiate a forced rotation (Figure 2.6(a)). The rotation of the debris resulted in a significantly more random trajectory and grounding point. The obstacle also reduced the peak onshore velocity of the debris, likely as a result of the energy lost in the rotation of the debris.

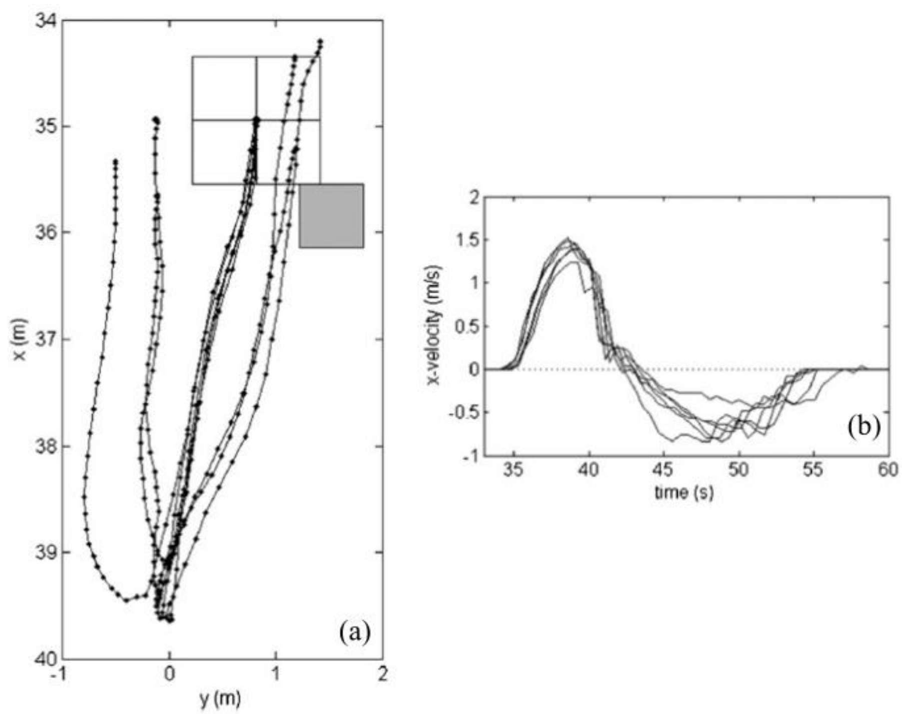

Figure 2.6: Repeatability of debris motion for a single debris. (a) Trajectory of debris; (b) Velocity of debris (adopted from Rueben et al. (2014)).

2.3 Physical Modelling of Debris Impact Loads

The primary approach to the modelling of debris loads has been on the impact force of a single debris on a structure (*FEMA P646*, 2012). As a result, the focus of current tsunami guidelines solely consider the impact of single debris. Nouri et al. (2010) examined the impact of a single wooden log on a structure. The force-time history of the bore and debris impacting the structure are shown in Figure 2.7. The debris impact resulted in an increase in the peak force from 250 N to 650 N (Figure 2.7(a)). Occasionally, the debris impacted the structure a second time (Figure 2.7(b)) resulting in a second smaller peak. Nouri et al. (2010) also examined the impact duration of the debris and found that the impact duration was constant regardless of variation in log mass and velocity.

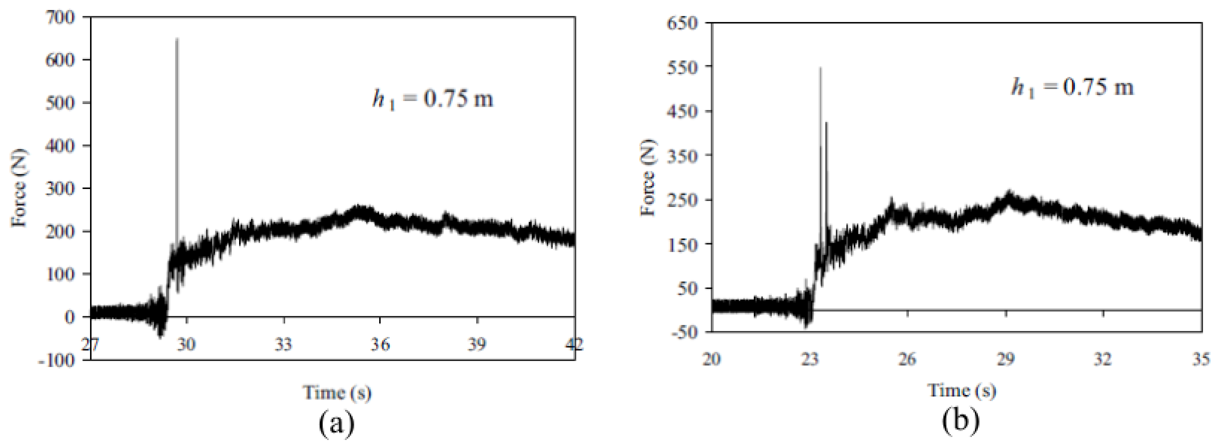

Figure 2.7: Debris impact with a structure in a dam break bore. (a) Single impact with the structure; (b) multiple impacts with the structure (adopted from Nouri et al. (2010)).

The majority of debris impact research has gone into the modelling of maximum debris impact force as the maximum force will determine future design guidelines. The most common approach to the modelling of debris impact is the contact-stiffness method. The debris is modelled as a log impacting a rigid structure (Haehnel and Daly, 2004).

$$F_{i,max} = u\sqrt{k(m_d + C_M m_f)} \tag{2.6}$$

Where u is the velocity of the debris, k is the contact stiffness, m_d is the mass of the debris, C_M is the added mass coefficient (dependent on debris geometry and density), and m_f is the mass of displaced fluid. Matskevitch (1997) included a reduction in the impact force as a result of the eccentricity (e), the relation of the debris center of gravity to the impact axis, and Haehnel and Daly (2004) considered the obliqueness (β) of the impact, the angle of the debris surface to the impact.

$$e = \frac{1}{\sqrt{1 + \left(\frac{\varepsilon_0}{r_i}\right)\left(1 + \mu\left(\frac{r_0}{\varepsilon_0}\right)\right)}} \quad (2.7)$$

$$\beta = sin\varphi \quad (2.8)$$

Where ε_0 is the distance from the center of gravity of the debris to the point of impact, $r_i$is the radius of gyration of the debris, μ is the coefficient of friction between the debris and structure, r_0 is the radius of the log, and φ is the angle of impact relative to the log surface. Haehnel and Daly (2004) examined the effects of eccentricity (Figure 2.8(a)) and obliqueness (Figure 2.8(b)) on the impact force. From the analysis of the impact force, Haehnel and Daly (2004) derived Equation 9. The eccentricity of the impact results in a decrease in the impact force proportional to the distance of the impact away from the center of gravity of the debris. The obliqueness of impact generally decreased in a sine function from a 90^o impact (long axis perpendicular to the structure), however for a 0^o impact, the impact force was at a maximum.

$$F_{i,max} = e\beta u\sqrt{k(m_D + C_D m_f} \quad (2.9)$$

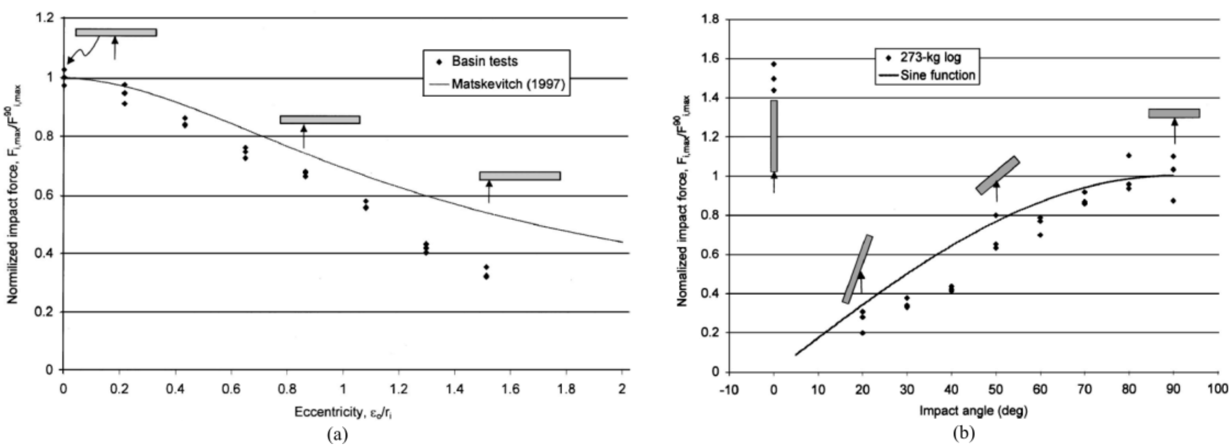

Figure 2.8: Debris impact on a structure. (a) Effect of eccentric impact on structure; (b) Effect of oblique impact on structure (adopted from Haehnel and Daly (2004)).

Riggs et al. (2014) evaluated the added mass coefficient by examining the impact of an aluminum box on a structure in-air and in-water. The in-water tests were performed by connecting an aluminum specimen to guidewires within a flume. The flume used a long wave generator to generate a wave that propagated the aluminum specimen along the guidewire towards the structure. The in-air tests were performed by connecting the aluminum specimen to a pendulum system that accelerated the specimen to a velocity matching the velocity in the in-water tests. As can be seen in Figure 2.9, there is very little difference in the peak impact force between the in-air and in-water tests. The slight difference in impact forces is represented by the added mass of water that needs to also be decelerated with the impacting debris. Moreover, Riggs et al. (2014) determined that the difference in impact force was unaffected by the debris impact velocity. Therefore the findings do not support the use of the added mass coefficient in the evaluation of debris impact force.

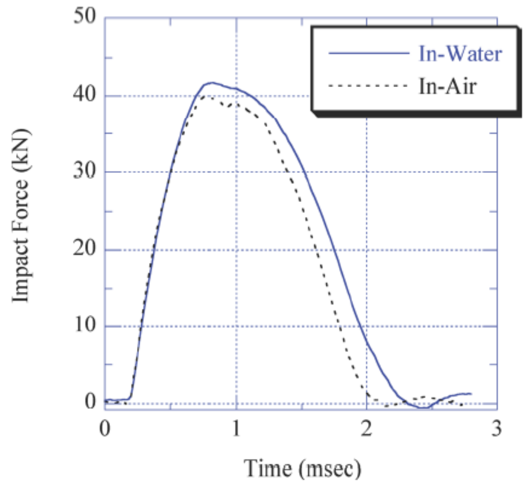

Figure 2.9: Impact testing of in-water (blue line) and in-air (black dotted line) of aluminum specimen on a structure (adopted from Riggs et al. (2014)).

Aghl et al. (2014) expanded upon the work by Riggs et al. (2014) to develop a one-dimensional bar model that accurately estimated the impact demand of a debris impact event. The model once again considered the structure to be rigid therefore the impact force was completely dependent on the properties of the debris. The impact force (F) was derived from the 1D wave equation, assuming the debris responds uniaxially to the impact (Equation 10). The impact force equation was very similar to that of the contact-stiffness approach (Equation 6) without the added mass of the fluid. For the 1D wave equation to be correctly evaluated the stiffness of the debris must be considered as the equivalent stiffness of a 1D bar (k_d) (Equation 11).

$$F = u\sqrt{k_d m_d} \tag{2.10}$$

$$k_d = \frac{EA_d}{L_d} \tag{2.11}$$

Where u is the impact velocity, m_d is the mass of the debris, E is the Young's modulus, A_d is the cross-sectional area of the debris, and L_d is the length of the debris. The derived formula also resulted in a constant impact force for the duration of the elastic impact, resulting in a rectangular impact pulse with a duration of t_d.

$$t_d = 2\sqrt{\frac{m_d}{k_d}} \tag{2.12}$$

Aghl et al. (2014) evaluated the 1D bar model with in-air experiments performed by accelerating debris (at full scale) into structures using a pendulum system. The experiments were performed with a wood pole, steel tube, and shipping containers. Figure 2.10 shows the results of the impact of shipping containers impacting the structure compared to the impact model (solid black line).

The force and time were non-dimensionalized using the impact model results. The peak impact force was estimated within 5% for all the impact experiments. The impact duration was also well predicted in the cases of direct or close to direct impact of the shipping container (Figure 2.10(a)-(b)), however as the container impacted at the corners the impact was not elastic, as was modelled, resulting in a significant difference in the analytical and experimental impact duration. Each debris impact had a characteristic shape: half-sine (wood pole), rectangular (steel tube), and trapezoidal (shipping container). For all experiments, the impulse (area under the curve) for the impact model was less than the experimental results, quantified by the impact ratio (IR), indicating that the impact model is a conservative estimate of the impulse.

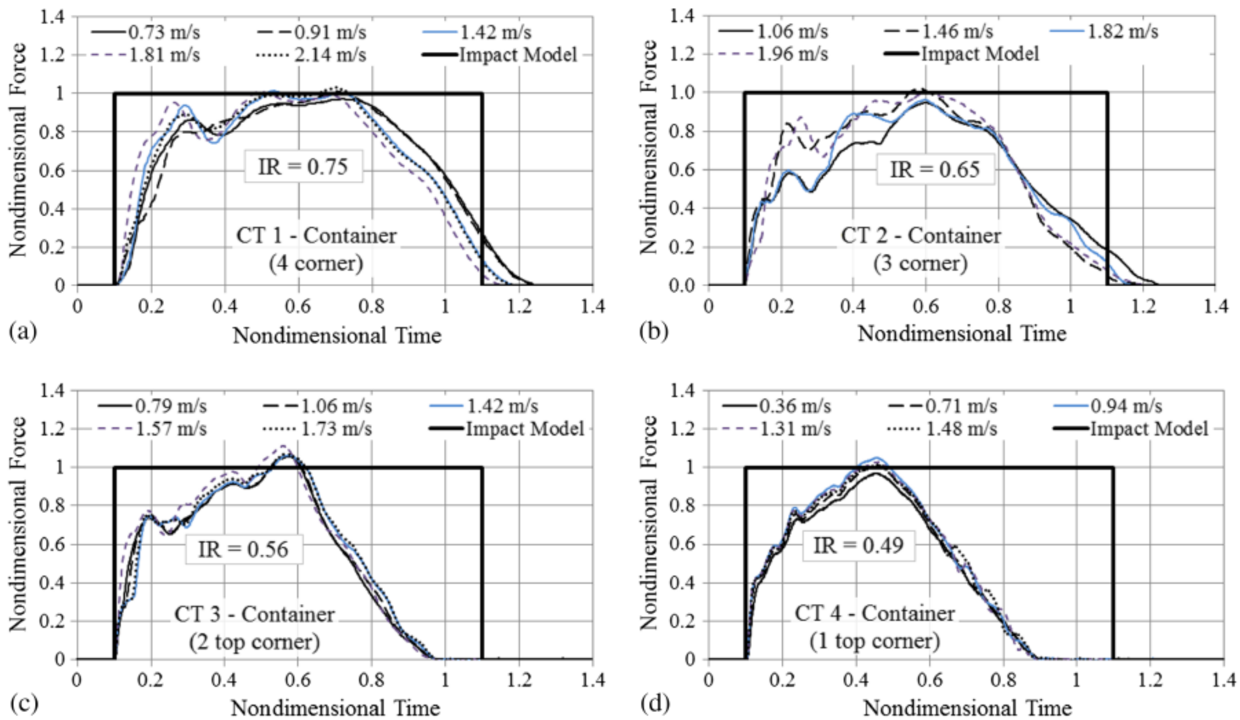

Figure 2.10: Force-time history of in-air shipping container experiments. (a) Direct impact of the shipping container with structure (all four corners impact); (b) three corners impact structure; (c) two top corners impact structure; and (d) one top corner impacts structure (adopted from Aghl et al. (2014)).

Al-Faesly (2016) examined the impact force of debris entrained within dam-break flow conditions with different debris geometries. Al-Faesly (2016) determined that the slenderness ratio of the debris (length of debris/diameter of debris) affected the maximum velocity of the debris, which in turn influences the maximum impact force. The position of the debris within the bore also had a significant effect on the impact forces as debris entrained further behind the bore front tended to run-up the structure, resulting in larger impact angles and therefore smaller impact forces. Similarly to Haehnel and Daly (2004), Al-Faesly (2016) determined that the impact force of the debris was a function of the debris velocity and debris orientation. Al-Faesly (2016) also noted that the distance between the long axis of the debris and the central axis of the structure was critical in evaluating the debris impact force.

Debris entrained within the flow can also result in additional loads on structures, particularly when the debris forms a dam in front of the structure or between columns, referred to as debris damming or accumulation (Robertson et al., 2007). The hydrodynamic force on a structure can be estimated by using a similar equation to the drag force (F_D):

$$F_D = \frac{1}{2} C_D \rho_f A U^2 \tag{2.13}$$

Where C_D is the drag coefficient, ρ_f is the density of the fluid, A is the cross-sectional area, and U is the flow velocity. The debris dam created by the debris will increase the cross-sectional area, which will in turn increase the hydrodynamic force (Yeh et al., 2014).

From river engineering, within which debris damming has been extensively studied due to the build-up of debris at bridge piers, depending on the shape of the structure the drag coefficient may vary as a result of the dam (Parola, 2000). The dam creates a blockage, further restring the flow path, the blockage results in a large increase in the flow depth. The debris dams also can result in increased scour as they tend to re-direct the flow pattern resulting in increased scour underneath the debris dam (Pagliara and Carnacina, 2013).

The objective of the present study does not aim to evaluate debris impact and damming loads on structures, however the examination of the variables considered when evaluating debris impact forces are important to focus on the information that will be relevant for future research. From this review, debris velocity is clearly the most important variable to consider when evaluating debris impact force as velocity appears in all of the equations for determining impact force. Orientation also is important in determining the obliqueness of impact, which Haehnel and Daly (2004) determined was important in evaluating peak impact forces and can also play an important role in determining if a debris dam will form (Bocchiola et al., 2006).

2.4 Numerical Modelling of Debris Motion

The numerical modelling of fluid-solid interactions is a common issue in several fields of engineering. One of the primary issues is the numerical model needs to be able to reproduce all the physically relevant scales that affect the fluid-solid interaction (Canelas et al., 2015). However, the physical scales that affect the interaction are often not clear, resulting in these models requiring a high level spatial and temporal resolution. This difficulty has led to attempts to simplify the fluid-solid interaction by providing one-way coupling between the phases. One-way solid-fluid coupling considers the solids as massless marker particles that moved unconstrained on the water surface (Wu et al., 2014). One-way fluid-solid coupling causes the solids to move in relation to the fluid without the solids affecting the fluid. The one-way coupling methods can provide good results if the scale of the interaction between the phases are disproportionate in one direction, however for many cases this is not the case. Two-way dynamic coupling of fluid and solid numerical solvers have increasingly become more popular as computational resources have scaled to be able to handle the required demands of the two-way models but the investigation is still very much in the early stages.

Lou and Jin (2014) applied an Arbitrary Lagrangian Eulerian (ALE) model within LS-DYNA to estimate the collision force of objects drifted by wave run-up. Due to the high computational cost associated with the ALE model, the calculation needed to be performed on a Dawning supercomputer. The ALE model used the incompressible Navier-Stokes equations (Equation 14-15) and tracked the free-surface using the Volume-of-Fluid (VOF) free-surface tracking technique. The fluid structure interaction was modelled using an equation of St-Venant's elastic bodies (Equation 16).

$$\rho_f \frac{\partial v_t}{\partial t}|_\chi + \rho_f c_j \frac{\partial U_i}{\partial \chi_j} = \frac{\partial \sigma_{ij}}{\partial \chi_j} + \rho_f b_i \tag{2.14}$$

$$\frac{\partial \rho_f}{\partial t}|_\chi + c_i \frac{\partial \rho_f}{\partial \chi_i} + \rho_f \frac{\partial U_i}{\partial \chi_i} = 0 \tag{2.15}$$

$$\rho_{st} \frac{\partial^2 d}{\partial t^2}|_X = \frac{\partial \sigma_{ij}}{\partial x_i} + f_i \tag{2.16}$$

Where b_i represents the body force, U_t is the fluid velocity field, χ is the ALE coordinate systems, ρ_f is the density of the fluid, c_j is the ALE convective velocity, X is the Lagrangian based coordinate system, ρ_{st} is the density of the structure, and d is the displacement of the structure. The structure and fluid are coupled through specific nodes and a penalty method was introduced to track the relative displacement between the coupling nodes which is proportional to the force.

Lou and Jin (2014) used the ALE numerical model to evaluate experimental results of two debris types: vehicle and shipping container; impacting a breakwater with a solitary wave acting as the forcing condition. Each debris type was examined for three different weights: empty, half-loaded, fully-loaded. Due to the penalty method imposed on the fluid-solid interaction the draft of the debris was slightly larger than that calculated using force balance. The force-time history can be observed in Figure 2.11. The loaded containers reached their global maximums at a different time than the empty container due to the difference in drafts. As the containers contact the breakwater, the contact area between the water and the breakwater decreased resulting in a decrease in the wave force. Once the containers have passed over the breakwater this no longer occurs, and since the empty container immediately passed over the breakwater, this phenomena did not occur.

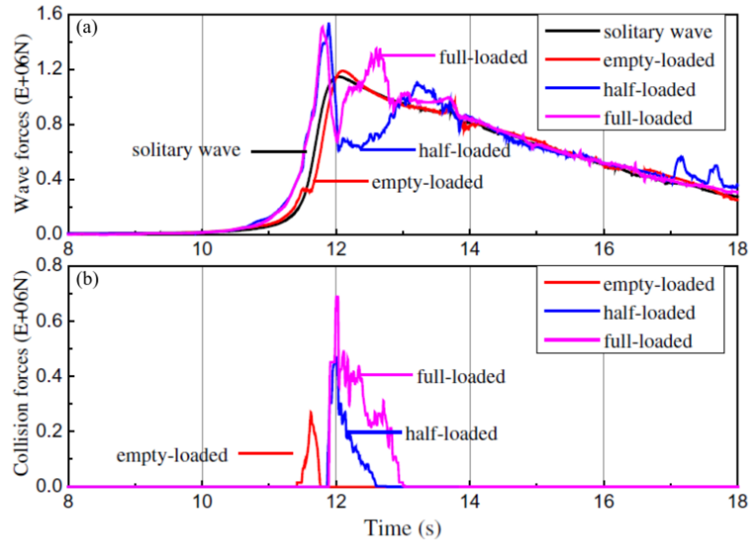

Figure 2.11: Impact Forces on a breakwater. (a) Wave forces; (b) impact forces (adopted from Lou and Jin (2014)).

Wu et al. (2014) used the Navier-Stokes equations with the VOF free-surface tracking technique, and used a Large Eddy Simulation (LES) model as the turbulence model to calculate the flow field around the solids. Additionally, Wu et al. (2014) used Partial Cell Treatment (PCT) to locate the faces of the solids. The basic principle of the PCT is similar to the VOF method where each cell was assigned a value between zero and one indicating the phases present in the cell. When the solid phase was present within the cell, the cell is assigned a porosity that reduces the effective volume of the cell, and in the case where the cell was completely solid, the cell was removed from the Navier-Stokes equation calculations. The calculated porosity was used to adjust fluxing quantities, such as momentum and mass. The motion of the floating body was determined using the Discrete Element Method (DEM) to calculate the translation and rotation. The translation was calculated using Newton's equations of motion and the rotation was calculated using Euler's equations. The forces on the solid were calculated by integrating the fluid pressures on the surface of the solid.

The model from Wu et al. (2014) was validated using two laboratory experiments: a positively buoyant box in a tank of water and a negatively buoyant box in a tank of water. The boxes were released in the tank and the motion of the box was tracked using cameras. The model showed a generally good comparison between the numerical and experimental results with the maximum difference in displacement of 0.0044 m. The difference was due to the numerical simulation showing the negatively buoyant box rebounding off the bottom of the tank whereas the experimental results showed no such phenomena.

Smoothed Particle Hydrodynamics (SPH) has increasingly been used in the modeling of free-surface flows (Gomez-Gesteira et al., 2012) and has been shown to be able to simultaneously deal with multiple body dynamics (Amicarelli et al., 2015). However, very few current models can capably handle the transport of moving bodies in free-surface flow. Primarily, the current models have modelled the moving bodies as a rigid body of Moving Particle Simulations (MPS) fluid particles with an imposed rigidity (Canelas et al., 2013). While the models had achieved generally good results (Manenti et al., 2008, Rogers et al., 2009), the modelling of the interactions between the body and the fluid were not based on rigid body contact laws (Canelas et al., 2013).

Canelas et al. (2013) incorporated a DEM model where the inter-particle rigid body forces are taken from rigid body contact laws. The boundary particles of the rigid body are taken as fluid particle allowing the DEM model to be coupled with the SPH model. The contact force between the fluid and rigid body particles are decomposed into a repulsion force, which also takes into consideration the deformation of the particle, and a damping force, to take in consideration for energy lost during deformation. The coupled model was validated using a dam break experiment entraining PVC cubes (shown in white Figure 2.2). The top of Figure 2.2 shows the experimental results whereas the bottom shows the results of the SPH model. While the model and the experimental results had qualitatively similar results, the study noted that that the bottom friction was not properly modelled resulting in the motion of the debris (particularly of the bottom box) to lag behind the experimental results. Moreover, due to the high computational cost associated with the coupled model resulted in the particle resolution being too low to properly resolve the water surface and bore profile.

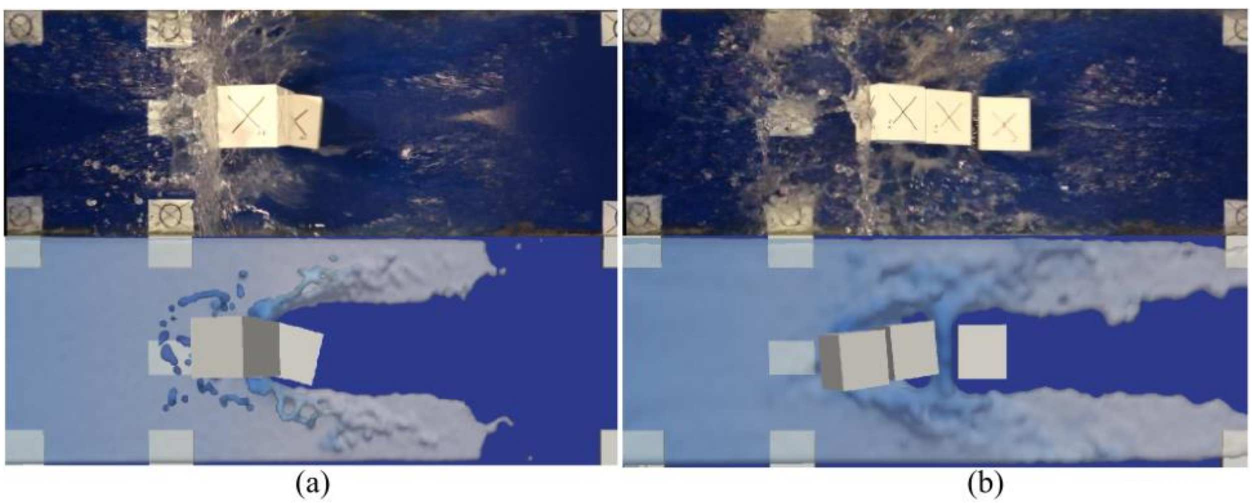

Figure 2.12: Comparison of experimental (top panes) and SPH-DEM coupled model (bottom panes) for two time intervals (adopted from Canelas et al. (2013)).

Amicarelli et al. (2015) modelled the moving bodies using the MPS method, however used a modified boundary condition, proposed by Adami et al. (2012), for a more stable pressure gradient around the moving bodies. The solid-solid interactions were also adjusted by the addition of a coefficient to the repulsive boundary conditions proposed by Monaghan (2005) to better preserve global momentum and kinetic energy through the body-body interactions. The SPH model was validated using a 2D wedge falling into a water tank. The study compared the acceleration of the experimental and numerical model with generally good accuracy (Figure 2.13). The authors did note some spurious fluctuations of pressure resulting in some of the error seen in Figure 2.13. The pressure fluctuations are a commonly noted problem with SPH models (Gomez-Gesteira et al., 2012, St-Germain et al., 2013).

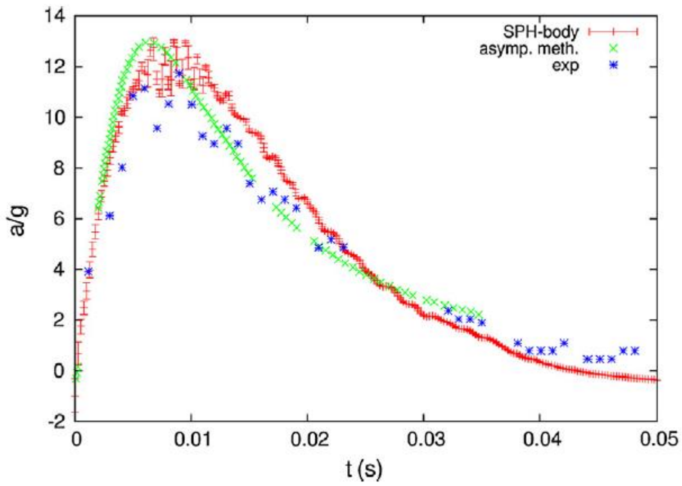

Figure 2.13: Normalized acceleration of 2D wedge entry into water tank (adapted from Amicarelli et al. (2015)). SPH model (red), semi-analytical solution (green), and experimental (blue).

The numerical model used in Amicarelli et al. (2015) was also used to qualitatively examine 3D test cases where debris interacted with a bore front and two sets of obstacles. The bore was developed using a dam break and the debris was tracked using cameras. The numerical model resulted in good results when comparing both the trajectory and the orientation of the debris was relatively well reproduced. The presence of the obstacles resulted in the formation of recirculation zones in front of the obstacles furthest downstream and the body dynamics were maintained through this highly non-linear zone.

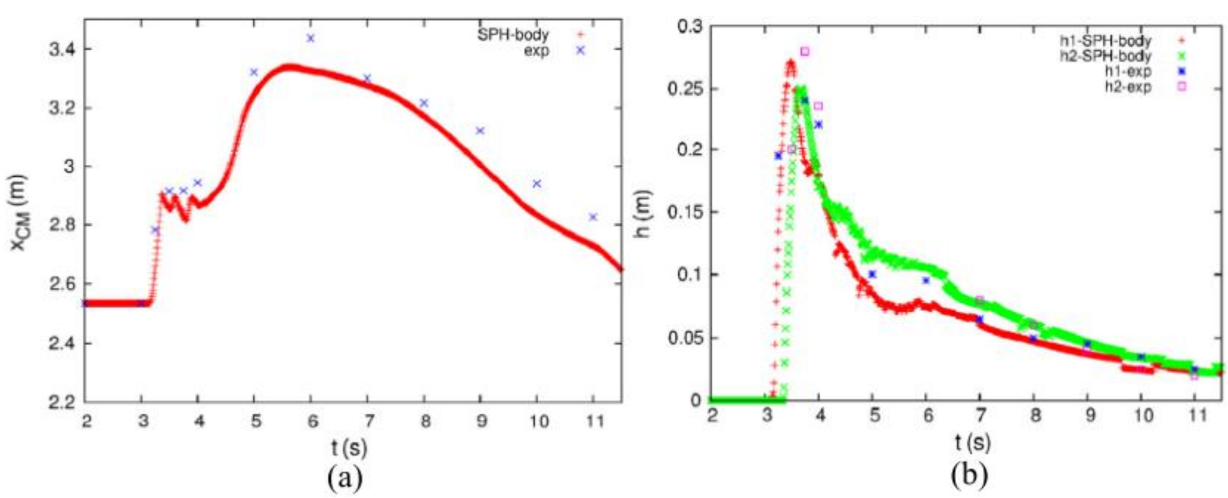

Figure 2.14: Comparison of SPH model and experimental results of debris transport in dam break conditions. (a) Debris transport in the flow direction; (b) Water surface elevation (adopted from Amicarelli et al. (2015)).

Canelas et al. (2015) presented the most recent version of the DualSPHysics with its many improvements on current modelling of fluid-solid interactions. The primary difference in the model presented by Canelas et al. (2015) was the addition of a δ-SPH term to the continuity equation which helps in the interface description between the solid and fluid phase. The rapid change in the density at the interface results in the pressure and density fluctuations that can be seen in many SPH fluid-solid modelling. The SPH model showed promising results when examining the rising of a submerged positively buoyant cylinder. The SPH model compared well to the analytical solution for the linear acceleration when the Reynold's number was laminar and showed a noticeable shift in acceleration as the boundary layer transitioned to turbulent flow (Figure 2.15(b)). The model also showed the stabilisation of the density fields indicating that the δ-SPH term helping handle that particular common problem.

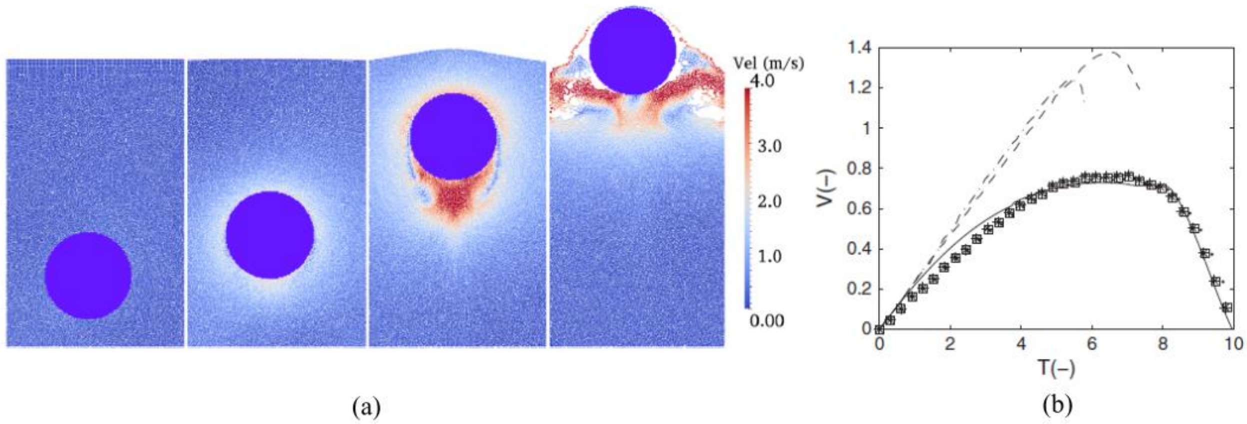

Figure 2.15: SPH model of a positively buoyant cylinder in a water tank. (a) Time lapse of the rising cylinder; (b) Comparison of SPH model (black squares) to analytical solution (dashed line) and VOF model (solid line) (adopted from Canelas et al. (2015)).

While the work by Canelas et al. (2015) and Amicarelli et al. (2015) showed a lot of promise in the SPH fluid-solid modelling, there is still many issues that have yet to be thoroughly evaluated. Amicarelli et al. (2015) presented a method of handling solid-solid interactions, the contact mechanics were never evaluated. Canelas et al. (2013) coupled the SPH model with a DEM, however the large computational cost associated with the coupling makes the use of the coupled model unfeasible for many studies. The addition of solid deformation and inelastic collisions would also greatly improve the applicability of the model throughout coastal and hydraulic engineering.

2.5 Discussion

Debris motion and entrainment in tsunami engineering, to this point, has been examined in few and limited studies. Based on the extensive literature review conducted as part of the current research, the following points are important considerations in the evaluation of debris dynamics:

- The spatial and temporal scaling of tsunami wave conditions in a laboratory setting is one of the most challenging problems in tsunami engineering. Currently, the most promising methods of developing appropriate bore front and time scale conditions are the elongated solitary wave (Goseberg et al., 2013) and the dam break wave (Chanson, 2006).
- Forensic engineering surveys have identified debris loading as an important parameter for structures located in the impact zone of tsunamis condition, yet determining debris motion and impact forces are difficult after the event has occurred due to the large

quantities of debris entrained with inundating tsunami surges and difficulties determining the source of the debris (Naito et al., 2014).

- Debris can have a wide variety of properties: Naito et al.'s (2014) examination of the 2011 Tohoku tsunami determined debris could range from construction materials to shipping vessels.
- Experimental modelling has been difficult due to the random nature of debris motion and the research has clearly shown that there are many variables that affect the motion of debris, from debris type to obstacles to hydrodynamic conditions (Matsutomi, 2009). However, the general characteristics of the debris motion have been found to be repeatable (Rueben et al., 2014, Yao et al., 2014).
- Hydrodynamic conditions and the buoyancy of the debris dictate the type of motion of the debris (sliding, saltation, or floating), which in turn affects their maximum spreading and velocity (Imamura et al., 2008).
- From extensive debris impact tests, the critical properties of debris motion for determining maximum impact forces were identified as their velocity and orientation (Haehnel and Daly, 2004, Nouri et al., 2010, Aghl et al., 2015).
- The orientation of the debris can significantly affect the debris entrainment process (Braudrick and Grant, 2000) and can also affect the formation of debris dams on structures (Bocchiola et al., 2006).
- The numerical modelling of debris motion has also shown significant progress in developing modelling techniques that are capable of evaluating debris motion. Recent progression in coupled two-way solid-fluid solvers potentially offer more accurate solutions for debris motion (Canelas et al., 2015).

To aid with both the understanding of debris motion and entrainment as well as future numerical modelling research, a systematic evaluation of debris motion is needed to provide high-quality data and insight into the debris motion aspects. Based on the literature review conducted by the author, the focus of this study is to:

- Develop non-invasive tracking techniques for the rapid and accurate evaluation of debris motion, particularly focusing on the trajectory of the debris, on determining critical areas for debris impact, as well as estimating the debris velocity and orientation to evaluate potential maximum impact forces.
- Examine the maximum spreading of debris and compare those results to the limited and conservative estimates of debris spreading proposed from field surveys of tsunami affected areas.
- Examine the entrainment of debris in tsunami flow conditions, particularly focusing on the effect of debris entrainment on the overall motion of the debris.
- Evaluate the relative repeatability of debris motion, to evaluate whether a probabilistic analysis of debris motion pattern is a valid approach to debris motion.
- Evaluate the acceleration and maximum velocity of the debris. As the velocity controls the maximum impact forces, determining the magnitude and instant of the maximum impact velocity is essential in determining critical loads on structures.

Chapter 3. Non-invasive Spatio-Temporal “Smart” Tracking in Turbulent Flows with Application to Debris-laden Tsunami Inundation (JHE-ASCE, 2016)

3.1 Introduction

3.1.1 Motivation

Violent hazardous flows occur in conjunction with natural disasters such as tsunamis (Fritz et al., 2006, Goseberg, 2013), flash floods, and storm surges. Such extreme flows are occasionally initiated as a result of technical failures of man-made structures such as dams or dikes triggered by earthquakes, riverine floods and malfunction of the hydraulic discharge systems followed by overtopping (Pilotti et al., 2011). Depending on the triggering source, such violent flows may significantly vary spatially. Tsunami waves can affect coastlines either regionally or globally in correlation with the location and magnitude of the triggering earthquake or landslide. In the case of storm surges, their spatial extent may cover hundreds of kilometres along a coast whereas wave fronts of rapid riverine flooding, flash floods, dike and dam breaches usually affect regions adjacent to the river pathway over various distances. Although the spatial pattern of these phenomena is likely to differ, they all have in common one element: a transient nature combined with rapid spatio-temporal changes in the water level and associated velocities. Wave fronts exhibit steep bore-like surface elevation gradients (Chanson, 2006) as well as abrupt changes in velocity and strong turbulence intensity. The hydraulic features of violent flows thus have the potential to entrain enormous amounts of sediment and debris.

In this context, large pieces of debris or boulders conveyed by the violent flow pose specific danger to engineered structures (Como and Mahmoud, 2013, Piran Aghl et al., 2015) and the particles’ spatio-temporal position and orientation is thus of importance. Amongst those structures are evacuation shelters, bridge piers, breakwaters, and lifeline infrastructure which should resist the impact load with minimum damage. Apart from single debris impact events, multiple debris impacts are conceivable as recently documented through extensive media coverage during the 2011 Tohoku Tsunami.

The integral structural response of an engineered structure or that of individual members of the structure with respect to the drag, surge, and impact hydrodynamic loading was determined experimentally (Nistor et al., 2009). However, it was challenging to separate the load component of individual impact events from the base shear force measurements acquired by the dynamometer mounted on the base of the structure impacted by hydraulic bores. Determining the scale effects as potentially being induced by the unscaled air bubbles in the advancing bore front

(Chanson, 2009) and the magnitude of potential multi-debris impact events under such conditions is even more complicated.

The separation of hydrodynamic and impact forces in laboratory conditions requires the measurement of the debris position, orientation as well as its 3D acceleration in time and space in order to derive inertial forces based on Newton's 2nd law for each single piece of debris. Based on sensor data, individual debris impact events can be determined.

3.1.2 Objectives and novelty of research

To shed light on the debris spreading occurring during the on-land propagation of tsunami-induced inundation or during the motion of a dam-break wave (Naito et al., 2014) and on the subsequent loading of structures due to their impact (Nouri et al., 2010), a measurement system which is capable to record individual position, orientation and inertial acceleration of debris pieces has to be developed. Such as system termed herein "smart" debris (Shafiei et al., 2014) is presented and discussed in this study. In this regard, wireless sensors recently proved to be beneficial in a study by Tsakiris et al. (2015) who assessed the parameter frame under which the burial depth of radio frequency identification RFID transponders can be determined for the use in scour and riverine applications. However, the determination of the position, orientation, and inertial forces of single debris pieces carried by turbulent flows remains a challenge in hydraulic and coastal engineering. Thus, the objective of this paper is to present and discuss a new experimental technology and method to acquire information related to multiple floating or partially submerged debris in a non-intrusive manner, under the constraint that visual detection is not a priori needed. The goal is also to advance the state-of-the-art of the current experimental tools used to track individual objects in 6DOF in a non-intrusive, yet accurate manner.

3.1.3 Literature review – Debris motion and debris tracking

Each unconstraint object moving in space has three translational and three rotational degrees of freedom. Hence, six degree of freedom (6DOF) object tracking aims at determining the spatial positions and orientations of a given object. Object tracking which oftentimes simply refers to their spatial position rather than holistically including also their orientation is of interest in a vast number of different science and engineering fields. Typical applications include detecting and tracking single pedestrians, groups and their dynamics (McKenna et al., 2000), planning path for autonomous robots (Ge and Cui, 2000), underwater autonomous vehicle navigation (Lee et al., 2012), planning of urban military operations (Rantakokko et al., 2011), and controlling a helicopter flight by means of visual positioning in the field of aeronautics (Amidi et al., 1999). To a significant extent, computer and machine vision applications rely on camera- or video-based data recording for their object tracking. Vision-based methods however render problems in disambiguating occlusions of particular objects in given images (McKenna et al., 2000) which typically occurs in cases of floating or partially-submerged debris. A non-exhaustive list of alternative techniques capable to track objects comprises infrared radiation, active RFID (Ergen et al., 2007), ultrasonic waves (Addlesee et al., 2001), wireless local area network (Khoury and Kamat, 2009), and Bluetooth techniques (BT) (Lu et al., 2007).

The use of object-tracking devices relying on electromagnetic waves such as RFID, WIFI or BT is intrinsically difficult in hydraulic and coastal engineering since strong attenuation occurs as the propagating waves are subject to density jumps such as air-water interfaces or even by propagating through moist air (Gibbins, 1986). However, it has been analytically shown by Jiang and Georgakopoulos (2011), that electromagnetic waves are capable to penetrate through air-water interfaces. The transmission and propagation losses depend to a great extent on the frequency range at which the signal is sent: lower frequencies are more advantageous as they allow for deeper electromagnetic wave penetration when compared to the higher frequencies. The second important factor for the transmission of electromagnetic waves is conductivity which is lower for fresh water compared to the sea water, thus making this technology more suitable for applications in riverine or laboratory environments involving freshwater (Benelli and Pozzebon, 2013).

To date, off-line location detection based on the available electromagnetic wave-based systems has rarely been applied to hydraulic and coastal engineering problems. Benelli et al. (2012) used RFID at 125 kHz frequency to trace pebbles on an Italian coastline to monitor beach morphology. The RFID tags were attached to regular pebbles which were then manually released into the swash zone. A percentage of 53% of the pebbles were then recovered within a range of 0.40 m in a-posteriori campaign after a major storm event. Linear trajectories and main transport paths were thereby reconstructed from the application of RFID technology. Allan et al. (2006) used a passive RFID system to study the evolution of beach morphology. They were able to detect individual gravel stones after a storm event in up to 1.0 m depth with reasonable detection rates and were also able to quantitatively determine the long- and cross-shore tracer transport rates. Another RFID system was successfully applied in river hydraulics to recover tagged tracers by Nichols (2004) with the purpose of testing laboratory-based sediment transport formulations against field data. A tracer recovery rate of up to 96% was reported and the system was classified to provide reliable information even under difficult field conditions in a low cost manner. A similar study by Lamarre et al. (2005) used RFID tags to trace individual clasts in the Moras Creek with a bottom slope of 2% in Quebec, Canada with great success.

To the authors' knowledge, aside from the determination of the 3-axis orientation of the debris, their online location detection has not been reported in the hydraulic engineering literature. The application of refined, modern measurement technology has the capability to unlock further potential in the fields of hydraulic and coastal engineering.

3.2 *"Smart" debris*: System description

3.2.1 Design

The "smart" debris system is designed to record the trajectory, orientation and inertial acceleration of an individual object using a Lagrangian approach. The system consists of Bluetooth-based sensor components to determine the position and an additional motion-sensor to record debris rotations. Both system components are fitted in a water-proof housing inside the debris. In the present study, this is a down-scaled 20-feet-shipping container, whose dimensions are: $l \times w \times h = 0.15 \times 0.06 \times 0.06\, m^3$. Although this debris was particularly chosen to study floating container dispersion due to turbulent flows, smaller housing dimensions are conceivable with an minimum inner dimension with a length, width and height of 0.05, 0.03 and

0.015 m, respectively. Figure 3.1 presents the individual components of the “smart” debris system.

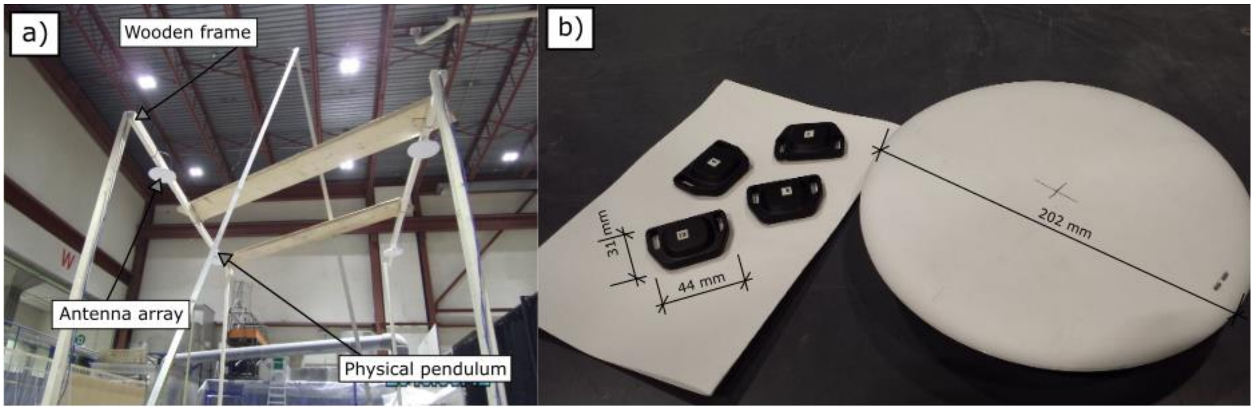

Figure 3.1: Photographs of the individual components of the “smart” debris system. a) Antenna array of the Quuppa system with antennae (white discs), b) single antenna (right) and a number of RFID tags.

The position and orientation tracking system comprises of low-cost of-the-shelf instrumentation units which were integrated into the described “smart” debris system. As shown in Table 3.1, cost for a motion sensor unit at the time of writing was approximately 200 US$. The real-time locating system (RTLS) which is fully scalable with respect to the number of antennae and tags was purchased as a demonstration system for indoor deployment with 25 RFID tags and 5 locator antennae. Cost for the system was approximately 200 US$ at the time of writing, but may significantly differ if the spatial application scale alters.

3.2.2 Detection of debris spatial position

For the determination of their spatial position, the “smart” debris system uses a RTLS. This technology was selected for its most important performance indicators: accuracy, range, sampling frequency, and cost (Marco et al., 2008). Following thorough product review of these indicators, the technology provided by Quuppa Oy (www.quuppa.com) was selected. The applied system adapts a radio technology (radio frequency triangulation) based on a modified Bluetooth Low Energy (BLE) standard. Modifications by Quuppa to the existing BLE standard used were aimed at improving positional accuracy and the estimation of the angles (azimuth, elevation) between a BLE tag and a connected BLE locator by calculating the angle of arrival of the BLE signal. Table 3.1 presents a list of specifications for the debris position measurement. These were found using so-called battery-power tags and locators (beacons) which were able to detect the angle-of-arrival of a radio signal in an interference-free 2.4 GHz band emitted by the tags. Two types of locator antenna are available: an indoor antenna intended for ceiling mounting of up to 12 m height and an outdoor version with a range of up to 300 m leading to sub-meter accuracy (Oy, 2014). For the indoor antennae system, Ham (2015) found that the antenna range extended up to 50 m under undisturbed conditions. The number of locators and their position and orientation in space determined whether and how accurate the system detected the position of the tags attached to a moving object. The reference coordinate system in which the position of tags is reported was defined using a software planning tool (Site Planner & Deployer Tool (SPD), version 4.2, license ‘Ultra’). The planning tool also assisted the authors during the deployment process.

Table 3.1: List of sensor specifications used for the “smart” debris system.

	3D Position	3D Orientation
Manufacturer	Quuppa Oy (www.quuppa.com)	YEI Corporation (www.yeicorp.com)
Product	High Accuracy Indoor/Outdoor Positioning Demo System (Indoor Antenna LD-6L with nominal range of 12 m)	TSS-DL (3-Space Data-logging)
Nominal accuracy (meters or degrees)	± 0.1 m	± 1°
Latency (ms)	100	-
Nominal Sampling rate (Hz)	100	250 (AHRS), 1000 (IMU)
Working principle	Radio technology, BLE	Blend of accelerometer, gyroscope, magnetometer
Number of units to operate	< 25 (limit of the test system)	Standalone, unlimited
Approximate Unit Cost (at time of writing)	~ 200 US$ (per RFID tag including peripheral hardware share)	~ 250 US$

The debris positional raw data were recorded as a single ASCII-format file and further processed using an exponential moving average and a Kalman filter supported by the positioning engine. In this study, a custom Kalman filter has been implemented using a Matlab-code developed to account also for the error estimations for the system.

3.2.3 Kalman filter

A linear Kalman filter was used to improve the accuracy of the measured spatial position recordings output by the real-time location system assuming measurements to be biased by constant white noise (Anderson and Moore, 1979, Hayking, 2001). The equation of state (state vector with spatial coordinates) for the position measurements for time step *k* reads:

$$x_t = \begin{bmatrix} x \\ y \\ z \end{bmatrix} \tag{3.1}$$

The underlying process model described by Kalman filter notation is expressed as follows:

$$\overline{x_t} = \phi x_{t-1} + Bu_t + w_t \tag{3.2}$$

Matrix ϕ denotes the state transition model referring to the time step *t–1*, while the optional control input term, Bu_t, is zero in the current case as the "smart" debris has no quantifiable external input controlling its trajectory during motion. The vector w_t represents the normal distributed process noise (zero mean, Gaussian white noise) with covariance Q. This covariance matrix, Q, was in this case estimated based on the moving average filtering technique of the originally recorded measurements. Furthermore, a model measurement is related to the current true state of the system to the measurements *z* at the time step *k* through matrix C_t. This measurement model reads:

$$z_t = Cx_t + v_t \tag{3.3}$$

Measurements are biased by instrument or calibration errors: thus, an appropriate associated measurement noise v_t (zero mean, Gaussian white noise) had to be added.

The predictive step forecasts (index *t*) a system state, x_t^f, and provides a measure of the error associated with this estimate, P_x^f, based on the obtained previous measurements and the error covariance. A corrective (index *c*) step then optimizes the previous forecast step by minimizing the error covariance, P_x^c. The current prediction x_t^c is combined with current measurements to refine the state estimate. The correction step is accomplished by the following equations describing the corrected system state x_t^c and its associated error covariance P_x^c:

$$x_t^c = x_t^f + K_t\left(z_t - C_t x_t^f\right) \tag{3.4}$$

$$P_x^c = (I - K_t C_t)P_t^f \tag{3.5}$$

In this correction step, the so-called Kalman gain K_t, a weight between the forecasted and measured data, was computed as follows:

$$K_t = P_t^f C_t^T \left[C_t P_t^f C_t^T + R_t\right]^{-1} \tag{3.6}$$

The estimation of the internal, hardware-dependent errors of the debris position system is accomplished through internal routines provided by the manufacturer and output as a time-depending covariance matrix. However, the process error covariance for the position system tags exposed to various tested motions was not identifiable and thus, the window length for the moving average filtering technique was adjusted by trial-and-error to optimize the Kalman filter performance.

3.2.4 Detection of debris orientation

A low-cost motion sensor manufactured by YEI Corporation was used to record 3D (three-dimensional) debris orientation and their inertial accelerations. The motion sensor consisted of tri-axial, temperature-compensated, on-board chipset sensors which recorded the acceleration, gyration, and strength of magnetic field. Without prior data analysis, the motion sensor serves as an inertial measurement unit (IMU) recording at a sampling frequency of up to 1 kHz. By means of sensor fusion (temperature-compensated integration of 3-axis accelerometer, 3-axis magnetometer, and 3-axis gyroscope) and after treating raw data using user-definable filters (i.e. quaternion-based Kalman filter, amongst others) the motion sensor turns into a miniature, high-precision, high-reliability, attitude and heading reference systems (AHRS) which operates in real-time. The system consists of a self-contained 3D body motion tracking device available at low cost, small size and weight, low latency and reduced jitter. Recorded data is stored on an internal memory card, thus turning the sensor into a standalone data recording device. Acceleration data has potential for integration with respect to time in order to derive debris velocity and their position vectors as well. However, readings from the single sensors integrated into the IMU are only stable over short-time. Without explicit treatment, integration errors accumulate significantly over a short period due to sensor drift and jitter such that double integration is not feasible to provide the position. Antonello et al. (2011) summarized that double-integration of accelerometer data might be beneficial over short periods of time and only for fast motions when high-pass filtering was applied; in most other cases, double-integration led to large errors. The drift that affects the gyroscope, especially during static or quasi-static conditions, can be compensated by using the magnetometer readings which yield a reasonably good estimation of the absolute orientation of the sensor with respect to the magnetic North pole. Thus, using the IMU in the vicinity of ferrous materials can easily bias the on-board magnetometer.

The orientation of debris equipped with the motion sensor with respect to the local coordinate system is recorded in a user-definable form. Eulerian angles, rotation matrices or quaternions are selectable. In addition, raw, scaled, and unbiased data of the sensors can be obtained in space and time.

For measurements reported herein, time-histories of orientations as well as the initial debris orientation were recorded in unit quaternion form. Specifically, the rotation or orientation of a rigid body can be unambiguously defined by the use of quaternion notation with quaternions having unit length. A quaternion as defined by Hamiltonian algebra can be interpreted as a vector in three-dimensional Euclidean space and a scalar:

$$a \equiv a_1 + a_2 \cdot i + a_3 \cdot j + a_4 \cdot k \equiv (a_1, a) \tag{3.7}$$

Where the vector $a = [a_2, a_3, a_4]$ represents an axis in the 3D Euclidean space coordinate system. The scalar a_1 can be seen as an angle around which a rotation of any geometric identity takes places. The quaternion notation is conveniently chosen over Eulerian rotations as it does not involve singularities such as the Euler representation around angles of ±90°. For the purpose of comparing rotation time-histories with those derived from motion sensor recorded quaternions, conversion routines were used for the relevant of the twelve Euler rotation sequences (Henderson, 1977).

3.2.5 Combined detection of the debris position and debris orientation

The time-synchronization of all computers used to record or setup the sensors was achieved through the application of the Network Time Protocol (NTP) (Mills, 2006) which is capable to synchronize computer clocks to millisecond (ms) accuracy under ideal circumstances. The setup used was a client-server construction where the computer with the Quuppa positioning engine also ran an instance of the NTP server and subsequently broadcasted its local time over the local area network through user datagram protocol (UDP) messages. Another computer was used to manage the motion sensors which ran a NTP client which synchronizes their local computer clocks by listening to the broadcast messages from the NTP server. The accuracy of the synchronization process was monitored continuously while using the computers and its accuracy was around 30 ms on the average. The Quuppa positioning engine made direct use of the NTP server, whereas the clocks of the used motion sensors had to be manually set at a recurring interval as the standalone sensors have no continuous connection with any computer to automatize the clock adjustment process.

3.3 "Smart" debris: Validation

3.3.1 Experimental test setups

Validation of the proposed 6DOF debris tracking system was accomplished under thoroughly controlled conditions in the Civil Engineering Hydraulics Laboratory of the University of Ottawa, Canada. In total, 52 tests were conducted to investigate the overall system performance under a) static, b) constant velocity, c) submergence, and d) oscillatory conditions. Figure 3.2a and b presents the plane and side-views of the test setup used for the validation. Figure 3.2a presents the experimental setup which involved a physical pendulum mounted within the AOI and also shows the location of the temporary basin used to conduct tests with submerged RFID tags actuated along the laboratory track. Figure 3.3b details position of the RFID tags for the static and dynamic experiments; additionally the second physical pendulum and the track orientations used are depicted.

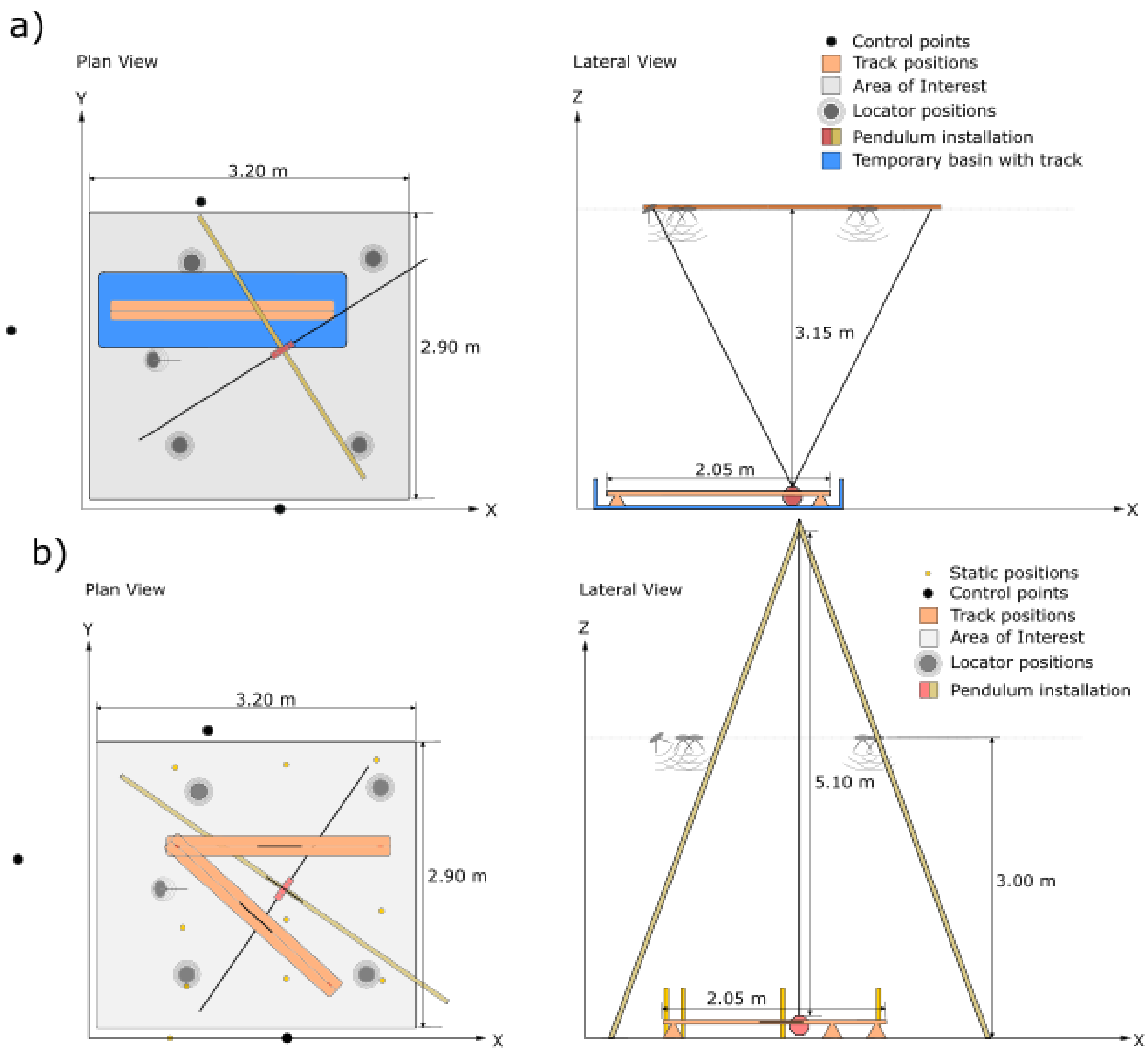

Figure 3.2: Testing bank for validation. a) Laboratory track with low-friction cart propelled by an electric actuator with pulley and thread. b) Orientation test specimen (dodecagon) and attached motion sensor, coordinate system to describe orientation angles in space.

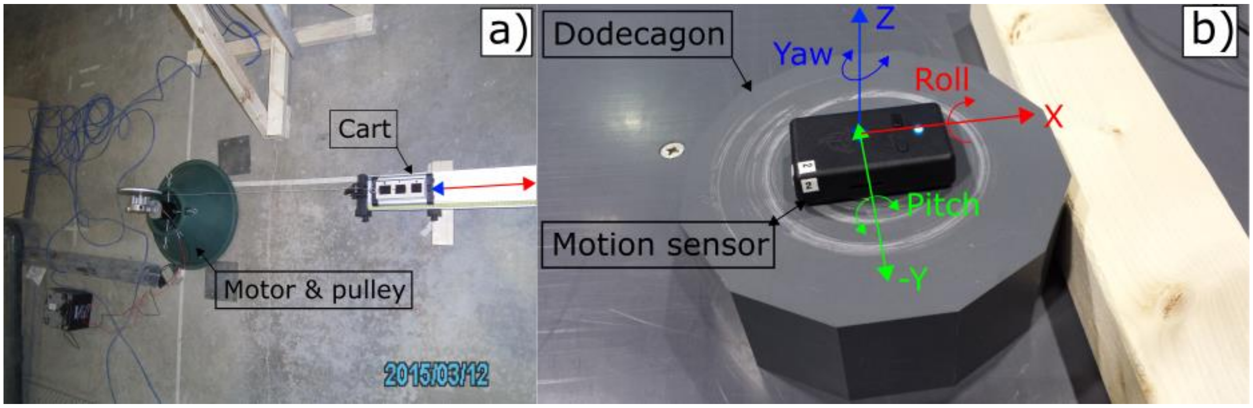

Figure 3.3: Experimental setup for the testing of the positioning system and the motion sensor for a) step 1 oscillatory setup and submergence setup and b) for static conditions, constant velocity, and step 2 oscillatory setup.

Table 3.2 details the experimental runs and the performance indicators achieved during the tests. The performance of the positioning system and the motion sensors is evaluated using the standard error *SE*, root mean square error, *RMSE*, maximum error E_{max} and the standard deviation *SD* when appropriate. For the positioning system, the standard error was in reference to the difference in positioning between the experimentally and true positions of the tags. For the motion sensors, the standard error referred to the difference between the experimentally and true orientation of the IMU. The tracking performance of the data acquisition system was assessed by comparing the motion/rotation recordings of objects moving on controlled, predetermined trajectories. The experimental stand consisted of a laboratory track on which a low friction cart was moved either manually or with an actuator-pulley system. The cart and the actuator were connected through a nylon thread curled on rotating disc with a diameter of 120 mm. The antennas for the position measurement system were mounted on a wooden frame approximately 3 m above ground. The wooden frame was supplemented with a mounting for a pendulum to accomplish oscillatory motion of the tag. For the manual measurements of the true values, a timer, a laser rangefinder (Leica Disto™ D8, ±1 mm accuracy) and an orientation test specimen (CNC-milled to 0.1° precision) were used. Figure 3.3a shows the laboratory track, the electric actuator with pulley and the thread (diameter 0.25 m) used to propel the cart. Figure 3.3b shows the orientation test specimen (dodecagon) manufactured from PVC.

Table 3.2. Experimental runs and tag-averaged metrics in the form of SE in x-, y-, z-direction, standard deviation (SD), root mean radial spherical error (DRMS) distance, and mean root standard error (MRSE) describing performance of the positioning system and of the motion sensor.

Expt	2D / 3D	Tags	z-level	Type	Rep.	Duration	SEx	SEy	SEz	SDx	SDy	SDz	DRMS	MRSE
[#]		[#]	[m]	[-]	[-]	[s]	[m]	[m]	[m]	[m]	[m]	[m]	[m]	[m]
1	2D	14	0.00	Static	1	120.00	0.08	0.05	0.00	0.01	0.01	0.00	0.10	0.10
2	3D	14	0.00	Static	1	120.00	0.07	0.06	0.10	0.01	0.01	0.02	0.11	0.16
3	3D	14	0.25	Static	1	120.00	0.07	0.06	0.19	0.01	0.01	0.02	0.11	0.23
4	3D	14	0.50	Static	1	120.00	0.07	0.06	0.41	0.01	0.01	0.02	0.10	0.42
5	3D	1	0.14	Const. Vel.	1	10.20	0.06	0.06	-	0.04	0.05	-	0.09	-

6	3D	1	0.14	Const. Vel.	2	10.20	0.06	0.06	-	0.04	0.06	-	0.09	-
7	3D	1	0.14	Const. Vel.	3	10.20	0.04	0.08	-	0.04	0.06	-	0.09	-
8	3D	1	0.14	Const. Vel.	1	10.20	0.07	0.11	-	0.05	0.06	-	0.13	-
9	3D	1	0.14	Const. Vel.	2	10.20	0.09	0.13	-	0.05	0.06	-	0.16	-
10	3D	1	0.14	Const. Vel.	3	10.20	0.06	0.13	-	0.04	0.07	-	0.14	-
11	3D	1	0.14	Const. Vel.	1	6.10	0.08	0.07	-	0.05	0.06	-	0.11	-
12	3D	1	0.14	Const. Vel.	2	6.10	0.05	0.08	-	0.04	0.06	-	0.09	-
13	3D	1	0.14	Const. Vel.	3	6.10	0.04	0.07	-	0.03	0.05	-	0.08	-
14	3D	1	0.14	Const. Vel.	1	6.10	0.07	0.08	-	0.05	0.06	-	0.11	-
15	3D	1	0.14	Const. Vel.	2	6.10	0.08	0.08	-	0.04	0.06	-	0.11	-
16	3D	1	0.14	Const. Vel.	3	6.10	0.08	0.13	-	0.04	0.06	-	0.15	-
17	2D	1	z(t)	Oscillatory	1	40.00	0.25		-	-	-	-	-	-
18	2D	1	z(t)	Oscillatory	2	40.00	0.09		-	-	-	-	-	-
19	2D	1	z(t)	Oscillatory	3	40.00	0.09		-	-	-	-	-	-

The standard error *SE* is computed as follows:

$$SE = \sqrt{\frac{\sum_1^n (X_t - X_m)^2}{n}} \tag{3.8}$$

where: n – number of samples, X_t time-history of true quantity during a finite recording period, X_m time-history of measured quantity. The equation for the maximum error can be expressed as:

$$E_{max} = \max(X_t - X_m) \tag{3.9}$$

The standard deviation (*SD*) which characterizes the data scatter around the measured mean values is:

$$SD = \sqrt{\frac{\sum_1^n (X_m - \mu)^2}{n}} \tag{3.10}$$

with the mean of the measured values being:

$$\mu = \sum_1^n X_m / n \tag{3.11}$$

In the case of the dynamic tests (e.g. constant velocity) which involved debris motion trajectories rather than static positions, the mean value of a spatial component was computed after de-trending their respective time-history using Fast Fourier transformation in order to obtain meaningful standard deviations. Similar to satellite navigation metrics, 2D horizontal and 3D spatial error can be determined based on the root mean squared (*DRMS*) distance and the mean radial spherical error (*MRSE*) which are defined by the squared *SE* for the three spatial components *x*, *y*, and *z*:

$$DRMS = \sqrt{SE_x^2 + SE_y^2} \tag{3.12}$$

$$MRSE = \sqrt{SE_x^2 + SE_y^2 + SE_z^2} \tag{3.13}$$

Assuming a Gaussian process behavior for the debris motion, the probability for 2D horizontal measurements to reside with a circle with radius of *DRMS* centered at the true position is p = 63.2 %. The probability for a measurement to be contained in a sphere with radius *MRSE* centered again at the true position decreases slightly to p = 61.0 % for the 3D case (Hofmann-Wellenhof et al., 2003). In order to quantify the true spatial distance between the true and measured positions, the Euclidian distance, $\parallel d_{eu} \parallel$, which is defined as the magnitude of the vector connecting the vectors pointing to the two considered positions, is expressed as the square root of the dot product:

$$\parallel d_{eu} \parallel = \sqrt{\mathrm{p}_t \cdot \mathrm{p}_m} \tag{3.14}$$

3.3.2 Accuracy of debris position measurements in 2D and 3D set-ups

The performance of the positioning system was tested using carefully-controlled laboratory tests. The system was tested in both 2D and 3D mode. The two modes differ in that they either provide the debris position based on the calculation of the angle-of-arrival in horizontal (2D) coordinates or, in addition to the 2D case, the vertical component is also provided for the 3D tests. In case of the 2D-mode, the vertical coordinate is pre-set with the manually-adjusted height of the plane of interest (e.g. 0.25 m). The tags were then positioned according to Figure 3.3b (yellow positions) inside the area of interest (AOI). For the static test setup, three different vertical positions were tested.

For the height of 0.00 m (corresponding to the floor level), the tags were positioned directly on the concrete floor. For the elevations of 0.25 and 0.50 m, the tags were placed on top of 3 x 5 cm wooden posts. Time-history of the positioning system was recorded for periods of 120 s for each test.

Figure 3.4 presents the Kalman-filtered spatial components of the static tag position derived by the positioning system in 2D-mode. Recorded data points are plotted against their true position which was manually derived using a laser rangefinder. An average sampling rate of 24 Hz was used and data was color-coded by the Euclidian distance (Equation 3.14) between the measured positions and the true position. The precision in the horizontal plane, which is commonly seen as the amount of scatter which a measurement exhibits, was remarkably good. In statistical terms, the tag-averaged standard deviation along the x- and y-axis was low with SD_x=SD_y=0.01 m. The accuracy, defined as the distance between the true and the measured positions, reached standard error values between $SE_{x,y}$=0.05 – 0.08 m on the average. According to Figure 3.4, the accuracy of the measurements in 2D-mode was spatially distributed across the AOI with better accuracy values around the center and less so along the edges of the AOI. The *DRMS* value predicted 61% of the measured positions to reside within 0.10 m of the true position.

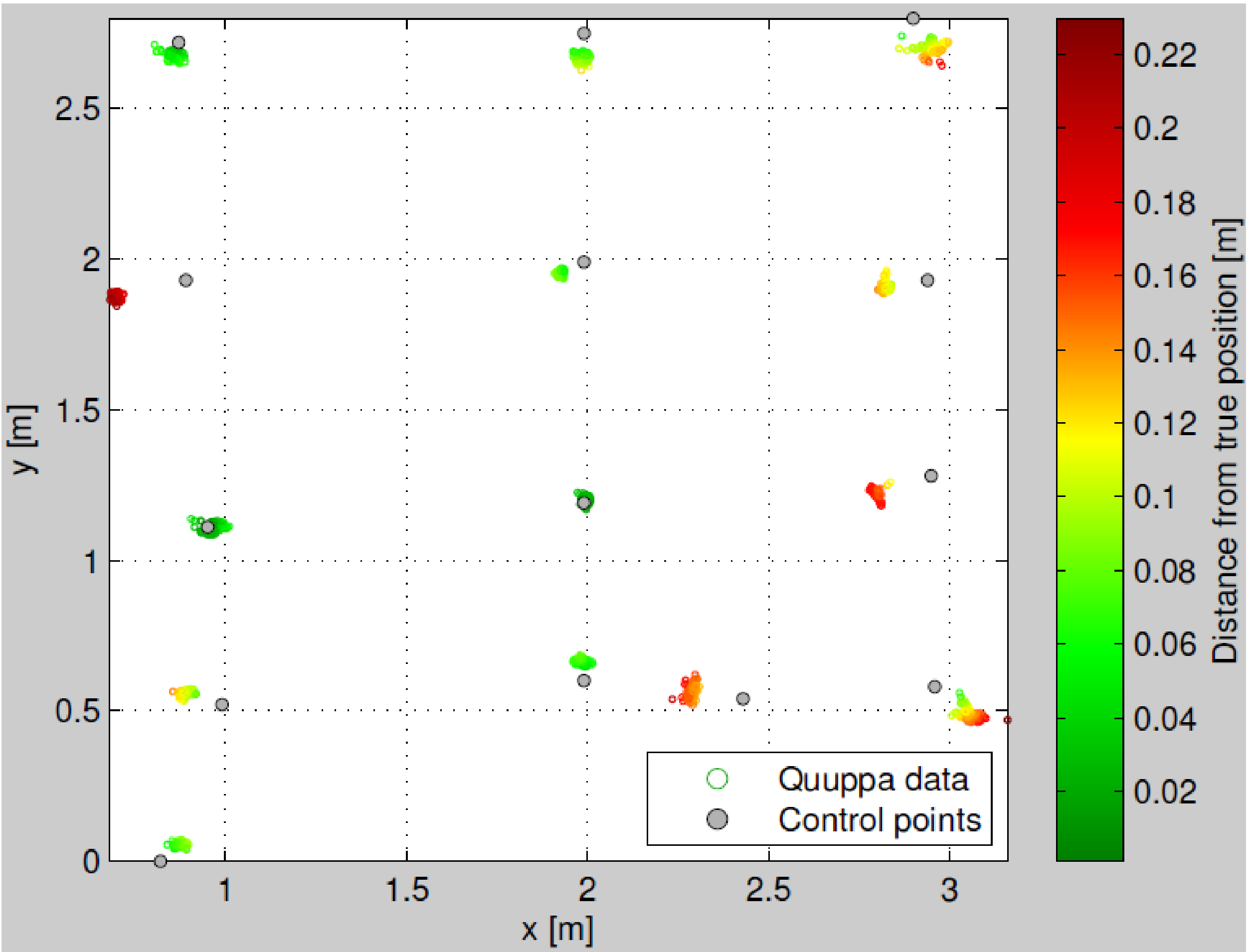

Figure 3.4: Static position measurements of 14 RFID tags in 2D-mode for experimental run 1 - color bar indicates the Euclidian distance between the true and the measured position. a) 3D-view, b) 2D: *XY*-plane, c) 2D: *XZ*-plane, and d) 2D: *YZ*-plane.

In comparison with the 2D-mode, Figure 3.5 presents an identical set of tags distributed in the plan with height *z* = 0.0 m. Measurements were however performed by switching the positioning system to 3D-mode in order to assess how this influences the system performance. As shown in Figure 3.5 (see experimental run 2), the tracking performance in the horizontal plan was equally good, with a low average standard deviation and larger standard errors. The directionality and distribution of the deviation between measured and true positions of the tags were identical between the two measurements which leads to the conclusion that this was most likely related to the characteristic travel path the radio wave communication of the RTLS between the tags and the receiver antennae took. In general, any obstructions in between a tag and the antennae potentially influences the positioning result as radio waves could undergo damping, reflection or refraction while propagating non-homogeneously cluttered space. Based on this observation, it can also be ruled out that the system internally distinguishes between the processing of 2D or 3D positions, and thus, in the following tests, all positions were measured in 3D-mode only. The vertical position measurements depicted in Figure 3.5 were less accurately determined as the standard deviation error of the measurements was doubled and, more importantly, the standard error in the vertical yielded tag-average values of SE_x=0.10 m with individual values in the range of up to 0.40 m. It is however conspicuous, that those individual values of the standard error were mostly recorded close to the x-axis and close to the coordinate origin where, in the present experimental set-up, a massive steel column structural member was located. It is likely that the presence of the steel column was partially responsible for these high standard error values. However, due to space limitations, it was not possible to move the experimental arrangement further away. An in-depth discussion addressing the error sources of the innovative 6DOF system is presented further in the discussion section.

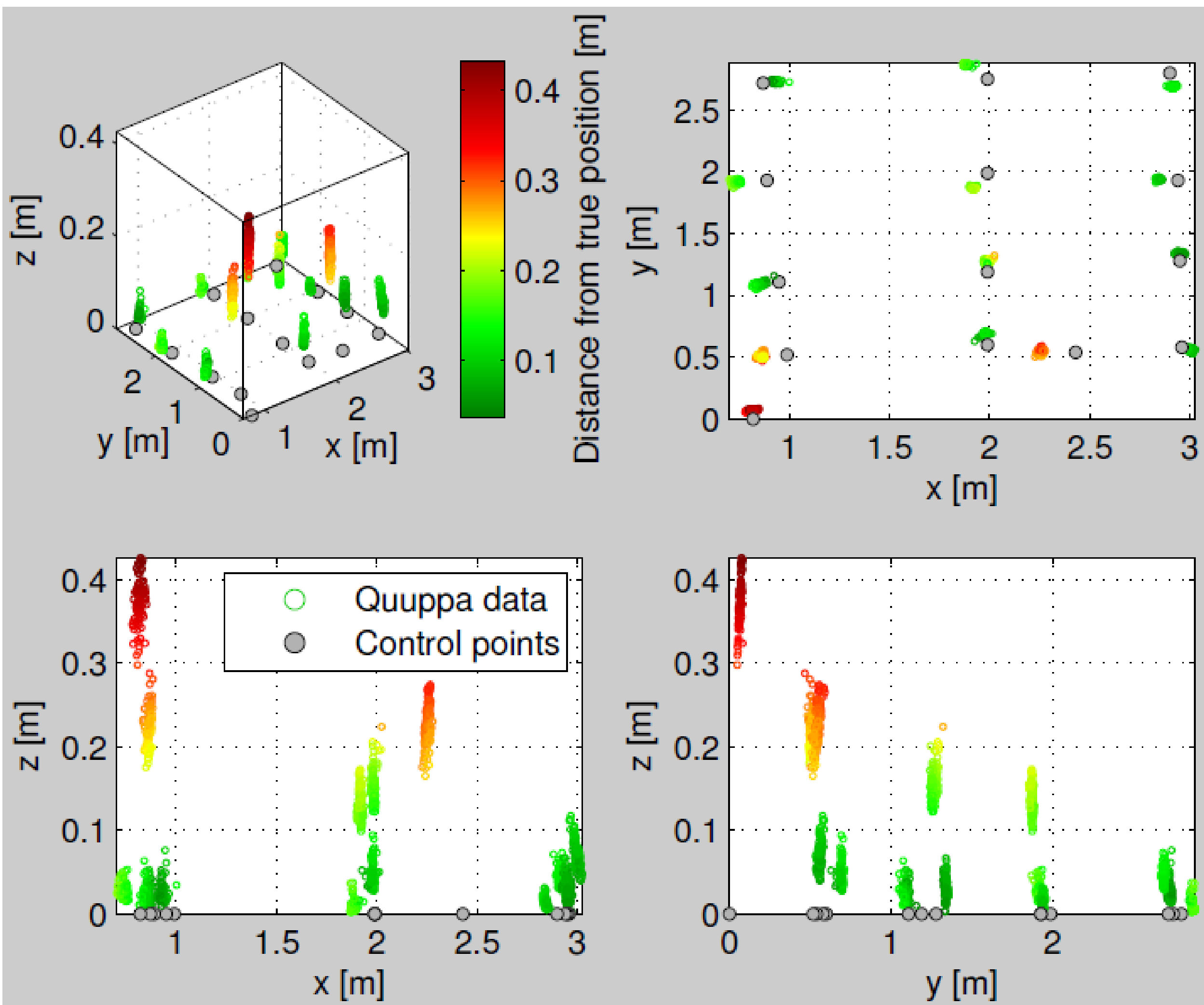

Figure 3.5: Static position measurements of 14 RFID tags under controlled laboratory conditions, color bar indicates the Euclidian distance between the true and the measured position. a) 3D-view, b) plain view (*XY*), c) *XZ*-plane, and d) *YZ*-plane.

3.3.3 Debris position tracking results under constant velocity

The performance of the debris positioning system was tested under dynamic conditions by tracking debris moving at constant velocity along a precise laboratory track and a low friction cart on top of which a tag was fixed. Two different velocities were selected for these tests (0.20

m/s and 0.34 m/s). As shown in Figure 3.3b, the orientation of the laboratory track was varied in order to identify whether its absolute position had any noticeable influence on the position tracking results. The constant velocity of the system was accomplished using a frequency-controlled actuator which actuated a pulley with a diameter of 0.13 m. Once the constant speed actuator was adjusted, the elapsed time for the cart to be pulled along the track was recorded in 6 repetitions. The true velocity was finally determined by dividing the track length by the averaged elapsed time.

The travelling distance from the origin of the cart position along the track with respect to the elapsed time is shown in Figure 3.6a. In total, results for 12 different dynamic tests using 2 cart velocities, 2 track orientations and 3 repetitions are presented. The distance travelled by the cart was calculated based on the measured, Kalman-filtered position components in the horizontal plane. The true position of the cart calculated using the predetermined velocity induced by the constant speed of the actuator was then compared with the measured position. The *SE* and *SD* values in the horizontal plane, as well as the *DRMS* values, were obtained and are listed in Table 3.2 (exp. runs 5-16). In line with the previous set of tests for the static case, standard errors in x and y were found to be in the range of *SE* = 0.04 – 0.13 m. Marginally, larger values were obtained for the standard deviation (*SD* = 0.03 – 0.07 m). This increase in scatter indicates that the dynamic process involved likely influenced the position system results. The increase in cart velocity did not affect the positional accuracy and precision to a traceable extent. Near the end of the oblique track, increasing orientation differences between the true and the measured track were observed. Most likely these are attributed to the manual process of stopping the cart motion. Overall, it was apparent that the positioning system was capable of reproducing the true tag trajectory attached to the cart in space and time. Moreover, a comparison between the different repetitions performed proved that the system is able to measure tag position in space and time while being moved along a laboratory track without notable deviation between runs.

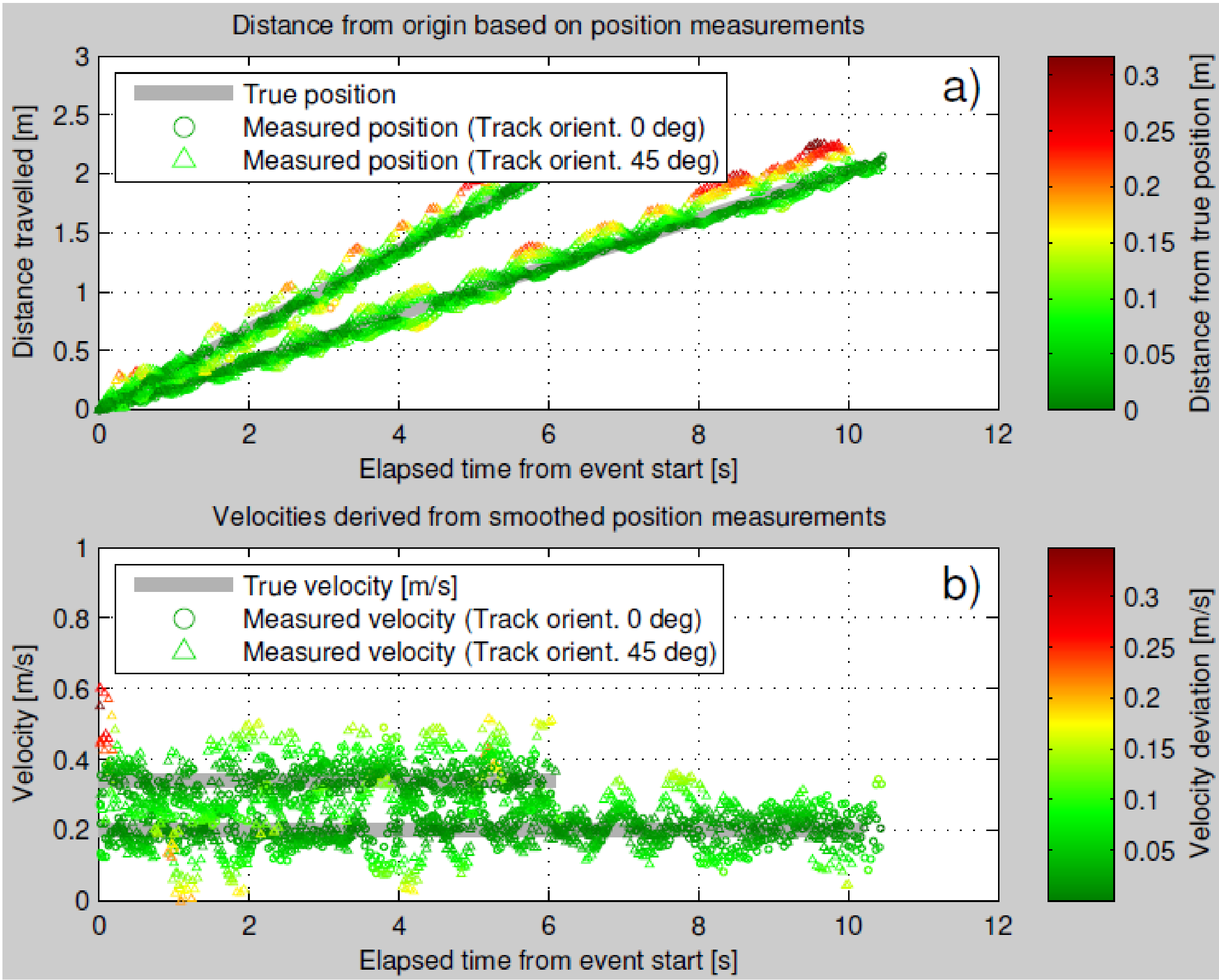

Figure 3.6: Dynamic position tracking of a cart equipped with one RFID tag driven at constant speed 0.2 m/s and 0.34 m/s along two different track orientations.

Velocities shown in Figure 3.6b were derived through temporal differentiation of the measured position time-history. For reference, the true, constant velocities are represented by gray lines. The spatial, Kalman-filtered position components were discretely differentiated to obtain instantaneous cart velocities. Velocity deviations were similarly color-coded based on the absolute difference between the derived velocities and the true values. The derived velocities were very scattered around the true velocities tested although the measured position component time-history were first Kalman-filtered and further smoothed with a moving-average filter with a window width of 50 samples (~1.0 s). Apparently, the positioning system was capable to reproduce the order of magnitude of the pre-set velocities at most whereas detailed temporal variation could only be estimated based on the positioning system performance reliably.

3.3.4 Spatio-temporal tracking of the oscillatory motion

In order to validate the positioning system capabilities with respect to tracking oscillatory motions such as periodic wave impacts or repeated motion of armor stone elements, a physical pendulum (shown in Figure 3.3b) with a length of 5.1 m was used as a simplified validation model. In order to initiate oscillation, its initial horizontal deflection was set to 1.69 m (θ_0 =

$-0.337\ rad$) while the vertical deflection was set to 0.59 m. The equation of motion to describe the linear, damped pendulum motion was derived based on Newton's second law in rotational form substituting the pendulums torque and moment of inertia leading to the following second-order differential equation:

$$\frac{d^2\theta}{dt^2} + \frac{c}{m}\frac{d\theta}{dt} - \frac{g}{l}sin\theta = 0 \tag{3.15}$$

The ratio of the damping coefficient, *c*, to the mass of the pendulum, *m*, was determined to be *c/m* = 0.016. Under the assumption of linearity equity ($\sin\theta = \theta$), Equation 3.15 reduces to:

$$\frac{d^2\theta}{dt^2} + \frac{c}{m}\frac{d\theta}{dt} - \frac{g}{l}\theta = 0 \tag{3.16}$$

The Euler-Cromer method was used to solve Equation 3.15 numerically (Giordano and Nakanishi, 2006). The resulting temporal evolution of the deflection angle measured between the pendulum thread and the vertical (Figure 3.3) was compared to the experimental results obtained from the positioning system. Based on the measured horizontal deflection, the deflection angle was also calculated using the known pendulum length and the measured deflection.

A comparison between the analytically-derived angle of deflection, θ, and the trigonometrically-derived angle based on the positioning system is shown in Figure 3.7 for the case when a single tag was used for 9 subsequent cycles and 3 independent repetitions. The difference between the measured and true recordings was color-coded in units of angular degrees. The positioning system is very capable to track the oscillatory motion in temporal space. Time history of the deflection angle was found to be accurately in phase with the oscillatory motion. The amplitudes of the oscillatory motion was generally well reproduced. The first three cycles of the oscillatory motion however showed less agreement, especially around the turning points of the oscillations. As time elapsed, those differences decreased significantly. The differences between the individual recordings are also remarkably small, pointing to an acceptable level of accuracy when tests were repeated. As shown in Table 3.2, standard errors obtained in the horizontal plane were again found to be in the range of 0.09 and 0.24 m for the 3 repetitions considered. Absolute differences in angular units were up to 0.12 rad. The average angular differences however were found to be exceptionally low with 0.043, 0.015, 0.014 rad.

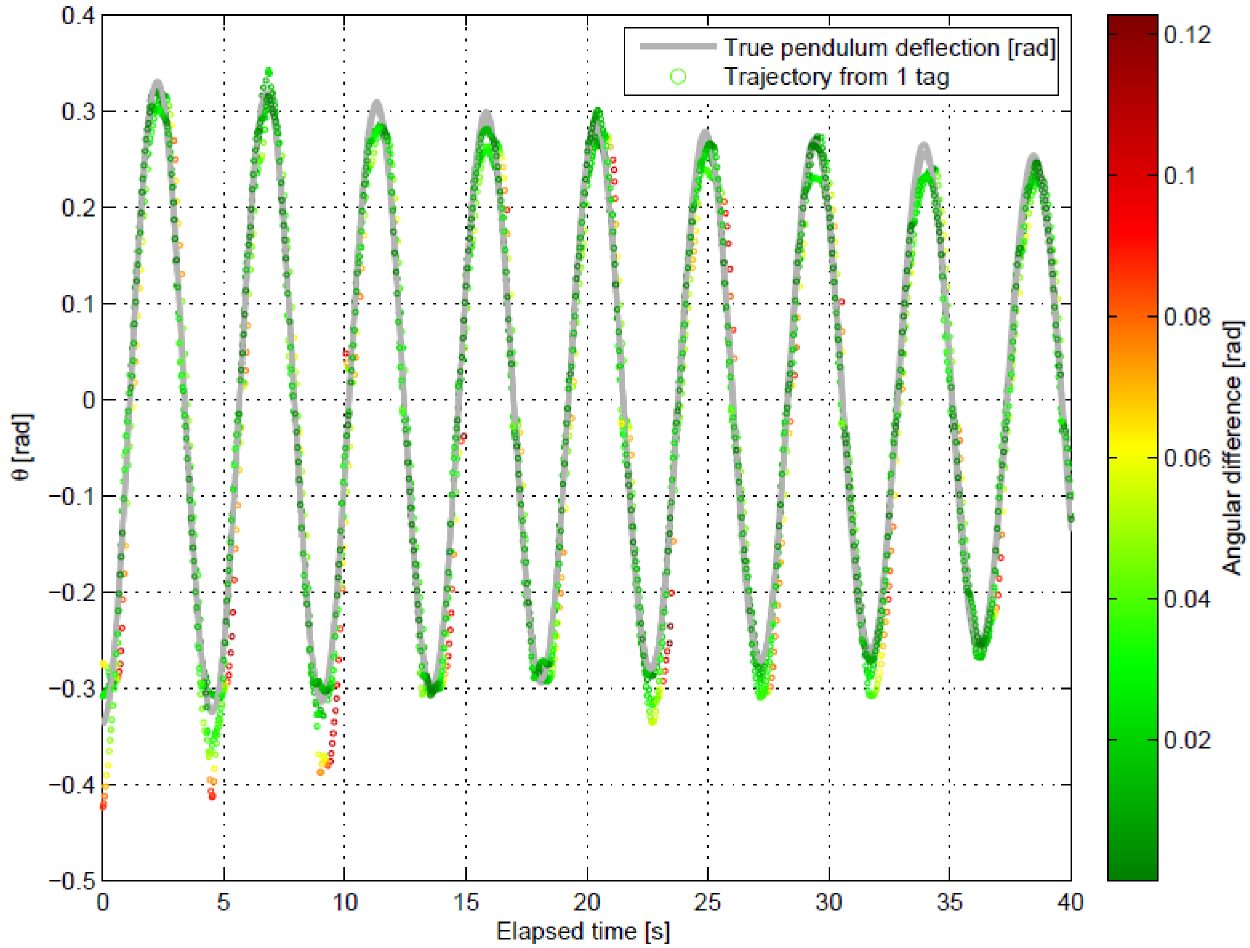

Figure 3.7: Comparison of the analytically-derived and measured deflection angles θ for a linear, damped pendulum based on the tracking of the position of one tag. Data are color-coded by the theta differences in rad.

3.3.5 Orientation measurements with attitude heading reference systems

A motion sensor unit was utilized to measure the orientation of the "smart" debris system. The orientation was defined as the rotation around the three fixed coordinate axes as shown in Figure 3.3. Yaw angles were thus defined to be rotations around the vertical axis whereas roll and pitch depicted the respective rotations around the two horizontal axes. Validation of the motion sensor was accomplished by comparing the recorded rotations against a fixed rotation around each axis. The resulting time history of the validation against dynamic rotation steps is plotted in Figure 3.8 for the measured rotations (subscript m) around the (x,y,z)-axis (yaw - $\varphi_{z,m}$, roll - $\varphi_{x,m}$, and pitch - $\varphi_{y,m}$) over the elapsed time since the rotation event start.

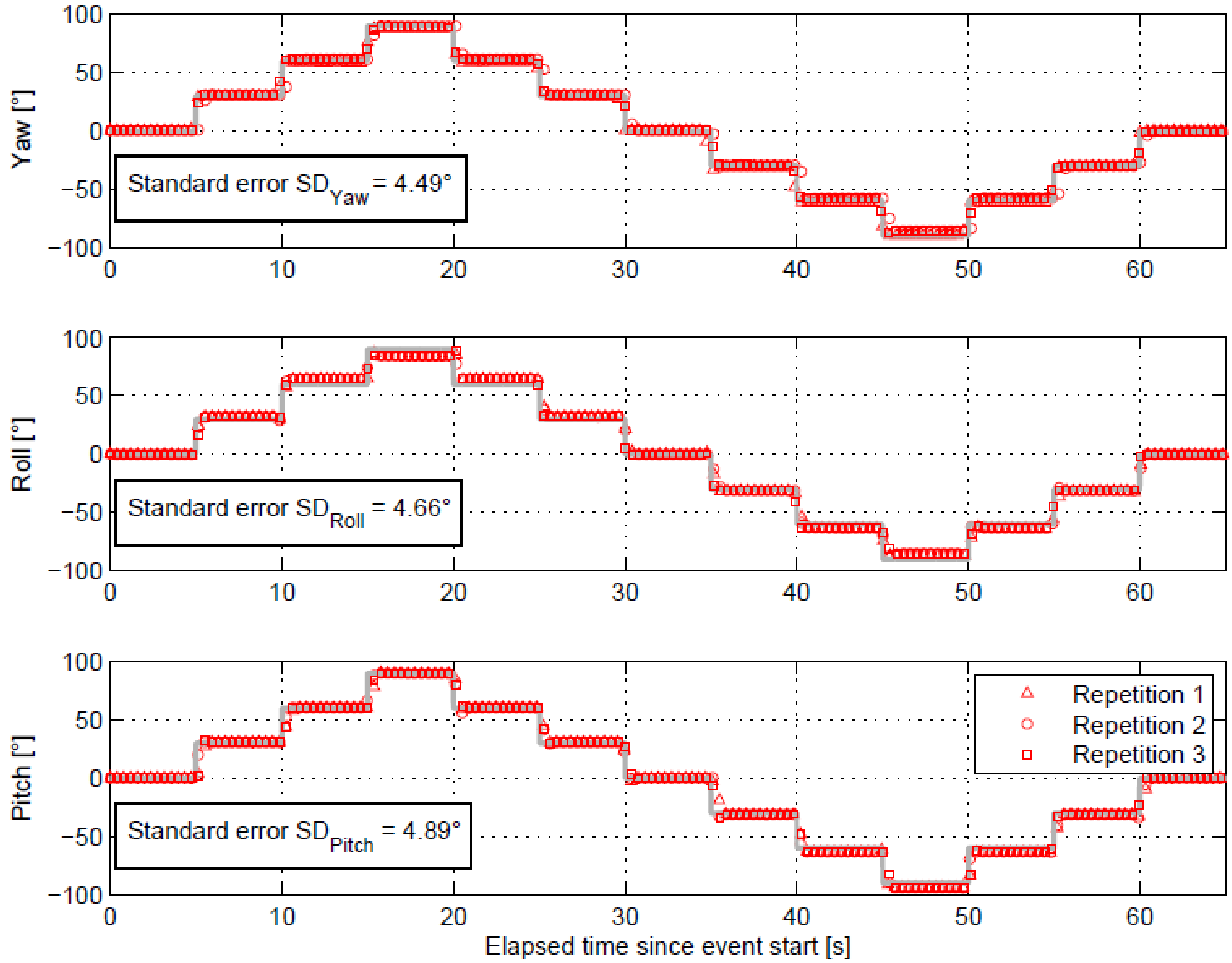

Figure 3.8: Orientation measurement of yaw, roll, and pitch compared with the true orientation step function for three repetitions, mean standard deviations are given in the sub-panels.

The time-dependent true (subscript t) angle $\varphi_{i,t}(t)$ with i={x,y,z}, which was manually prescribed with the help of a timer and the orientation test specimen and which is shown in Figure 3.2, can be defined in terms of the unit step function (Abramowitz and Stegun, 1965) as follows:

$$\varphi_{i,t}(t) = \sum_{1}^{n=13} \varphi_0 \, H(t - 5n) \tag{3.17}$$

$$H(t) = \begin{cases} 0.0 & t < 0 \\ 0.5 & t = 0 \\ 1.0 & t > 0 \end{cases} \quad \text{Heaviside step function} \tag{3.18}$$

$$\varphi_0(n) = \begin{cases} 30° & n = 1,2,9 \dots 13 \\ -30° & n = 3 \dots 8 \end{cases} \tag{3.19}$$

Good agreement was found between the true rotational motion of the test specimen orientation and the measured (Euler) angles which were converted from the quaternion recordings. In Table 3.2, the calculated error metrics are listed for the tests conducted: standard errors are generally very small, varying between 3.1° and 6.8°. The maximum absolute relative errors were less than

5.3% and the coefficient of correlation between the true and the measured orientation was R=0.99 or above for all orientation measurements. It can be thus concluded that the applied motion sensor is generally capable to provide meaningful spatial orientation tracking ensuring this “smart” debris system to be a full 6DOF measurement device.

3.3.6 Influence of submergence on the positioning results

Figure 3.9 highlights the influence of submergence of BLE-tags used to measure the position of the “smart” debris. An inflatable pool was used to submerge the laboratory track, the cart and one BLE-tag. The cart was driven along the track at constant speed, as shown in Figure 3.9a using 9 different water levels in the pool. The 0.0 m level corresponds to the water surface elevation being right below the tag housing while negative values refer to water levels below the tag. Submergence depth is measured between the lowest level of the BLE-tag and the surface elevation. The distance travelled is plotted over the time elapsed since the cart motion started. Figure 3.9b shows the standard error and the standard deviation of the measurements accomplished. For 0.035 m tag submergence, an exponential increase in the standard error indicated the limit up to which the system provided meaningful results. Most interestingly, this limit corresponds well with findings of Benelli and Pozzebon (2013) whose report confirmed a physical submergence limit due to a loss of signal strength of electromagnetic waves after transitioning from air into water. Along with a significant decrease in accuracy, the sampling frequency decreased as well, indicating that the wireless connection between the BLE tag and the locator may have experienced signal loss. Thus, the system was not able to provide the position of the “smart” debris below a critical submergence depth of 0.035 m. However, transport processes that involve short-term transient sinking and rising of floating objects could still be accommodated by finding difference positions by double-integration of the accelerometer data delivered by the motion sensor. This however will only be a viable option in cases when loss-of-communication events for the RTLS are of short nature with error accumulation remaining insignificant. At present, further research is needed to assess the system performance from this point of view.

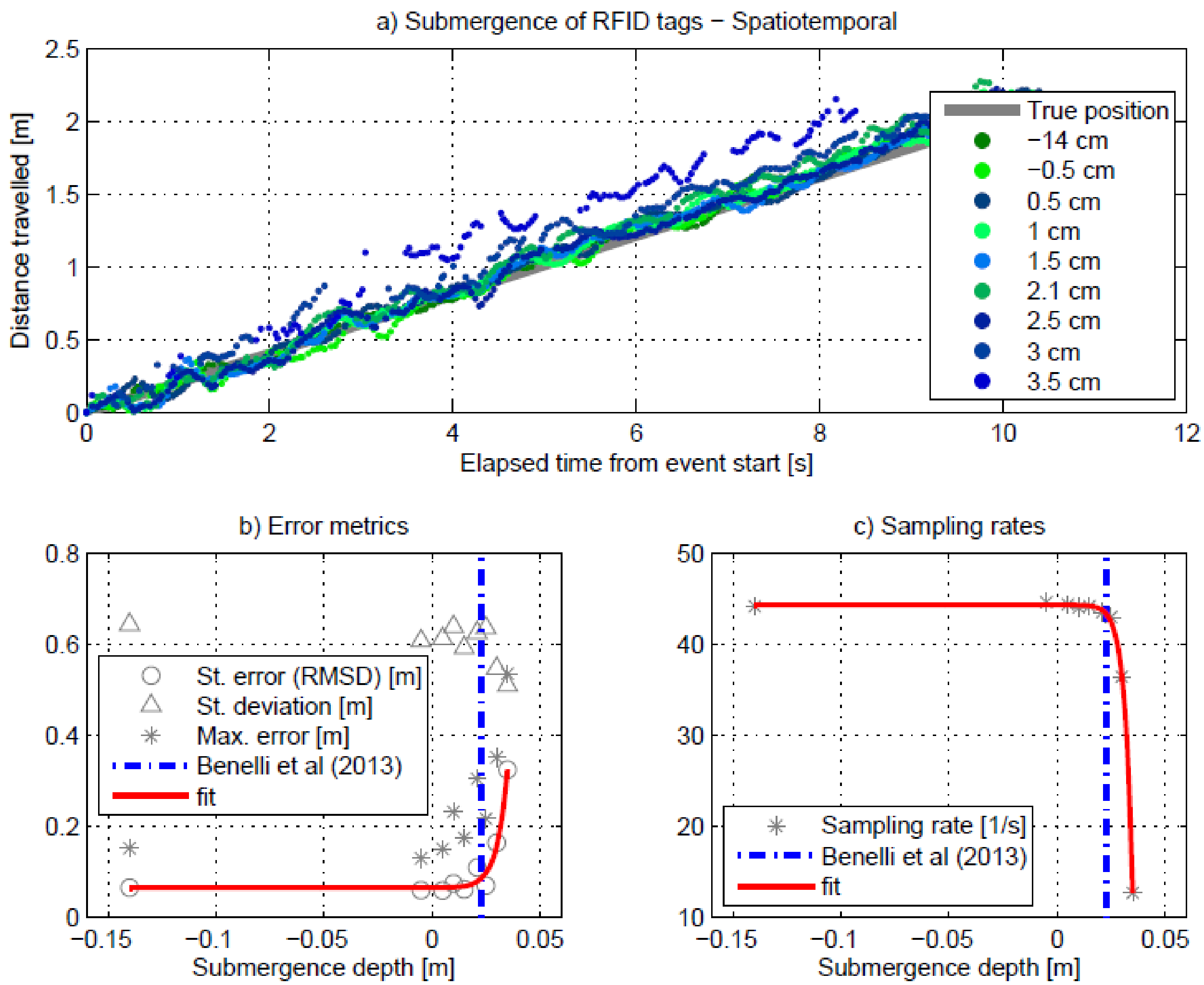

Figure 3.9: Dynamic position tracking of a carriage equipped with one BLE tag driven at constant speed, 0.2 m/s, along one track orientation for 9 different water levels (7 tests with submergence, submergence measured between lowest level of housing and surface elevation) inside the test basin. For track position and orientation see Figure 3.2. a) Positions of the BLE tag over elapsed time. b) Error metrics and an exponential fit relating the *RMSD* to the submergence depth. c) Development of sampling rates over the submergence depths and an exponential fit of the achieved experimental data.

3.4 Hydraulic and coastal engineering applications

3.4.1 Experimental setup

The proposed and validated tracking system was then applied to a specific application involving the debris transport of down-scaled 20-feet shipping containers over a horizontal harbor apron. The experiments were conducted in the newly built Tsunami Wave Basin at Waseda University, Tokyo, Japan. The basin has dimensions of 9.00 m x 4.00 m with a maximum basin depth of 0.35 m. A horizontal harbor apron with an area of 4.0 x 4.5 m and an elevation of 0.26 m above the basin bottom was constructed at the end of the wave basin. The apron has a vertical quay wall facing the wave maker. Waves were generated by the wave generator located at the opposite end of the wave basin. The wave generator system can generate solitary waves using the release of a volume of water from vacuum tanks by means of a controlled air valve system. Waves with a solitary-type wave front profile and prolonged wave tail features were generated. For the experiments reported, a wave with a maximum wave height of 0.12 m propagated in a constant water depths of d=0.23 m. The approaching wave collided with the vertical apron front face, steepened significantly, and eventually propagated over the apron as broken bore. The bore entrained and carried the shipping container models which incorporated the “smart” debris system. Shipping containers were scaled with Froude similitude in 1:40 length scale assuming a 20-feet (2.4 x 2.4 x 6.0 m) and an weight of 18,920 kg reflecting an international average as reported by Knörr and Kutzner (2008). The experiment performed tested the performance of the “smart” debris system to accurately measure the spatial and temporal displacement of multiple shipping container moving over a harbor apron.

3.4.2 Debris spreading angle

Knowledge of the spatio-temporal spreading of potential debris sites is quintessential for disaster preparation, preparedness, and hazard mapping. In a post-mortem study, Naito et al. (2014) presented observations and an analysis of containers and vessels displacement during the flood induced during the 2011 Great East Japan Earthquake and Tsunami. They found that the largest amount of debris was concentrated within an angular sector delineating by ±22.5° from a transect normal to the shoreline. Although this is the first time such an analysis was carried out, the recommended angle was merely based on one site-specific tsunami event, rendering additional numerical and experimental research necessary. In this context, the innovative “smart” debris system was employed to track individual pieces of debris in space and time under carefully controlled laboratory conditions.

Results shown in Figure 3.10 demonstrated that the system is capable of recording the space and time history of the individual down-scaled shipping containers over the apron area following their displacement by a tsunami-like bore. In-depth information about the spatial distribution of multiple debris locations during their transport by the transient tsunami-like bore was recorded using the “smart” debris system during an experiment involving a 3 debris x 3 debris arrangement as shown in Figure 3.10. The recorded displacement showed that the containers remained within the proposed displacement sector proposed by Naito et al. (2014). A clear distinction between trajectories of the first, second, and third row of debris was determined. By repeating experiments it was found that the displacements were random in nature requiring a stochastic approach for the prediction of their spatial spreading. Based on the preliminary results involving only the use of a horizontal apron over which the debris were displaced by the bore, a smaller delineation zone might be advisable.

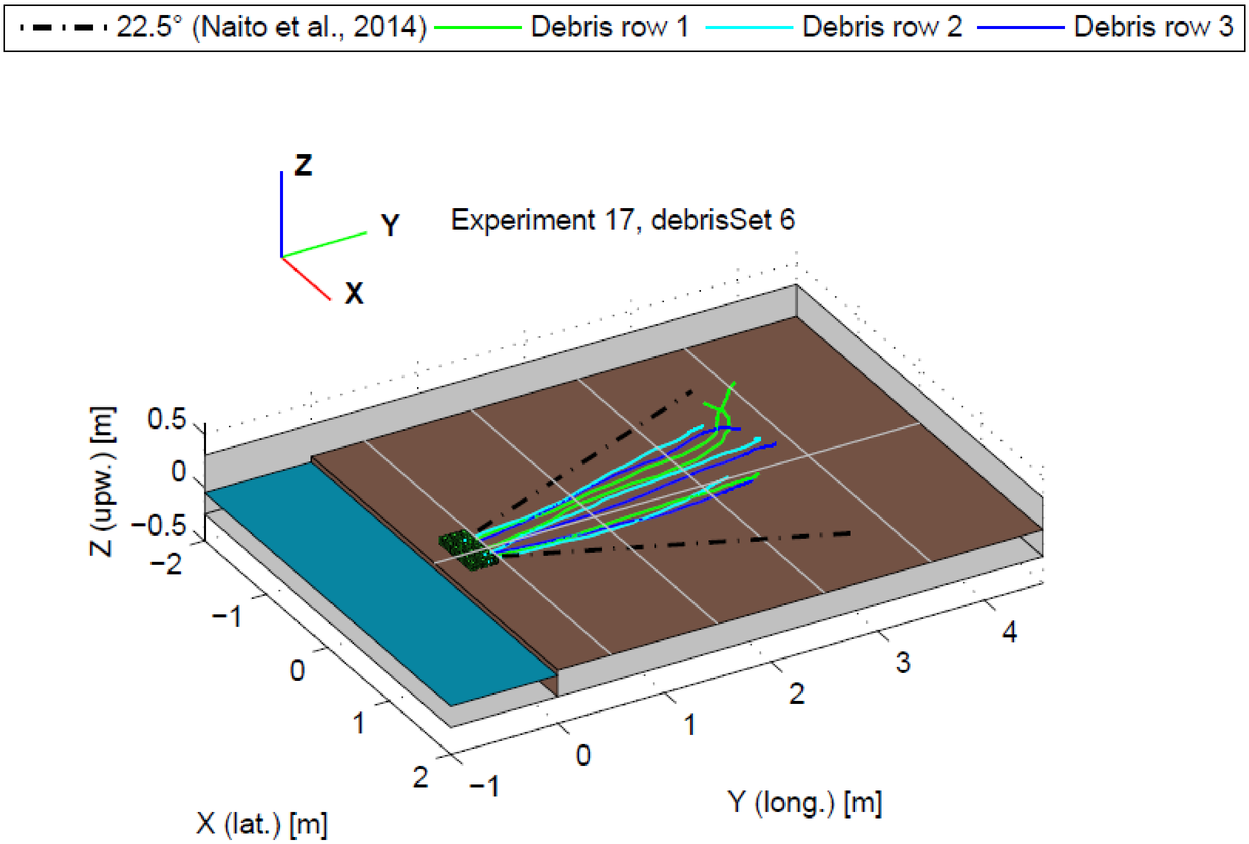

Figure 3.10: Debris motion tracking on a horizontal apron induced by hydraulic bore generated by a broken solitary wave for an arrangement of 3 x 3 debris elements.

3.4.3 Debris orientation measurement around vertical axis

Besides tracking the spatial position of debris, this "smart" debris system was designed to measure the 3-axis orientation with reference to the initial body coordinate system when at rest. It is important under transient flow conditions to simultaneously record the rotational motion along with the transitional one in order to better understand how the flow interacts with the immersed, floating debris. The determination of rigid body time history of its spatial orientation can provide unique information for the calibration and validation of numerical models under development by various researchers. For example, Canelas et al. (2015) applied the Smoothed Particle Hydrodynamics (SPH) Method to fluid-solid interaction problems and validated the model with a buoyant rigid body recovering from an unstable to a stable state. The application of the proposed "smart" debris system allows for the unrestricted recording of 6DOF motion of partially submerged objects within a transient flow.

The time history of the yaw angle component of the orientation vector was measured and compared with camera-based determination of the angle for an experiment employing a single shipping container equipped with the "smart" debris system as shown in Figure 3.11. The measured time history of the yaw angle was compared against angles obtained from processing video-recordings of the debris transport process. These video-recordings were obtained with a high-definition camera (Basler pi1900-gc) working with a sampling rate of 25 Hz. The video-camera system was time-synchronized with the "smart" debris system prior to each experimental test.

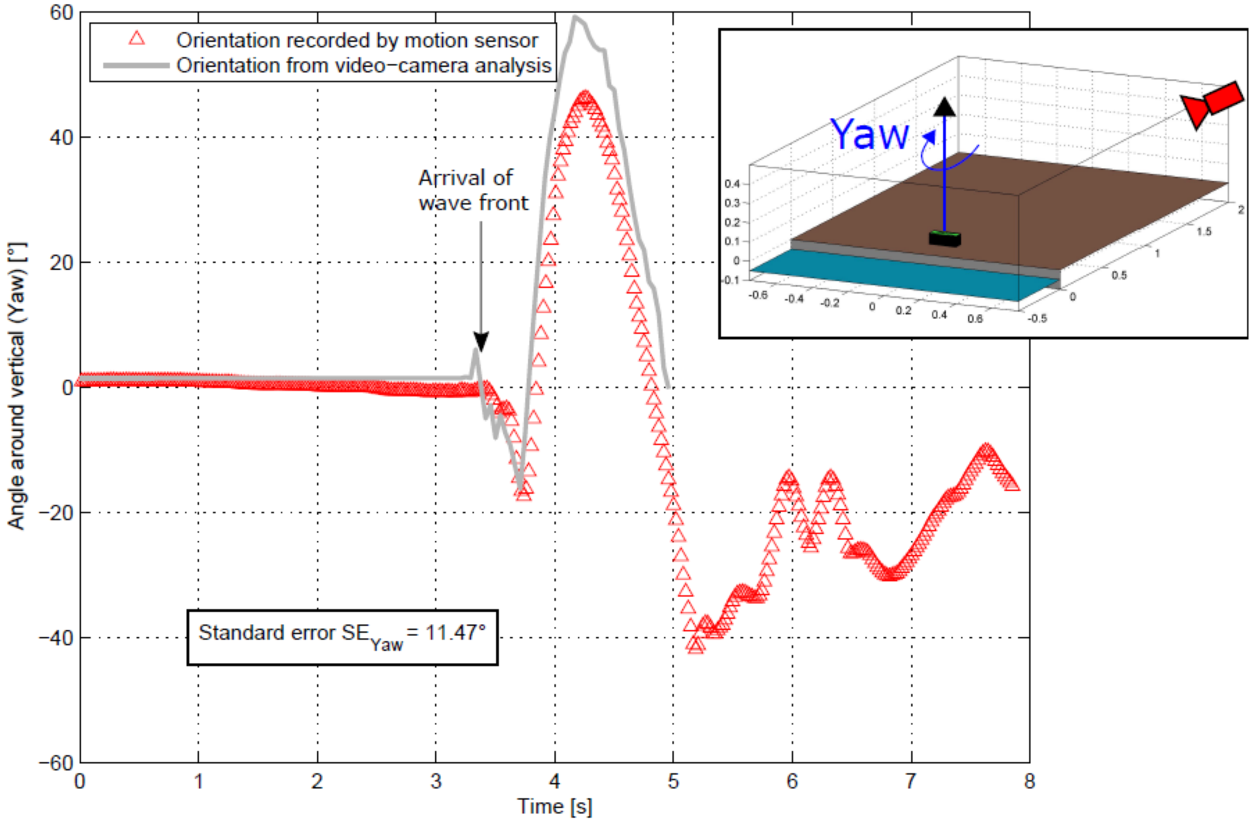

Figure 3.11: Time history of the yaw angle component of the orientation vector of a single container compared to the yaw angle determined by video-recording data analysis. The arrow indicates the arrival of the wave front at the apron's edge. The camera positon for the video-based analysis is indicated.

It appears that the video analysis -determined and the motion sensor-determined yaw angles matched favorably with respect to the general rotation of the shipping container. A remarkably good match of the phase and turning points of the angles was observed. However, while the first turning point determined from the video recordings agreed well the values determined from the motion sensor, the yaw was underestimated at the instant of the second turning point by a few degrees. The overall standard error for the comparison between the video analysis and the "smart" debris determination of the yaw angle was calculated at SE_{Yaw}=11.47°. The time history of the yaw angle calculated from the video analysis was potentially biased by the video-based determination of the top corners of the shipping container. It was interesting to note that the largest absolute difference between the two time histories occurred within the time-span when the highest velocities lead to slightly blurred images which subsequently made the detecting of the debris corners more difficult. In addition, spatial distortion stemming from the image referencing with respect to the apron plane affected the video analysis as the container corners were at least 0.06 m elevated above the apron plane. On the other hand, a magnetometer-based motion sensor bias was noticed during the pass-by of the motion sensor above the metal screws which fixed the construction boards of the apron.

3.5 Discussion

3.5.1 General aspects

To advance the state-of-the-art of the current experimental tools used to track individual objects in 6DOF in a non-intrusive, yet accurate manner, a novel measurement “smart” system was developed. The system was termed “smart” debris system as it was originally intended to focus on studies dealing with tsunami debris motion. The measurement of the space and time position of individual “smart” debris was accomplished with a real-time location system which uses electromagnetic waves. During the system development and validation tests, a tag used for the positioning system was enclosed in a water-tight housing, along with the applied motion sensors. The system is fully non-intrusive, without any cable connections. In order to minimize error accumulation related to the motion sensor, it was thus important to open the “smart” debris housing in order to set the motion sensor’s internal clock. Periods without manual clock synchronization of more than a couple of hours would inevitably have led to time shifts between the position and orientation readings which had to be corrected manually. To circumvent this additional step, tests employing motion sensors with wireless connections were also conducted during the system development – however, these were unsuccessful. This was because no stable data connection could be maintained when the bore violently impacted the debris in some of the tests. Additionally, the maximum communication range between the motion sensor and its connection dongle was effectively limited; and was no more than 3.0 m.

Despite the ability of the proposed “smart” debris system to track positions in time and space, 3D orientation readings will be beneficial for debris impact studies and numerical modeling of such setups. As was pointed out by Haehnel and Daly (2004) in a study addressing the impact forces of drift wood in rivers, the debris’ orientation was found to be pivotal in determining impact forces. Due to the random nature of turbulence in an approaching flow entraining a piece of debris and irregularities in debris’ initial placement in laboratory studies it will however be difficult to yield favorable agreement between experimental debris studies and numerical comparisons on a per-experiment basis. It is however believed that transitioning to stochastically meaningful experimental work using the proposed “smart” debris system with higher numbers of experimental runs will allow to obtain datasets with probabilistic content describing debris orientation in time and space; these in turn can be compared with numerical results more easily as then mean statistic values are compared rather than individual debris’ trajectories.

3.5.2 Accuracy of BLE-based positioning systems

The accuracy of BLE-based positioning system is generally known to be influenced by five factors. The first three refer to system’s characteristics and geometry while the other two are related to the environment in which the system is deployed. Firstly, since the angle of arrival of the electromagnetic waves between the locators (ceiling-mounted) and the tags is assessed for the estimation of its position, it is crucial to determine the locator’s spatial position as accurately as possible. A rangefinder with an accuracy of ±1.0 mm was used to measure the distance and positions were further computed by three-line trilateration with the planar laboratory floor set as reference level. Secondly, the orientation of the each locator in the antenna array had to be known *a priori* for an accurate position result. Reliable and accurate mounting of the antenna was achieved by attaching them to a rigid frame placed above the test area in the preliminary laboratory tests taken place at the University of Ottawa as well as during use in the Waseda University Tsunami Basin. Thus, the system was deployed as accurately as possible and with instruments which were an order of magnitude more accurate than the positioning system output. Thirdly, the geometric position of the antennae to the BLE tags is of utmost importance. In global positioning systems, the metric *dilution of precision* (DOP) is utilized to quantify how well the satellites are positioned with respect to the ground receiver. The better the satellites are spatially distributed across the visible sky, the smaller the DOP value and the better is the accuracy of the position determination. Likewise in the presented experiments, an acceptable spatial distribution of the antennae in the horizontal was possible, but as the antennae were all mounted at the same vertical level, poor vertical distribution was achieved. As a result, the standard errors $SE_{x,y}$ of the position measurements were always smaller than the vertical standard errors SE_z. Optimization of the antennae mounting is thus a key element in improving position recordings for future experiments.

On the environmental side, any BLE-based positioning system is also influenced by the amount of obstruction within and around the deployment area which can potentially reflect or diffract electromagnetic waves. The authors ensured that no unnecessary obstructions were present in the transmission space during the laboratory validation testing at the University of Ottawa. Additionally, the transmission space during the wave basin tests was kept free of obstructions. Fourthly, the system accuracy is also influenced by the instantaneous orientation of the BLE tags with respect to the antennae (McCarthy et al., 2009). A further quantification of this aspect was however outside of the scope of this study.

3.5.3 Sampling frequencies of the “smart” debris system

Experimental planning often requires the estimation of the sampling frequency of measurement devices. The proposed 6DOF system was therefore assessed. Based on the static validation tests, sampling rates, f_S, obtained for a varying number of tags are plotted in Figure 3.12.

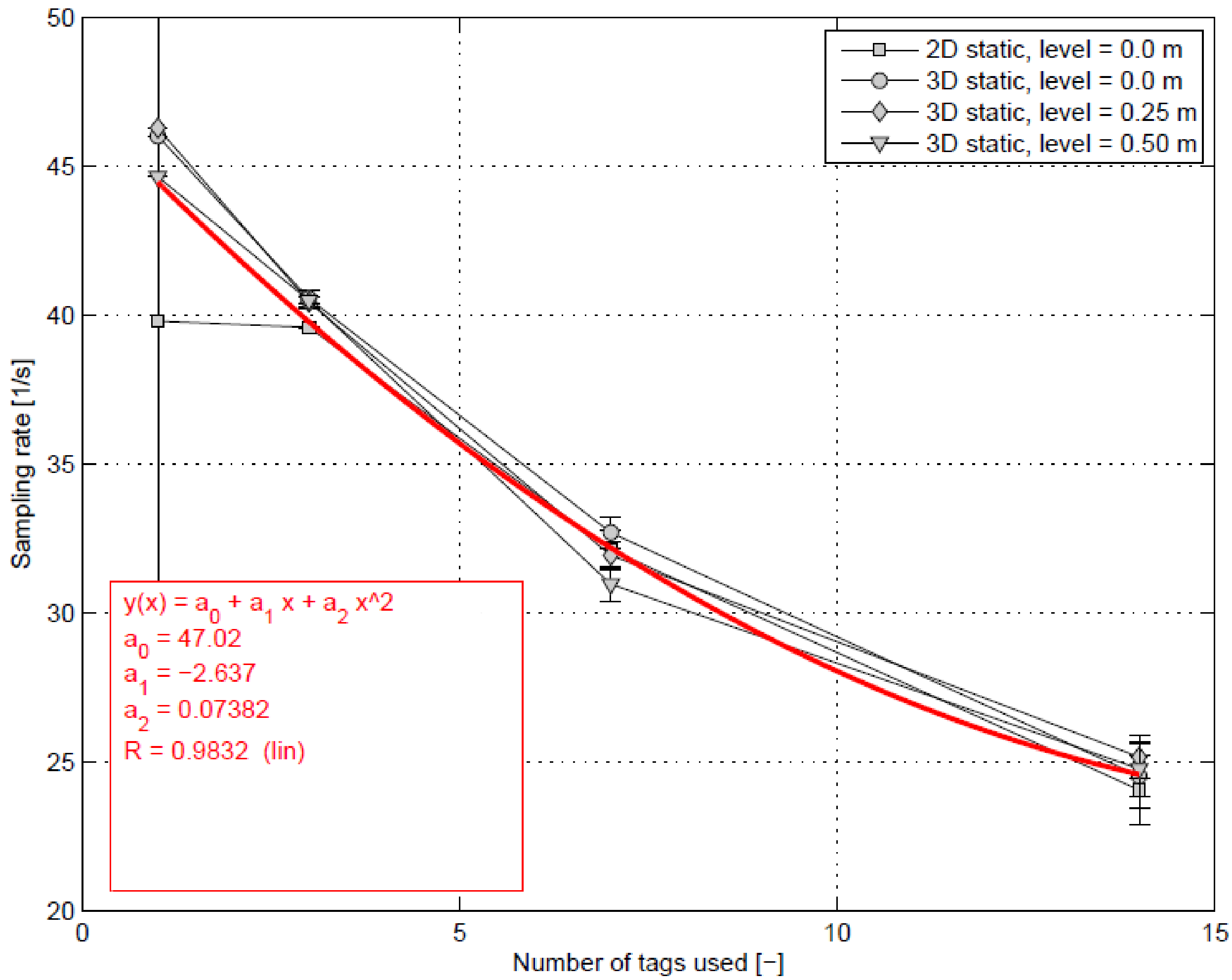

Figure 3.12: Sampling rates obtained with the positioning system in 2D/3D-mode position measurements for different numbers of BLE tags, 1, 3, 7, 14 pcs.

The sampling frequencies were averaged over 3 repetitions and the individual standard deviations for those repetitions is displayed in the form of error bars in Figure 3.12. The data transmission bandwidth by electromagnetic waves is limited to an upper limit which depends on the available hardware, the signal processing speed as well as the frequency range used. Single tag measurements yielded highest sampling rates in the range of f_S=44.0 – 47.0 Hz. Sampling rates decreased with increasing number of tracked tags due to an increasing amount of data associated with more communication between the tags and the locators. A regression analysis allowed the parameterization of the sampling rate f_S depending on the number of tags, n, which is given by the empirical quadratic equation:

$$f(s) = 48.42 - 3.01 \cdot n + 0.10 \cdot n^2 \tag{3.20}$$

Sampling frequencies of orientation measurements obtained with a motion sensor were in a range which depended on the type of measurement accomplished with the device, the filter mode applied, and the amount of data written to the storage drive. Sampling frequencies around 120 Hz were achieved in Kalman-filtered orientation mode and quaternion orientation time history written to the storage drive. Higher sampling frequencies are generally possible with less computationally expensive filter routines. Smallest sampling frequencies in the range of f_S=25 – 30 Hz were obtained with the same settings, but with the additional output parameters tared and untared Eularian angles and all corrected raw data for latter analysis.

As shown above, achievable sampling rates range between 25 and 47 Hz depending on the "smart" debris' setup. With respect to the application case of debris transport over a horizontal apron, those sampling rates provide a lower bound of information to analyse debris motion as time scales are reasonably resolved. A more challenging application will be the usage of the system to study debris impact to vertical structures. In this case time scales of the impact force occurrence and the debris motion approaching a vertical structure entrained in a flow will be somewhat different. In the case of advancing tsunami bores, Lukkunaprasit et al. (2009) and Nouri et al. (2010) report sampling rates for the measurement of hydrodynamic forces on structures between 500 and 1,000 Hz. Tsunami-driven debris collision times which essentially govern the impact forces are reported to range between 0.05 and 0.1 s (Matsutomi, 2009), suggesting that similar sampling rates as those used for the hydrodynamics will suffice to accurately capture forces spikes during impact. On the debris motion side, time scales are arguable larger; debris rotations which govern the magnitude of impact forces (Haehnel and Daly, 2004) happen slower than the impact force exerted on a vertical structure. As shown in Figure 3.11 for the case of the container rotations while propagating on a horizontal apron, orientation readings of the sensor well capture its rotational motion; it is thus argued that the "smart" debris system is principally capable to provide suitable data in this context. Technological advances will certainly improve sampling rates in the coming years beyond the current limit.

3.5.4 Applicability of "smart" debris for field studies

Firstly, the developed "smart" debris system has potential to improve existing methods to track sediment grains and pebbles in rivers as well as on shores. Budgeting sediments in rivers is nowadays commonly accomplished with sediment traps or by equipping pebbles with passive RFID tags which could then be recovered after major flood or storm events in a time-expensive manual manner (Carré et al., 2007, MacVicar and Roy, 2011, Nathan Bradley and Tucker, 2012). Transient information on sediment transport rates supplementing snapshots of transport rates from sediment traps after flood events could become available by applying "smart" debris components such as the positioning system in this context. This could be accomplished by submerging an array of locator antennae in waterproof housings along a river transect in order to register BLE-tagged pebbles online during a flood event. Equally, such instrumentation might improve studies aiming at understanding beach morphology continuously instead of basing information only on post-storm assessment (Benelli et al., 2012, Bertoni et al., 2012). Challenges in this regard will be optimal antennae ranging and battery power optimization.

Secondly, an even more promising field of application could be continuous field tracking of drift wood dynamics in river sections. To date, the temporal dynamics of drift wood travelling in rivers remains poorly understood as was recently outlined by MacVicar et al. (2009). Schenk et al. (2014) implemented an online tracking of drift wood in transit on the Roanoke River, NC, USA, by using 433 MHz RFID tags. Their RFID instrumentation allowed to investigate drift wood along a longer reach of the river; it also included assessment of log jam formation and decay. In this context, the "smart" debris system could be beneficial to deepen insight into log jam formation and decay would be influenced by individual pieces of log. The usage of the Quuppa LD-7L (long range) outdoor antennae would allow for recording of individual trajectories in the vicinity of potential log jam locations. Motion sensors could deliver supplementary information on the individual rotational rates of the logs involved.

Thirdly, novel applications of the "smart" debris system in regard to sports analytics are conceivable as 6DOF could be monitored holistically whereas in recent applications mostly singular degrees of freedom were addressed. In sports analytics, personally worn devices for tracking body parameters such as heartrate, positions in field or rotational accelerations of body members become increasingly important to improve competitive skills (Leser et al., 2011, Twist et al., 2013, White and MacFarlane, 2015).

3.6 Conclusions

A system based on integrated wireless sensors was developed to track partially submerged or floating debris in violent flows with up to 6DOF in experimental studies. The system consisting of a motion sensor for debris orientation measurement and an indoor positioning device based on BLE was termed "smart" debris. Individual sensors were synchronized as accurate as 30 – 50 ms based on the NTP protocol. Validation tests under stringently controlled laboratory conditions and an application test program was conducted in the Waseda University using a wave basin which can generate strongly non-linear solitary waves. The subsequent tsunami-like highly turbulent bore revealed a promising application of the proposed system for hydraulic and coastal engineering applications. The system renders an alternative to image-based tracking devices which may fail under conditions of obstructed sight and large number of debris. Several specific conclusions drawn from the results of this extensive test program are:

Horizontal positioning accuracy was found to be in the range of 0.05 – 0.25 m, with standard deviations in the range of 0.01 – 0.07 m. Vertical positioning error was found to be of up to 0.042 m, with a standard deviation up to 0.02 m. The error and the standard deviation depend on the amount of obstruction in the area where the positioning system is deployed. That influenced the positioning system negatively and a number of reasons for this were identified.

The quality of the indoor positioning system was proven to be satisfactory within a typical space of 9.0 m^2 under static tests conditions as well as in conditions with constant debris motion velocity. Additionally, the capacity of the "smart" debris system to track oscillatory motions as of a lab pendulum was successfully demonstrated. However, it was shown that the accuracy of the vertical direction is of one order of magnitude lower than the accuracy in the *x*-*y* test plane. A remedy is to increase the number of receiver antennae and improve their spatial distribution.

The measurement of the time-history of the debris orientation revealed a standard deviation under real experimental conditions in a wave basin of SD = 11.4°. Potential errors were due to magnetic disturbances caused by the motion sensors across the ferromagnetic nails. In order to reliable make use of the orientation readings, the proximity of the motion sensors to any ferromagnetic elements has therefore to be minimized when the “smart” debris are utilized.

It was demonstrated that the “smart” debris system provides useful data such as spreading angles for up to 9 debris and the time history of the yaw angle of the debris being transported on a harbor apron after being set in motion by an approaching broken wave.

The proposed system is deemed capable to advance future hydraulic and coastal engineering experimental applications with more detailed knowledge about individual 6DOF time-histories. Potential areas of future application might include the study of drift wood trajectories during flooding (Crosato et al., 2013), detailed tsunami debris studies (Nakamura et al., 2012), or the motion of armor stone elements in breakwaters.

3.7 Link to Chapter 4

While the sensor-based tracking method provided accurate results, a secondary novel method was developed to provide a redundant tracking method to ensure correct and accurate data for the experiments performed at Waseda University, Tokyo, Japan. Using the camera system already in place for the tracking of the bore front and observation of the debris entrainment, a novel camera-based tracking algorithm was developed to track the trajectory and orientation of the debris throughout each experiment. The camera-based tracking algorithm is further presented in Chapter 5.

Chapter 4. Optical Tracking of Debris Motion in High-Velocity Flow (CEJ-JSCE, 2016)

Preprint of an article published in Coastal Engineering Journal, Vol. 58, No. 2 (2016). DOI: 10.1142/S0578563416500054 © World Scientific Publishing Company. http://www.worldscientific.com/worldscinet/cej

4.1 Introduction

The urbanization of coastlines worldwide has resulted in an increased research emphasis on extreme events such as tsunamis, storm surges and floods. Tsunamis have been of particular concern, as catastrophic loss of life and widespread damage has recently been felt during the 2011 Tohoku tsunami in Japan and the 2004 Indian Ocean tsunami, with the latter claiming over 220, 000 lives and costing over US$319 billion in damages (Ioualalen et al., 2007). The concentrated efforts of researchers worldwide have led to a focus on building standards as they relate to tsunami impact loads and effects. The focus of these standards has generally been related to the hydrodynamic forces associated with tsunami bores (Haehnel and Daly, 2004, Palermo et al., 2009, Nouri et al., 2010, St-Germain et al., 2013) and the inundation of tsunamis through coastal communities (Goseberg et al., 2013), but little research has gone into the movement and impacts of debris entrained within the bore. The US Federal Emergency Management Agency (FEMA) has developed multiple design guidelines, FEMA P646 (2008, 2012) and FEMA P-55 (2011), which use a contact-stiffness method of determining impact force, where the maximum impact force is a function of the velocity, mass and stiffness of the debris. However, the design guidelines state that whether or not debris impact will occur is less of a concern as long as a reasonable allowance is made for debris impact. Naito et al. (2014) and Charvet et al. (2014) noted in their assessments of the 2011 Tohoku tsunami that debris impact played a significant role in building damage, but current standards do not have provisions for quantifying the movement of debris, resulting in the conservative standards outlined by FEMA (2012).

The assessment by Naito et al. (2014) examined the motion of debris within the tsunami event. Using the results of a post-mortem field survey, coastal areas at high risk for debris impact could be identified. The study examined the movement of structural materials, wood structures, steel ships and shipping containers. Debris spreading was determined by inferring the motion of debris based on impacts sites found on coastal structures. Entrained debris widely ranged in size, material, and origin. However Naito et al. (2014) focused on determining the motion of the shipping containers as the containers will be concentrated in port environments. Based on these field observations, a spreading angle of ± 22.5^{o} was derived as a conservative estimate of the maximum spreading angle of shipping containers, though the authors noted that the surrounding environment would have a significant effect on the motion.

The random nature of the debris movement and collisions make the determination of debris spreading in an experimental setting difficult. Matsutomi (2009) used experimental results to determine the probability of a single piece of driftwood colliding with a vertical structure. The probability function was approximated using a normal distribution and separated into two parts: the driftwood location in relation to their origin, and the time for the driftwood to reach the structure. Both distribution functions were dependent on the size and shape of the driftwood as well as the Froude number of the incoming bore. Yao et al. (2014) examined the motion of scaled-down coastal houses in a solitary wave; a Gaussian kernel was assumed and density functions were derived to determine the maximum draft of the debris and the final positions. Adjusting the initial position of the debris and the wave height, the authors concluded that wave height had the most significant effect on the motion of the debris.

Imamura et al. (2008) examined the transport processes of single negatively buoyant rectangular boxes, mimicking scaled-down boulders, in a dam break flow. Varying the impoundment depth and the size of boxes, the authors found the movement of the boxes to be highly repeatable, with the boxes initially being transported by saltation and by rolling until the bore velocity was significantly lowered to allow for sliding. The authors also noted that the initial orientation of the long axis of the box, i.e., whether parallel or perpendicular to the flow, significantly affected the final resting position of the box. Debris orientation is also critical when considering impact forces, as eccentric impacts produce significantly lower impact forces (Matskevitch, 1997, Haehnel and Daly, 2004).

As can be seen from these studies, many factors contribute to the overall motion of debris within an inundating bore. Therefore, to determine debris motion and impact forces requires quick and accurate methods to be derived to evaluate the position and orientation of the debris. Previously, studies have often relied on the final displacement to determine the motion of debris, without considering the intermediate steps in the process (Imamura et al., 2008, Naito et al., 2014, Yao et al., 2014). Without these steps other factors, such as the effect of the surrounding environment and obstacles, cannot be properly evaluated. Historically, the tracking of debris would be determined by archaic video analysis from camera readings, going frame-by-frame through the video recordings of the experimental tests, which can be very time-consuming. Multi-object tracking has been an important topic in a variety of fields, such as surveillance, human-computer interfaces and traffic (Zhou et al., 2009). However, the implementation of these methods in coastal engineering has been much less common. Particle Tracking Velocimetry (PTV) uses an object-tracking methodology to determine flow velocity fields and the spatial structure of turbulence; however, large numbers of particles are needed for accurate results (Cowen and Monismith, 1997). Recently, Rueben et al. (2014) applied an object-tracking technique that used dots on the top of a box as a binary identifier to track debris motion and rotation. Each box had a number of dots on the top of the box that identified the box as well as the orientation. Additionally, the study used Particle Image Velocimetry (PIV), to track bore characteristics. This method allowed for multiple containers to be automatically and consistently tracked throughout the entire length of a test run. However, the debris for this type of tracking must be large enough to identify the markers on the lid while still identifying the color surrounding the markers, which can restrict scalability.

With the final objective of better understanding the movement of shipping containers in high velocity flow, this paper presents a novel application of multi-object optical tracking techniques. The method aims to:

- Automatically track multiple containers. The algorithm must track the containers accurately and consistently for useful results.
- Be applied to uniformly built containers in order to limit the preparation time needed for implementation of the algorithm.
- Deal with varying lighting conditions that allow the algorithm to be more robust.
- Scalable to multiple container sizes.

The object-tracking algorithm proposed in this paper was written using MATLAB and OpenCV (Bradski, 2000), and validation was performed using results from experiments performed at the Waseda University in December 2014. The algorithm has to track uniformly built shipping containers in real-world coordinates and assign unique identifiers to each container, to be maintained throughout the test run. The algorithm also had to deal with a variety of lighting conditions, as the flume at Waseda University, in Tokyo, Japan, was outside.

The paper is organized as follows: Section 2, "Experimental Setup", presents the tsunami wave basin, instrumentation, containers and experimental protocol; Section 3, "Manual Object Tracking", outlines the method used to validate the results from the multi-object tracking algorithm; Section 4, "Multi-Object Tracking", outlines the processes involved in the novel object-tracking method; Section 5, "Results", presents a comparison of the object-tracking method to a manual tracking method; Section 6, "Discussion" will discuss the challenges involved in the object-tracking algorithm; and the last section, Section 7, "Conclusion" presents recommendations for future research.

4.2 Experimental Setup

4.2.1 Tsunami Wave Flume

The experiments were conducted in the Coastal Engineering and Management Laboratory at the Department of Civil and Environmental Engineering at Waseda University, Tokyo, Japan. A 4.00 m wide and 9.00 m long newly constructed tsunami wave basin (TWB) was utilized (Figure 4.1). The TWB was equipped with a four-chamber overhead reservoir fillable with a vacuum pump (TST-150, Sato Vac Inc., Japan) utilizing the negative pressure principle. The maximum achievable hydraulic head with reference to still water elevation was 0.77 m. The water impoundment was released through computer-controlled air valves (SVB1V-50F-02HS, CKD Corporation, Japan) with a maximum opening diameter of 0.054 m positioned on the top side of the reservoir chambers. The volume contained in the impoundment flowed through a gap of 0.10 m between the TWB bottom and the front side of the reservoir.

The model of a flat, rigid horizontal harbor apron was constructed at 3.95 m from the overhead reservoir. This bathymetry was chosen to simulate a tsunami propagating over a modern port environment. The horizontal bottom in front of the vertical quay, which separated the harbor area from the seaward part of the model domain, was intended as an area for propagating the released water. A right-handed coordinate system with an origin at the midpoint of the edge of the quay wall was used throughout the tests. The y-axis was positive in the direction of the wave propagation.

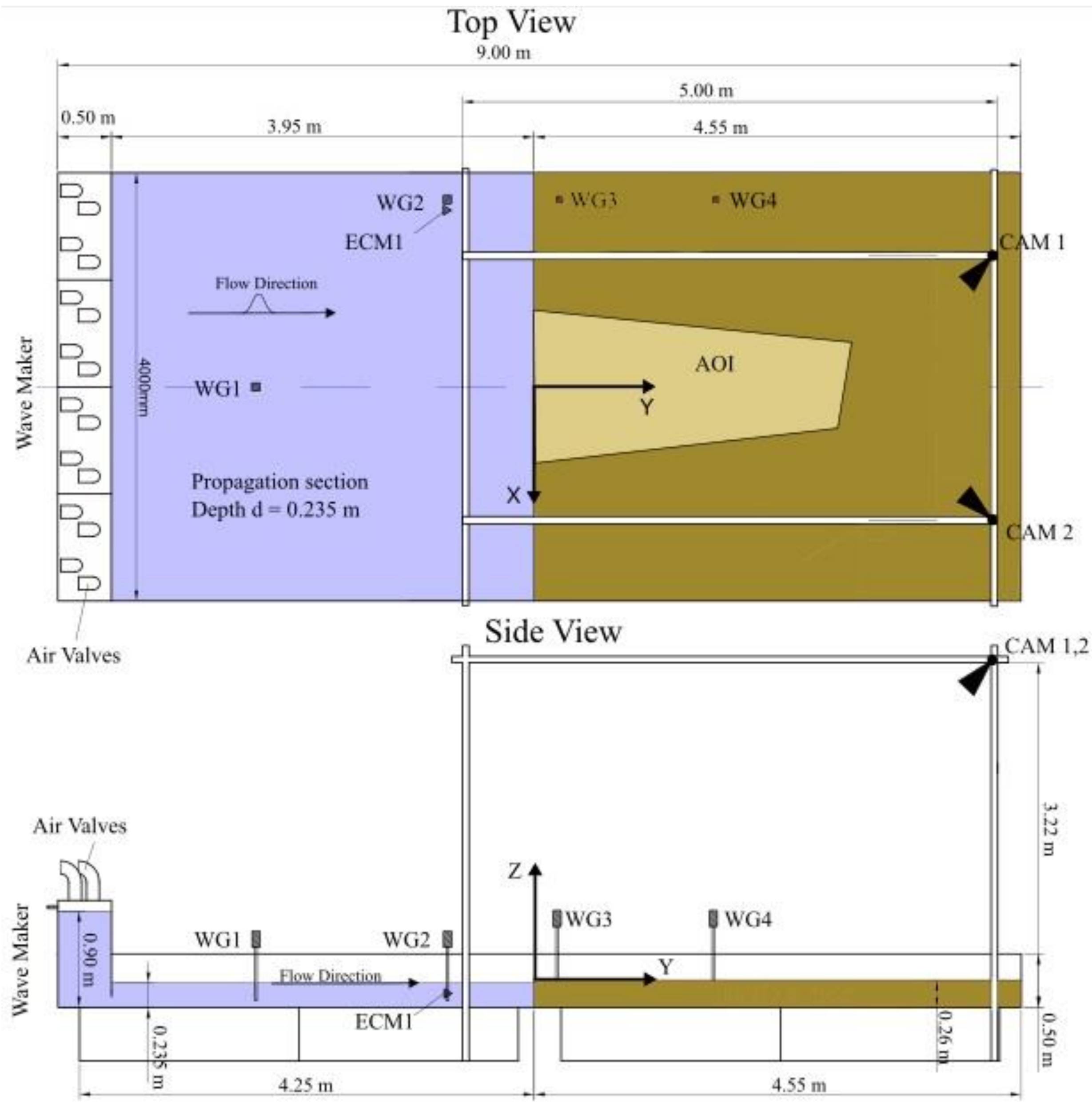

Figure 4.1: Tsunami Wave Basin (TWB) at Waseda University in Tokyo, Japan. The TWB was 9 m long, 4 m wide. The seaward section (initial 3.95 m) consisted of a constant depth of 0.235 m (blue), a vertical quay of 0.25 m height was built followed by a flat horizontal harbour area (brown). WG – wave gauge, ECM – electro-magnetic current meter and CAM – high definition camera.

4.2.2 Instrumentation

Figure 4.1 depicts the positions of the instrumentation mounted to the frame and in the wave basin. Four wire resistance wave gauges (KENEK Co., Ltd., Japan) were mounted at various positions along the basin, sampling at 100 Hz. Data were acquired using an acquisition unit

(VM-806H, KENEK Co. Ltd, Japan). Two gauges were positioned on the harbor area, and the remaining gauges were used to measure the water level in the seaward section. An electro-magnetic current meter (ECM) was used, with its sensor head submerged 0.075 m below the still water level in order to avoid air contact during the passage of the wave. The wave gauges were calibrated against a laboratory caliper prior to the installation of the wave gauges, and yielded a correlation coefficient greater than 0.99 for the entire process.

Two high-definition (HD) cameras (Basler AG, pi1900-32gc, Germany) were mounted at the harbor end of the wave basin on an instrument frame at a height of 2.95 m above the harbor and pointing towards the apron edge. The mutual footprint of the two cameras projected to the harbor area plane (z = 0.00 m) are detailed in Figure 4.1 as the area of interest (AOI) which was defined based on fixed-zoom lenses mounted to the cameras. The cameras were software-synchronized and operated at a sampling rate of 25 Hz.

To investigate the motion of debris propelled by an advancing tsunami bore, standard 20 foot shipping containers (ISO668/688) were down-scaled based on Froude similitude by a length scale of 1 to 40. Each down-scaled shipping container, as shown in Figure 4.2, was manufactured of positively buoyant polyethylene (PE-HMW, 0.92 g/cm³) to match an average gross weight W = 14,400 kg (Knörr and Kutzner, 2008). The overall dimensions of the container were 0.15 x 0.06 x 0.06 m, with an approximate draft of 0.025 m. The total weight of a single container was determined by three separate weightings, and yielded an average total weight of 0.226 kg.

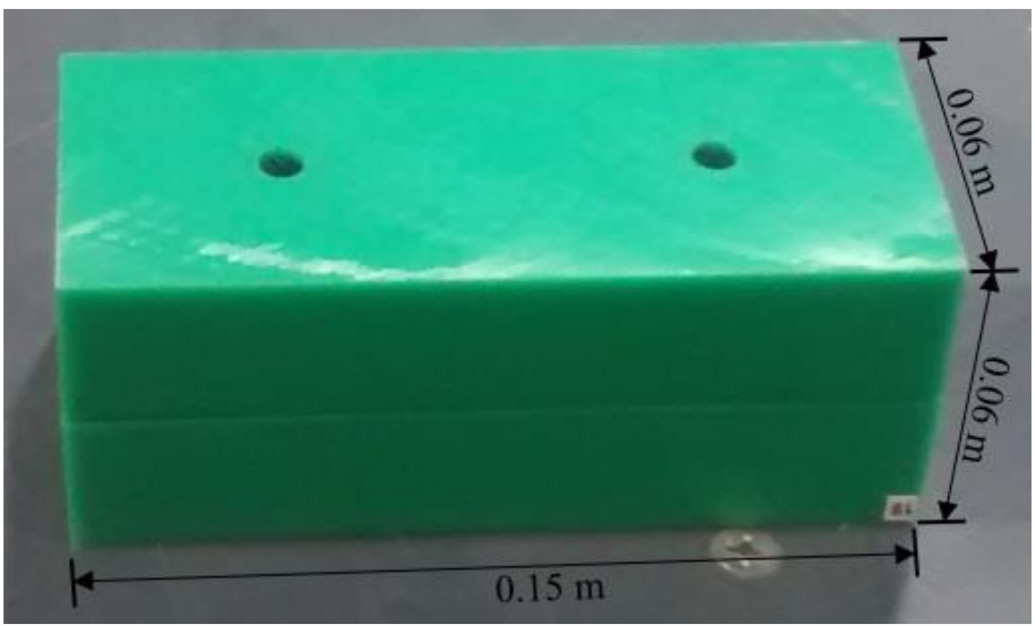

Figure 4.2: Scaled down 20 foot shipping containers made from polyethylene. Dimensions: 0.15 m x 0.06 m x 0.06 m.

4.2.3 Experimental Protocol

The study examined 48 separate test runs, with 6 of those runs being used in the validation of the object-tracking algorithm presented in this paper (shown in Figure 4.4). The water depth in the seaward part of the TWB was maintained at a constant 0.235 m, leaving a freeboard of 0.015 m between the still water depth and the level of the harbor area. For all the experiments performed, the initial hydraulic conditions were kept identical in order to properly implement and evaluate the image processing method proposed herein. Figure 4.3 depicts the time histories of the measured free surface elevation as well as the flow velocities from the ECM from baseline Experiment 1 with full, immediate air valve opening. The hydrodynamic data show that the initial bore front exhibits characteristics similar to those of a solitary wave (Munk, 1949) with a significant tail. The average wave height at the edge of harbor (WG2) was 0.14 m above the still water depth. The maximum flow velocity at a distance of 0.3 m from the apron edge was of 0.82 m/s and occurred 0.15 s after the peak water surface elevation. The wave height at the debris location (WG3) was 0.07 m and the wave height 1.70 m into the harbor area (WG4) was 0.02 m with a flow duration of ~ 5 s. The peak bore front velocity, as the bore propagated over the apron, was 2.8 m/s. The water levels provide substantial room to allow for free container propagation and prevent the grounding of the container. Due to the setup of the horizontal apron in TWB, the flow does not exhibit a receding flow phase.

Flow conditions were also scaled using the same scale used as the shipping containers (1 in 40). At prototype scale, flow depths on the apron ranged from 0.8 to 2.80 m which falls within some of the field survey data from the 2004 Indian Ocean Tsunami (Borrero, 2005, Fritz et al., 2006) who reported flow depths between 0.5 m and 9 m in built-in city environments. The scaled-up maximum bore velocity was 17.7 m/s, which is significantly larger than the bore front velocities found in the field (~2.5 m/s) (Borrero, 2005) or in laboratory conditions (~4.8 m/s) (Goseberg and Schlurmann, 2014). However, for built-in environments, the bore front velocities measured during these experiments are comparable to those observed in the 2004 Indian Ocean Tsunami (10-15 m/s) or in Japan (Chock et al., 2013).

The containers were placed with the centroid of the first row of containers located at 0.23 m from the apron’s edge in onshore direction, while the second row was placed at 0.31 m, and the third row at 0.40 m. The centroid of the central container was placed on the y-axis and the centroids of the outside container were placed 0.18 m apart to each side of the Y-axis (+/- y/axis). For the experiment with six containers, they were stacked in two layers with one row of three containers, again, keeping a distance of 0.23 m between the container centroids and the apron’s edge. The spacing between containers was set at 0.03 m apart in both the x- and y-direction.

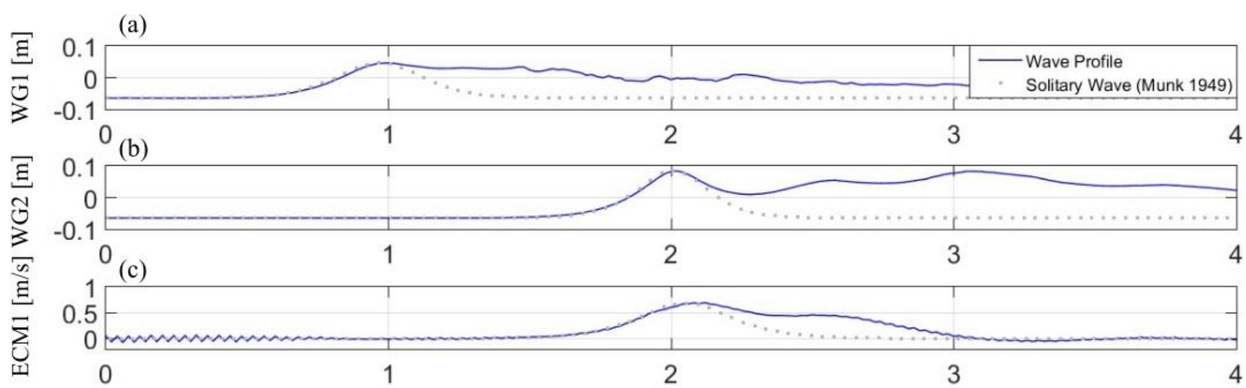

Figure 4.3: Comparison of the Wave Profile Time-Histories from Wave Gauge 1 (a), Wave Gauge 2 (b), and ECM1 with the analytical solution for a solitary wave (grey dots) by Munk (1949) - position of the WGs and ECM1 are shown in Figure 4.1.

4.3 Manual Object Tracking

For validation purposes, a comparison between the manually analyzed camera images and the multi-object tracking algorithm results was conducted to assess the general suitability of the algorithm, which has not yet been widely applied in hydraulic and coastal engineering. The two-dimensional (2D) trajectories obtained with the algorithm were subsequently compared with positional information gathered from the manual method. The camera images were read in automatically using a MATLAB code developed by the authors. The four corners of the top of the container were selected to determine their pixel coordinates. The stored image coordinates were then projected from pixel space into real-world SI-unit space onto the harbor plane based on control points at the extrema of the AOI depicted in Figure 4.1. Centroid coordinates of the selected quadrilateral were then computed form the corner coordinates. An estimated accuracy of ±10 pixels was obtained during the manual selection of the container corners in the images due to image blur related to the maximum available shutter speed of the cameras. Pixel-to-real-world coordinate ratios varied based on the non-orthographic angular field provided by the cameras. Values ranging from 6.41 – 10.74 pixels/cm in the x-direction and 5.59 – 5.92 pixels/cm in the y-direction were obtained. Thus, the SI-unit-based accuracy of the manual image processing was determined to be in the range of 0.01 – 0.02 m in the x-direction and 0.02 m in the y-direction. However, this does not infer that the optical system provides true real-world coordinates as there may have been errors in the initial measurement of the control points. Thus all subsequent comparisons between either recordings should rather be interpreted qualitatively.

4.4 Multi-Object Tracking

4.4.1 Method Work Flow

The object-tracking algorithm is separated into two sections: object detection and object tracking. Object detection is used to examine each frame and determine the position of the container. There are many different methods of object detection, such as background subtraction, scale-invariant feature transform (SIFT), and color thresholding (Pavlopoulos et al., 2007, Park et al., 2008, Xia et al., 2010). Since the containers used were a single color (green), Color Thresholding was determined to be the best method to detect the objects and limit noise. Object tracking assigns a unique identifier to each container and maintains the identifier through the length of the test run. Using a Kalman Filter and the Hungarian Algorithm, unique identifiers can be assigned by predicting the position of each container in the next frame and assigning the detected containers to the closest predicted position; the following sections will further describe in detail the object-tracking algorithm.

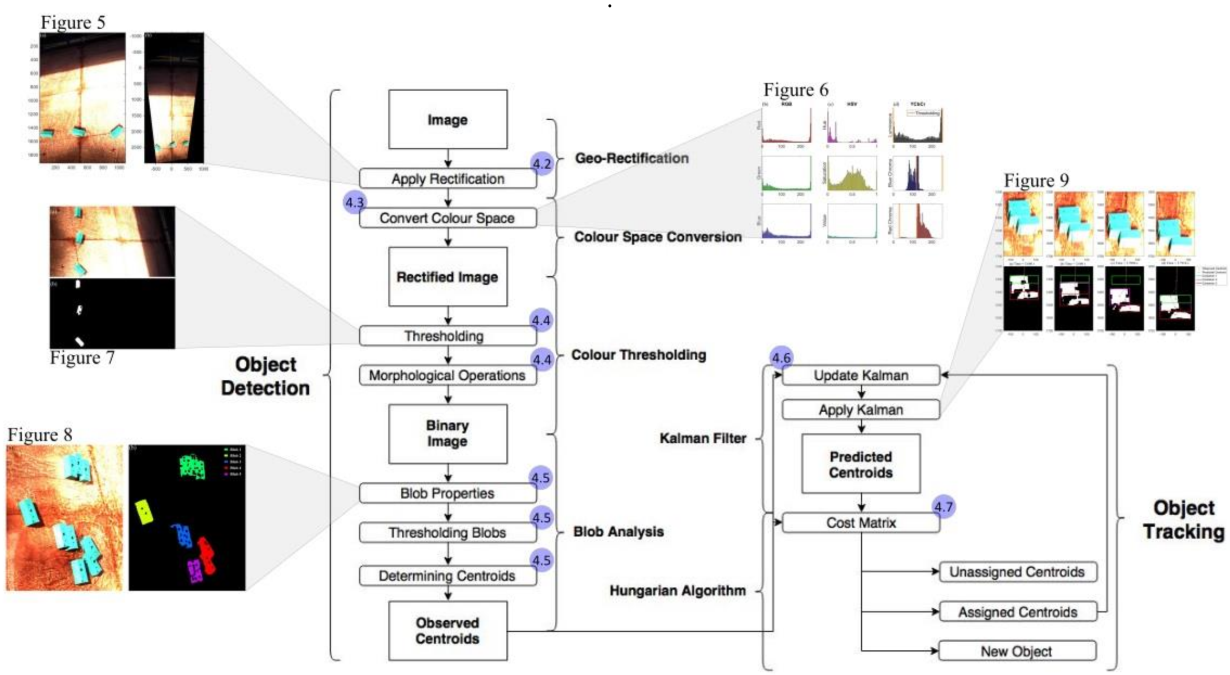

Figure 4.4: Object-Tracking Algorithm Workflow. The algorithm is separated into two primary components: Object Detection and Object Tracking. The sections which discuss each component of the workflow are depicted by the violet circles.

4.4.2 Geo-rectification

Image rectification is needed to take the camera-frame (pixel) coordinates and transform them to real-world coordinates. The coordinates are transformed using an implicit approach that requires three or more known (ground) control points (Holland and Holman, 1997). The transformation of the coordinates requires three separate adjustments: scaling (S_s), rotation (R_θ) and translation (D_{x_0,y_0}). Since the pixel coordinates in both the image plane (${}^{i}p_j$) and the flume plane (${}^{f}p_j$) are known, an equation for each control point can be generated using the equation below.

$$ {}^{f}p_j = D_{x_0,y_0} * S_s * R_\theta * {}^{i}p_j \tag{4.1} $$

$$ \begin{bmatrix} x_f \\ y_f \\ 1 \end{bmatrix} = \begin{bmatrix} 1 & 0 & x_0 \\ 0 & 1 & y_0 \\ 0 & 0 & 1 \end{bmatrix} \begin{bmatrix} s & 0 & 0 \\ 0 & s & 0 \\ 0 & 0 & 1 \end{bmatrix} \begin{bmatrix} cos\theta & -sin\theta & 0 \\ sin\theta & cos\theta & 0 \\ 0 & 0 & 1 \end{bmatrix} \begin{bmatrix} x_i \\ y_i \\ 1 \end{bmatrix} \tag{4.2} $$

$$ x_f = x_i * s * cos\theta - y_i * s * sin\theta + x_0 \tag{4.3} $$

$$ y_f = x_i * s * sin\theta + y_i * s * cos\theta + y_0 \tag{4.4} $$

Solving the system of equations will determine the scale factor (s), the angle of rotation (θ) and the coordinates of translation (x_0, y_0). The variables can then be used to transform all the pixels in the image to real-world coordinates, as outlined in Figure 4.5. The left image shows the raw image that would be taken from the camera, with typical pixel coordinates, which always begin in the top left corner and move in the positive direction in the downward and right directions. The right image shows the image once the transformation has been applied. The image now shows the image in the plane of the flume, outlining the AOI in Figure 4.1. The coordinates are translated into the real-world coordinates system with the origin at the apron edge.

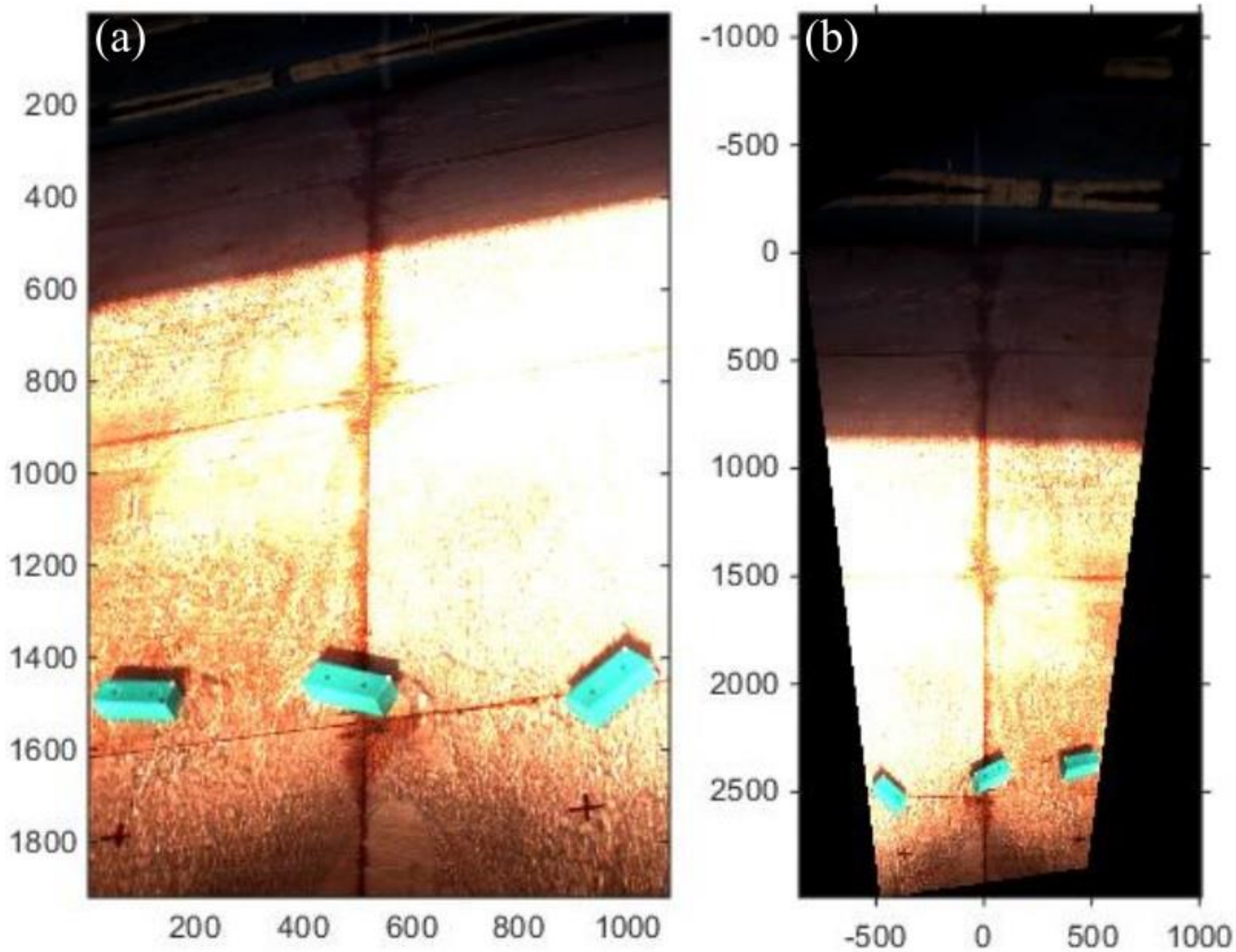

Figure 4.5: Image from Experiment 9 having undergone the Geo-rectification process. (a) original image in pixel coordinates. Camera images typically have the origin in the top left corner of the image. (b) image in real-world coordinates. The origin is at the apron edge as shown in Figure 4.1.

4.4.3 Color Space Conversion

An image color space is a three-dimensional geometric space with axes that are appropriately defined such that symbols for all possible color perceptible by humans would exist (Kuehni, 2003). The color space of the image is critical in the object detection algorithm, as a color space that can identify a color in the smallest range of values will limit the amount of noise in the resultant binary image. Color spaces have generally been developed for convenience, so a wide variety of spaces has been developed for various needs, such as hardware, user control and hardware design (Grundland and Dodgson, 2005).

The two color spaces most commonly used in expressing images are Red-Green-Blue (RGB) and Hue-Saturation-Value (HSV). However, both color spaces have a lot of redundancies associated with the expression of individual colors (Chai and Bouzerdoum, 2000), which makes Color

Thresholding difficult (further detailed in Section 4.4.4). Due to the need to reduce the redundancies in order to transmit television images, a family of color spaces was developed in the past to separate the RGB color space into luminance and chrominance, specifically in this case Luminance (L), Blue-Difference Chroma (C_b), Red-Difference Chroma (C_r). The YC_bC_r color space is not an absolute color space, and therefore RGB data must be made available to convert to the YC_bC_r space. Equation 4.5-4.7 are used to convert from RGB to the YC_bC_r color space:

$$Y = 0.299 * Red + 0.587 * Green + 0.114 * Blue \tag{4.5}$$

$$C_b = 128 - 0.017 * Red - 0.332 * Green + 0.500 * Blue \tag{4.6}$$

$$C_r = 128 + 0.500 * Red - 0.419 * Green - 0.081 * Blue \tag{4.7}$$

Luminance captures the intensity of the color, Blue-Difference Chroma captures the colors between Yellow and Blue, and Red-Difference Chroma captures the colors between Green and Red. This color space allows the green of the containers to be captured in the C_b and C_r values, and the difference in lighting due to the flume being outdoors can be captured using Y. Figure 4.6 shows the histograms of the different color spaces of the image, shown in (a). In the Red-Difference Chroma histogram (d), there is a noticeable clump of values, below 120, clearly separate from the other values, which is a result of the existence of three containers. Finding a color space that can clearly define the difference between the object being tracked and the background makes the next step, Color Thresholding, significantly easier.

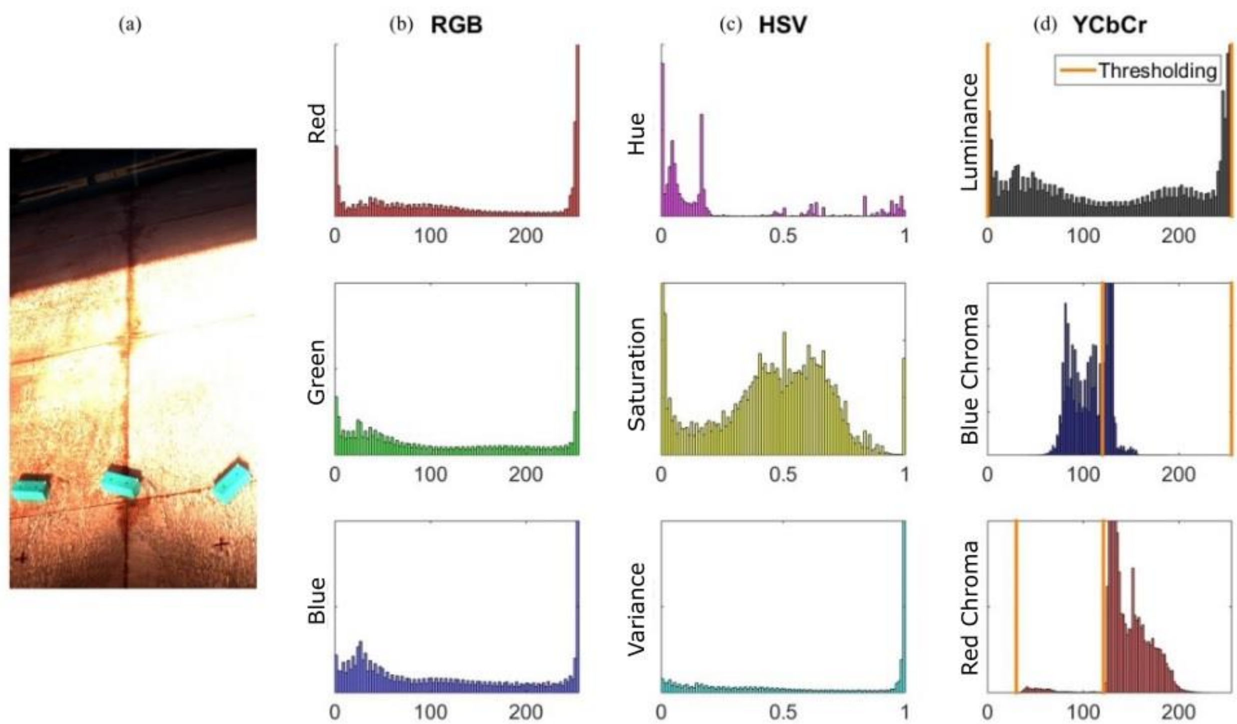

Figure 4.6: Histograms of color spaces for varied-light images from Experiment 9 (a). (b) Histogram of the RGB color space; (c) histogram of the HSV color space; and (c) histogram of the YC_bC_r color space along with the values used in the Color Thresholding.

4.4.4 Color Thresholding

Image segmentation is a common image processing technique that subdivides an image into regions or objects based on discontinuity or similarity (Raof et al., 2008). Color Thresholding uses similarity between pixels to segment the image based on predefined thresholds. Once the criteria are determined, the Color Thresholding algorithm examines each pixel and applies a Boolean operation to determine if the pixel falls within the threshold (then assigned a "1") or outside the threshold (then assigned a "0"). From the thresholding results, a binary image can be created, as shown in Figure 4.7(b). In the image, the "1" pixels are shown in white and the pixels outside the threshold ("0") in black. Noise represents the uncertainty (or error) in the binary image related to stray pixels falling within the thresholding values (Cowen and Monismith, 1997). Mathematical morphology has been shown to be useful in the processing of binary images, particularly in noise suppression (Comer and Delp, 1999). Mathematical morphology is based on the principle that the image in question displays too much information, and the morphological operations manage the loss of information through successive transformations (Serra, 1986). The resulting image has well-defined objects that can then be examined using Blob Analysis.

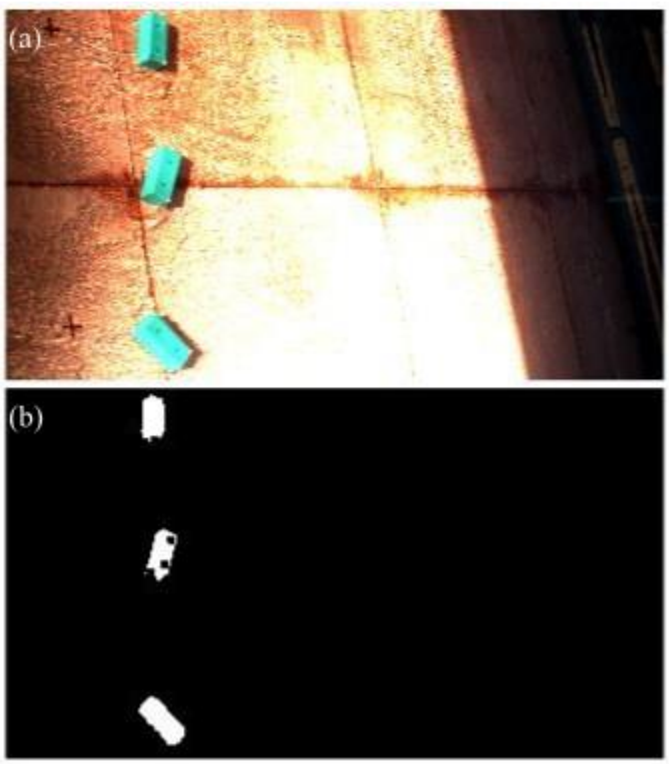

Figure 4.7: Binary Image after Color Thresholding and Morphological Operations have been applied. (a) Original image; (b) binary image.

4.4.5 Blob Analysis

On the basis of the binary images obtained from the previous Color Thresholding step, it was then important to identify the regions where the objects to be tracked resided. Among other methods, such as point detection, edge detection and blob analysis (Dutta and Chaudhuri, 2009, Salvi, 2012, Pribyl et al., 2013), Blob Analysis was found to be most consistent in identifying blobs of interconnected “1”-type pixels. In general, Blob Analysis consists of identifying the blobs in the binary image, identifying the number of containers within each blob and determining the important properties of each blob (Chen et al., 2007). A blob is found by identifying regions of connected “1” pixels in the binary image. Each blob is assigned an integer to allow the algorithm to distinguish between different blobs. The issue with Blob Analysis, as can be seen in Figure 4.8, is that when agglomeration of the containers occurs, the Blob Analysis algorithm will identify all connected containers as one blob (Cucchiara et al., 2003). Based on extensive analysis of the motion of the connected containers, thresholding of the area of the blob and the solidity (area of “1” pixel in the blob divided by total area of the blob) was used to identify the number of containers within each blob. Once the number of containers was determined, the important properties of the containers were established, such as the centroid, bounding box and orientation of the long axis. Due to this method of determining the number of containers within each image, the debris requires a significant geometric feature, in this case the long axis of the container, for the algorithm to determine the orientation of the container. In cases without the significant geometric feature, the algorithm would be unable to determine the orientation of multiple debris within the blob. The centroid derived from the Blob Analysis is referred to as the “observed centroid”.

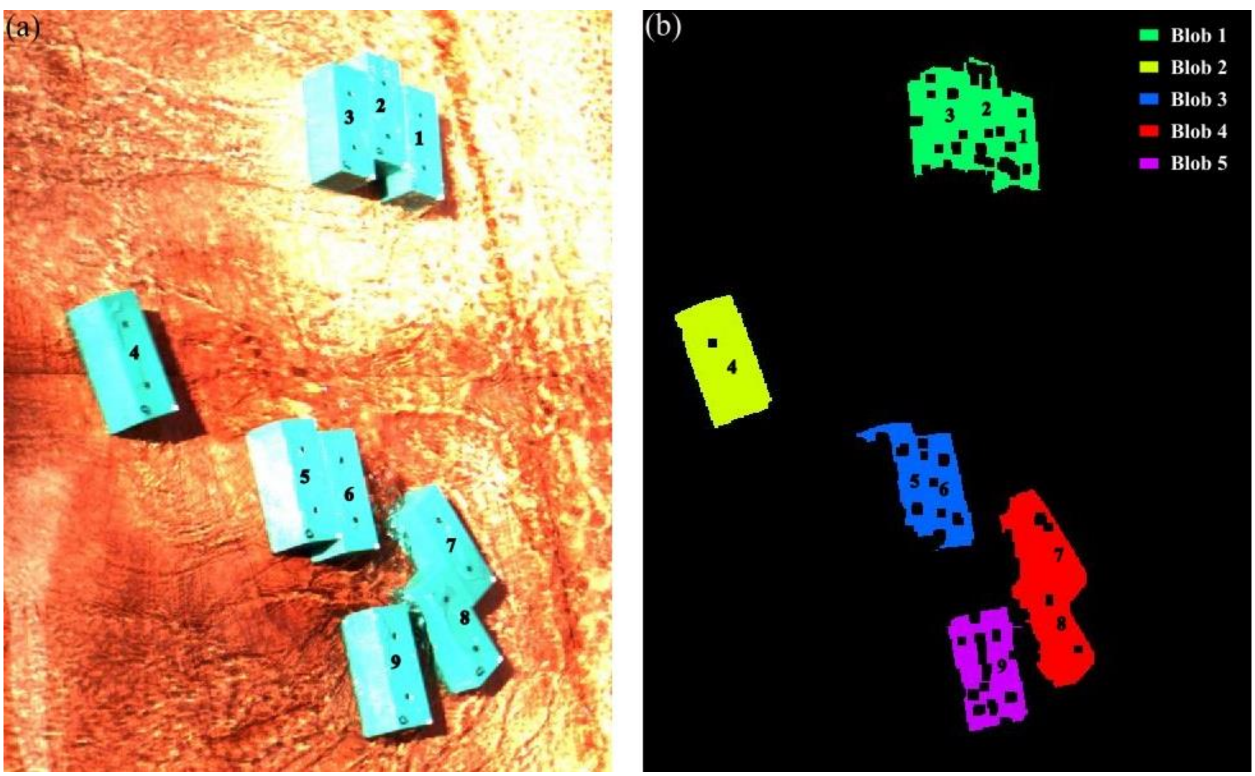

Figure 4.8: Binary image after Blob Analysis has been performed. (a) Original image from Experiment 17; (b) binary image with each color corresponding to a different blob. (b) Shows the issue of multiple containers being combined into one blob when containers touch.

4.4.6 Kalman Filter

One of the key issues in object tracking is being able to maintain the identification associated with the unique containers from frame to frame. A constant-velocity Kalman Filter is a common technique used in object tracking (Chan et al., 1979), and also qualitatively matches the container dynamics observed in the flume. The filter provides a predicted centroid location, and using the Hungarian Algorithm (discussed below), the predicted centroid will be matched to an observed centroid to maintain the unique identification of the container. The filter essentially acts to adjust where the algorithm will search the next frame for the same container. The Kalman Filter is derived using simple 2D kinematics equations for displacement and velocity.

$$x_t = x_{t-1} + \dot{x}_{t-1} * \Delta t + \frac{1}{2} * \ddot{x}_{t-1} * \Delta t^2 \tag{4.8}$$

$$\dot{x}_t = \dot{x}_{t-1} + \ddot{x}_{t-1} * \Delta t \tag{4.9}$$

Where $\dot{x}$ is the velocity in the x-direction, $\ddot{x}$ is the acceleration in the x-direction and Δt is the sampling interval. Applying Equation 4.8 and Equation 4.9 in both the x- and y-direction allows the equations to be inserted into the state and measurement equations of the Kalman Filter:

$$\overline{x_t} = \phi * x_{t-1} + B * u_t \tag{4.10}$$

$$\begin{bmatrix} x \\ y \\ \dot{x} \\ \dot{y} \end{bmatrix}_t = \begin{bmatrix} 1 & 0 & \Delta t & 0 \\ 0 & 1 & 0 & \Delta t \\ 0 & 0 & 1 & 0 \\ 0 & 0 & 0 & 1 \end{bmatrix} * \begin{bmatrix} x \\ y \\ \dot{x} \\ \dot{y} \end{bmatrix}_{t-1} + \begin{bmatrix} \frac{\Delta t^2}{2} & \frac{\Delta t^2}{2} & \Delta t & \Delta t \end{bmatrix} * \begin{bmatrix} \ddot{x} \\ \ddot{y} \\ \ddot{x} \\ \ddot{y} \end{bmatrix}_{t-1} \tag{4.11}$$

$$\overline{z_t} = C * \overline{x_t} \tag{4.12}$$

$$\bar{z}_t = \begin{bmatrix} 1 & 0 & 0 & 0 \\ 0 & 1 & 0 & 0 \end{bmatrix} * \begin{bmatrix} x \\ y \\ \dot{x} \\ \dot{y} \end{bmatrix}_t \tag{4.13}$$

where $\overline{x_t}$ is the predicted state vector at time t, ϕ is the state transition matrix, x_{t-1} is the state vector at time $t-1$, B is the input matrix, u_t is the acceleration input vector, $\overline{z_t}$ is the measured state vector at time t and C is the measurement matrix. When the predicted centroid is matched to an observed centroid, the state vector is updated with the observed centroid coordinates; alternately, if the predicted centroid is not assigned to an observed centroid, the state vector remains the same and is passed on to the next time interval. Figure 4.9 shows an example of when the object detection does not detect the container outlined in green; the Kalman Filter will maintain the forward trajectory of the container so in the final pane, where the container is once again detected by the object detection, the centroid is assigned to the correct container path.

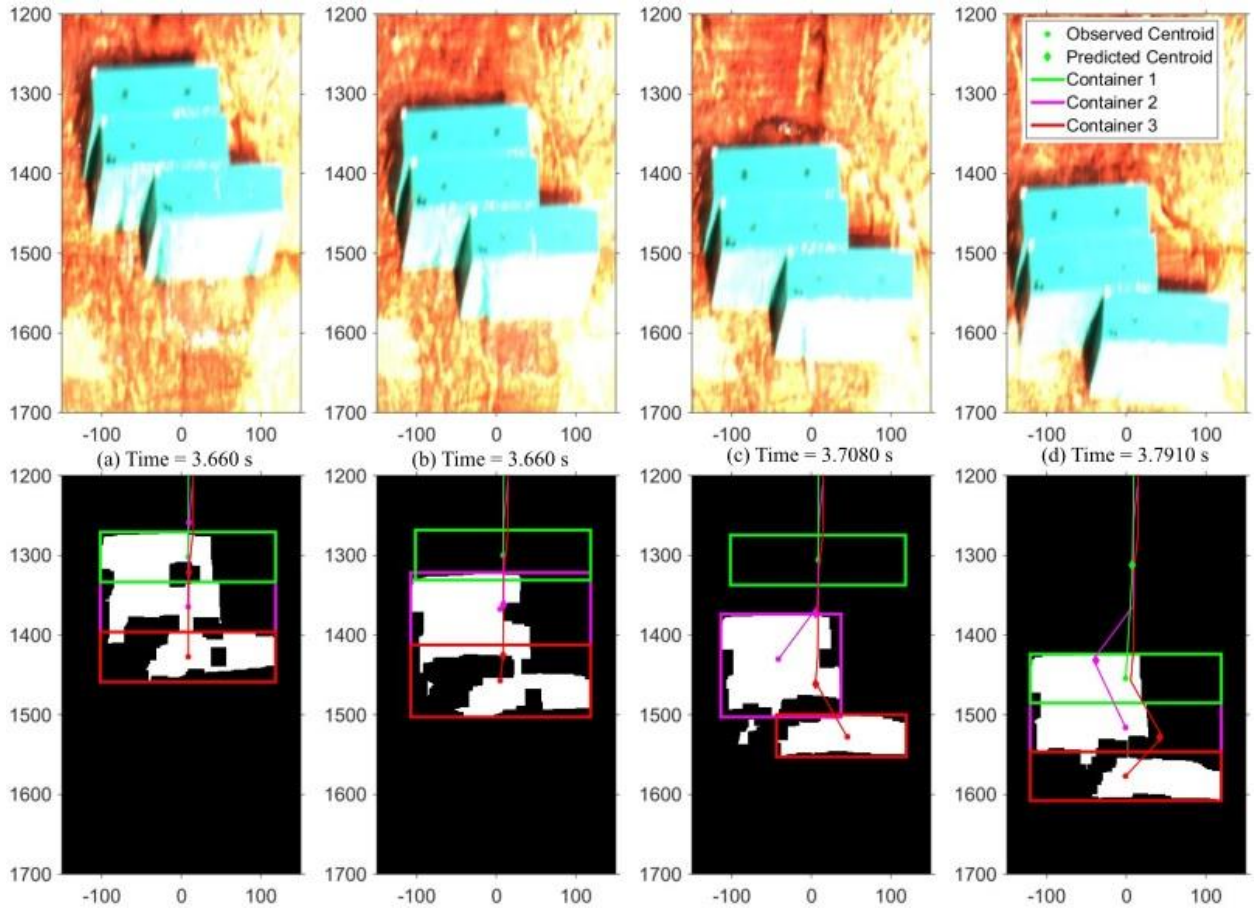

Figure 4.9: The Kalman Filter maintains the unique identifiers even when the containers are touching. The top row shows the frame being processed by the detection algorithm. The bottom row shows the binary image being processed by the tracking algorithm. The centroid captured by the detection algorithm is shown as a solid circle. The centroids predicted by the Kalman Filter is shown as a diamond.

4.4.7 Hungarian (Munkres) Algorithm

Once the object-tracking algorithm has the observed centroids from the object detection and the predicted centroids from the Kalman Filter; the algorithm must assign the observed centroids to the correct container. This can be done using the Hungarian (Munkres) Algorithm (Munkres, 1957), which is a special type of linear programming that can achieve excellent computational savings (El-Anwar and Chen, 2012). In the case of the object detection algorithm, the Hungarian Algorithm will optimize the assignment of the observed centroids to the nearest predicted centroids. The algorithm works by finding the solution with the smallest associated cost: in this case, the sum of the distances ($\sum d_{i,j}$) between the predicted and observed centroid:

$$d_{i,j} = \sqrt{\left(P_{x,i} - O_{x,j}\right)^2 + \left(P_{y,i} - O_{y,j}\right)^2} \tag{4.14}$$

Where $P_{x,i}$ is the x-coordinate of the predicted centroid, $O_{x,j}$ is the x-coordinate of the observed centroid, $P_{y,i}$ is the y-coordinate of the predicted centroid, and $O_{y,j}$ is the y-coordinate of the observed centroid. Finding the distance between each predicted and observed centroid develops the cost matrix (C). The number of rows will correspond to the number of predicted centroids (i), and the number of columns will correspond to the number of observed centroids (j), e.g. if there are two observed centroids and three predicted centroids a 3x2 cost matrix will be derived.

$$C = \begin{bmatrix} d_{1,1} & d_{1,2} & d_{1,3} & \cdots & d_{1,j} \\ d_{2,1} & d_{2,2} & d_{2,3} & \cdots & d_{2,j} \\ \vdots & \vdots & \vdots & \ddots & \vdots \\ d_{i,1} & d_{i,2} & d_{i,3} & \ldots & d_{i,j} \end{bmatrix} \tag{4.15}$$

The Hungarian Algorithm, however, has two assumptions that are not fulfilled here (El-Anwar and Chen, 2012). First, the cost matrix should be balanced (equal number of columns and rows), and in many cases there are either more or fewer observed centroids than predicted centroids due to noise in the image. Second, each predicted centroid should have only one assigned observed centroid, and if the containers are occluded, the predicted centroid will not have an observed centroid assigned. Therefore, a modified Hungarian Algorithm developed by Bourgeois and Lassalle (1971) is used to solve the rectangular matrix. The algorithm applies a dummy row or column to the matrix that will make the matrix square, allowing the traditional Hungarian algorithm to proceed.

An issue unique to image-processing assignment occurs when a container is occluded and, simultaneously, noise causes the algorithm to recognize an observed centroid that is not truly a container. This would result in a centroid being incorrectly assigned when using the modified Hungarian Algorithm. Therefore, a threshold called the "cost of no assignment" is applied to the assignment algorithm. The threshold is applied once assignment has been made, for each assignment that is made, the algorithm examines the cost matrix for the distance between the assigned observed and predicted centroids. If the distance between the centroids exceeds a pre-designated "cost of no assignment", the observed centroid are considered as noise, and the predicted centroid will receive no assignment.

Using this algorithm, each frame from the experimental runs is converted into real-world coordinates and into the YC_bC_r color space using Geo-rectification and Color Space Conversion. Each frame is then analyzed to determine the positions of the centroids containers using Color Thresholding and Blob Analysis. The Kalman Filter, associated with each unique container, predicts the position of the centroid based on the previous positions of the container. The Hungarian Algorithm assigns the observed centroids to the predicted centroids, allowing the algorithm to identify the containers. The assigned observed centroids are used to update the Kalman Filter for predicting the container position in the next frame.

4.5 Results

The accuracy of the algorithm is evaluated using the results from the manual tracking method (see Section 3.3), and analyzed in this section. Table 4.1 outlines the experimental runs used in validating the object-tracking algorithm. Three experiments with one container were performed, one with three containers, one with six containers and one with nine containers. The results from the algorithm were then compared to the manual object tracking results to determine accuracy metrics. Equation 4.16 outlines the primary accuracy metric, mean squared error (MSE), which defines the mean error of the algorithm for each container over an experimental run:

$$MSE = \frac{1}{n} * \sum_{i=1}^{n} \sqrt{\left(A_{x,i} - M_{x,i}\right)^2 + \left(A_{y,i} - M_{y,i}\right)^2} \tag{4.16}$$

where *n* is the number of images used in the experimental run, "i" is the current image frame being evaluated, $A_{x,i}$ is the x-coordinate of the centroid from the algorithm, $M_{x,i}$ is the x-coordinate of the centroid from the manual tracking, $A_{y,i}$ is the y-coordinate of the centroid from the algorithm, and $M_{y,i}$ is the y-coordinate of the centroid from the manual tracking. To demonstrate various sources of error, the Average Error in both the x- and y- directions was also determined, shown in Equation 4.17. The Euclidean distance between the algorithm results and the manual tracking results is used to outline the error in each image, therefore the determining the error of the algorithm through time, is shown in Equation 4.18.

$$Average\ Error = \frac{1}{n} * \sum_{i=1}^{n} |A_i - M_i| \tag{4.17}$$

$$Error\ (t_i) = \sqrt{\left(A_{x,i} - M_{x,i}\right)^2 + \left(A_{y,i} - M_{y,i}\right)^2} \tag{4.18}$$

Where t_i is the time the image was captured, A_i is the x- or y-coordinate from the algorithm, and M_i is the x- or y-coordinate from the manual tracking method. As can be seen in Table 4.1, the MSE for the experiments with one, three and six containers had values of less than 6 cm. The error in these cases is dependent on the container surface that is captured by the Color Thresholding. Since the manual tracking, which is used to evaluate the error in the algorithm, uses the lid of the box to determine the centroid, any amount less than the entire lid of the container or more, such as capturing the side of a container, will result in a shift in the centroid from the true position determined by the manual tracking method. With nine containers, the algorithm performs poorly. Due to an increase in the number of container-container collisions, the algorithm begins passing unique identifiers between containers. This results in containers completing the test run with different identifiers than at the beginning of a run, therefore a larger error.

Table 4.1: Experimental protocol with number of containers, unique identifier of each container and the standard error calculated with Equation 4.15 and Equation 4.16.

Experiment (#)	Number of Containers	Container Number	Average Error in X-direction (m)	Average Error in Y-direction (m)	MSE (m)
1	1	2	0.0045	0.0230	0.0238
5	1	2	0.0042	0.0182	0.0327
7	1	2	0.0036	0.0119	0.0133
12	3	2	0.0044	0.0132	0.0227
		3	0.0021	0.0355	0.0443
		4	0.0059	0.0227	0.0324
43	6	2	0.0123	0.0127	0.0195
		3	0.0088	0.0586	0.0598
		4	0.0063	0.0148	0.0175
		5	0.0139	0.0269	0.0321
		6	0.0184	0.0191	0.0298
		7	0.0081	0.0149	0.0185
17	9	2	0.1263	0.6876	0.7009
		3	0.1654	0.0716	0.1906
		4	0.0894	0.0352	0.1063
		5	0.1467	0.1844	0.2428
		6	0.1670	0.0854	0.1954
		7	0.0953	0.2141	0.2391
		8	0.0477	0.0932	0.1137
		9	0.0262	0.0462	0.0581
		10	0.0468	0.0767	0.0954

Table 3.1 also shows the average error in both the x- and y-directions. As can be seen, the error in the y-direction is between 3-16 times higher than in the x-direction. Similar to the phenomena described in Imamura et al. (2008), the long-axis containers would orient parallel to the flow direction. The result was that the long axis of the containers was located in the y-direction. The direction of the long axis consistently determined the range of the greatest error: as the loss of the amount of the container detected was proportional to the geometric dimension of the container.

Experiments 1, 5 and 7 each had one container for the run, and the results are shown in Figure 4.10. The motion in the x- and y-directions is shown in Figure 4.10 (a). Due to the relatively random nature of the bore breaking at the apron, the interaction between containers is not exactly the same; however, the motion can be considered as being qualitatively similar. Similar to the results from Rueben et al. (2014), the motion in the flow direction is essentially one-dimensional. Experiment 7 shows a distinct change in direction around 1.5 m, likely due to irregularities in the apron. Figure 4.10 (c), (d), and (e) show the number of detections in each image. The algorithm consistently tracks one container for the majority of the experimental run. At the end of each run, due to lack of lighting in the downstream direction the containers begin to fall outside of the Color Thresholding range and detection of the containers is lost. When the detections have been lost, the Kalman Filter is relied upon to predict the centroid position in the next frame; this results in the increase in error that can be seen at the end of each run, illustrated in Figure 4.10 (b):

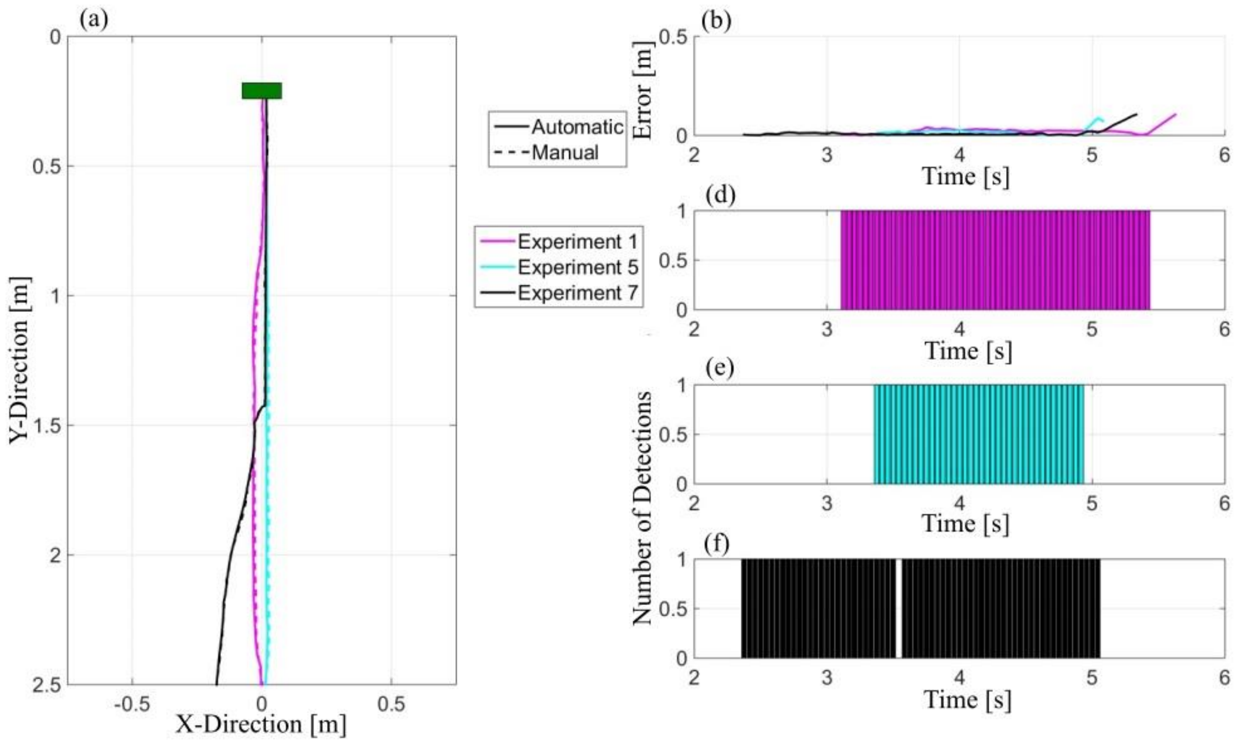

Figure 4.10: Experiments 1, 3 and 7 – one container. (a) motion of the containers in x and y; (b) error between the object-detection and tracking algorithm and the manual results; and (c), (d) and (e) number of containers detected in each image for Experiments 1, 3 and 7, respectively.

Experiment 12 also shows the increase in error (Figure 4.11 (b)) at the end of each test run due to the loss of detection. The error is more pronounced because detection of the containers is lost at different times. D2 reaches the area in the frame where detection will be lost first, resulting in the container spending longer in that area. The Kalman Filter for D2 relies upon increasingly older positions, as no new position data is passed to the filter, to predict the next position of the container and this results in significantly larger error. The same can be seen in Figure 4.12 as the number of detections is gradually reduced, corresponding with an increase in the error. Figure 4.11 (a) show the motion of the three containers, D3 exhibits qualitatively similar motion to the previous experiments. However, the containers on the outside of the configuration (D2 and D4) show significantly more motion in the x-direction, particularly after 1.5 m. The motion of the containers in the x-direction may be due to irregularities on the apron, as more abrupt changes in the container motion can be seen around 1.5 m in Figure 4.11 (a).

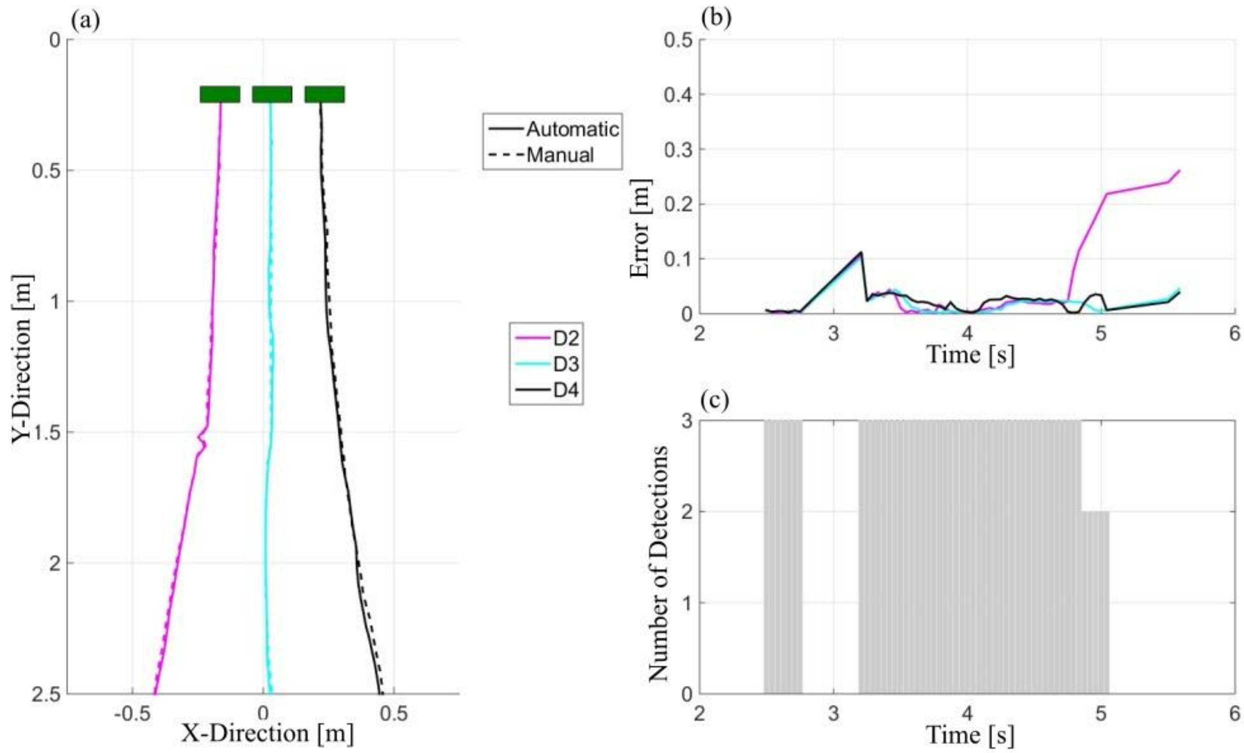

Figure 4.11: Experiment 12 – 3 containers. (a) Motion of the containers in x and y; (b) error between the object-detection and tracking algorithm and the manual results; and (c) number of containers detected in each image.

Figure 4.11 outlines the problems that can occur because of the variation in light caused by the outdoor basin. Around 3 seconds, no containers are detected. This corresponds to the point where the containers cross a clear difference in lighting conditions (as can be seen Figure 4.5 and Figure 4.6). The rapid change in lighting conditions results in the algorithm losing the containers, increasing the error seen in Figure 4.11 (b). As the algorithm loses detection of the container, the Kalman Filter continues to estimate the next position of the container based on the previous motion of the container and the kinematics equations. The estimation maintains the identifier of the container and provides an approximate position of the container. However, since the motion of the container does not exactly follow the kinematics equations, the motion error begins to grow with each subsequent frame during which the container cannot be detected. Once the algorithm detects the containers again, the error returns to a consistent value (around 0.02m) and the Kalman Filter is continually updated with the new position information.

In Experiment 43, containers were initially stacked, resulting in the top containers obscuring the bottom containers from the above-mounted video-camera. This resulted in only three containers being initially identified by the tracking algorithm (Figure 4.12 (c)). As the bore impacted the containers, there was significant wave overtopping that resulted in all containers being obscured from view and a sharp increase in the error (Figure 4.12(b)). Once the containers surfaced, the algorithm could then track all six of them. The increase in the number of containers resulted in the tendency for the debris to propagate in agglomerations of multiple debris. The agglomeration tended to make it difficult to determine the tracks of individual containers. In Figure 4.12 (a), containers D2 and D5 propagated as an agglomeration of debris. Based on the size of the detected pixels within the agglomeration, the algorithm correctly identified that there were two containers within the agglomeration. However, the algorithm could not correctly identify how the debris were positioned in the agglomeration which resulted in an increase in error as the centroids are estimated to be through the centerline of the agglomeration. As containers D2 and D5 separated (around y = 1.70 m), the centroids could be more accurately determined.

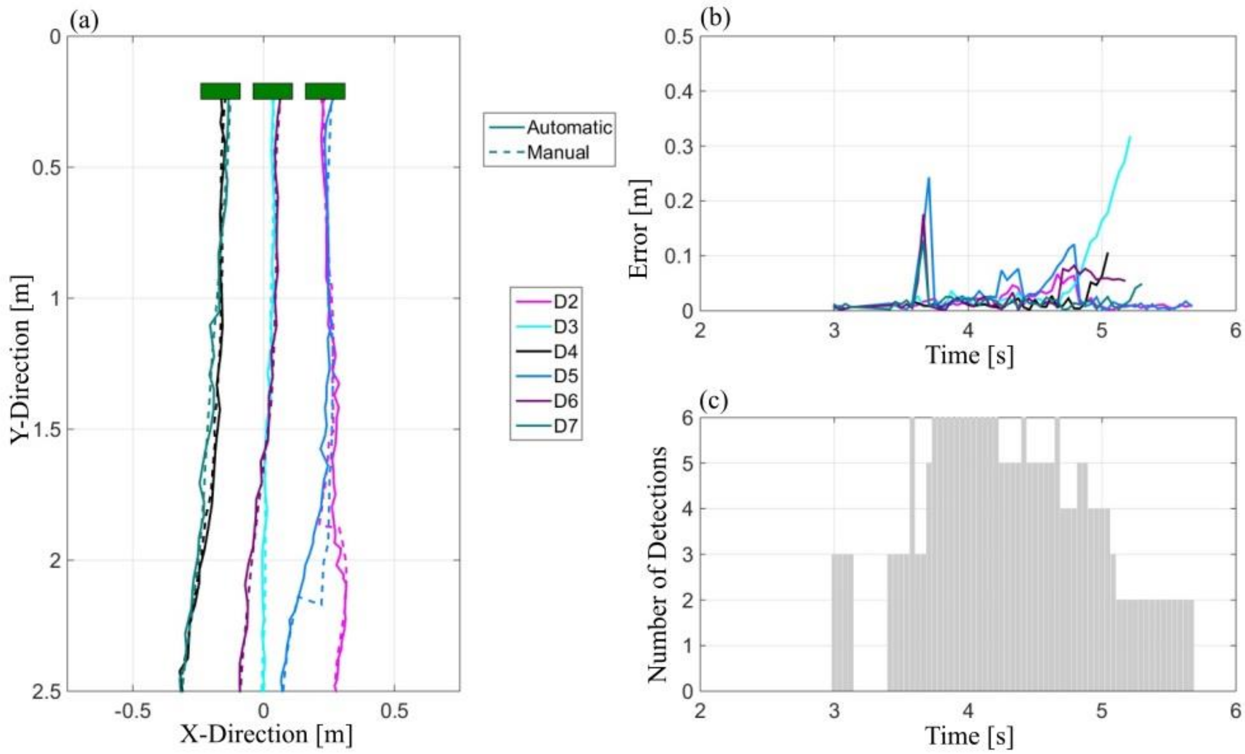

Figure 4.12: Experiment 43 – 6 containers. (a) Motion of the containers in x and y; (b) error between the object-detection and tracking algorithm and the manual results; and (c) number of containers detected in each image.

In Experiment 17, the object-detection and tracking algorithm was significantly less accurate when tracking nine containers, as shown in Figure 4.13. The increase in the number of containers resulted in multiple sources of error which affect the accuracy of the algorithm. Due to the increased number of containers, the initial impact of the bore with the containers again resulted in the wave overtopping the containers, briefly submerging the containers and obscuring them from view. However in the case of six containers, the debris motion was initiated before the wave completely obscured the containers. In the case of nine containers, the initiation of the motion of the containers occurred while the containers were obscured. The algorithm therefore did not detect the centroids to update the Kalman Filter with the motion of the containers. This will result in, throughout the time where the containers are occluded by the wave, the algorithm still considering the containers as stationary. Therefore, when the containers are once again visible, the Kalman Filter is still predicting the containers to be in their initial configuration before the wave impacted the containers and far from the correct observed centroids, which have propagated shoreward. This results in a difficult assignment process, often resulting in container being assigned incorrect identifiers.

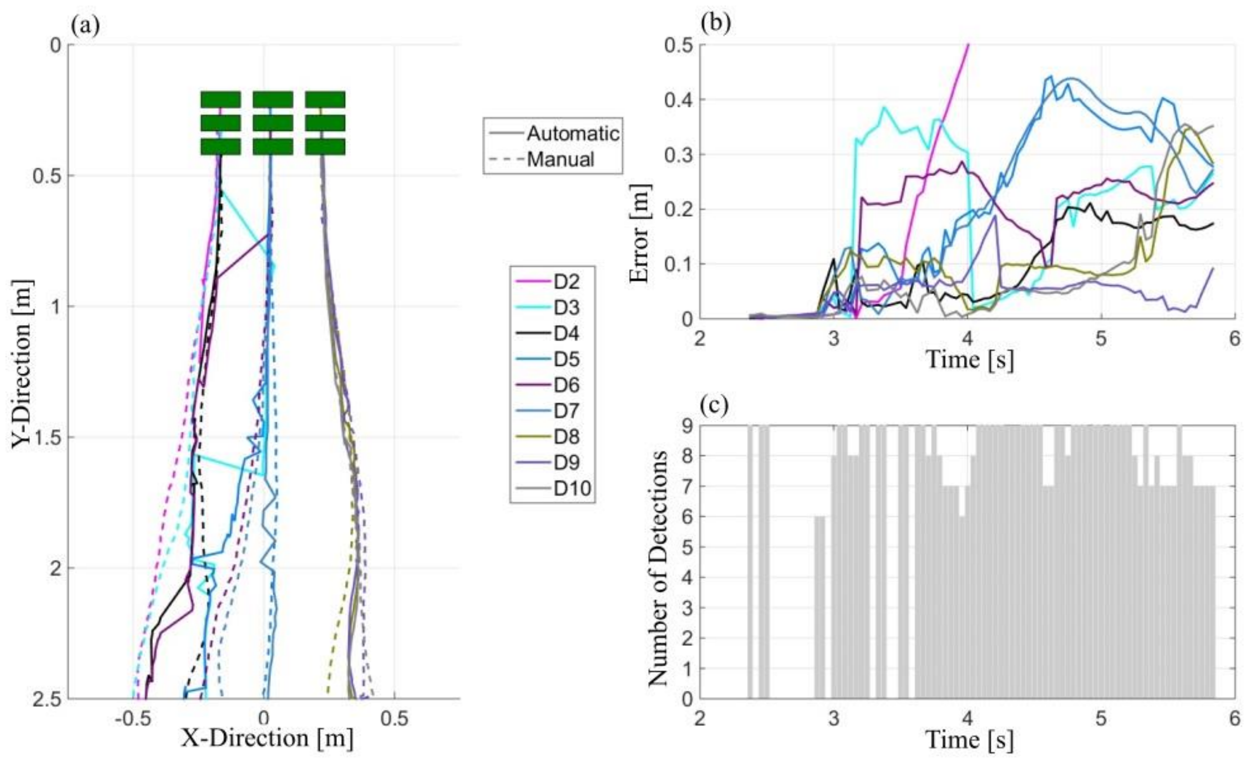

Figure 4.13: Experiment 17 - 9 containers. (a) Motion of the containers in the x- and y-directions; (b) error between the automatic and manual results; and (c) number of containers detected in each image.

Figure 4.13 (c) shows the number of detections throughout the experiment runs are inconsistent. Ideally, as was the case shown in Figure 4.10, the number of detections are equal to the number of containers. This allows for a simple assignment process of one observed centroid assigned to one predicted centroid. Due to the increased number of containers and multiple rows of containers in Experiment 17, on contact containers would not immediately dissociate, causing the algorithm to group multiple containers into one blob. The algorithm would attempt to determine the number of containers in each blob if a large area was detected, but due to the inconsistent tracking of the amount of the container, significant gray areas exist. This results in the number of containers being over- or underestimated, and hence the number of detections being over- or underestimated.

4.6 Discussion

The accuracy of any camera-based object-detection and tracking algorithm will always be highly dependent on the quality of the images being processed by the algorithm. The algorithm relies on the Color Thresholding to initially identify the containers, so determining a strict thresholding limit that will find the containers and eliminate the noise is important. Due to the TWB used for the experiments discussed here being located outdoors, the inconsistent lighting made determining a strict threshold limit difficult. The light not only between experimental runs was inconsistent, but also during the run, as some portion of the harbor area would be shaded or exposed to sunlight. To properly address the lighting issue, a larger threshold was used to track the containers throughout the run and as was discussed in 4.4.3, the color space was adjusted to take into consideration the changing light conditions. The adjustment in color space allowed for the containers to be tracked consistently through each run, but had some drawbacks. The increase in the range of the thresholding leads to an increase in the amount of the container surface that is detected by the algorithm. Therefore, the sides of the container would occasionally be tracked, since the shaded and lighted color of green must be considered. Since the manual method of tracking the containers considers the centroid of the container as the center of the top of the box any shift in the centroid from the center results in an increase in error. A more controlled lighting environment, inside or in a consistently shaded area, would suffice and would provide significantly improved accuracy.

The primary concern with tracking a large number of container is maintaining the unique identifiers during collisions between containers. The Kalman Filter was designed considering a constant velocity, and therefore, when a collision occurs, the predicted centroid is predicted based on data from previous time steps and will continue to move along its previous path. Depending on the collision angles, this can occasionally result in the identifiers switching between containers upon impact, significantly skewing the results. Another aspect of the container collision error is when the containers agglomerate upon impact. Since the containers are touching, the algorithm will consider the resulting blob in the binary image as one detection. Using the properties of the region, thorough analysis of the experiments, thresholds were developed that could approximately determine how many containers were within each blob. However, again due to the inconsistent lighting, there was significant overlap in the thresholds for the different number of containers. Figure 4.9 shows an example of where frame (a) correctly identifies that three containers are present within the blob, frames (b) and (c) can only identify two containers within the image and the third centroid begins to rely upon the predicted centroid, and then in frame (d) the algorithm is once again able to detect the correct number of containers.

There are currently image processing techniques that could help improve the image processing algorithm presented in this paper. Adaptive Kalman filtering could allow for the algorithm to be more robust in estimating the debris motion in the event of collisions. Also, incorporating a check step to identify a significant increase in area of a blob or rapid changes of debris direction would allow for increased accuracy when collisions occur (Weng et al., 2006). Moreover, with a better understanding of the motion of debris, the equations of motions that dictate the predictions of the Kalman Filter could be updated to improve the estimation of the Kalman Filter and therefore the assignment process of the algorithm. Alternatively, Omidvar et al. (2014) applied a modified Hough transformation to identify individual soil particles within a soil matrix. The Hough transformation examines the gradient field of an image to identify the centroid of a particle. A modification of this technique could potentially allow for the centroids of the individual containers to be identified when the agglomeration of the containers occurs. The identification of the centroid throughout the agglomeration would significantly improve the tracking of the debris as the debris are agglomerated.

In addition to having more consistent and intense lighting conditions, improvements to the experimental setup could further enhance the capabilities of the proposed algorithm. Using images from both the HD cameras used in this experiment and applying the algorithm to images taken simultaneously from two or more such cameras would allow for the algorithm to also track the motion of the containers in the vertical direction, using a similar algorithm for correlating the information in each image as proposed by Vousdoukas et al. (2009). The blur induced by the shutter speed of the HD cameras occasionally resulted in the algorithm falsely detecting the containers as being larger. This made determining the size of the containers and therefore the number of containers detected in the image difficult. Using a high-speed HD camera would greatly reduce the blur in the images and provide a more accurate evaluation of the container size.

The application of the algorithm discussed in this paper can be widened to the broader field of coastal and hydraulic engineering. Within coastal engineering, the scalability of the algorithm would allow it to be used in the tracking of debris in the field during large-scale hydraulic events, such as tsunamis, storm surges, or dam-breaks. The algorithm could be further extended to river engineer applications such as tracking the motion of large woody debris (LWD) in river systems (Ali and Tougne, 2009, Schmocker and Hager, 2013). Additionally, the algorithm could provide tracking of painted pebble for the understanding of the short-term and long-term sediment movement rates in both field and laboratory conditions (Persico et al., 2005). The algorithm could also be extended for use in monitoring of ice flows to determine the safety and loading conditions exerted on hydraulic and off-shore structures (Smirnov and Bychkova, 2015).

4.7 Summary and Conclusions

This paper presents an analysis of a camera-based object-tracking method to track the movement of shipping containers in high-velocity flows. Test runs were performed with one, three and nine scaled-down shipping containers on an elevated apron fronted by a propagation section. The simulated shipping containers were tracked using a combined object-detection and tracking algorithm that analyzed the images captured by overhead cameras. The algorithm integrated Color Thresholding, Blob Analysis, Kalman Filter and Hungarian Algorithm to accurately capture the motion of the containers throughout the experimental runs.

Based on this work, the following conclusions can be drawn:

- The algorithm can accurately and consistently provide centroid position throughout the experimental run.
- The algorithm can accurately and consistently track up to six uniformly built shipping containers, though increased numbers of containers could likely be tracked as long as there were minimal collisions and agglomeration of the containers.
- The algorithm is less accurate due to the inconsistent lighting conditions; improvements in experimental setup, in particular consistent lighting, will further increase the algorithm's accuracy.
- The algorithm is scalable; no factors within the algorithm are size-dependent.

Finally, while the algorithm is only applied here for container motion problems, the possibility of application in other aspects of coastal engineering is significant. The ability of the algorithm to track uniform objects and maintain unique identifiers has potential for use in many real-world and experimental scenarios. Tracking armor stone displacement by wave action, tracking scour through time around structures, debris motion from real-world footage, along with many other coastal problems can benefit from using this algorithm and evaluate the motion of objects of interest with unprecedented detail.

4.8 Link to Chapter 5

Using the two debris tracking methods presented in Chapters 4 and 5, the methods were used in the tracking of debris in a new Tsunami Wave Basin at Waseda University (Tokyo, Japan). Multiple debris configurations were evaluated to determine the effect of the number of debris on the maximum displacement and spreading angle of the debris. The results of these experiments are presented in Chapter 6.

Chapter 5. Experimental Investigations of Debris Dynamics over a Horizontal Plane (JWPOCE-ASCE, 2016)

5.1 Introduction

Tsunamis and large scale coastal disasters, such as 2004 Indian Ocean Tsunami, 2010 Chilean Tsunami, the 2011 Tohoku Tsunami, and the Typhoon Haiyan in 2013 outlined the catastrophic effects of these high volume, high velocity inland flooding. The damage from these events amounted to billions of dollars and led to massive human loss of life. The extent of the damage occurring in the aftermath of the 2011 Tohoku Japan tsunami was particularly troublesome as many engineered reinforced concrete structures were destroyed (Mori et al., 2011). The majority of the damage from these large scale events are a result of the inundation and associated hydraulic forces (Charvet et al., 2014, Naito et al., 2014) and evaluation of these damages resulted in research focusing on the hydrodynamic loading on structures (Ramsden, 1996, Arnason et al., 2009, Nouri et al., 2010, St-Germain et al., 2012, 2013, Bremm et al., 2015). However, a number of literature and field surveys also noted that the impact force of water-borne debris can cause significant damage to most structures and particularly to critical infrastructure (Mizutani et al., 2005, Madurapperuma and Wijeyewickrema, 2012, 2013, Paczkowski et al., 2012, Como and Mahmoud, 2013, Linton et al., 2013, Palermo et al., 2013, Ko et al., 2015, Shibayama et al., 2015). Water-borne debris can also accumulate onto structures and columns increasing thus the drag force exerted and transmited on the structural components (Robertson et al., 2007) or lead to increased scour at the base of these structures (Yeh et al., 2014). Figure 5.1 depicts an example location impacted by a particularly steep and bore-like tsunami wave front captured by eye-witnesses at Kuji harbour in the Iwate province during the 2011 Tohuku Japan Tsunami. The snapshots of the impact process are each 2 s apart showing a pronounced, steep wave front which is characterized by breaking-induced turbulence and an elongated tail of water surging over the horizontal harbour surface with maximum inundation depth reported to be in the range of 8 to 9 m (PARI, 2011).

Figure 5.1: 2011 Tohoku tsunami waves impacting the harbour of Kuji, Iwate Prefecture, Japan, (https://www.youtube.com/watch?v=sh54ahaMle4, 0:38 min, 0:40 min, 0:42 min). Panels a) – c) show snapshots of the bore front impacting the revetment with 2 s interval.

Research into impact forces caused by water-borne debris has primarily focused on the magnitude of the impact force itself (Haehnel and Daly, 2004, Nouri et al., 2010, Riggs et al., 2014, Aghl et al., 2015); with significantly less focus on the probability and potential for debris impact. The result has been a lack of explicit provisions regarding the probability and potential of debris impacts in tsunami and flooding hazards guidelines and provisions worldwide. Existing guidelines often will apply a conservative approach that requires all buildings to be designed for full debris impact (*FEMA P-55 2011, FEMA P646 2012)*, something which can result in more expensive structures.

One of the reasons for emphasis placed mostly on the magnitude of the debris impact force rather than on the probability/potential of impact has been the difficulty in determining appropriate techniques to quantify debris movement. Following the 2011 Tohoku Tsunami, Naito et al. (2014) examined debris impact sites and determined the debris' original location from satellite images. From these investigation, Naito et al. (2014) determined the potential debris spread area to be within ±22.5°, enclosing an area equal to 50 times the plan area of the debris. The accuracy of the site assessment during forensic tsunami investigations was hard to evaluate as determining the debris' original location was difficult in the aftermath of the tsunami, resulting in a rather conservative approach for the Naito et al. (2014) method. However, for practical purposes, this is acceptable and useful. At the same time, identifying the type of debris that impacts a structure was equally difficult as pieces of debris could be any object that is entrained and carried within the flow, such as shipping containers, wooden poles and vehicles.

In a laboratory setting, Imamura et al. (2008) examined the motion of scaled down boulders dislocated by a dam break wave. The motion of the boulders was qualitatively examined and their final displacement was quantified. The displacement of most boulders was dependent on their initial orientation as a boulder placed with the longer axis perpendicular to the flow direction traveled significantly further than those placed with their longer axis parallel to the flow. Imamura et al. (2008) also noted that while the motion of the boulders was random, the characteristics of their entrainment were similar: boulders initially moved by saltation until the flow velocity sufficiently slowed for the boulders to begin sliding. Yao et al. (2014) examined the motion of scaled down coastal houses and used an optical tracking method to determine their final and maximum displacement. The displacement of the coastal houses were largely dependent on the hydrodynamic conditions. The inflow had to surpass a critical depth to immediately entrain the houses: otherwise, houses acted as a barrier to the flow, resulting subsequently in shorter displacement of the houses and also a reduction in the extent of the inundation limits.

While the methods mentioned above yield information regarding the motion of the containers once the flood event has occurred, an in-depth understanding of the debris motion is needed to help identify high-risk areas of debris impact, debris accumulation as well as debris damming in the event of these catastrophic events. The identification of debris motion and their final resting place could also help in the recovery process of more valuable debris such as shipping containers, vehicles, and shipping vessels. Concentration and distribution of debris across a flood plain affected by tsunami inundation can potentially offer important information to early disaster recovery response while guiding focused efforts towards those regions with highest need. High-quality data on debris motion will also help calibrate and validate new numerical models describing the debris motion. Hence, a non-invasive, accurate data acquisition system is needed to obtain in a single, synchronized manner all of the necessary information. Shafiei et al. (2014) used accelerometers to track the displacement of displacement of debris as they were carried by a highly turbulent bore. Subsequently, the entrained debris impacted a vertical free-standing structure. The focus of their study was on debris impact forces and evaluating the impulse-momentum approach to calculating the forces. Rueben et al. (2014) used an object-tracking and detection algorithm to optically track the motion of boxes entrained within a rapidly-moving bore. The algorithm could consistently track the motion and orientation of up to nine boxes entrained within the incoming bore. While their algorithm performed well for the experiments in question, the algorithm could not track boxes which were in any way occluded or submerged by the incoming bore or any potential obstacles.

This study presents new experimental data covering debris spreading and its maximum longitudinal displacement by applying a novel non-invasive technique of tracking debris motion with 6 degrees-of-freedom (DOF), the system components and accuracy are more thoroughly presented in Goseberg et al. (2016). The motion of the debris in a turbulent bore, initiated by the impact of a solitary wave at the edge of a vertical quay wall mimicking a port environment, is analyzed to determine the capability of this novel system; the potential variables affecting the motion of the debris are investigated then in particular.

5.2 Objective and Scope

The purpose of this experimental study was to scrutinize how a highly turbulent bore entrains and displaces multiple debris units, representing scaled-down shipping containers, over a horizontal plane. A volume of water released from an elevated reservoir using the direct control of the reservoir pressure chamber air valves was used to form a wave-induced turbulent bore propagating over a horizontal plane mimicking a quay with adjacent harbor area. A number of different arrangements of debris units were tested to investigate how those arrangements are impacted by the energy of the incoming hydraulic bore. Positions and orientations of single debris units were tracked in time and space with an innovative, yet non-intrusive wireless sensor system, which performed satisfactory even in cases when direct sight was obstructed. Resulting information regarding the whereabouts of the debris was used to compare with published angle of spread of debris dispersal published by Naito et al. (2014).

In this paper, the experimental setup to determine debris dynamics over the horizontal plane and the wave basin test facility are described in detail. Then, the instrumentation including the applied 6DOF, multi-debris positioning and orientation system is detailed. The experimental procedure, data acquisition and pre-processing, the choice of the initial debris arrangements/combinations, as well as the sequential steps for the experimental runs are documented. Time-histories of the water surface elevation throughout the wave basin and over the horizontal plane together with the spatio-temporal whereabouts of the multiple debris units as well as the lateral and longitudinal debris drift are reported. The debris concentration factor is introduced by defining a spreading angle margined by the outermost occurrence of debris during their drift trajectory. This spreading angle is calculated as:

$$\theta(t) = arctan\frac{\left(x(t) - x(t_0)\right)}{\left(y(t) - y(t_0)\right)} \tag{5.1}$$

where θ(t) is the actual spreading angle of a single debris unit, x(t), y(t) are positions in the (x,y)-space with respect to the global coordinate system while the net displacements are obtained by subtracting the current debris position from their initial position, ($x(t_0)$, $y(t_0)$) (Fig. 2).

5.3 Experimental Setup

5.3.1 Waseda University Tsunami Wave Basin and Model Geometry

The experiments were conducted in the Coastal Engineering and Management Laboratory at the Department of Civil and Environmental Engineering of Waseda University in Tokyo, Japan. For these tests, a newly-constructed tsunami wave basin (TWB) with horizontal dimensions of 4-by-9 m was utilized (Figure 5.2). On the North side of the basin, the TWB was equipped with a four-chamber pressurized overhead reservoir controllable by a vacuum pump (TST-150, Sato Vac Inc., Japan) equipped with progressive release valves. The maximum, achievable hydraulic head of the reservoir with reference to still water level in the wave basin was of 0.77 m. The water impoundment was released through computer-controlled air valves (SVB1V-50F-02HS, CKD Corporation, Japan) with a maximum opening diameter of 0.054 m positioned at the top of the reservoir chambers.

An elevated, rigid horizontal apron area was constructed 3.95 m from the wave maker. This experimental setting was chosen to simulate tsunami wave impact inside a modern port environment with a container apron, typical for many coastal regions around the world. The horizontal portion of the basin, located in front of the vertical quay which separated the harbor area from the sea-part of the model domain, was the propagating area for the waves generated by the released water from the vacuum reservoir. A right-handed coordinate system shown in Figure 3.1, with the origin at the transversal midpoint on the edge of the quay wall was the reference system used throughout the tests. The y-axis pointed towards the South, the direction of the wave propagation being positive away from the apron inland. The vertical axis was taken positive opposite to the gravity vector with z = 0 at the elevation of the apron area.

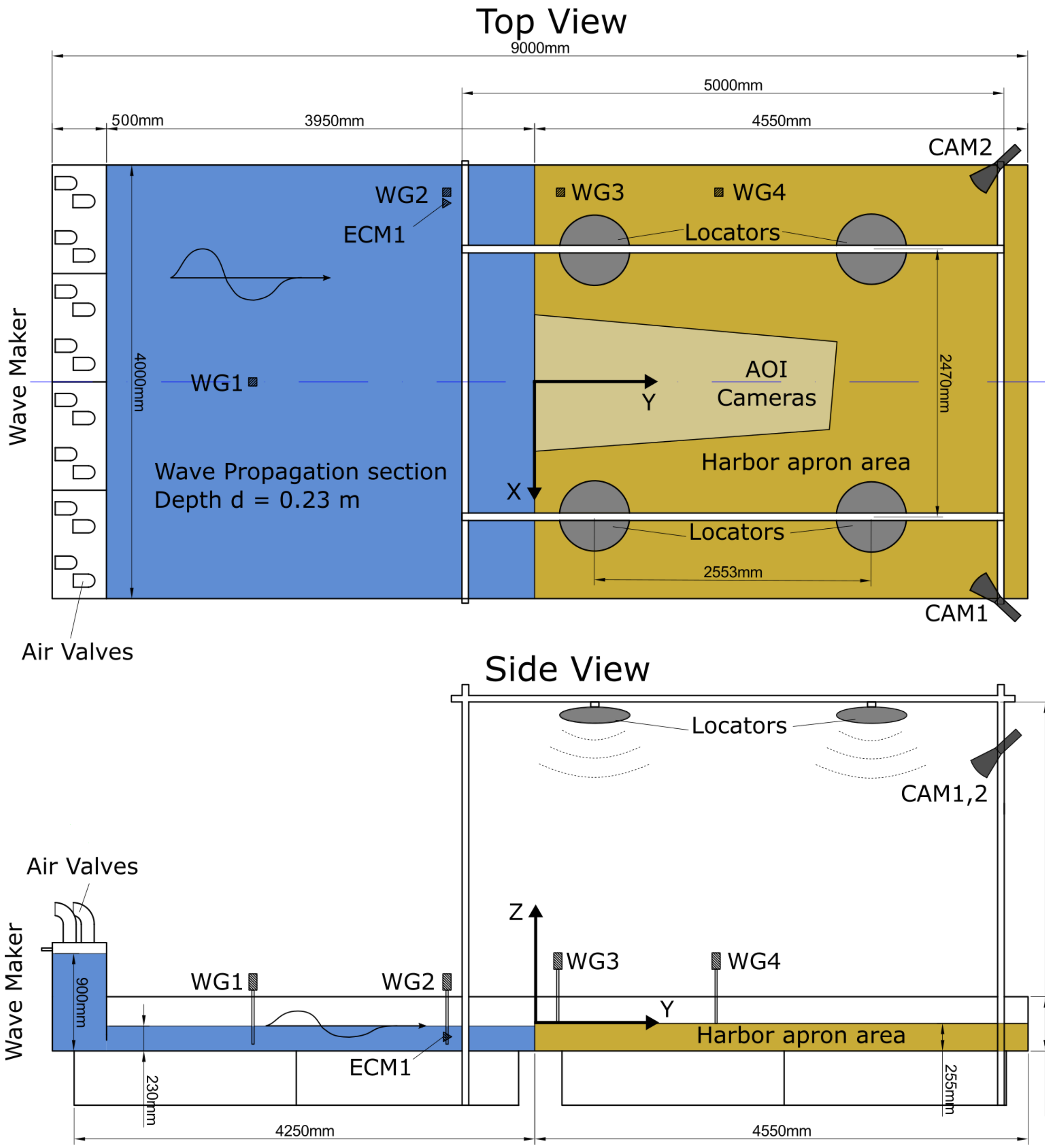

Figure 5.2: TWB setup in plan and side view with bathymetry and location of the instrumentation, instrument frame, and key dimensions (units in mm). WG – wave gauge, ECM – electro-magnetic current meter, CAM – high definition camera; locators are part of the real-time positioning system. Area of interest (AOI) of the cameras is indicated in gray color.

5.3.2 Instrumentation

Figure 5.2 depicts the positions of the instrumentation used for these tests with respect to the geometry of the wave basin. Four wire resistance wave gauges (manufacturer: KENEK Co., Ltd., Japan) were mounted at various positions in the wave basin, sampling at 100 Hz and connected to a data acquisition unit (manufacturer: VM-806H, KENEK Co. Ltd, Japan). Two of them were positioned within the harbor basin area while the remaining two were used to record the water level on the initially dry harbor apron (Figure 5.2). An electro-magnetic current meter (ECM, manufacturer: KENEK Co. Ltd, Japan) was operated with its sensor head submerged 0.075 m below the still water level in order to avoid contact with the air during passage of the wave trough. Prior to the installation, the wave gauges were thoroughly calibrated against a laboratory caliper. The calibration yielded a correlation coefficient larger than 0.99 for the entire calibration process.

Two high-definition (HD) cameras (Basler AG, pi1900-32gc, Germany) were additionally mounted at the Southern end of the wave basin instrument frame at a height of 2.95 m above the apron area and pointing towards the apron edge separating the harbor area from the sea-side. The mutual footprint of the two cameras projected onto the harbor apron (z = 0.00 m) are detailed in Figure 5.2 through the area of interest (AOI) which was defined based on the field of view of the fixed-zoom lenses mounted to the cameras. The cameras were synchronized by software means and operated at a sampling rate of 25 Hz. The cameras were used to verify the position of the debris and that of the bore front position.

For the determination of individual debris positions, a real-time locating system (RTLS, manufacturer: Quuppa Oy, Finland) capable of tracking up to 25 debris specimen at a sampling rate of up to 50 Hz was installed. This RTLS system, whose locator antennae positions are depicted in Figure 5.2, uses radio trilateration based on a modified Bluetooth Low Energy (BLE) protocol to track the debris specimen with greater accuracy and better angular estimation than conventional Bluetooth techniques (Goseberg et al., 2016). All instrument locations are listed in Table 5.1.

Table 5.1: Instrument location during the moving containers tests.

Instrument name	**Instrument ID tag**	**X [m]**	**Y [m]**	**Z [m]**	**Notes**
WG1	CHT6-30-1	0.00	-2.60	--	
WG2	CHT6-30-2	-1.75	-0.81	--	
WG3	CHT6-30-3	-1.75	0.24	--	
WG4	CHT6-30-4	-1.75	1.70	--	
ECM1(X)	VMT2-200-04P	-1.65	-0.81	-0.10	Collocated with WG2
ECM2(Y)	VMT2-200-04P	-1.65	-0.81	-0.10	Collocated with WG2
CAM1	pi1900-32gc	2.00	4.20	2.95	Pointed to AOI
CAM2	pi1900-32gc	-2.00	4.20	2.95	Pointed to AOI
LOC1	9			3.15	Downward looking
LOC2	10			3.15	Downward looking

LOC3	11			3.15	Downward looking
LOC4	12			3.15	Downward looking

5.3.3 Instrumented Debris Specimen

To investigate the motion of debris propelled by an advancing tsunami-like bore, 20 feet shipping containers (designed based on the ISO668/688 standard) were down-scaled based on a 1:40 length scale. The downscaled container models were manufactured based on an optimized design and batch-produced in order to assure identical dimensions and weights.

The down-scaled shipping container shown in Figure 5.3 was manufactured using positively buoyant polyethylene (PE-HMW, 0.92 g/cm³) to match the average weight of a full shipping container at prototype scale, W = 14,400 kg (Knörr and Kutzner, 2008).

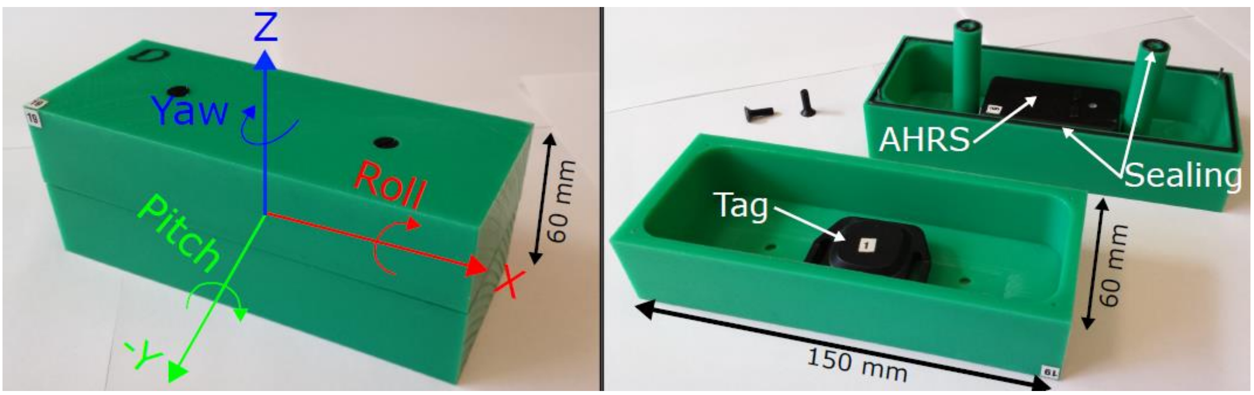

Figure 5.3: Down-scaled 20 feet shipping container model used as debris.

The scaled shipping container had dimensions of 0.06 x 0.06 x 0.15 m with an approximate draft of 0.025 m. Shipping containers were modelled in an idealized manner in this study. A first approximation assumed that the container weight will contribute in the most significant manner to the entrainment and transport processes. It is acknowledged though that factors such as contact surface roughness, mass distribution, or container material stiffness, features certainly affect the overall process although the sensitivity of these factors is currently difficult to estimate and model. In this study the average container weight, homogeneously distributed, was adopted to obtain average debris dynamics. Future studies will reveal how sensitive these dynamics are to the previously mentioned additional factors. The model was designed and manufactured to be waterproof, but, at the same time, to be easily dismantled as the sensors contained inside had to be read out from each experiment. The "smart" debris system consisted of motions sensors (3-Space Logging, Yost Eng., USA) used to record three-dimensional orientations and one locator tag placed inside and underneath the upper face of the specimen was used in each container model. The motion sensor and the locator tag were tightly attached to the inside walls of the container model using Velcro tape. The coordinate system used and the sign convention for the rotation angles were defined as shown in Figure 5.3. The upper container half and the motion sensor inside were labelled individually at one corner to keep track of the initial orientation of the specimen during placement on the apron. The total weight of a single container model was determined by three repeated weighing which yielded an average total weight of 0.226 kg which included one motion sensor (0.048 kg) and one location tag (0.010 kg). The coefficient of static friction between the container model and the plywood of which the apron was built was estimated to be approximately 0.4, similar to the coefficient of static friction between plastic and wood (Malhotra and Subramanian, 1994).

5.3.4 Container Models Arrangements

To investigate the dynamics of container models moving across a harbor area, different types of initial container arrangements (debris sets) were selected and tested (Table 2). Although the number of potential debris sets are numerous, a first selection was made based on practical and realistic considerations. The container's center of volume in the first row of containers was always placed at y=0.23 m, or 8.00 m in prototype from the container side walls with respect to the apron's edge. This location was chosen based on the space required by the gantry cranes, and/or the trains and trucks which usually operate between the edge of the quay wall and the container storage area. Similarly, the inter-debris spacing was estimated on the operational consideration that a common reach stacker requires approximately 1.20 m of space - at prototype scale - to operate between container stacks. Current standardized container storage operations allows stacking heights of 5 or more layers. Notwithstanding the fact that many more containers can be arranged in large numbers and on wider surfaces in the case of a real harbor, the total number of container models and the selected number of layers had to be restricted due to the experimental facility constraints. Therefore a maximum of 18 containers and 2 layers were selected. Containers were placed on top of each other without any additional connection between them. Multiple repetitions were performed for each debris arrangement to provide more data for the analysis conducted and to help in the identification of outliers. As containers' side surfaces were smooth, adhesive forces between the containers at each stacking level are conceivable, at least in the presence of water. Experimental conditions were therefore kept identical by drying off all container surfaces before setting containers in place for each experimental run. Adhesive forces between the containers were therefore kept constant not to affect their dynamics during the motion initiation.

Table 5.2. Debris arrangements used in the experiments.

Debris Arrangement	Total amount of container models used	Inter-container distance [m]	No. of apron-parallel rows	No. of container layers	Initial yaw angle [°]	Number of Repetitions
debrisSet1	1	--	1	1	0	5
debrisSet2	1	--	1	1	90	3
debrisSet3	3	0.03	1	1	0	3
debrisSet4	3	0.03	1	1	90	3
debrisSet6	9	0.03	3	1	0	3
debrisSet7	9	0.03	3	1	90	3
debrisSet9	18	0.03	3	2	0	2

debrisSet10	18	0.03	3	2	90	2

5.4 Experimental procedure

5.4.1 Data Acquisition Systems and Processing

Sensors data were recorded using a combination of different data acquisition systems. Wave gauges and current meter data were recorded at a sampling rate of 100 Hz using a DAQ unit running on a personal computer (Fenek Co. Ltd., Japan). Additionally, a software-based frame grabber was used to record camera images with a frequency of 24 Hz and was synchronized using the computer clock. Then, a Linux-based system ran the positioning engine which was used to determine (x,y,z)-positions in space with a sampling rate which was dependent on the number of container models (debris) applied per experiment. The positioning engine (manufacturer: Quuppa Oy, Finland) allowed for tracking positional information of the debris in 3D based on radio technology. Sampling rates of 25 Hz were successfully achieved during tests which employed up to 18 debris units. In addition to the positioning engine, a Network Time Protocol server (NTP) was operated on the Linux-PC. The NTP server broadcasted the synchronous computer clock time into the network connected to the DAQ computer. According to the NTP-server output, synchronization accuracy in the order of 30 ms was achieved during the tests. Finally, a third PC, used to set and read-out the motion sensors on a regular basis was also connected to the NTP-synchronization network. All the data time-histories were related to a set reference time which was defined as the instant of occurrence of the peak water surface elevation recorded at WG1.

5.4.2 Experimental Methodology

The water depth in the TWB was set to 0.235 m during all tests, leaving thus a freeboard of 0.015 m between the harbor still water level and the level of the apron area. As the wave generated by the wave maker approached the edge of the quay wall, it underwent shoaling over the horizontal harbor basin. As the wave approached the vertical quay wall, it broke over its edge increased and steepened because of the partial reflecting occurring at the vertical wall which induced a partial standing wave. The broken wave generated a hydraulic bore which propagated over the horizontal bottom and entrained the container models within the highly turbulent flow. Before each test, the wave maker vacuum reservoirs were filled with an identical volume of water resulting in a hydraulic head of 0.67 m above the harbor still water level. The filling level of the vacuum chambers was controlled to ensure the same hydraulic conditions. Prior to this water volume release, the container models (debris) fitted with the sensors units were closed, sealed, and then placed according to predetermined arrangement patterns shown in Table 5.2. In order to activate the built-in motion sensors fitted inside the debris units, an initial acceleration in the form of a sudden energetic shake of the debris was induced and, immediately after, the container models (debris) were finally placed back onto the apron area. Markers on the apron surface and spacers were used to accurately place the units before each test. Following this procedure, an overall placement accuracy of ±5 mm was achieved. Subsequently, all sensor systems were initiated and the air valves of the wave maker were opened synchronously via remote-control to initiate the wave generation and its subsequent propagation.

5.4.3 Manual Image Processing

The spatio-temporal position of individual debris units was recorded by means of the “smart” debris system described in the Experimental Setup. For validation purposes, a comparison between the manually-analyzed video-camera images and the “smart” debris system was conducted to assess the general suitability of this innovative system, which has not yet been widely applied in hydraulic and coastal engineering. The two-dimensional (2D) trajectories obtained with the “smart” debris were subsequently compared to the positional information gathered from the camera footage. Video-camera images were read in automatically using a Matlab code developed for this purpose in order to manually select the image coordinates in pixel space where the upper four corners of the individual debris unit resided. For an example of the corner selection the reader is referred to panels shown in Figure 5.5 where one single debris unit is tracked through sample image frames. Subsequently, the stored image coordinates were transformed from the pixel space into the real-world, SI-unit space based on the control points at each corner of the AOI depicted in Figure 3.1. Centroid coordinates of the manually-selected quadrangle were then computed from the corner coordinates. Also, the relative angle of rotation around the vertical axis of the relative debris unit coordinate system was determined. Due to some image blur generated by the maximum available shutter speed of the cameras an estimated accuracy of ±10 pixel was attained during the manual selection of the upper debris corners. Pixel to real-world coordinate ratios varied depending on the non-orthographic angular field provided by the video-cameras. Values ranging from 6.41 – 10.74 pixel/cm in the (x)-direction and 5.59 – 5.92 pixel/cm were obtained. Thus, the SI unit- based accuracy of the manual image processing was determined to be in the range of 0.01 to 0.02 m in (x)-direction and 0.02 m in the (y)-direction. In comparison, Goseberg et al. (2016) achieved an accuracy ranging from 0.03 to 0.05 m (1.2 to 2.0 m at prototype scale) in horizontal plan for the “smart” debris: this level of accuracy was identical to the one attained in this study for this particular issue. Accuracies of the camera-based system were therefore slightly better than for the current processing.

5.5 Results

5.5.1 Hydrodynamic Data

Fig. 4 shows the time-histories of the measured water surface elevation and the horizontal particle velocity from baseline debrisSet1 with full, instantaneous air valve opening, where t = 0.0 s refers to the instant in time when the wave maker was started.

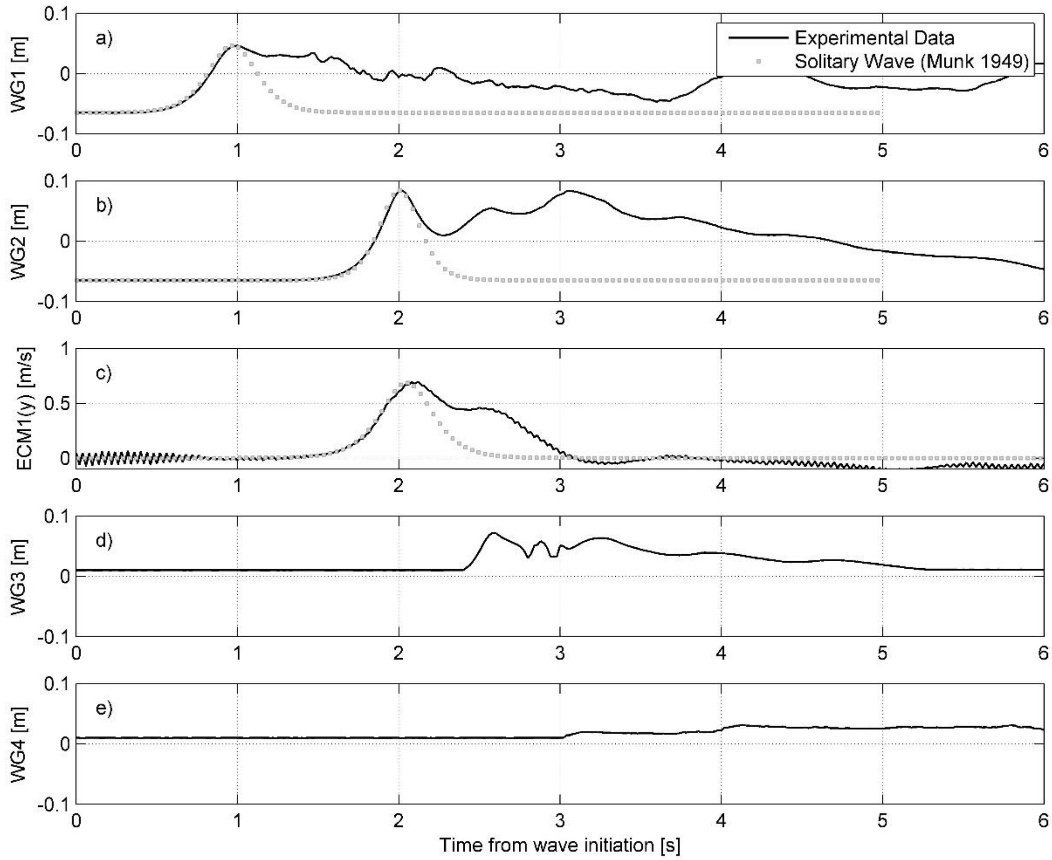

Figure 5.4: Time-history of water surface elevation and the horizontal particle velocity from baseline debrisSet1 with full, instantaneous air valve opening. (a) and (b) Resistance wave gauges located near the wave maker and in front of the quay wall edge, respectively, in comparison with analytical solitary wave solution (Munk, 1949). (c) Time-history of the velocity measured by electro-magnetic current meter in y-direction (wave propagation) and comparison with velocity from the analytical solitary wave solution (Munk, 1949). (d) and (e) Resistance wave gauges located on the apron (see Figure 5.2).

Figure 5.4(a) shows the time-history of the water surface elevation recorded by the first wave gauge located in 1.35 m distance from the wave generator and compares the resulting wave with the analytical solitary wave solution published by Munk (1949). Free surface elevation time histories recorded by WG1 and WG2, shown in Figure 5.4(b), are related to the z-axis origin of the reference coordinate system as shown in Figure 3.1. Hydrodynamic conditions were scaled using Froude similitude. The presence of the vertical quay wall and the non-linear dynamics of the elongated solitary wave train induced a substantial wave height increase of the leading wave front (approximately 34%), accompanied by a sudden increase in steepness (due to a partial standing wave as an effect of the partial reflection of the elongated solitary wave) and subsequent breaking. Favorable agreement with the analytical solitary wave solution of Munk was obtained for the wave front at both WG1 and WG2 locations. Figure 5.4(c) presents the time history of the horizontal water particle velocity in a water depth of 0.16 m (z = -0.09 m) and compares it to the horizontal particle velocity obtained from the analytical solitary wave solution presented by Munk (1949) on the basis of earlier findings of McCowan (1891). An important observation in the present case and which places the wave closer to a longer solitary wave than the analytical solution is that only the wave front resembles a solitary wave but high water levels comparable to the maximum of the wave crest are maintained in the wave tail. According to Madsen et al. (2008), the generic, classical solitary wave should not be used for tsunami modelling over a sloping bottom or as a propagation model for tsunami across the oceans, as significant errors in the spatial and temporal scales occur when they are compared to real tsunami waves. However, more recently elongated solitary waves were successfully generated in laboratory conditions. These waves had favorable length and time scales (Goseberg et al., 2013). Despite all debate about appropriate tsunami representations in laboratory environment, to date it is that the application of the solitary wave front is a reasonable means to cope with hydrodynamic loads in the context of initial near-shore impact and debris studies (Chinnarasri et al., 2013, Strusinska-Correia et al., 2013, Esteban et al., 2014, Seiffert et al., 2014, Yao et al., 2014). Combining a solitary wave front shape with a substantialy long wave tail represents a reasonable procedure to model near- and on-shore tsunami effects and it was thus chosen as a driving hydrodynamic forcing factor in the present study. Figure 5.4(d) and (e) show the time-histories of water surface elevation on the harbor area. The approaching wave broke at the edge of the quay wall and further propagated over the apron in the form of a tsunami-like broken bore with significant wave-induced turbulence. A maximum bore height of 0.08 m was observed at the location of the debris arrangements (at y=0.24 m from the edge of the apron). This was capable to lift debris units vertically and propel them in the direction of the bore propagation. Figure 5.4(e) shows, that at a distance of y=1.7 m away from the apron's edge, the maximum bore height was still 0.03 m and thus deep enough to induce debris motion without substantial grounding.

The duration of flow was approximately 3-4 s, which scales up to 19-25 s at prototype scale. This was significantly shorter than a typical tsunami inflow duration which can range from several minutes to several hours (Kinsman, 1965, Okal and Synolakis, 2016). There is a significant amount of literature addressing near-shore impact and debris transport as caused by tsunami (Chinnarasri et al., 2013, Strusinska-Correia et al., 2013, Esteban et al., 2014, Seiffert et al., 2014, Yao et al., 2014). Madsen et al. (2008) argued that, despite the fact that the overall tsunami wave train has key influence on the total inundation duration, the much shorter initial inflow is significant for local tsunami effects such as debris impact and surge forces. The presence of short riding waves with periods of 10-15 s are confirmed by eye-witness reports (Madsen et al., 2008). Thus, for a preliminary investigation of the motion of debris, the duration of the flow used herein was sufficient to evaluate debris entrainment and their overall motion. However the results will not necessarily scale to a practical application apart from the case of a well-confinded harbor basin such as the model considered herein. It is acknowledged that further research needs to focus on debris spreading set off by the longer components of a tsunami wave.

5.5.2 Debris Dynamics

Figure 5.5 presents four image frames recorded by CAM2 for debrisSet6 at 0.00, 3.62, 3.86, and 5.07 s, respectively. Time 0.00 s time refers to the moment when the wave generation was initiated by the wave maker. Debris units were entrained by the approaching bore (in Figure 5.5 moving from the bottom of the frames in upward direction); one particular single debris unit was indicated by a red polygon throughout the frames to highlight one random motion. Figure 5.5b) depicts the instant when the elongated solitary wave, following breaking at the edge of the quay wall edge, hits the debris arrangement. As shown in Figure 5.5b), by the white pixels occurring in front of the debris stack, strong turbulence occurs at this particular instant and this subsequently entrains all debris. Since turbulence cannot properly be scaled using Froude similitude (She and Leveque, 1994), the direct effects of turbulence at prototype scale will be significantly different than those occurring at model scale. Scale effects, as those induced by the unscaled air bubbles in the advancing bore front (Chanson, 2009) and the magnitude of potential multi-debris impact events under such conditions are challenges which need further investigation.

The most dominant transport mode observed during the experimental series was sliding or sliding-yaw rotation, depending on the transient turbulent flow responsible for the debris motion. Initially, most of the debris motion was sliding in the direction of the advancing bore. At later instances and mostly due to friction with the apron and due to inter-debris collisions, the sliding-yaw rotation motion occurred and was observed during the debris motion. While this study only examined debris motion for one type of surface, further research is needed to determine the effect of the debris-ground friction on the dominant transport mode.

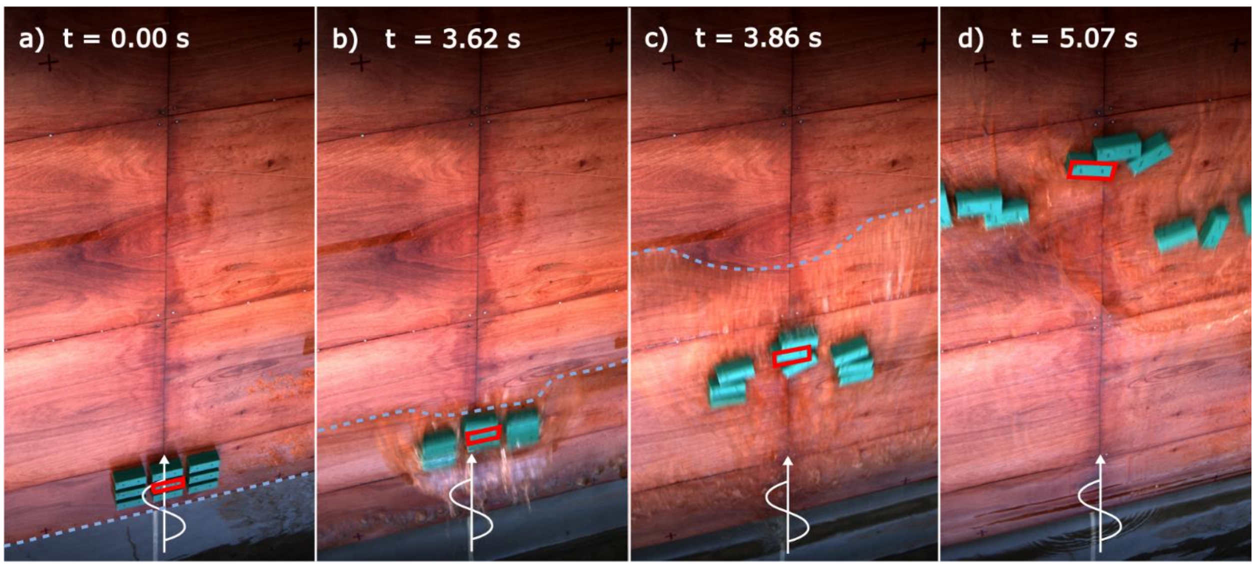

Figure 5.5: Unprocessed image frames taken at four time instances for the debrisSet3 as listed in Table 5.2- Wave approaches from the bottom of the image frames. Grey dashed line represents the approximate bore front; red polygon identifies center debris unit through the image frames.

It was also observed, that the moving shoreline was deformed in the presence of the debris group as seen in Figure 5.5b) and c). Although the contrast of the flow motion with respect to the harbor area surface was not sufficient to run automatic edge detection, it was possible to outline the moving bore front (dashed line). The downstream region of the bore front behind the debris site was delayed due to a sheltering effect caused by the debris arrangement compared with the image of the shoreline sections left and right of the disturbance. The disturbance grew over time indicating that the deformation of the bore front was highly dynamic and depended on the actual dispersion of the single debris units advected by the flow field.

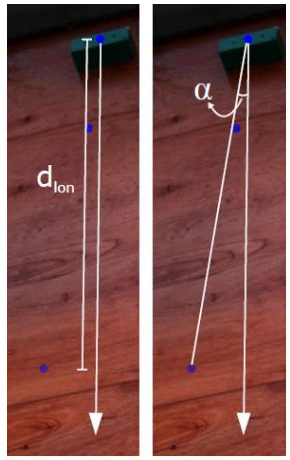

Figure 5.6: Definition of the displacement in the longitudinal direction (d_{lon}) and the debris spreading angle (α) from the center of the initial position of the container to the center of the final position of the debris.

The spatial extent of the debris motion was defined by the debris displacement in the y-direction (longitudinal displacement, Figure 5.6(a)) and by their angle of displacement in the x-direction, or the spreading angle, Figure 5.6(b)). Figure 5.7(a) shows the time-history of the debris displacement in y-direction (longitudinal axis of the apron) of three individual debris units being entrained by the incoming bore, where t = 0.0 s refers to the instant when the wave was initiated. The continuous position recordings by the "smart" debris, which was capable to span across the entire apron area, was subsequently compared with position obtained from the manual image processing. The "smart" debris recordings were filtered with an exponentially weighted moving average (EWMA) by the position engine software.

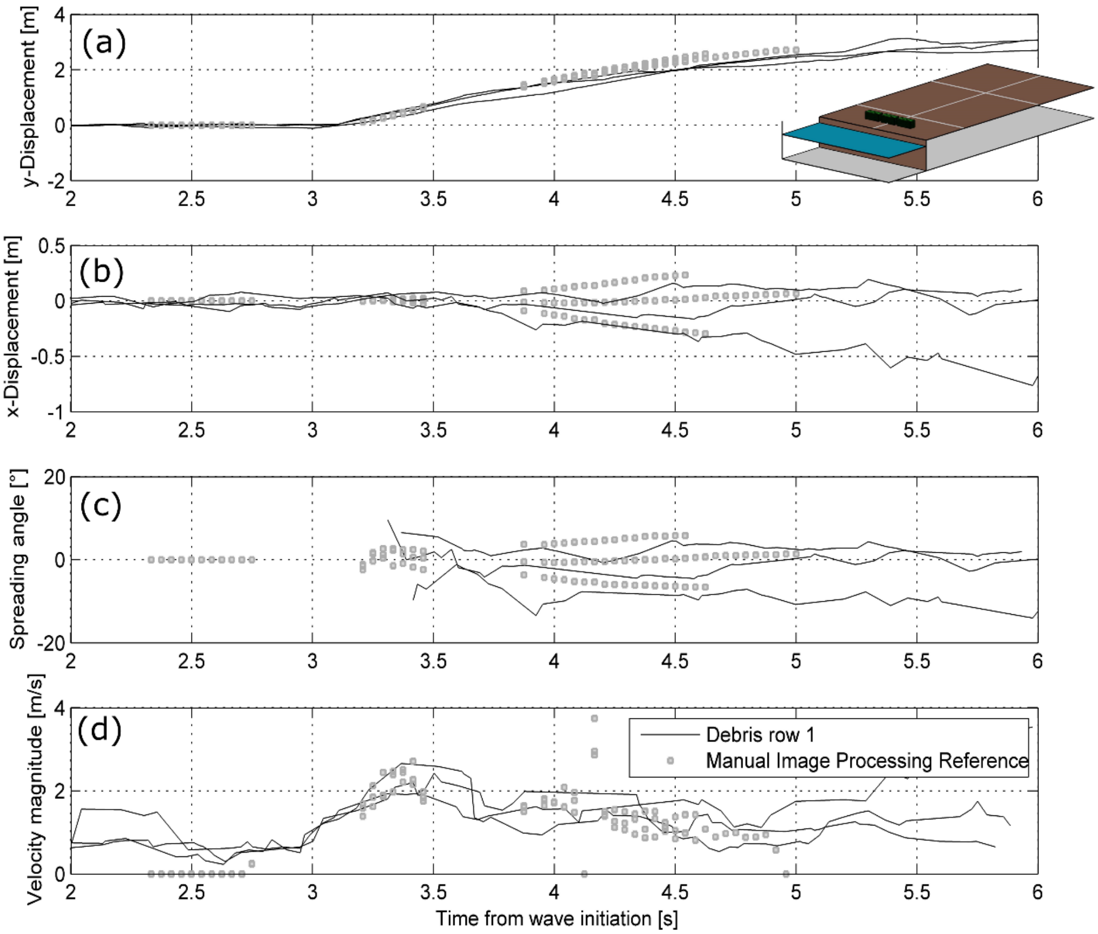

Figure 5.7: Time-history of debris dynamics: (a) and (b) are the (x-direction and, (y-direction - displacement respectively, (c) is the, spreading angle and (d) is the velocity for experiment 9 using the chosen wave condition and debris arrangement 3 (Table 5.2). Time-histories are compared to the reference data obtained using manual image processing. Inset indicates the initial debris arrangement.

Due to the limited AOI provided by the camera setting, manually derived optical displacement data are only available for y < 2.5 m. Synchronization problems also resulted in some data recording gaps but, generally, the error between the two methods was in agreement with errors indicated in Goseberg et al. (2016). Figure 5.7(b) shows the debris unit displacement in the x-direction for the same debrisSet 3 and compares it to the optically-derived reference data. The agreement between the “smart” debris and the manually-derived displacement data is reasonable; the general trend of the debris motion is represented well. Individual debris unit motion is distinguishable in this experimental run. The initial motion of the debris was in the longitudinal direction: the lateral motion (in x-direction) does not occur until ~0.4 s after the instant when the longitudinal motion was initiated. The longitudinal displacement occurs due to the momentum transfer initiated by the turbulent bore approaching at the initial debris arrangement given the orthogonal placement of debris units with respect to the wave propagation direction.

Subsequently, the breaking-induced turbulence, inter-debris collisions, imperfections in the debris arrangement, as well as the spatially-varying pressure/velocity fields result also in momentum transfer in the lateral direction. However, the latter is less dominant than the transfer of momentum in longitudinal direction. In the case of the reference data though, outer debris tends to move laterally at equal rates over time. “Smart” debris derived debris position data suggest that, although at some later stage in the entrainment process, the lateral motion reverts towards the (y)-axis for the debris originally positioned at y = 0.23 m. Figure 5.7(c) presents the spreading angle time-history for the three debris units according to Equation 5.1, which also agrees reasonably well with the manually-derived reference data. However, the “smart” debris based debris spreading angles show a larger amount of scatter which is probably due to the smaller rate at which the lateral motion develops. It was recently shown by Goseberg et al. (2016), that the use of Kalman filtering leads to better accuracy of the “smart” debris data. Figure 5.7(d) presents the time-history of the velocities of the three debris units dispersed across the apron based on “smart” debris information and the manually-derived reference data. Velocity magnitudes $|v(t)|$ were calculated using the vector arithmetic exploiting Pythagorean Theorem for the component velocities v_i with $i = x, y, z$.

“Smart” debris based data had a velocity component before t = 3.0 s despite the containers not moving due to the jitter in the calculation of the position by the positioning engine. However, these were accurately recorded through the manually derived image processing. During the debris displacement process, data from either measurement system matched well and indicated peak velocity magnitudes of up to 2.6 m/s which occurred around t = 3.4 s. Thereafter, velocity magnitudes decreased linearly until t = 5.0 s. No more reference data were available outside the camera’s AOI, yet the “smart” debris data stagnated at around 1.0 m/s. Velocity magnitudes inferred from the “smart” debris position data were significantly scattered despite the exponentially weighed moving average filter employed. Filtered position data used for the velocity calculation still inhibited significant fluctuations which resulted in a high variability in the time-history of the velocity. In future studies, advanced filtering is recommended to correctly infer velocities from “smart” debris data. Additionally, the use of higher sampling frequencies are also likely to improve results.

5.5.3 Spatial Debris Distribution

Figure 5.8 shows the trajectories of the debris unit entrained by the approaching bore across the apron area: the motion in the frames shown in Fig. 8 started from the bottom of the panels as indicated by the wave symbol. In this figure, the initial positions of the debris are indicated using opaque green boxes while their subsequent trajectories are color-coded according to the debris’ initial row number, with row numbers increasing with increasing distance from the edge of the quay wall. In order to relate the resulting spatial dispersion of the debris units to the tsunami bore, the angle of spread suggested by Naito et al. (2014) is plotted in Figure 5.8 with two dash-dotted black lines for reference.

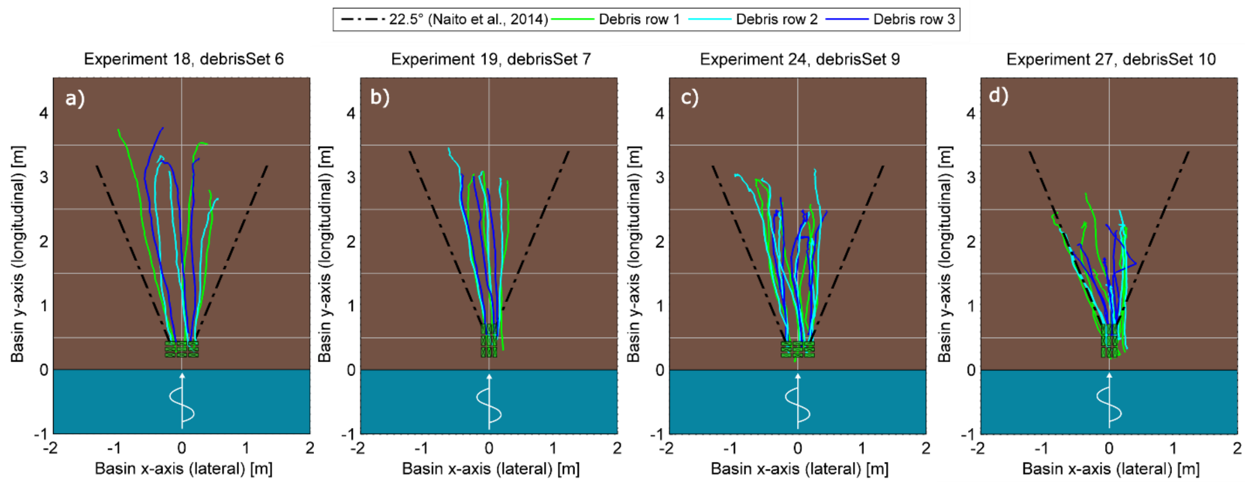

Figure 5.8: Multiple debris unit trajectories in the (x,y)-plane for tests 18, 19, 24, 27 using the baseline wave condition and a) debrisSet6, b) debrisSet7, c) debrisSet9, and d) debrisSet10 as listed in Table 5.2. Dash-dotted line indicates suggested angle of spread of ±22.5° with respect to each side of the direction of the initial wave approach as proposed by Naito et al. (2014). Trajectories are color-coded based on their initial row position, row 1 being the closest to the quay wall edge.

As shown by Figure 5.8a) – d) the observed debris trajectories were always contained within the spreading angle proposed by Naito et al. (2014). In general, smaller spreading angles were observed for these idealized cases where neither obstacles nor topographic features, such as slopes, were present. The previously prescribed spreading angle of ±22.5° with respect to each side of the direction of the initial wave approach which was proposed based on post-mortem field assessments after the 2011 Tohoku Earthquake and Tsunami seems to be conservative enough for the emergency planning engineer.

Besides calculating the debris spreading angle, some more basic observations highlighted how the initial debris orientation, as well as the number of debris stacks influenced debris dynamics across the apron area. Firstly, a comparison between Figure 5.8a) and b) as well as Figure 5.8c) and d) reveals that the total inland (longitudinal) displacement of the debris was dependent on the initial orientation of the debris arrangement. The total inland displacement decreased by approximately 0.5 m happens for an initial debris orientation of 90° (shorter side of the debris facing the sea) and this observation holds true for both the tests conducted with one or two layer debris arrangements. This is due to the difference in the impulse and momentum transfer per directly exposed face area for the two debris orientations involved. The layers of containers resulted in a larger initial friction force that needed to be overcome by the hydrodynamic forces in order to initiate container motion. However, once the friction force was overcome, the container placed at the top would topple over and both this and the underlying containers would move as individual, independent pieces.

5.5.4 Longitudinal displacement of debris

Debris motion is initiated when the wave-induced bore front hits the front face of the debris units leading to a sudden transfer of energy from the bore to the debris unit at rest. The energy extracted from the bore is then gradually converted into kinetic energy which eventually propels the debris whose displacement was observed to be a function of time and space. Matsutomi (2009) described a similar energy transfer mechanism for drift wood carried by a constant velocity flow. He found that the dimensionless acceleration distance, needed to induce a debris velocity equal to that of the ambient flow velocity, ranged between 3 to 19 (non-dimensionalized by the debris length). However, in the case of the present experimental setting, due to the rapidly decaying transient flow velocity of the bore across the apron area, a quantification of such an acceleration distance for the present results was impracticable.

Secondly, it is observed that an increase in the number of debris layers resulted in a decrease in the total inland (longitudinal) debris displacement due to the advancing bore; for trajectories shown in Figure 5.8b) and d), a reduction of approximately 0.5 m in the longitudinal debris displacement was measured when compared to the one-layer cases. Aside from the momentum transfer per increasing front face area, an increase in the total debris weight per unit area (horizontal) was also responsible for the decrease the total inland (longitudinal) debris displacement since a layered and hence heavier stack increases the breakaway torque required to initiate the debris motion. Equally, the energy contained in the bore per front unit had to accelerate twice the number of debris when compared to the single layer cases.

Based on the above made observations it was then possible to relate maximum longitudinal displacement to the number of debris used in each experimental run. As qualitatively described above, a quantitative (linear) relationship was found between the maximum observed longitudinal displacement in longitudinal (inland) direction and the number of debris units. Figure 5.9 shows the longitudinal displacement, d_{lon}, versus the total number of debris units used for each experiment, N. Experiments were each repeated three times for most of the debris arrangements and the maximum longitudinal displacement was defined by the authors to be the (y)-coordinate most distant from the edge of the quay wall. For this analysis, EWMA-filtered position data recorded by the “smart” debris system were used only.

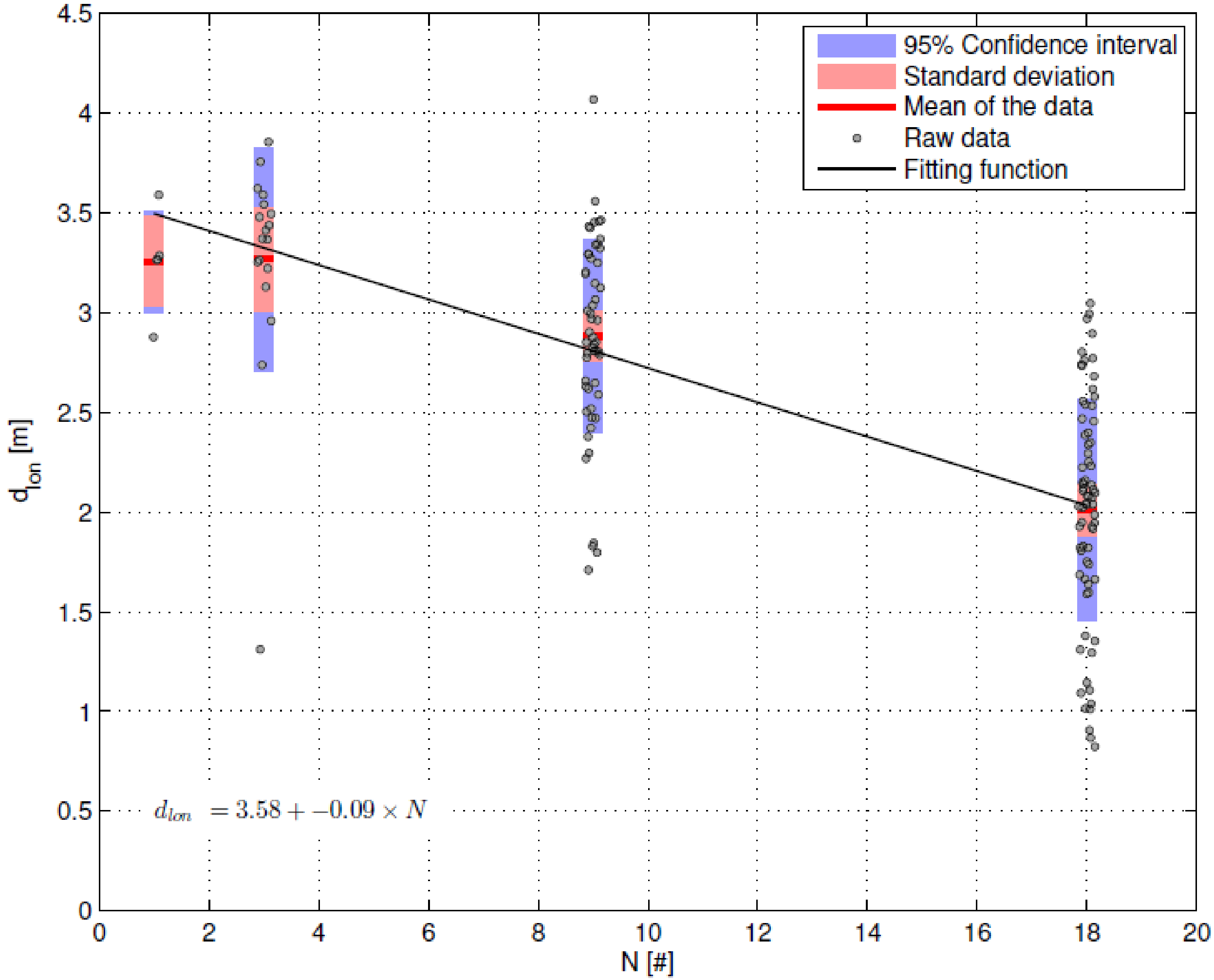

Figure 5.9: Maximum longitudinal displacement of debris units versus the total number of debris units used in each experiment. Mean (red), standard deviation (purple) and 95% confidence intervals (rose) provide statistics per debris number clusters.

A linearly decreasing trend function was fitted to the data based on the mean values of the data, as described by Equation 5.2. This function confirmed that for the same amount of available bore energy, an increase in the number of debris units resulted in shorter inland displacement:

$$d_{lon} = 3.58 - 0.09 \cdot N \tag{5.2}$$

Although the observed tendency seems straightforward at first, an unexpected increase in data scatter can be observed. As shown in Figure 5.9, standard deviations (Kenney, 1962) of the maximum longitudinal debris displacement increased as a function of debris units, and were of ±0.25 m, ±0.56 m, ± 0.48 m, ±0.56 m for debris units of 1, 3, 9, and 18, respectively. Conversely, assuming a normal distribution, the 95% confidence intervals (Kenney, 1962) decreased from ±0.22 m, to ±0.26 m, ±0.13 m, ±0.13 m for debris units of 1, 3, 9, and 18, respectively. It is also noted, that there is a decreasing number of data points contained in the confidence intervals plotted and shown in Figure 5.9. It is thus conjectured that the observed increase in data scatter is an expression of the randomness of the process under investigation. An increasing number of debris units is meant translates into an increase in the number of potential interactions between debris units among themselves as well as their interaction with the incoming bore. This leads to a decrease in the available energy which, in turn, causes debris units to be displaced more randomly along the penetration trajectory for an increasing number of debris units.

5.5.5 Maximum Angle of Spreading of Debris

Fig. 5.10 shows the the maximum angle of spreading, θ, as defined by Equation 5.1 as a function of the number of debris units, *N*. Similar to the maximum longitudinal displacement, experimental tests were each repeated 3 times and the maximum angles of spreading were determined considering the time-history of the spreading angle and the maximum angle of spreading per debris unit used in each experiment. In a subsequent step, the positive and negative maximum angles of spreading were adjusted based on their mean values in order to cope with minor experimental asymetries which occurred in the lateral (x) direction. Assuming a normal distribution, the mean (red bar) , the standard deviation (Kenney, 1962) (in purple), and the 95% confidence intervals (Kenney, 1962) (in pink) were calculated for each class of debris unit amount N in order to express the statistical nature of this data subset. It was found that a linear fit of the largest and smallest maximum spreading angle values represented reasonanbly well the overall behavior of debris propelled by the incoming bore.

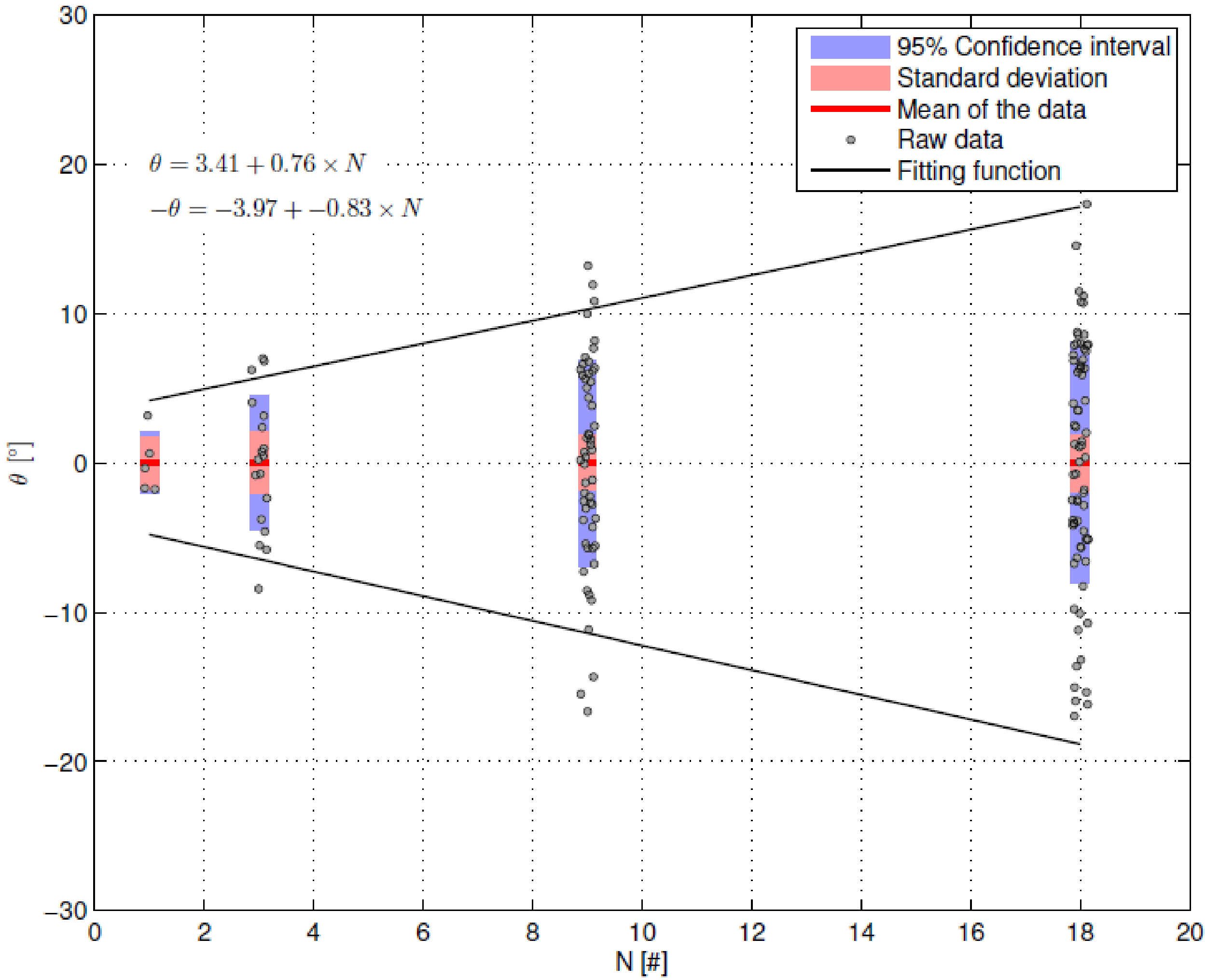

Fig. 5.10. Positive and negative spreading angles, θ, versus the number of debris units present. Mean (red), standard deviation (purple) and 95% confidence intervals (pink) provide statistics for the data per debris number cluster.

Given the specific bounds of the conducted study, the spreading angle θ yields approximately:

$$\theta = 3.41 + 0.76 \cdot N \tag{5.3}$$

$$-\theta = -3.97 - 0.83 \cdot N \tag{5.4}$$

The y-intercept and the slope of the linear fit could be simplified without loss of generality by parameter averaging to:

$$\pm\theta = \pm 3.69 \pm 0.80 \cdot N \tag{5.5}$$

For debris unit amounts N of 1 and 3, an increase in data scatter was observed which indicates that the presence of neighboring debris units in the lateral direction has some influence on the random dispersion of the debris. The 95% confidence intervals were found to be ±1.79°, ±2.08°, ±1.84°, and ±1.87° for debris units of 1, 3, 9, and 18, respectively. Similarly to the random nature of the maximum longitudinal displacement described in Section 5.5.4, the angle of spreading θ was found to vary significantly, suggesting thus a high amount of randomness which influences the entire dispersion process. The standard deviation for the spreading angle θ was of ±2.04°, ±4.50°, ±6.90°, and ±8.10° for debris units of 1, 3, 9, and 18, respectively. Just as in the case of the debris longitudinal displacement, this large increase in the standard deviation for each debris amount subset indicates that inter-debris collision and turbulence brought about by the bore interaction with the individual debris units significantly influences the randomness and finally the level of uncertainty of the results presented herein.

5.6 Discussion

An examination of Figure 5.8 clearly shows differences between the proposed angle of spreading proposed by Naito et al. (2014) and those found in the current study. This inconsistency however does not imply that either result may be inaccurate. While results and suggestions by Naito et al. (2014) were based on post-tsunami forensic analysis of debris (shipping containers) spreading and given the complex inundation features, the diverse topography, the presence of buildings in the areas of entrainment and dispersion as well as the characteristics of the flow, a resulting spreading angle of ±22.5° was proposed to account for debris impact on surrounding infrastructure. To date, their study is unique with respect to debris spreading and can thus be seen an upper, practical bound until more research becomes available. The present results focus on the relationship between the angle of spreading and the longitudinal displacement with the number of debris units. The longitudinal displacement and the spreading angle were determined to be a function of the number of debris: an increase in the number of debris results in an increase in the spreading angle and a decrease in the longitudinal displacement. At the same time, the direct use of the method discussed in Naito et al. (2014) results in an increase in the longitudinal displacement as a result of the increased number of debris (the spreading area being proportional to the plan area of the debris). This is interpreted to be the result of choosing fixed spreading angle bounds (±22.5°). Contrastingly, as found in this study, the spreading angle also varies with the number of debris. Hence, the use of the method proposed by Naito et al. (2014) would still hold if a varying spreading angle was adopted instead of using an a priori set, static one. Also, for less debris, a smaller spreading angle would result in a larger longitudinal displacement, whereas with more debris, a larger spreading angle would result in a smaller longitudinal displacement. Further investigation into the variation in spreading angle is needed to further develop a probabilistic evaluation of the variation in spreading angle.

The angles of debris spreading, even for the largest number of debris units used were found to be within the bounds of the Naito et al. (2014) proposed ±22.5°. However, larger spreading angles may occur in tsunami events with varying conditions. The presence of macro-roughness elements, varying topography and built environment can heavily influence hydrodynamic conditions, as well as the debris transport rendering future research of these aspects highly necessary. It is thus advised that coastal and port planners and engineers carefully judge how debris could be dispersed by an incoming coastal flood based on the potential number of debris, the local topographic features, and the infrastructure present in the area and on hydraulic conditions from a potential tsunami.

Figure 5.9 presents a relationship between the maximum longitudinal debris displacements versus the number of debris entrained and shows a linearly fit of the available experimental data using Equation 5.2. This linear fit was derived based on the use of up to 18 debris units propelled by a single broken tsunami –like bore. A negative slope of 0.09 was found for the linear equation inferring that, for a significantly larger amount of debris, the maximum longitudinal displacement could be significantly reduced. This however cannot be disproved or confirmed based on the currently available data set as time restrictions prevented additional experimental tests focussing on this particular aspect. Increasing the number of debris, and similarly important, their unit weight per planar area given through number of stacking layers and loading, appears to affect how the debris are dispersed inland. Further research is therefore required to clarify where the upper limits for the relationship between the maximum longitudinal displacement and the number of debris are.

Fig. 5.10 shows spreading angles of single individual debris units plotted with respect to the total number of debris used in each experimental run. Based on preliminary statistical parameters such as the 95% confidence interval and the standard deviation, it was possible to conclude that the observed process is of extremely random in nature, with increased randomness as a function of the total amount of debris involved. Based on the available amount of time, three repetitions were conducted for each of the planned experimental tests. However, reliable statistical parameters could not be derived based on the number of repetitions. This explains why so many of the plotted data points reside outside the 95% confidence intervals found.

This experimental study examined the relationship between the number of containers to the longitudinal displacement and spreading angle for an incipient sequence of motion under flow conditions similar to a tsunami-induced turbulent bore. The study is limited by its scale as shipping yards in coastal areas are most often significantly larger and have more containers than the eighteen (18) which were considered herein. The time scale of the flow also does not entirely correspond to field data of tsunami-affected communities; it is acknowledged that this will have an influence on the longitudinal displacement of debris at prototype scale. For tsunami flows of longer duration, it is expected that debris' longitudinal displacement will increase with a lesser degree of dependency on the amount of debris displaced. However, this investigation attempts to evaluate the overarching effects of the number of debris and debris configuration on the debris spreading area. Results found will also have significant value in the context of validating numerical models eventually capable of predicting debris transport in more realistic flow conditions. However, the investigation does begin to evaluate the overarching effects of the number of debris and debris configuration on the debris spreading area. In order to further understand debris motion and provide practical guidelines for debris motion and potential impacts, additional experimental work should be performed to get a probabilistic view of the basic processes of debris entrainment and motion. The ultimate goal of this work would be to provide benchmark data for the calibration and validation of numerical models capable of simulating debris motion at much larger scales in space and time. However, the authors are pointing out to the lack of adequate experimental facilities capable of addressing tsunami inundation space and time scales. Hence, a hybrid approach considering the experimental work focusing on certain aspect or instant of debris motion (such as the present study) and numerical models calibrated based on these sequential experimental data could be used.

5.7 Summary and Conclusions

This study presents results of an experimental research program which focused on investigating some of the recommendation regarding the motion of debris entrained by tsunami-like coastal inundation in a port areas. Aside from the experimental program the work involved a significant volume of data processing and analysis, especially given the random nature of the motion of multiple debris units in a number of different debris arrangements in an approaching tsunami-like bore. The debris depicting down-scaled 20-feet shipping containers were entrained by a hydraulic forcing element in the form of a turbulent bore generated by the sudden breaking of an elongated solitary wave. The debris were dispersed in the sequel of the initial impact of the bore front with the debris placed at their initial position. Once the tsunami-like bore hit, individual debris units were entrained in the flow and carried inland up to the point where the draft of the debris became smaller than the local flow depth. Based on the analysis of the recorded data, the authors drawn the following conclusions:

- Single debris units were dispersed by an approaching broken tsunami-like bore in random fashion: as such, the characteristics of their motion varied for repeated experiments with identical conditions.
- The elongated solitary wave which broke at the edge of the quay wall model and transformed into a broken tsunami-like bore which advanced on the horizontal harbor area (apron). While advancing over the apron, the bore front was significantly delayed by the characteristics of the debris' initial arrangement as bore momentum was transferred to the initially at rest debris units.
- An innovative "smart" debris system, used for the first time in a hydraulic and coastal engineering application was subsequently compared to a reference data set obtained from camera readings and good agreement was found between the debris motions identified using these two systems.
- The experimental setting employed a variety of instruments which proved their applicability and accuracy for tracking of up to 18 single debris units subject to dynamic conditions, a unique feature of this study which was never attempted before in this field of application. Using this instrumentation, detailed debris motion studies become possible for future experiments.
- For a given amount of energy contained in the approaching tsunami-like bore, the maximum longitudinal (inland) displacement was found to be a function of the total amount of debris units. A linear trend was found as a first order approximation of the observed behavior of the debris units.
- Similarly, the angles of spreading of debris were found to be a function of the total amount of debris units utilized in experimental tests for the applied tsunami-like bore. Spreading angles were also approximated by linear functions which described their dependency on the number of debris units positioned in the initial placement area. It was

observed that the experimentally found angle of spreading was generally within the bounds of the spreading angle proposed on the basis of post-disaster field investigations (Naito et al., 2014).

5.8 Link to Chapter 6

The evaluation of debris dynamics is a complex, multi-variate process. Previous studies into debris dynamics in river engineering examined the effects of the entrainment process (Braudrick and Grant, 2000, 2001). Similar studies of debris entrainment in tsunami-like flow condition have not examined the entrainment process. A study of the general characteristic of debris entrainment is presented further in Chapter 6.

Chapter 6. Flood Induced Debris Dynamics over a Horizontal Surface (Coastal Structures-ASCE, 2016)

6.1 Introduction

Large scale hydraulic events, such as tsunamis, storm surges and dam breaks, cause widespread damage to surrounding communities. Interactions between inundating water propagating through built-in environments has been subject of studies regarding tsunami inundation (Cox et al., 2008, Goseberg and Schlurmann, 2014) and long wave run-up reduction (Goseberg, 2013). The hydraulic forces from these events have been well documented (Ramsden, 1996, Arnason et al., 2009, Nouri et al., 2010, Bremm et al., 2015). However, forces from floating debris entrained within the flow have been much more difficult to quantify (Charvet et al., 2014, Yeh et al., 2014). Post-tsunami forensic investigations of devastated coastal communities has shown that the identification of debris impact sites can be extremely difficult as many variables need to be considered, such as debris size, initial location, surrounding environment, kinematics of the debris on impact and debris damming (Chock et al., 2013, Naito et al., 2014, Yeh et al., 2014).

Understanding and quantifying the characteristics of debris is of particular importance in identifying high-risk communities, which need to better prepare for debris impact. Debris motion is difficult to evaluate in forensic site assessment as the motion must be determined by back-tracking from a debris impact site. Often, the initial location cannot be located as most debris types are spread all around the area investigated (Naito et al., 2014). These difficulties considered, along with the rarity of these large scale events, the evaluation of debris motion is primarily investigated through an experimental setting. Matsutomi et al. (2008) and Matsutomi (2009) evaluated the effect of debris spacing on their entrainment, the hydraulic conditions and developed probability density functions for the motion of the debris and the subsequent impact forces. Imamura et al. (2008) examined the entrainment mechanisms of negatively buoyant objects within a bore. Yao et al. (2014) examined scaled-down coastal houses entrained by a broken solitary wave and evaluated the overall motion of the houses using probability functions. Rueben et al. (2014) evaluated the motion of boxes within both the on-shore direction as well as a result of subsequent drawdown.

All studies listed herein found that, while the general characteristics of the debris motion are similar between successive tests, the random nature of debris entrainment and collisions were not identical during tests using identical hydrodynamic forcing factors (waves, bores, etc.). This is a problem common to both debris motion and debris impact force and the authors consequently developed probability density functions (Matsutomi, 2009, Yao et al., 2014) or simplified models to explain the motion and impact force (Matsutomi et al., 2008, Aghl et al., 2015). Due to this random nature, large amounts of tests and data must be derived to properly characterize the debris motion. In this paper, a novel, non-invasive debris tracking system, herein termed “smart” debris, along with video footage, is used to characterize the entrainment and motion of the debris. The “smart” debris allows debris to be tracked with 6 degrees-of-freedom (DOF) capability and returns high-quality kinematic data for the length of each experimental run.

6.2 Testing Methodology

6.2.1 Wave Flume

The experiments were conducted in the Coastal Engineering and Management Laboratory at the Department of Civil and Environmental Engineering at Waseda University, Tokyo, Japan. For these tests, a newly-constructed tsunami wave flume (TWF) of 4-by-9 m dimension was utilized (Figure 6.1). The TWF was equipped with a four-chamber overhead reservoir, fillable with a vacuum pump (TST-150, Sato Vac Inc., Japan). The maximum achievable hydraulic head with reference to still water elevation was 0.77 m. The water impoundment was released through computer-controlled air valves (SVB1V-50F-02HS, CKD Corporation, Japan).

At the opposite end of the wave basin an elevated, rigid horizontal apron, mimicking a harbor platform, was constructed. This setting was chosen to simulate a tsunami wave attack on a modern port environment. A vertical quay wall separated the “sea” section of the basin from the horizontal apron. A right-handed coordinate system with the origin at the midpoint of the edge of the quay wall was used throughout the tests. The y-axis is positive in the onshore direction of the wave propagation positive. The vertical axis was positive opposite to the gravity vector with $z = 0$ at the elevation of the apron area.

Figure 6.1 also depicts the positions of the instrumentation in the wave basin, and mounted to the instrument frame which were used for this study. Four wire resistance wave gauges (KENEK Co., Ltd., Japan) were mounted at various positions in the basin, sampling at 100 Hz by a data acquisition unit (VM-806H, KENEK Co. Ltd, Japan). Two of them were positioned in the harbor basin and the remaining were used to gauge the water level on the initially dry harbor area (Table 1). An electro-magnetic current meter (ECM) was operated with its sensor head submerged 0.075 m below the still water level in order to avoid air contact during passage of the wave through.

Two high-definition (HD) cameras (Basler AG, pi1900-32gc, Germany) were additionally mounted at the apron end of the wave basin on an instrument frame at a height of 2.95 m above the apron area and pointing towards the quay wall edge. For the determination of individual debris positions, a real-time locating system (RTLS, Quuppa Oy, Finland) capable of tracking up to 25 debris models at a sampling rate of up to 50 Hz was installed. The applied system, whose locator antennae positions are depicted in Figure 6.1, uses radio trilateration based on a modified Bluetooth Low Energy (BLE) to track the motion of the debris.

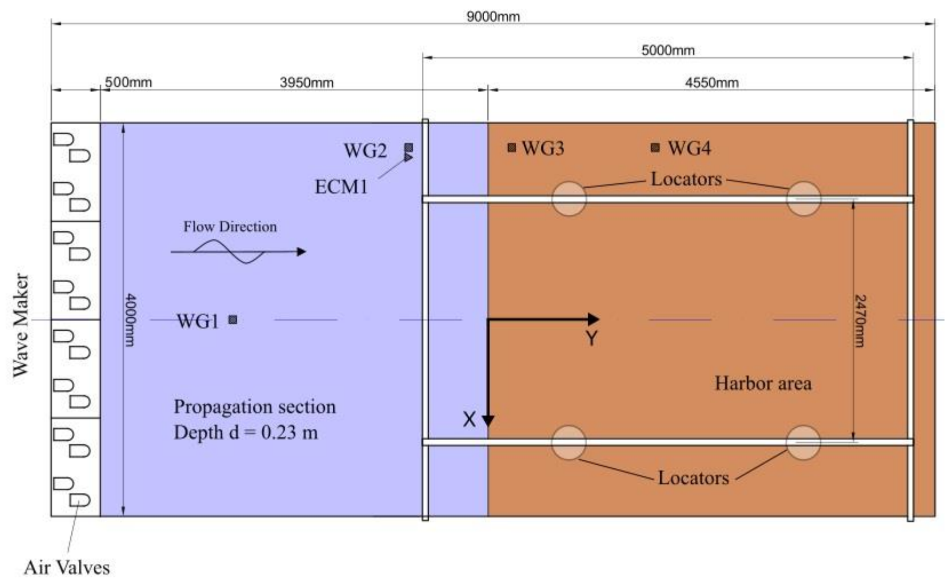

Figure 6.1: Top view of the Tsunami Wave Flume (TWF) at Waseda University in Japan.

6.2.2 “Smart” Debris

To investigate the motion of the “smart” debris entrained by an advancing bore, 20’ shipping containers (ISO668/688) were down-scaled based on Froude similitude at a length scale of 1 in 40. The down-scaled shipping container, shown in Figure 6.2, were manufactured from positively buoyant polyethylene (PE-HMW, 0.92 g/cm³). The scaled shipping container had overall dimensions of 0.06 x 0.06 x 0.15 m with an approximate draft of 0.025 m. Motions sensors (3-Space Logging, Yost Eng., USA) were used to record three-dimensional orientation. The coordinate system and its subsequent rotation angles were defined according to Figure 6.2. Likewise, one locator tag underneath each upper face of the specimen was used per “smart” debris to track the x,y,z positioning in combination with the RTLS. The motion sensor and the locator tag were tightly attached to the inside walls of the debris housing with Velcro tape: together they provided 6 DOF positioning information. The total weight of a single debris was determined by three repeated measurements and yielded an average total weight of 0.226 kg including that of one motion sensor (0.048 kg) and of the location tag (0.010 kg).

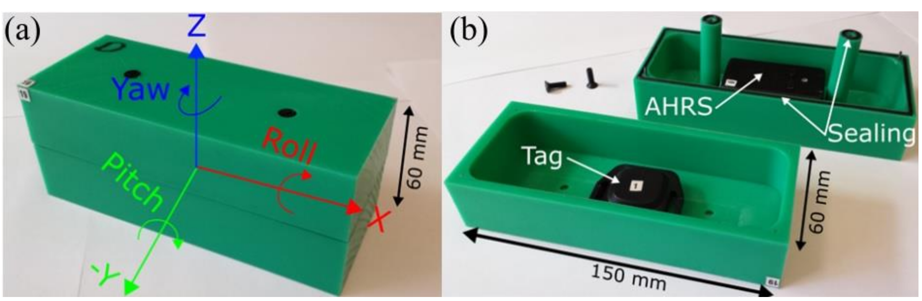

Figure 6.2: "Smart" Debris. (a) debris closed and sealed (b) tracking system (motion sensor and positioning tag) encased within the debris.

6.2.3 Experimental Protocol

To investigate the dynamics of the debris, different types of debris configurations were considered. Throughout the experiments, the center "smart" debris of the first row was always placed at y=0.23 m and the spacing of each "smart" debris was set at 0.03 m. Eight different debris configurations were examined with 1, 3, 9 or 18 debris and an initial orientation angle of either 0^{o} or 90^{o}. Given space limitations, only three of the configurations are discussed herein: debrisSet1, debrisSet3 and debrisSet6 (Table 6.1).

Table 6.1: Specifications of the debris arrangements

Case	Experiments	Total number of debris used	Inter-debris spacing (m)	No. of apron-parallel debris rows	Initial orientation angle (°)
debrisSet1	1	1	--	1	0
debrisSet3	9	3	0.03	1	0
debrisSet6	17	9	0.03	3	0

The water depth in the TWF was set to 0.235 m during the tests, leaving a freeboard of 0.015 m between the still water level and the level of the apron. Before each test, the wave maker reservoirs were filled with an identical volume of water resulting in a hydraulic head of 0.67 m above the still water level. The total amount of water impounded in the reservoir and released by the opening of the computer-controlled air valves was 1.2 m^3.

6.3 Results

The experiments conducted as part of this test program generated large amounts of data describing the motion of the debris. Due to this, only selected results are presented herein. The focus of this paper is to identify characteristic flow features and the characteristic features of the entrainment of the debris itself. The results are presented in three sections: "Hydrodynamics" which examines the wave profile of the approaching bore; "Initiation of Motion" which examines the pickup and initial propagation of the debris for different debris configurations and identifies features of the debris motion and, "Debris Motion" which examines the motion of the debris over the duration of the experiment and further examines how debris are affected by the initial placement configuration.

6.3.1 Hydrodynamics

The wave was generated by the release of a determined volume of water from the overhead reservoir shown in Figure 6.1. The wave propagates through the water-filled basin ("sea" section) in the +y direction, breaks at the vertical quay (y = 0 m) and further propagates over the apron area as a turbulent bore. The wave front profile in the "sea" section of the TWF showed good agreement with analytical solution for a solitary wave published by Munk (1949). The wave front resembles a solitary wave but higher water levels are maintained in the wave tail. The average wave height at the edge of harbor (WG2) was 0.14 m above the still water depth, 0.07 m at the debris location (WG3). The wave height at 1.70 m past the edge of the apron area (WG4) was 0.02 m with a sustained flow duration of approximately 5 s. Water levels provide substantial draft to allow for free debris propagation and prevent their grounding.

Though generic solitary wave have been found to have order-of-magnitude errors in the effective temporal and spatial duration (Madsen et al., 2008), more recent examples of a solitary wave with elongated tails have shown to have much more favorable length and time scales (Goseberg et al., 2013). The duration of the flow is significant enough to maintain the flow characteristics for the length of the apron in the TWF and the wave front of solitary wave has also been used to model hydrodynamics loads in recent studies of near-shore impacts and debris motion (Chinnarasri et al., 2013, Seiffert et al., 2014, Yao et al., 2014).

6.3.2 Initiation of Motion

The entrainment of the debris was examined using images from the Basler HD cameras. The motion is recorded from the first frame in which the bore had contacted the debris (Time = 0.000s) until the debris is fully entrained within the bore. The common characteristic of the entrainment for all debris configurations is shown as a solid green line, which indicates the splash, and a dashed blue line, which shows the affected bore front.

The general characteristics of the entrainment of the debris as well as of the flow features are relatively similar throughout different debris configurations. Upon initial impact of the bore with the debris, the bore splashes up and forward, and the debris records little movement (Figure 6.3(b)). The bore to each side of the debris configuration continues unaffected and creates a horseshoe shaped bore with a steep bore front on the sides of the debris (shown by the blue dashed line). Since there is little initial movement of the debris, water begins to build up behind them until the friction force between the debris and the apron is overcome and debris start sliding (Figure 6.3(c)). While the debris is moving at slow speed, the horseshoe bore continues to extend perpendicular and parallel to the flow direction. Once the debris accelerates, the water buildup behind the debris pushes forward causing the steep front of the horseshoe bore to flatten out and move at a faster velocity than the debris (Figure 6.3(d)). The flattened bore pushes under the sliding debris, entraining them within the bore and accelerating the debris until they attain the same velocity as bore (Figure 6.3(e)).

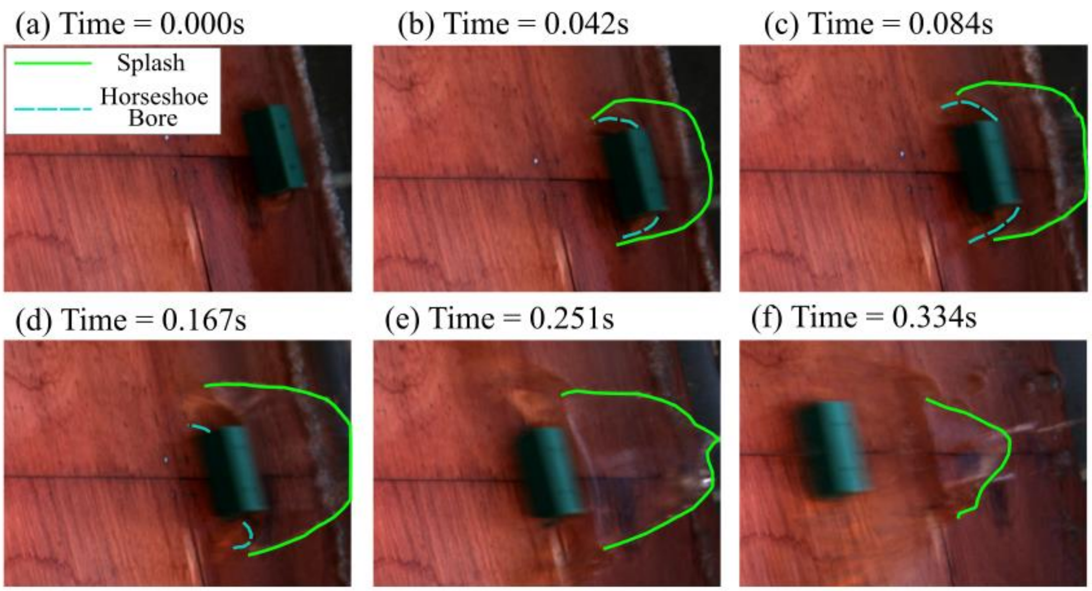

Figure 6.3. Experiment 1: one debris, time is relative to the first frame in which the wave contacts the debris.

Figure 6.4 shows the experiment performed with three “smart” debris. The general characteristics of the debris entrainment and flow features remain relatively similar to the single debris case. However, when the splash occurs, there appears to be a significant amount of interference between the water and debris, which leads to little water passing through the spacing between debris (Figure 6.4(b)). This results in the three debris pieces initially acting as a single block. Hence, water will build up behind the three containers until the friction force is overcome. The horseshoe bore will then occur around the outside edge of this “unitary” block since there is not enough room between the debris for individual horseshoe bores to form (Figure 6.4(b-c)). Similarly to the single debris experiment, the horseshoe bore is maintained until the motion of the three debris is initiated and the horseshoe bore begins to further flatten out.

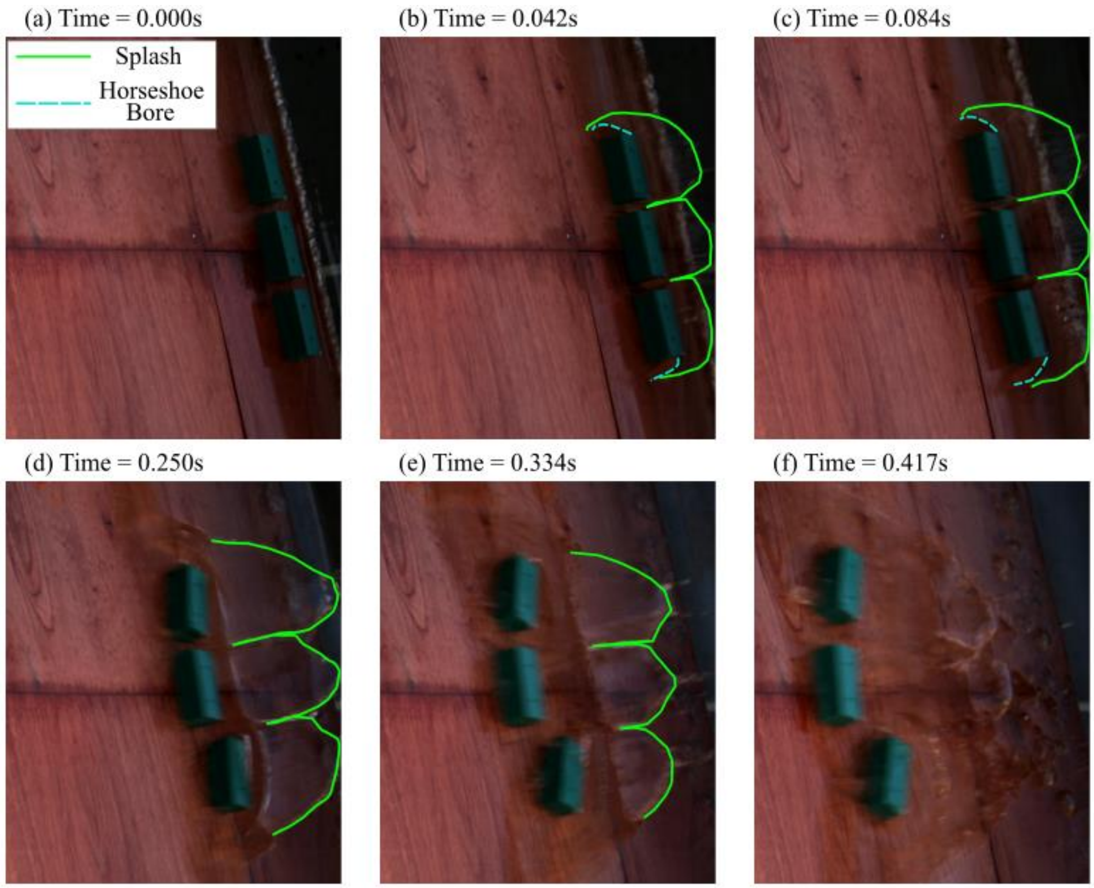

Figure 6.4. Experiment 9: three debris.

Figure 6.5 shows the experiment that was performed with nine debris arranged in two rows parallel to the edge of the apron. Again, similar flow patterns and debris motion can be observed as in the previous two experiments. On bore impact, little water passes between the debris causing the entire debris configuration to act as a single block, with the horseshoe bore forming again on the outside edges of the configuration and the water builds behind the debris. The buildup of water behind the debris acts in steps. The water builds up, then it overcomes the friction force between the debris and the apron while initiating row one's motion. Further, row one impacts row two, again causing a buildup in water. In this case, the horseshoe bore will not begin to flatten out until the motion of the final row of debris is initiated (Figure 6.5(e)). The longer time required to initiate the debris motion can be observed as the water splash, which for other configurations falls well behind the debris, falls on top of the them, briefly obscuring the camera view (Figure 6.5(f)).

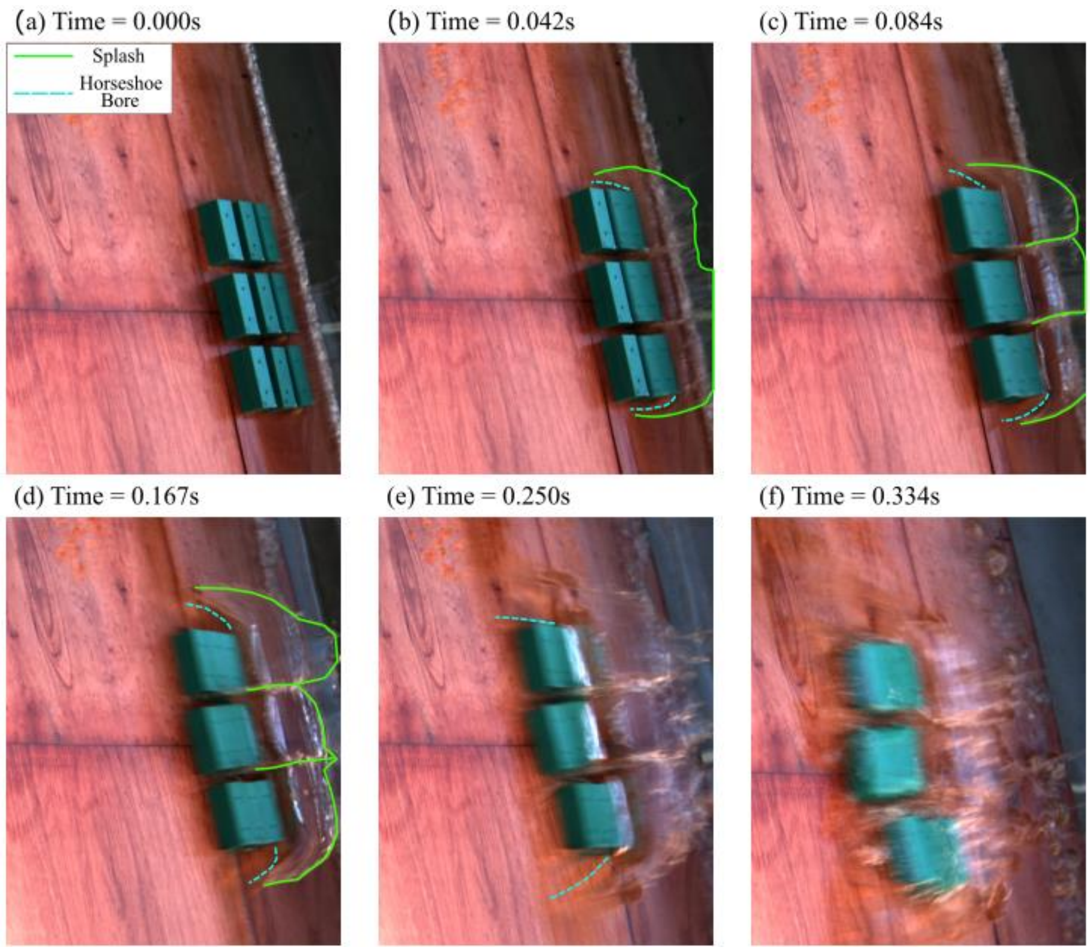

Figure 6.5. Experiment 17: nine debris.

The identification of the similar initial motion of debris allows for a qualitative assessment of how the debris configurations may affect the overall motion. Figure 6.5 shows that the energy necessary to entrain the debris arranged in multiple row configurations will likely need to be greater than that capable of moving a single row comprising of the same number of debris. The process through which the bore initiates the motion of the debris occurs in steps when there is a multiple row configuration. The bore initially impacts the first row and water builds up behind the debris. Motion is initiated until the first row contacts the second row and the debris does not initiate the motion of the second row. The water must then build up behind the first and second row to initiate the motion of both debris rows. This process likely leads to a large amount of energy dissipation through turbulence and debris-apron friction that would otherwise be lower than when debris are arranged in single row configurations.

The process also shows that the friction between the debris and the apron is critical in determining the amount of energy necessary to initiate the sliding, and the subsequent entrainment of the debris by the bore. As the friction increases, the energy required to move the debris increases significantly as well. Hence, less energy would be available to displace the debris. Further investigation into the effect of the friction force (and its difficult scaling) is needed, as a change in friction results delays in motion initiation or motion initiation in the form of saltation or rolling, which could significantly affect the overall process.

6.3.3 Debris Motion

Figure 6.6 depicts the debris trajectories for the three experiments outlined in the section above. The initial position of the debris is shown as green boxes and the color of the debris trajectories is determined by their initial row position: green for the front row debris, blue for the debris in the second row and dark blue for the third row. Based on the site assessment of the 2011 Tohoku Tsunami performed by Naito et al. (2014), the debris spreading angle was observed to be ±22.5^{o} with respect to the direction of the incoming flow. The bounds of the spreading angle of Naito et al. (2014) is represented by the black dashed line in Figure 6.6.

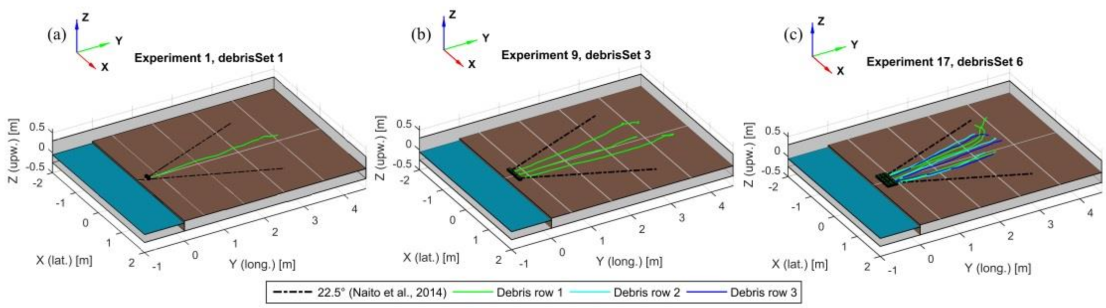

Figure 6.6. Debris trajectories for Experiment 1 (a), Experiment 9 (b) and Experiment 17 (c).

As shown in Figure 6.6, the trajectories all of the debris fall well within the bounds of the spreading angle suggested by Naito et al. (2014). The debris with no obstructions and a free flow path (Figure 6.6(a-b)) move essentially parallel to the flow direction. When more debris rows are added, as in Figure 6.6(c), the debris trajectories are obstructed by the subsequent debris rows and more collisions occur. Collisions between the debris result in a deviation from the free flow path of a single, resulting in the larger spreading angle in the x-direction. It should be noted, that the experiment was performed using ideal conditions, with no obstacles and a flat topography. Therefore, the ±22.5^{o} spreading angle is considered conservative enough as the effect of obstacles and topography will affect the motion of the debris.

The occurrence of collisions, along with more flow energy required to initiate debris motion results in shorter longitudinal displacement (displacement in y-direction) of the debris when multiple rows of debris are present. The dissipation of the initial inflow energy from these two processes, along with the increase in debris displacement in the x-direction (debris spreading) will result in less inland propagation. Due to the decaying nature of the incoming bore, the longitudinal displacement cannot be compared with results found for the maximum inundation limits of debris, discussed in Naito et al. (2014).

6.4 Conclusions

The debris motion is significantly affected by the initial pickup resistance. Analyzing the motion of the debris shows that the motion, under the hydraulic conditions used in this study, has similar characteristics between different debris configurations. Due to the small space between the debris, little water passes between the debris causing multiple debris to act as a single block. This would suggest the initial motion of the debris, regardless of the number of debris, is relatively similar. However, it cannot be ruled out that larger inter-debris spacing would cause this pattern to change.

The overall motion of the debris is dependent on the number of debris present within each experimental run. When more debris are present, and since throughout the experiments the wave characteristics were kept consistent, the increase in the debris-debris collisions and the increased energy required for initial entrainment result in a shorter longitudinal displacements. The debris-debris collisions also results in deviation from the natural, relatively straight path of a single debris, with a wider spreading angle

The problem of debris motion is difficult to analyze and quantify due to the large number of hydraulic and environmental variables that can affect the motion in such hydraulic events. This novel, non-invasive tracking technique presented herein has shown promise in evaluating the kinematics of the debris motion. However, more research is needed to identify and analyze all variables at play. Applying a stochastic technique to the debris motion problem is likely required to properly evaluate and quantify the random nature of processes involved.

6.5 Link to Chapter 7

While the evaluation of the maximum displacement and spreading angle of debris is valuable in determining critical areas for debris impact, intermediate variables such as debris velocity and orientation are important for determining debris impact forces. Using the camera-based tracking algorithm, the velocity and trajectory of the debris were evaluated and discussed in the context of critical impact loads in Chapter 7.

Chapter 7. Optical Tracking of Debris in Extreme Hydrodynamics Conditions (CSCE, 2016)

7.1 Introduction

The 2011 Tohoku Japan Tsunami was one of the most tragic and destructive natural disasters, with over 15,500 fatalities and an estimated $209.8 billion (USD) dollars in damage (Fujii et al., 2011, Kazama and Noda, 2012). The primary reason for the extraordinary extent of the damage was due to the fact that coastal communities and associated infrastructure located within the tsunami inundation area lacked the necessary capacity to handle the extreme hydrodynamic forces (Esteban et al., 2015). As a result, a worldwide sustained research effort focused on identifying the loading conditions occurring in the extreme hydraulic events.

Although Canada has avoided extreme damage, similar to the one in 2011 Tohoku Tsunami in Japan, due to tsunamis in recent history. However, the West Coast of Canada and the United States of America (USA) is vulnerable to tsunamis, generated from earthquakes occurring along the Pacific "Ring of Fire", which have the potential to be nearly as large as the tsunami that struck Japan in 2011 (Clague et al., 2003, Palermo et al., 2009). The increased risk to the West Coast of North America has led the American Society of Civil Engineers (ASCE) to develop a new standard, written in mandatory language, specifically targeting communities at risk of tsunami events (*ASCE 7: Tsunami Loads and Effects, 2016*). While these standards cannot prevent damage from a tsunami, appropriate design and preparedness of at-risk communities can greatly reduce the devastation level of such events (Johnston et al., 2005, Taubenböck et al., 2009, 2013).

Building failure due to debris impact has been reported in some forensic engineering site assessments of tsunami-stricken regions (Charvet et al., 2014). However, the impact forces and areas at-risk of debris impact are difficult to evaluate (Yeh et al., 2013). Determining areas at risk of debris impact requires an in-depth understanding of the debris motion as many variables affect their overall motion, such as properties of the debris (i.e. mass and geometry), surrounding environment as well as flow conditions (Matsutomi et al., 2008, Matsutomi, 2009, Naito et al., 2014). For impact loading, which is the variable that determines the design condition of at risk structures, the velocity and orientation of debris on impact are critical properties of the debris motion to consider (Matskevitch, 1997, Haehnel and Daly, 2004, Aghl et al., 2015). The examination of debris motion has been difficult due to the random nature of the process Matsutomi (2009). The examination of the motion has been particularly difficult in an experimental setting due to a lack of methods that can quickly, accurately and non-invasively track the motion of the debris. Historically, debris motion has been evaluated by determining the maximum inundation and final resting position of the debris using image-by-image analysis (Imamura et al., 2008, Matsutomi, 2009). However, this method is time-consuming and does not capture the intermediate steps involved in debris motion such as the maximum velocity and orientation. Recently, more sophisticated image processing techniques have been used to evaluate the debris motion (Yao et al., 2014) as well as wirelessly equipped debris ("smart" debris) for quicker and more accurate evaluation of debris motion (Shafiei et al., 2014, Goseberg et al., 2016).

Figure 7.1: Debris impact on structures following the 2011 Tohoku Japan Tsunami (Nistor, 2011).

This paper examines the motion of scaled-down 20-feet shipping containers (debris) on a horizontal bottom using a novel image processing algorithm that quickly and accurately tracks the trajectory and orientation of the debris in high velocity flow. The objectives of this paper is to analyze:

- The repeatability of the debris motion.
- The effect of the initial orientation of the debris on the debris motion under extreme flow conditions.
- The effect of the distance from the initial debris site on the potential impact forces of the debris.

The paper consists of the following sections: the "Experimental Setup" section outlines the test setup at Waseda University, Tokyo, Japan and briefly outlines the necessary equipment. For a more in-depth description of the experimental setup, see Nistor et al. (2016). The "Debris Tracking" section outlines the camera-based debris tracking algorithm that was used in evaluating the debris motion. The algorithm is further described in Stolle et al. (2016). Finally, "Results and Discussion" analyzes the results of the experiments focusing on the debris trajectory and velocity while "Summary and Conclusions" outlines the findings of the paper and the potential next steps in the research.

7.2 Experimental Setup

7.2.1 Tsunami Wave Basin

The experimental program was conducted in the Coastal Engineering and Management Laboratory at the Department of Civil and Environmental Engineering at Waseda University, Tokyo, Japan. For these tests, a newly-constructed Tsunami Wave Basin (TWB) was utilized (Figure 7.2). The TWB was equipped with a four-chamber overhead reservoir, fillable with a vacuum pump (TST-150, Sato Vac Inc., Japan). The maximum achievable hydraulic head with reference to still water elevation was 0.77 m. The water impoundment was released through computer-controlled air valves (SVB1V-50F-02HS, CKD Corporation, Japan).

At the opposite end of the wave basin an elevated, rigid horizontal apron, mimicking a harbor environment, was constructed. A vertical quay wall separated the "sea" section of the basin from the dry, horizontal apron. A right-handed coordinate system with the origin at the midpoint of the edge of the quay wall was used throughout the tests. The y-axis was positive in the onshore direction of the wave propagation. The vertical axis was positive in opposite direction of the gravity vector, with $z = 0$ at the elevation of the apron area. Two high-definition (HD) cameras (Basler AG, pi1900-32gc, Germany) were mounted at the apron's end of the wave basin on an instrument frame positioned at a height of 2.95 m above the apron area and pointing towards the area of interest (AOI).

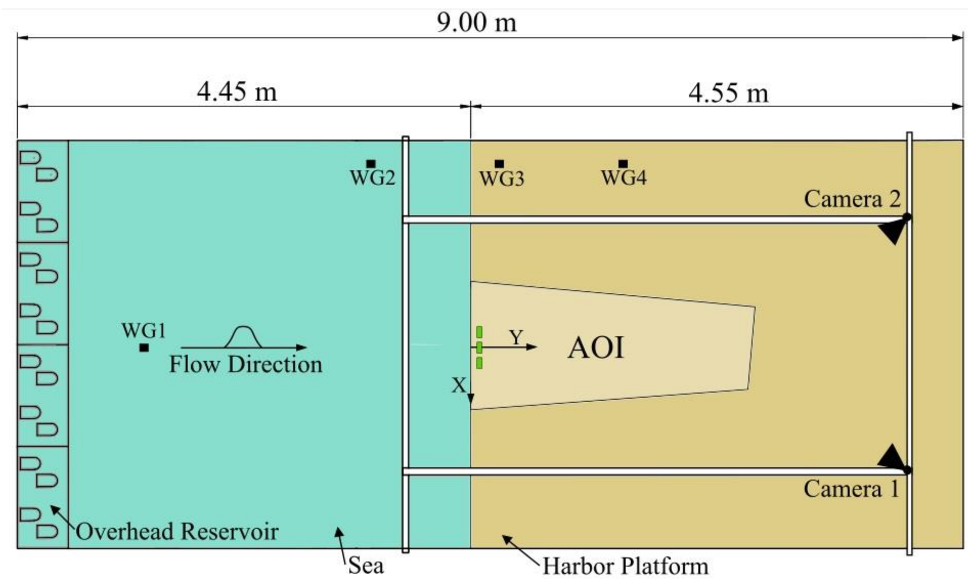

Figure 7.2. Tsunami Wave Basin (TWB) at Waseda University, Tokyo, Japan.

7.2.2 Debris Model

The debris consisted of an idealized 20-feet shipping containers (ISO668/688) down-scaled based on Froude similitude at a length scale of 1 in 40. The down-scaled shipping container, shown in Figure 7.3, were manufactured from positively buoyant polyethylene (PE-HMW, 0.92 g/cm³). The scaled shipping container had overall dimensions of 0.06 x 0.06 x 0.15 m with an approximate draft of 0.025 m. The debris was placed centered on the TWB harbor platform, 0.20 m in the positive y-direction from the vertical quay wall (Figure 7.2).

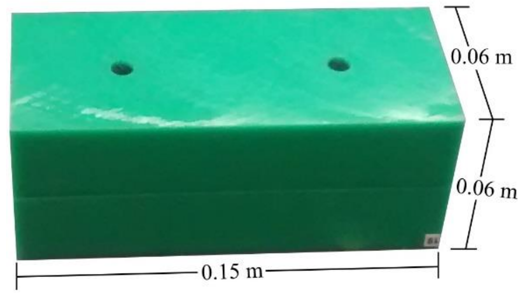

Figure 7.3. Debris model: scaled-down ISO shipping container (1:40 Froude scale).

7.2.3 Experimental Test Program

The paper presents the results of 13 of 45 experiments performed in the TWB at Waseda University (Table 7.1). The experiments comprise the effect of orientation and number of debris on the trajectory and velocity of the debris as the debris passed through the AOI. For each test, the water depth in the TWB was set to 0.235 m in the "sea" section, leaving thus a freeboard of 0.015 m between the harbor still water level and the level of the dry apron area. Before each test, the wave maker vacuum reservoirs were filled with the same volume of water resulting in a hydraulic head of 0.67 m above the harbor's still water level. The filling level of the vacuum chambers was controlled to ensure the same hydraulic conditions of the generated wave. The hydraulic head used in all tests was related to the total amount of water impounded in the reservoir chambers (1.2 m³ total volume) which was released by the opening of the computer-controlled air valves.

Debris were placed with the centroid of the debris 0.23 m from the edge. For experiments with one debris (E01 and E02), the centroid of the debris (D2) was placed on the y-axis. For experiments with three debris (E03 and E04), the centroid of D2 was placed on the y-axis and the spacing in the x-direction between the centroids of the debris to each side was 0.18 m (0.03 m spacing between the debris). The initial orientation of the debris was either 0^o, where long axis of the debris was placed perpendicular to flow direction, or 90^o, where the long axis of the debris was placed parallel to flow direction.

Table 7.1. Experimental Test Program

ID	Number of Debris	Initial Debris Orientation (^{o})	Initial Y-Position (m)	Test ID (#)
E01	1	0	0.23	1, 2, 3, 4, 5
E02	1	90	0.23	6, 7, 8
E03	3	0	0.23	10, 11
E04	3	90	0.23	12, 13, 14

7.2.4 Debris Tracking

A camera-based image processing algorithm was developed for the tracking of multiple uniform debris in high-velocity flow (Stolle et al., 2016). The objective of the algorithm was to quickly and accurately track the debris through the AOI to provide high-quality data of the motion of the debris. The algorithm used raw images recorded by the camera. By using image processing techniques determined the position and orientation of the debris within each frame. The algorithm was validated using a manual image-by-image selection of the debris for selected experiments from the Waseda University experimental program. This section provides a brief outline of the tracking algorithm, but a more detailed explanation can be found in Stolle et al. (2016).

The tests were performed at Waseda University in the Tsunami Wave Basin which is located outdoor. Therefore, the algorithm had to handle a large variety of lighting conditions. The primary method of dealing with this issue was to transform the traditional color space of the raw image (each pixel being expressed as a Red-Green-Blue value) into a three-dimensional luminance-chrominance color space (each pixel being expressed as a Luminance (Y)- Blue Chroma (C_b)- Red Chroma (C_r) value), which has less redundancies associated with the expression of an individual color (Chai and Bouzerdoum, 2000). The new color space allowed the algorithm to track the green color of the debris using the chrominance vales and the shading was expressed in the luminance. Moreover, the image must be transformed from the image plane to the camera plane using *geo-rectification*. Using control points located on the outside edges of the AOI, each pixel in the image could be placed within the coordinate system specified in Figure 7.2. The rectified image is shown in Figure 7.4(a).

Within each rectified image, the debris needed to be identified from the image background and water surface. Since the debris was of uniform green color, *color thresholding* (Harrabi and Braiek, 2011) was used to segment the image. *Color thresholding* used a Boolean operation on the three values used to express each pixel (Y-C_b-C_r) and if each value falls within the specified thresholds the pixel was assigned a “1” (white) or “0” (black). The *color thresholding* resulted in a binary image, as shown in Figure 7.4(b). An image processing technique, referred to as *blob analysis* (Salvi, 2012), searched the binary image for interconnected “1” pixels large enough to be the debris. *Blob analysis* also provided important geometric feature of the interconnected pixel, such as the centroid and long axis. The centroid was used in determining the trajectory of the debris and the long axis was used to determine the orientation of the debris.

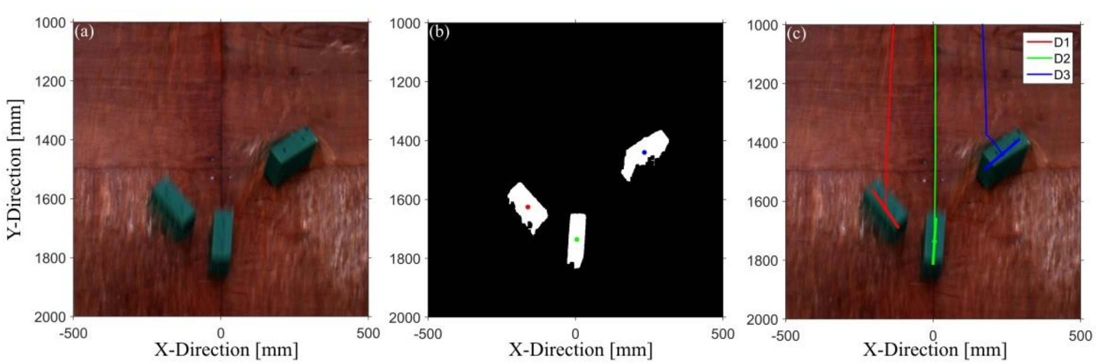

Figure 7.4. Camera-based optical tracking algorithm used in the tracking of debris (D1 – D3) motion. (a) Raw data frame from the camera; (b) binary image from the color thresholding; and (c) debris tracked using their centroid and orientation.

Based on the above mentioned steps, the debris was identified in each image. However, the information from each image had to be assigned to the unique debris to track it continuously through the AOI. This process was completed using a *Kalman filter* (Laplante and Neill, 2003). Based on the previous motion of the debris, the *Kalman filter* predicts the position of the debris in each image. With both the predicted position of the debris using the *Kalman filter* and the observed position of the debris, employing the *blob analysis,* a matching algorithm (Munkres, 1957) was used to match the observed positions at a given time to the observed positions recorded in the previous frames.

Figure 7.5 shows an example of the frame-by-frame tracking of video data from the experiments performed in the Tsunami Flume at Waseda University. The algorithm quickly and accurately tracks the trajectory of the debris and the orientation of the debris as it propagates through the area of interest. The algorithm performed well when compared to the manual method, except in cases where significant agglomeration occurred between the debris (Stolle et al., 2016).

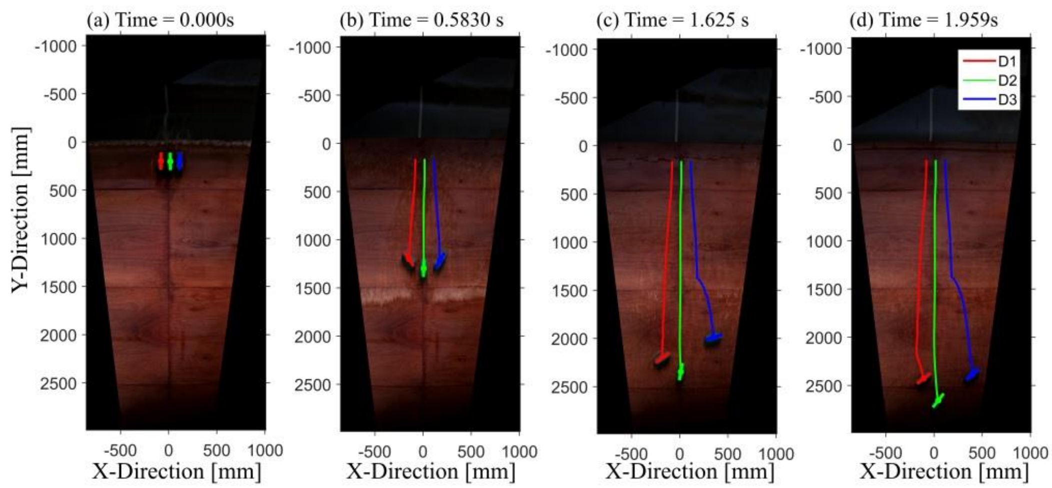

Figure 7.5. Trajectory of debris (D1 – D3) in experiment #12 (E04) at four instances in time: (a) 0.000 s; (b) 0.5830 s; (c) 1.625 s; (d) 1.959 s.

7.3 Results and Discussion

7.3.1 Hydrodynamics

The wave maker in the TWB impounded a head of 0.655 m in the overhead reservoirs, which was kept constant throughout all tests to maintain comparable hydrodynamics conditions. The water was released from the reservoir and would propagate through the "sea" section as an elongated solitary wave (Nistor et al., 2016). The wave front showed good agreement with the analytical solution for a solitary wave by Munk An elongated tail was generated after the wave front resulting in a longer duration flow compared to the solitary wave definition (Madsen et al., 2008). As the wave approached the vertical quay wall, the wave began to shoal and break, propagating over the horizontal apron as a tsunami-like surge as shown in Figure 7.6(c)-(d). A more in-depth discussion of the hydrodynamics can be found in Nistor et al. (2016).

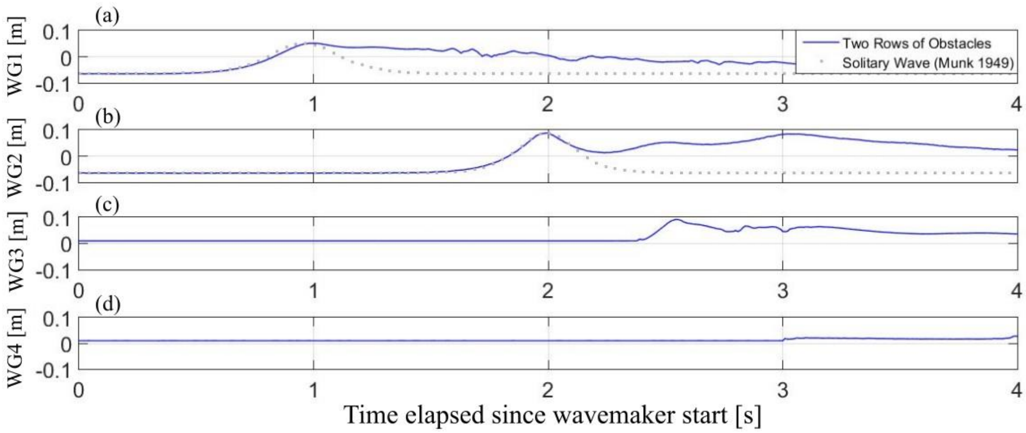

Figure 7.6. Time-history of water surface elevation at the four wave gages (WG) shown in Figure 1. The solitary wave profile is compared to the analytical solution by Munk (1949).

7.3.2 Debris Trajectory and Velocity

The trajectory of the debris was tracked by continuously monitoring the centroid of each debris throughout the AOI. With the centroid of each debris and the time stamp of each frame evaluated, the velocity of the debris could be further determined. In the evaluation of forces - later discussed in in Section 4.3 -the on-shore velocity (y-direction) was the component of interest as the structure perpendicular to the flow direction would experience maximum impact forces. Alternatively, as can be observed in Figure 7.7 and Figure 7.8, there is minimal motion in the cross-shore (x-direction) direction and minimal velocity. Due to this analysis, the velocity from herein on will only refer to the on-shore (y-direction) velocity. The orientation of the debris was determined by tracking the movement of the long axis of the debris.

As shown in Figure 7.7(a)-(b) and Figure 7.8(a)-(b), the trajectory of the debris with one and three debris was repeatable. The only case where there was significant deviation occurred when grounding of the one debris was observed in experiment #7. As debris propagated over the horizontal apron, likely due to the random nature of the turbulence of the incoming surge, the debris briefly contacts the apron resulting in a sharp deceleration at around 0.8 s (as shown in Figure 7.7(c)). As the debris propagated significantly slower than the surge, water built up on sides of the debris causing the debris to rotate towards the longer axis of the debris perpendicular to the flow direction. As the debris was rotating, the flow continued to act along the long axis resulting in the debris being pushed in the negative x-direction.

Unlike the trajectory, the orientation of the debris was significantly less repeatable. Overall, the debris tended to propagate in the same orientation as the initial position for each test for the length of the acceleration of the debris. However, as the debris decelerated as the debris fell out of the surge front, debris tended to orient perpendicular to the flow. As the debris slowed and the water surface elevation decreased, the debris contacted the horizontal apron resulting in periodic grounding similar to the more extreme case seen in experiment #7. Due to the random nature of the periodic grounding caused by the turbulent surge front, the orientation tends to display a similar pattern but with significant variation between the tests.

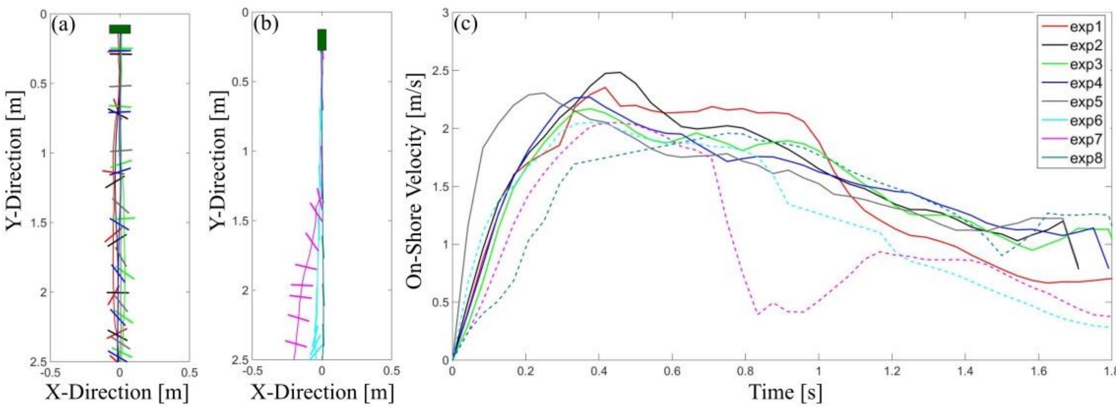

Figure 7.7. Motion and velocity of one debris. (a) the trajectory and orientation for E01; (b) the trajectory and orientation for E02; and (c) the on-shore (y-direction) velocity for E01 (solid line) and E02 (dashed line).

The velocity of the debris, as shown in Figure 7.7(c) and Figure 7.8(c), was also repeatable. For both the experiments with one and three debris, the debris oriented perpendicular to the flow reached a higher peak velocity. The debris velocities were between 6-14% higher than in the case of the experiments where debris were initially oriented parallel to the flow. The higher velocity was a result of the debris located perpendicular to the flow experiencing a greater drag force acting on the face of the debris, as the exposed cross-sectional area was larger (drag force is a function of cross-sectional area), resulting in larger accelerations (Imamura et al., 2008). However, once the debris had reached peak velocity, their subsequent deceleration was similar, regardless of their initial orientation of the debris.

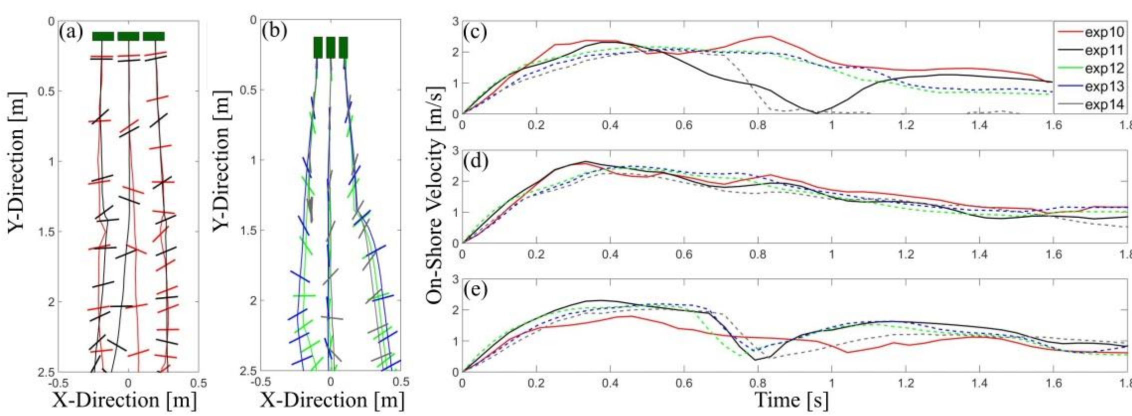

Figure 7.8. Motion and velocity of three debris. (a) Trajectory and orientation for E03; (b) trajectory and orientation for E04; and (c) on-shore (y-direction) velocity for E03 (solid line) and E04 (dotted line) for D1 (c), D2 (d), and D3 (e).

The grounding of the debris had no noticeable effects on their velocity after the debris had been re-entrained within the flow. The debris that briefly grounded quickly returned to similar velocities to those of the debris that had not grounded. As debris grounded, water built up behind them causing a wake around the debris with little water present in front of the debris. When the debris was released, the hydraulic head difference (gradient) between the front and back of the debris resulted in subsequent sharp acceleration, which returned the debris to the velocity of debris that did not ground.

7.3.3 Debris Impact Force

Current (*FEMA P646, 2008*) and upcoming (*ASCE 7: Tsunami Loads and Effects, 2016*) design standard for debris impact in extreme hydrodynamic flows rely exclusively on incoming velocity of debris for calculating the impact force. The equations used in the calculation of the forces are based on a simplified 1D bar model for the debris (Haehnel and Daly, 2004, Aghl et al., 2015):

$$F = u\sqrt{m_d k} \tag{7.1}$$

Where F is the impact force, u is the debris velocity at impact, m_d is the mass of the debris, and k is the lesser of the debris stiffness and the lateral stiffness of the impacted structural element. If the impacted structural element was not known, the stiffness was calculated using the elastic Young's modulus ($E = 1.9x10^9\ Pa$) of the debris material (Polyethylene) using:

$$k = \frac{EA}{L} \tag{7.2}$$

Where A is the cross-sectional area of the debris, and L is the long-axis of the debris. Previous work in debris impact testing indicated that maximum debris impact force occurred when the long-axis of the debris was perpendicular to the structure (Matskevitch, 1997, Haehnel and Daly, 2004, Aghl et al., 2015). The orientation of the impact would also significantly affect the impact force, however due to the highly random nature of the debris orientation, the maximum potential force was considered here.

Figure 7.9(a) compares debris velocities of all four experimental categories discussed. For the experiments with three debris, the peak velocities of the debris are up to 9% greater than the experiments with one debris. As the flow reaches the debris initially, there is little debris movement, thus causing the water to build up behind the debris. As the debris continued to remain stationary, water would continue to build up until the friction between the debris and the horizontal bottom was overcome. The built up water entrained and accelerated the debris within the flow propagating over the horizontal apron. This phenomena occurred for both experimental with one and three debris; however, due to more debris causing a larger blockage, the build up behind the three debris was increased. The result was greater acceleration and therefore higher peak velocities for the three debris experiments.

Figure 7.9(b)-(c) shows the potential debris impact force based on Equation 7.1 for one and three debris as a function of dimensionless space (Y), where y is the displacement in the flow direction and L is the length of the debris. Along the flow transect, the debris underwent a rapid increase in potential impact force near the debris site. From $Y = 2$ to $Y = 10$, the impact force plateaus until the debris began to decelerate and the impact forces significantly lowered. Based on these conditions, the near-field structure would be of most concern for debris impact as the impact forces would be significantly larger.

The debris reached a maximum potential force earlier when the debris was initially oriented perpendicular to the flow for both one and three debris. However, for the case of three debris, the peak forces occur closer to the aprons edge comparing to the case with one debris. As discussed earlier, the three debris accelerated faster as a result of the water build up behind the debris on initial impact with the surge, resulting in larger accelerations and therefore reaching peak velocities earlier than in the case with one debris.

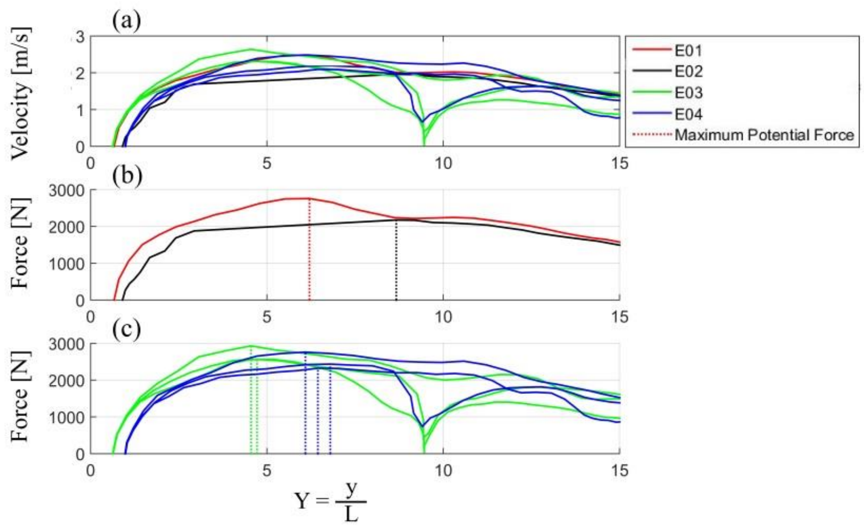

Figure 7.9. Impact forces due to debris propagates over the horizontal apron. (a) On-shore velocity for all groups; (b) and (c) Potential force over the apron from Aghl et al. (2015) for E01, E02 (b), E03, and E04(c) - dotted lines denote where the maximum force occurs.

7.4 Summary and Conclusions

This paper presents an analysis of debris motion using a novel, camera-based, optical tracking algorithm of experiments performed at Waseda University, Tokyo, Japan by the authors. The algorithm used multiple image processing techniques to quickly and accurately track the trajectory and orientation of the debris through the AOI. The experiments were run with one and three scaled-down shipping containers, orientated perpendicular or parallel to the flow direction, in an experimental setting mimicking a modern port environment. From this analysis, the following conclusions can be drawn:

- The repetitions of the experimental tests showed that the trajectory, as well as the velocity of the debris are consistent throughout all tests.
- Peak velocities of the debris oriented perpendicular to the flow direction occur earlier in time than the peak velocities of the debris oriented parallel to the flow.
- Peak velocities were greater when the debris was oriented perpendicular to the flow.
- Peak velocities of the experiments with three debris were larger than those observed during the experiments performed with one debris.
- Debris tended to orient towards the long axis perpendicular to the flow direction, regardless of their initial orientation.

While the work presented herein presents a brief analysis and explanation of the motion of debris, a more in-depth, detailed experiment with more experimental runs would allow for a probabilistic approach to better understand the phenomena involved. The analysis of the force of the debris on a structure would also help in the verification of the potential forces determined from these experiments.

Chapter 8. Conclusions and Recommendations for Future Work

8.1 Conclusions

Based on the analysis of the physical modelling of debris motion within tsunami-like flow conditions and the application of two novel debris tracking systems to the debris motion problem, the following conclusions can be drawn:

Debris Tracking

- This study presented a novel camera-based object tracking algorithm utilizing image processing techniques to track uniformly built debris. The algorithm can accurately and consistently track the motion of up to six debris and can also handle variable light conditions and the high-velocities associated with the present study.
- Significant agglomeration between the debris resulted in reduced accuracy from the camera-based algorithm. The agglomeration of debris caused the algorithm to lose the unique identifiers on each of the debris resulting in significant errors between the algorithm and manual tracking results.
- The study presented a novel sensor-based tracking system for the tracking of debris motion. The system consisted of BLE and IMU sensor to track the debris with 5DOF. Results obtained with this system demonstrated that it provided accurate, high-quality information of the debris position and was suitable for use in coastal and hydraulic engineering.
- The sensor system allows for accurate 2D tracking of up to 18 debris and can track debris in the partially submerged conditions.
- The BLE system was less accurate when tracking the vertical spatial component of the debris trajectory compared to the horizontal ones, though the scalability of the system could potentially allow for better accuracy with more locator antennae.

Debris Entrainment

- The initial debris entrainment showed similar hydrodynamic and motion characteristics regardless of their initial placement configuration. The process of debris entrainment was highly influenced by the sliding of the debris with the laying/stacking surface.
- Debris trajectory, orientation, and velocity are highly repeatable between experiments. The primary factor in the deviation from the general characteristics of the debris motion is the result of random collisions between the debris and with the surface over which they move. The collisions result in a loss of momentum which in turn reduces the debris longitudinal displacement. The collisions also deflect the debris from their relatively straight path resulting thus in a wider spreading angle.

- For a given hydraulic condition, the longitudinal displacement and the spreading angle of the debris are a function of the number of debris used in the initial configuration. Their dependency on the spreading area on debris configuration can generally be described by a linear function.
- The results from this experiment generally fall within the conservative estimations for debris transport detailed by Naito et al. (2014). However, this study found that an increase in the number of debris will result in a smaller longitudinal displacement, which counters the estimations by Naito et al. (2014) whose field observations were limited to few cases analyzed.
- Initial orientation of the debris significantly affected their peak velocity and acceleration. Determining the occurrence and the magnitude of the peak velocity will determine where the area of peak impact will occur.

The modelling of debris motion discussed herein helps identify some of the basic characteristics of the debris motion and identifies some of the primary variables that must be considered in the evaluation of the motion. These findings provide a basis for what must be considered in future studies but further work is needed to evaluate the effects of site specific conditions, such as micro- and macro-roughness, and hydrodynamic conditions.

8.2 Recommendations for Future Work

Based on the research findings from this physical modelling study the following areas are recommended for future numerical and physical work:

- A thorough investigation into the effect of the hydrodynamics on debris motion should be performed. Studies, such as those performed by Yao et al. (2014), showed that the hydrodynamic conditions will significantly affect the debris entrainment and since the grounding of the debris affected the debris motion, determining when or if entrainment and grounding occurs is important.
- The improvement of the camera-based object tracking algorithm (by the author) could be accomplished by utilizing current image processing technique to discern the difference between the individual debris within the agglomeration. The improvement of this algorithm would increase the functionality of the system in the larger fields of coastal and hydraulic engineering.
- The use of the “smart” debris system would allow for a more detailed evaluation of the impact forces of debris on a structure. The accelerometers (set at a higher sampling rate) could discern the impact accelerations and therefore the force of the debris impacting the structure.
- While this study provides a good initial experimental investigation into debris entrainment and motion, the random nature of debris motion should be more thoroughly evaluated using a probabilistic approach to develop a better understanding of the basic characteristics of debris motion.

- Using the basic characteristics of debris motion determined in this study to validate a numerical model will allow for a more detailed look into debris motion. The numerical model will also help in the evaluation of the scale effects of the physical model.

References

Abramowitz, M., Stegun, I.A. (Eds.), 1965. Handbook of Mathematical Functions with Formulas, Graphs, and Mathematical Tables, 9th ed, *Dover Books on Mathematics*. Dover Publications.

Adami, S., Hu, X., Adams, N., 2012. A generalized wall boundary condition for smoothed particle hydrodynamics. *Journal of Computational Physics* 231, 7057–7075.

Addlesee, M., Curwen, R., Hodges, S., Newman, J., Steggles, P., Ward, A., Hopper, A., 2001. Implementing a sentient computing system. *Computer* 34, 50–56.

Aghl, P., Naito, C., Riggs, H., 2014. Full-scale experimental study of impact demands resulting from high mass, low velocity debris. *Journal of Structural Engineering* 140, 04014006.

Aghl, P.P., Naito, C., Riggs, H., 2015. Estimation of demands resulting from inelastic axial impact of steel debris. *Engineering Structures* 82, 11–21.

Al-Faesly, T., 2016. Extreme Hydrodynamic Loading on Near-Shore Structures.

Al-Faesly, T., Palermo, D., Nistor, I., Cornett, A., 2012. Experimental modeling of extreme hydrodynamic forces on structural models. *International Journal of Protective Structures* 3, 477–506.

Ali, I., Tougne, L., 2009. Unsupervised video analysis for counting of wood in river during floods, *in: Advances Visual Computing*. Springer, pp. 578–587.

Allan, J.C., Hart, R., Tranquili, J.V., 2006. The use of Passive Integrated Transponder (PIT) tags to trace cobble transport in a mixed sand-and-gravel beach on the high-energy Oregon coast, USA. *Marine Geology* 232, 63–86.

Amicarelli, A., Albano, R., Mirauda, D., Agate, G., Sole, A., Guandalini, R., 2015. A Smoothed Particle Hydrodynamics model for 3D solid body transport in free surface flows. *Computers & Fluids* 116, 205–228.

Amidi, O., Kanade, T., Fujita, K., 1999. Visual odometer for autonomous helicopter flight. *Robotics and Autonomous Systems* 28, 185–193.

Anderson, B.D.O., Moore, J.B., 1979. Optimal Filtering. Prentice-Hall, Inc., Englewood Cliffs, N.J.

Antonello, R., Nogarole, I., Oboe, R., 2011. Motion reconstruction with a low-cost MEMS IMU for the automation of human operated specimen manipulation, *in: IndustrialElectronics(ISIE),2011IEEEInternationalSymposium*. IEEE, pp. 2189–2194.

Arikawa, T., 2011. Experimental study on tsunami disaster, *in: Proc.,7thInt.Workshop Coastal Disaster Prevention*.

Arnason, H., Petroff, C., Yeh, H., 2009. Tsunami bore impingement onto a vertical column. *Journal of Disaster Research* 4, 391–403.

Benelli, G., Pozzebon, A., 2013. Radio Frequency Identification from System to Applications, *in: Reaz, M.B.I. (Ed.),* INTECH, pp. 379–396.

Benelli, G., Pozzebon, A., Bertoni, D., Sarti, G., 2012. An RFID-based toolbox for the study of under- and outside-water movement of pebbles on coarse-grained beaches. *IEEE Journal of Selected Topics in Applied Earth Observation And Remote Sensing* 5, 1474–1482.

Bertoni, D., Sarti, G., Benelli, G., Pozzebon, A., Raguseo, G., 2012. Transport trajectories of “smart” pebbles on an artificial coarse-grained beach at Marina di Pisa (Italy): Implications for beach morphodynamics. *Marine Geology* 291-294, 227–235.

Bocchiola, D., Rulli, M., Rosso, R., 2006. Transport of large woody debris in the presence of obstacles. *Geomorphology* 76, 166–178.

Borrero, J.C., 2005. Field survey of northern Sumatra and Banda Aceh, Indonesia after the tsunami and earthquake of 26 December 2004. *Seismological Research Letters* 76, 312–320.

Borrero, J.C., Sieh, K., Chlieh, M., Synolakis, C.E., 2006. Tsunami inundation modeling for western Sumatra. *Proceedings of the National Academy of Sciences* 103, 19673–19677.

Bourgeois, F., Lassalle, J.-C., 1971. An extension of the Munkres algorithm for the assignment problem to rectangular matrices. *Communications of the ACM* 14, 802–804.

Bradski, G., 2000. . *Dr. Dobb's Journal of Software Tools*.

Braudrick, C.A., Grant, G.E., 2000. When do logs move in rivers? *Water resources research* 36, 571–583.

Braudrick, C.A., Grant, G.E., 2001. Transport and deposition of large woody debris in streams: a flume experiment. *Geomorphology* 41, 263–283.

Bremm, G.C., Goseberg, N., Schlurmann, T., Nistor, I., 2015. Long Wave Flow Interaction with a Single Square Structure on a Sloping Beach. *Journal of Marine Science and Engineering* 3, 821.

Canelas, R.B., Dominguez, J.M., Crespo, A.J., Gómez-Gesteira, M., Ferreira, R.M., 2015. A Smooth Particle Hydrodynamics discretization for the modelling of free surface flows and rigid body dynamics. *International Journal for Numerical Methods in Fluids* 78, 581–593.

Canelas, R.B., Ferreira, R.M., Crespo, A., Domınguez, J., 2013. A generalized SPH-DEM discretization for the modelling of complex multiphasic free surface flows, *in: 8thinternationalSPHERICworkshop*.

Carré, D.M., Biron, P.M., Gaskin, S.J., 2007. Flow dynamics and bedload sediment transport around paired deflectors for fish habitat enhancement: A field study in the Nicolet River. *Canadian Journal of Civil Engineering* 34, 761–769.

Carrier, G., Greenspan, H., 1958. Water waves of finite amplitude on a sloping beach. *Journal of Fluid Mechanics* 4, 97–109.

Carrier, G., Wu, T., Yeh, H., 2003. Tsunami run-up and draw-down on a plane beach. *Journal of Fluid Mechanics* 475, 79–99.

Chai, D., Bouzerdoum, A., 2000. A Bayesian approach to skin color classification in YCbCr color space, *in: TENCON2000.Proceedings*. IEEE, pp. 421–424.

Chan, Y.T., Hu, A.G.C., Plant, J.B., 1979. A Kalman Filter Based Tracking Scheme with Input Estimation. *Aerospace and Electronic Systems, IEEE Transactions on* AES-15, 237–244.

Chanson, H., 2006. Tsunami surges on dry coastal plains: Application of dam break wave equations. *Coastal Engineering Journal* 48, 355–370.

Chanson, H., 2009. Current knowledge in hydraulic jumps and related phenomena. A survey of experimental results. *European Journal of Mechanics-B/Fluids* 28, 191–210.

Charvet, I., Suppasri, A., Imamura, F., 2014. Empirical fragility analysis of building damage caused by the 2011 Great East Japan tsunami in Ishinomaki city using ordinal regression, and influence of key geographical features. *Stochastic Environmental Research and Risk Assessment* 28, 1853–1867.

Chen, J., Jiang, C., Yang, W., Xiao, G., 2015. Laboratory study on protection of tsunami-induced scour by offshore breakwaters. *Natural Hazards* 1–19.

Chen, T.-H., Lin, Y.-F., Chen, T.-Y., 2007. Intelligent vehicle counting method based on blob analysis in traffic surveillance, *in: InnovativeComputing,Information Control, 2007. ICICIC'07. Second International Conference*. IEEE, pp. 238–238.

Chinnarasri, C., Thanasisathit, N., Ruangrassamee, A., Weesakul, S., Lukkunaprasit, P., 2013. The impact of tsunami-induced bores on buildings. *Proceedings of the Institution of Civil Engineers: Maritime Engineering* 166, 14–24.

Chock, G., Robertson, I., Kriebel, D., Francis, M., Nistor, I., 2013. Tohoku, Japan, Earthquake and Tsunami of 2011: Performance of Structures Under Tsunami Loads. ASCE.

Clague, J.J., Bobrowsky, P.T., Hamilton, T., 1994. A sand sheet deposited by the 1964 Alaska tsunami at Port Alberni, British Columbia. *Estuarine, Coastal and Shelf Science* 38, 413–421.

Clague, J.J., Munro, A., Murty, T., 2003. Tsunami hazard and risk in Canada. *Natural Hazards* 28, 435–463.

Comer, M.L., Delp, E.J., 1999. Morphological operations for color image processing. *Journal of electronic imaging* 8, 279–289.

Como, A., Mahmoud, H., 2013. Numerical evaluation of tsunami debris impact loading on wooden structural walls. *Engineering Structures* 56, 1249–1261.

Cowen, E., Monismith, S., 1997. A hybrid digital particle tracking velocimetry technique. *Experiments in Fluids* 22, 199–211.

Cox, D., Tomita, T., Lynett, P., Holman, R., 2008. Tsunami inundation with macroroughness in the constructed environment, *in: Proc.31stInternationalConference Coastal Engineering, ASCE*. World Scientific, pp. 1421–1432.

Crosato, A., Rajbhandari, N., Comiti, F., Cherradi, X., Uijttewaal, W., 2013. Flume experiments on entrainment of large wood in low-land rivers. *Journal of Hydraulic Research* 51, 581–588.

Cucchiara, R., Grana, C., Piccardi, M., Prati, A., 2003. Detecting moving objects, ghosts, and shadows in video streams. *Pattern Analysis and Machine Intelligence, IEEE Transactions on* 25, 1337–1342.

Darienzo, M., Aya, A., Crawford, G.L., Gibbs, D., Whitmore, P.M., Wilde, T., Yanagi, B.S., 2005. Local tsunami warning in the Pacific coastal United States. *Natural Hazards* 35, 111–119.

Dutta, S., Chaudhuri, B.B., 2009. A statistics and local homogeneity based color edge detection algorithm, *in: Advances Recent TechnologiesCommunication Computing, 2009. ARTCom'09. International Conference*. IEEE, pp. 546–548.

El-Anwar, O., Chen, L., 2012. Maximizing the computational efficiency of temporary housing decision support following disasters. *Journal of Computing in Civil Engineering* 28, 113–123.

Ergen, E.., Akinci, B.., East, B.., Kirby, J.., 2007. Tracking components and maintenance history within a facility utilizing radio frequency identification technology. *Journal of Computing in Civil Engineering* 21, 11–20.

Esteban, M., Jayaratne, R., Mikami, T., Morikubo, I., Shibayama, T., Thao, N.D., Ohira, K., Ohtani, A., Mizuno, Y., Kinoshita, M., Matsuba, S., 2014. Stability of breakwater armor units against tsunami attacks. *Journal of Waterway, Port, Coastal and Ocean Engineering* 140, 188–198.

Esteban, M., Takagi, H., Shibayama, T., 2015. Handbook of Coastal Disaster Mitigation for Engineers and Planners.

FEMA P646, 2012. .
Fritz, H.M., Borrero, J.C., Synolakis, C.E., Yoo, J., 2006. 2004 Indian Ocean tsunami flow velocity measurements from survivor videos. *Geophysical Research Letters* 33.
Fujii, Y., Satake, K., Sakai, S., Shinohara, M., Kanazawa, T., 2011. Tsunami source of the 2011 off the Pacific coast of Tohoku Earthquake. *Earth, planets and space* 63, 815–820.
Ge, S.S., Cui, Y.J., 2000. New potential functions for mobile robot path planning. *IEEE Transactions on Robotics and Automation* 16, 615–620.
Gibbins, C.J., 1986. Improved algorithms for the determination of specific attenuation at sea level by dry air and water vapor, in the frequency range 1-350 ghz. *Radio Science* 21, 949–954.
Giordano, N.J., Nakanishi, H., 2006. Computational Physics, 2nd ed. Prentice Hall.
Gomez-Gesteira, M., Rogers, B.D., Crespo, A.J., Dalrymple, R., Narayanaswamy, M., Dominguez, J.M., 2012. SPHysics–development of a free-surface fluid solver–Part 1: Theory and formulations. *Computers & Geosciences* 48, 289–299.
Goseberg, N., 2013. Reduction of maximum tsunami run-up due to the interaction with beachfront development - application of single sinusoidal waves. *Nat Hazards Earth Syst Sci Disc* 1, 1119–1171.
Goseberg, N., Nistor, I., Mikami, T., Shibayama, T., Stolle, J., 2016. Non-invasive 6-DOF Multi-object Tracking in Violent Flow Through "smart" Debris with Application to debris-laden Tsunami Inundation. *JHE Under review*.
Goseberg, N., Schlurmann, T., 2014. Non-stationary flow around buildings during run-up of tsunami waves on a plain beach. *Coastal Engineering Proceedings* 1, 21.
Goseberg, N., Stahlmann, A., Schimmels, S., Schlurmann, T., 2009. Highly-resolved numerical modeling of tsunami run-up and inundation scenario in the city of Padang, West Sumatra, *in: Proc. 31st Int. ConferenceCoastalEngineering*.
Goseberg, N., Wurpts, A., Schlurmann, T., 2013. Laboratory-scale generation of tsunami and long waves. *Coastal Engineering* 79, 57–74.
Grundland, M., Dodgson, N.A., 2005. Color histogram specification by histogram warping, *in: ElectronicImaging2005*. International Society for Optics and Photonics, pp. 610–621.
Haehnel, R.B., Daly, S.F., 2004. Maximum impact force of woody debris on floodplain structures. *Journal of Hydraulic Engineering* 130, 112–120.
Ham, M. van der, 2015. Real Time Localization of Assets in Hospitals using Quuppa Indoor Positioning Technology.
Hammack, J.L., Segur, H., 1974. The Korteweg-de Vries equation and water waves. Part 2. Comparison with experiments. *Journal of Fluid mechanics* 65, 289–314.
Harrabi, R., Braiek, E., 2011. Color image segmentation using automatic thresholding techniques, *in: Systems,Signals Devices (SSD), 2011 8th International Multi-Conference*. IEEE, pp. 1–6.
Hayking, S., 2001. Kalman Filtering and Neural Networks. Wiley & Sons, New York.
Henderson, D.M., 1977. Euler Angles, Quaternions, and Transformation Matrices - Working Relationships (No. 77-FM-37). National Aeronautics and Space Administration, Lyndon B. Johnson Space Center, Huston, Texas.
Hofmann-Wellenhof, B., Legat, K., Wieser, M., 2003. Navigation: Principles of Positioning and Guidance. Springer Verlag, Wien.
Holland, K.T., Holman, R.A., 1997. Video estimation of foreshore topography using trinocular stereo. *Journal of Coastal Research* 81–87.

Imamura, F., Goto, K., Ohkubo, S., 2008. A numerical model for the transport of a boulder by tsunami. *Journal of Geophysical Research: Oceans (1978–2012)* 113.
Ioualalen, M., Asavanant, J., Kaewbanjak, N., Grilli, S., Kirby, J., Watts, P., 2007. Modeling the 26 December 2004 Indian Ocean tsunami: Case study of impact in Thailand. *Journal of Geophysical Research: Oceans (1978–2012)* 112.
Jiang, S., Georgakopoulos, S., 2011. Electromagnetic Wave Propagation into Fresh Water. *Journal of Electromagnetic Analysis and Applications* 3, 261–266.
Johnston, D., Paton, D., Crawford, G.L., Ronan, K., Houghton, B., Bürgelt, P., 2005. Measuring tsunami preparedness in coastal Washington, United States, *in: DevelopingTsunamiResilientCommunities*. Springer, pp. 173–184.
Kazama, M., Noda, T., 2012. Damage statistics (Summary of the 2011 off the Pacific Coast of Tohoku Earthquake damage). *Soils and Foundations* 52, 780–792.
Kenney, J.F., 1962. Mathematics of Statistics, *in: Keeping, E.S. (Ed.),* Van Nostrand, Princton, NJ., pp. 77–80.
Khoury, H.M., Kamat, V.R., 2009. Evaluation of position tracking technologies for user localization in indoor construction environments. *Automation in Construction* 18, 444–457.
Kinsman, B., 1965. Wind waves: their generation and propagation on the ocean surface. Courier Corporation.
Knörr, W., Kutzner, F., 2008. EcoTransIT: Ecological Transport Information Tool - Environmental Method and Data. IFEU Heidelberg.
Ko, H.T.-S., Cox, D.T., Riggs, H.R., Naito, C.J., 2015. Hydraulic experiments on impact forces from tsunami-driven debris. *Journal of Waterway, Port, Coastal and Ocean Engineering* 141, 04014043.
Kuehni, R.G., 2003. Color space and its divisions: color order from antiquity to the present. John Wiley & Sons.
Lamarre, H., MacVicar, B., Roy, A.G., 2005. Using Passive Integrated Transponder (PIT) tags to investigate sediment transport in gravel-bed rivers. *Journal of Sedimentary Research* 75, 736–741.
Laplante, P.A., Neill, C.J., 2003. A class of Kalman filters for real-time image processing, *in: ElectronicImaging2003*. International Society for Optics and Photonics, pp. 22–29.
Lee, D., Kim, G., Kim, D., Myung, H., Choi, H.-T., 2012. Vision-based object detection and tracking for autonomous navigation of underwater robots. *Ocean Engineering* 48, 59–68.
Leser, R., Baca, A., Ogris, G., 2011. Local positioning systems in (game) sports. *Sensors* 11, 9778–9797.
Linton, D., Gupta, R., Cox, D., Van De Lindt, J., Oshnack, M.E., Clauson, M., 2013. Evaluation of tsunami loads on wood-frame walls at full scale. *Journal of Structural Engineering (United States)* 139, 1318–1325.
Lou, Y.-F., Jin, X.-L., 2014. Numerical simulation of solitary wave and drifting object interacting with breakwater using the ALE method. *Coastal Engineering Journal* 56, 1450015.
Lu, M., Chen, W., Shen, X., Lam, H.-C., Liu, J., 2007. Positioning and tracking construction vehicles in highly dense urban areas and building construction sites. *Automation in Construction* 16, 647–656.
Lukkunaprasit, P., Thanasisathit, N., Yeh, H., 2009. Experimental Verification of FEMA P646 Tsunami Loading. *Journal of Disaster Research* 4, 410–418.

MacVicar, B.J., Piégay, H., Henderson, A., Comiti, F., Oberlin, C., Pecorari, E., 2009. Quantifying the temporal dynamics of wood in large rivers: Field trials of wood surveying, dating, tracking, and monitoring techniques. *Earth Surface Processes and Landforms* 34, 2031–2046.

MacVicar, B.J., Roy, A.G., 2011. Sediment mobility in a forced riffle-pool. *Geomorphology* 125, 445–456.

Madsen, P.A., 2010. On the evolution and run-up of tsunamis. *Journal of Hydrodynamics, Ser. B* 22, 1–6.

Madsen, P.A., Fuhrman, D.R., Schäffer, H.A., 2008. On the solitary wave paradigm for tsunamis. *Journal of Geophysical Research: Oceans* 113.

Madsen, P.A., Schaeffer, H.A., 2010. Analytical solutions for tsunami runup on a plane beach: single waves, N-waves and transient waves. *Journal of Fluid Mechanics* 645, 27–57.

Madurapperuma, M.A.K.M., Wijeyewickrema, A.C., 2012. Inelastic dynamic analysis of an RC building impacted by a tsunami water-borne shipping container. *Journal of Earthquake and Tsunami* 6.

Madurapperuma, M.A.K.M., Wijeyewickrema, A.C., 2013. Response of reinforced concrete columns impacted by tsunami dispersed 20’ and 40’ shipping containers. *Engineering Structures* 56, 1631–1644.

Malhotra, M., Subramanian, R., 1994. Textbook in Applied Mechanics. New Age International.

Manenti, S., Panizzo, A., Ruol, P., Martinelli, L., 2008. SPH simulation of a floating body forced by regular waves, *in: Proceedings 3rd SPHERIC Workshop*. pp. 38–41.

Marco, A., Casas, R., Falco, J., Gracia, H., Artigas, J.I., Roy, A., 2008. Location-based services for elderly and disabled people. *Computer Communications* 31, 1055–1066.

Matskevitch, D., 1997. Eccentric impact of an ice feature: linearized model. *Cold regions science and technology* 25, 159–171.

Matsutomi, H., 2009. Method for estimating collision force of driftwood accompanying tsunami inundation flow. *Journal of Disaster Research* 4, 435–440.

Matsutomi, H., Fujii, M., Yamaguchi, T., 2008. Experiments and development of a model on the inundated flow with floating bodies. *Coastal Engineering* 1458–1470.

McCarthy, U., Ayalew, G., Butler, F., McDonnell, K., Ward, S., 2009. The effects of item composition, tag inlay design, reader antenna polarization, power and transponder orientation on the dynamic coupling efficiency of backscatter ultra-high frequency radio frequency identification. *Packaging Technology and Science* 22, 241–248.

McCowan, J., 1891. On the solitary wave. *Phil. Mag.* 32, 45–58.

McKenna, S.J., Jabri, S., Duric, Z., Rosenfeld, A., Wechsler, H., 2000. Tracking groups of people. *Computer Vision and Image Understanding* 80, 42–56.

Mills, D.L., 2006. Computer Network Time Synchronization: The Network Time Protocol. Taylor & Francis.

Mizutani, N., Yamaguchi, S., Tomita, T., Miyajima, S., 2005. Experimental study on behavior of container on apron due to tsunami and its impact load, *in: Proceedings International OffshorePolarEngineeringConference*. pp. 640–645.

Monaghan, J.J., 2005. Smoothed particle hydrodynamics. *Reports on progress in physics* 68, 1703.

Mori, N., Takahashi, T., Yasuda, T., Yanagisawa, H., 2011. Survey of 2011 Tohoku earthquake tsunami inundation and run-up. *Geophysical Research Letters* 38.

Munk, W.H., 1949. The Solitary Wave Theory and Its Application to Surf Problems. *Annals of the New York Academy of Sciences* 51, 376–424.
Munkres, J., 1957. Algorithms for the assignment and transportation problems. *Journal of the Society for Industrial & Applied Mathematics* 5, 32–38.
Naito, C., Cercone, C., Riggs, H.R., Cox, D., 2014. Procedure for site assessment of the potential for tsunami debris impact. *Journal of Waterway, Port, Coastal and Ocean Engineering* 140, 223–232.
Naito, C., Riggs, H., Wei, Y., Cercone, C., 2016. Shipping-Container Impact Assessment for Tsunamis. *Journal of Waterway, Port, Coastal, and Ocean Engineering* 05016003.
Nakamura, T., Mizutani, N., Wakamatsu, Y., 2012. Study on drift behavior of container on apron due to tsunami-induced incoming and return flow. *Coastal Engineering Proceedings* 1, 16.
Nathan Bradley, D., Tucker, G.E., 2012. Measuring gravel transport and dispersion in a mountain river using passive radio tracers. *Earth Surface Processes and Landforms* 37, 1034–1045.
Nichols, M.H., 2004. A radio frequency identification system for monitoring coarse sediment particle displacement. *Applied Engineering in Agriculture* 20, 783–787.
Nistor, I., Goseberg, N., Mikami, T., Shibayama, T., Stolle, J., Nakamura, R., Matsuba, S., 2016. Hydraulic Experiments on Debris Dynamics over a Horizontal Plane. In Review (Journal of Waterway, Port, Coastal, and Ocean Engineering).
Nistor, I., Nouri, Y., Palermo, D., Cornett, A., 2009. Experimental investigation of the impact of a tsunami-induced bore on structures, *in: Proceedings Coastal Engineering Conference*. pp. 3324–3336.
Nistor, I., Palermo, D., Cornett, A., Al-Faesly, T., 2011. Experimental and numerical modeling of tsunami loading on structures. *Coastal Engineering Proceedings* 1, 2.
Nouri, Y., Nistor, I., Palermo, D., Cornett, A., 2010. Experimental investigation of tsunami impact on free standing structures. *Coastal Engineering Journal* 52, 43–70.
Okada, T., Sugano, T., Ishikawa, T., Ohgi, T., Takai, S., Hamabe, C., 2005. Structural design method of buildings for tsunami resistance (proposed). *Building Technology Research Institute, Building Centre for Japan* 15.
Okal, E.A., Synolakis, C.E., 2016. Sequencing of tsunami waves: why the first wave is not always the largest. *Geophysical Journal International* 204, 719–735.
Omidvar, M., Chen, Z., Iskander, M., 2014. Image-Based Lagrangian Analysis of Granular Kinematics. *Journal of Computing in Civil Engineering* 04014101.
Oy, Q., 2014. LD-7L Long Range HAIP Locator.
Paczkowski, K., Riggs, H.R., Naito, C.J., Lehmann, A., 2012. A one-dimensional model for impact forces resulting from high mass, low velocity debris. *Structural Engineering and Mechanics* 42, 831–847.
Pagliara, S., Carnacina, I., 2013. Bridge pier flow field in the presence of debris accumulation, *in: Proceedings InstitutionCivilEngineersWaterManagement*. Thomas Telford Ltd, pp. 187–198.
Palermo, D., Nistor, I., Nouri, Y., Cornett, A., 2009. Tsunami loading of near-shoreline structures: a primer. *Canadian Journal of Civil Engineering* 36, 1804–1815.
Palermo, D., Nistor, I., Saatcioglu, M., Ghobarah, A., 2013. Impact and damage to structures during the 27 February 2010 Chile tsunami. *Canadian Journal of Civil Engineering* 40, 750–758.

PARI, 2011. Damage assessment of ports in Tohuku region (Preliminary field survey report), Attachement 2: Reconnaissance results of respecitve ports, 23 March, 2011. Port and Airport Research Institute.
Park, C., Bae, K., Jung, J.-H., 2008. Object recognition in infrared image sequences using scale invariant feature transform, *in: SPIEDefense Security Symposium*. International Society for Optics and Photonics, p. 69681P–69681P.
Parola, A.C., 2000. Debris forces on highway bridges. Transportation Research Board.
Pavlopoulos, P.M., Zimeras, S., Kavantzas, N., Korkolopoulou, P., Agapitos, E., Patsouris, E., 2007. Segmentation of transitional cell carcinoma nuclei by nonsupervised thresholding in different color spaces. *Analytical and quantitative cytology and histology/the International Academy of Cytology [and] American Society of Cytology* 29, 271–278.
Persico, L.P., Nichols, K.K., Bierman, P.R., 2005. Tracking painted pebbles: Short-term rates of sediment movement on four Mojave Desert piedmont surfaces. *Water resources research* 41.
Pilotti, M., Maranzoni, A., Tomirotti, M., Valerio, G., 2011. 1923 Gleno Dam break: Case study and numerical modeling. *Journal of Hydraulic Engineering* 137, 480–492.
Piran Aghl, P., Naito, C.J., Riggs, H.R., 2015. Effect of nonstructural mass on debris impact demands: Experimental and simulation studies. *Engineering Structures* 88, 163–175.
Pribyl, B., Chalmers, A., Zemcık, P., 2013. Feature point detection under extreme lighting conditions, *in: Proceedings 28th Spring ConferenceComputerGraphics*. ACM, pp. 143–150.
Ramsden, J.D., 1996. Forces on a vertical wall due to long waves, bores, and dry-bed surges. *Journal of waterway, port, coastal, and ocean engineering* 122, 134–141.
Rantakokko, J., Rydell, J., Strömbäck, P., Händel, P., Callmer, J., Törnqvist, D., Gustafsson, F., Jobs, M., Grudén, M., 2011. Accurate and reliable soldier and first responder indoor positioning: Multisensor systems and cooperative localization. *IEEE Wireless Communications* 18, 10–18.
Raof, R., Salleh, Z., Sahidan, S., Mashor, M., Noor, S.M., Idris, F., Hasan, H., 2008. Color thresholding method for image segmentation algorithm of Ziehl-Neelsen sputum slide images, *in: ElectricalEngineering,ComputingScience Automatic Control, 2008. CCE 2008. 5th International Conference*. IEEE, pp. 212–217.
Riggs, H., Cox, D., Naito, C., Kobayashi, M., Aghl, P.P., Ko, H.-S., Khowitar, E., 2014. Experimental and Analytical Study of Water-Driven Debris Impact Forces on Structures. *Journal of Offshore Mechanics and Arctic Engineering* 136, 041603.
Robertson, I., Riggs, H.R., Yim, S.C., Young, Y.L., 2007. Lessons from Hurricane Katrina storm surge on bridges and buildings. *Journal of Waterway, Port, Coastal, and Ocean Engineering* 133, 463–483.
Rogers, B.D., Dalrymple, R.A., Stansby, P.K., 2009. SPH modeling of floating bodies in the surf zone. *01613782* 204–215.
Rueben, M., Cox, D., Holman, R., Shin, S., Stanley, J., 2014. Optical Measurements of Tsunami Inundation and Debris Movement in a Large-Scale Wave Basin. *Journal of Waterway, Port, Coastal, and Ocean Engineering* 141.
Saatcioglu, M., Ghobarah, A., Nistor, I., 2005. Effects of the December 26, 2004 Sumatra earthquake and tsunami on physical infrastructure. *ISET Journal of earthquake technology* 42, 79–94.

Salvi, G., 2012. An Automated Vehicle Counting System Based on Blob Analysis for Traffic Surveillance, *in: Proceedings International ConferenceImageProcessing,ComputerVision, Pattern Recognition (IPCV)*. The Steering Committee of The World Congress in Computer Science, Computer Engineering and Applied Computing (WorldComp), p. 1.

Schenk, E.R., Moulin, B., Hupp, C.R., Richter, J.M., 2014. Large wood budget and transport dynamics on a large river using radio telemetry. *Earth Surface Processes and Landforms* 39, 487–498.

Schmocker, L., Hager, W.H., 2013. Scale modeling of wooden debris accumulation at a debris rack. *Journal of Hydraulic Engineering* 139, 827–836.

Seiffert, B., Hayatdavoodi, M., Ertekin, R.C., 2014. Experiments and computations of solitary-wave forces on a coastal-bridge deck. Part I: Flat Plate. *Coastal Engineering* 88, 194–209.

Serra, J., 1986. Introduction to mathematical morphology. *Computer vision, graphics, and image processing* 35, 283–305.

Shafiei, S., Melville, B., Beskhyroun, S., Shamseldin, A., 2014. Preliminary investigation of the tsunami-borne debris impact on structures: a new method for impact force measurement, *in: 5thIAHRInternationalSymposium Hydraulic Structures*. The University of Queensland, pp. 1–9.

She, Z.-S., Leveque, E., 1994. Universal scaling laws in fully developed turbulence. *Physical review letters* 72, 336.

Shibayama, A., Kihara, N., Miyagawa, Y., Takabatake, D., Kaida, H., 2015. Large scale experiments on response of RC tide wall to tsunami debris impact, *in: Proceedings International OffshorePolarEngineeringConference*. pp. 817–821.

Smirnov, V., Bychkova, I., 2015. Satellite monitoring of ice features to ensure safety of offshore operations in the Arctic seas. *Izvestiya, Atmospheric and Oceanic Physics* 51, 935–942.

Spahn, H., Hoppe, M., Vidiarina, H.D., Usdianto, B., 2010. Experience from three years of local capacity development for tsunami early warning in Indonesia: challenges, lessons and the way ahead. *Natural Hazards and Earth System Sciences* 10, 1411–1429.

Sriram, V., Didenkulova, I., Sergeeva, A., Schimmels, S., 2016. Tsunami evolution and run-up in a large scale experimental facility. *Coastal Engineering* 111, 1–12.

St-Germain, P., Nistor, I., Townsend, R., 2012. Numerical modeling of the impact with structures of tsunami bores propagating on dry and wet beds using the SPH method. *International Journal of Protective Structures* 3, 221–256.

St-Germain, P., Nistor, I., Townsend, R., Shibayama, T., 2013. Smoothed-particle hydrodynamics numerical modeling of structures impacted by tsunami bores. *Journal of Waterway, Port, Coastal, and Ocean Engineering*.

Stolle, J., Nistor, I., Goseberg, N., 2016. Optical Tracking of Floating Shipping Containers in High-Velocity Flow. In Review (Coastal Engineering Journal).

Strusinska-Correia, A., Husrin, S., Oumeraci, H., 2013. Tsunami damping by mangrove forest: A laboratory study using parameterized trees. *Natural Hazards and Earth System Science* 13, 483–503.

Synolakis, C.E., Deb, M.K., Skjelbreia, J.E., 1988. The anomalous behavior of the runup of cnoidal waves. *Physics of Fluids (1958-1988)* 31, 3–5.

Tadepalli, S., Synolakis, C.E., 1994. The run-up of N-waves on sloping beaches, *in: Proceedings Royal SocietyLondonAMathematical,Physical Engineering Sciences*. The Royal Society, pp. 99–112.
Takahashi, S., Kuriyama, Y., Tomita, T., Kawai, Y., Arikawa, T., Tatsumi, D., 2011. Urgent survey for 2011 Great East Japan Earthquake and Tsunami disaster in ports and coasts—Part I (tsunami). Port and Air Port Research Institute.
Taubenböck, H., Goseberg, N., Lämmel, G., Setiadi, N., Schlurmann, T., Nagel, K., Siegert, F., Birkmann, J., Traub, K.-P., Dech, S., others, 2013. Risk reduction at the "Last-Mile": an attempt to turn science into action by the example of Padang, Indonesia. *Natural hazards* 65, 915–945.
Taubenböck, H., Goseberg, N., Setiadi, N., Lämmel, G., Moder, F., Oczipka, M., Klüpfel, H., Wahl, R., Schlurmann, T., Strunz, G., others, 2009. Last-Mile" preparation for a potential disaster–Interdisciplinary approach towards tsunami early warning and an evacuation information system for the coastal city of Padang, Indonesia. *Natural Hazards and Earth System Science* 9, 1509–1528.
Titov, V.V., Synolakis, C.E., 1998. Numerical modeling of tidal wave runup. *Journal of Waterway, Port, Coastal, and Ocean Engineering*.
Tsakiris, A., Papanicolaou, A., Moustakidis, I., Abban, B., 2015. Identification of the Burial Depth of Radio Frequency Identification Transponders in Riverine Applications. *Journal of Hydraulic Engineering* 141.
Twist, C., Waldron, M., Worsfold, P., Gabbett, T.J., 2013. Monitoring team sport athletes using global positioning system technology, *Global Positioning Systems: Signal Structure, Applications and Sources of Error and Biases*.
Vousdoukas, M., Velegrakis, A., Dimou, K., Zervakis, V., Conley, D., 2009. Wave run-up observations in microtidal, sediment-starved pocket beaches of the Eastern Mediterranean. *Journal of Marine Systems* 78, S37–S47.
Weng, S.-K., Kuo, C.-M., Tu, S.-K., 2006. Video object tracking using adaptive Kalman filter. *Journal of Visual Communication and Image Representation* 17, 1190–1208.
White, A.D., MacFarlane, N.G., 2015. Analysis of international competition and training in men's field hockey by global positioning system and inertial sensor technology. *Journal of Strength and Conditioning Research* 29, 137–143.
Wu, T.-R., Chu, C.-R., Huang, C.-J., Wang, C.-Y., Chien, S.-Y., Chen, M.-Z., 2014. A two-way coupled simulation of moving solids in free-surface flows. *Computers & Fluids* 100, 347–355.
Wu, T.Y., Murashige, S., 2011. On tsunami and the regularized solitary-wave theory. *Journal of Engineering Mathematics* 70, 137–146.
Xia, Y., Ning, S., Shen, H., 2010. Moving targets detection algorithm based on background subtraction and frames subtraction, *in: IndustrialMechatronics Automation (ICIMA), 2010 2nd International Conference*. IEEE, pp. 122–125.
Yao, Y., Huang, Z., Lo, E.Y.M., Shen, H.-T., 2014. A preliminary laboratory study of motion of floating debris generated by solitary waves running up a beach. *Journal of Earthquake and Tsunami* 8.
Yeh, H., Barbosa, A.R., Ko, H., Cawley, J.G., 2014. TSUNAMI LOADINGS ON STRUCTURES: REVIEW AND ANALYSIS. *Coastal Engineering Proceedings* 1, currents–4.

Yeh, H., Sato, S., Tajima, Y., 2013. The 11 March 2011 East Japan earthquake and tsunami: tsunami effects on coastal infrastructure and buildings. *Pure and Applied Geophysics* 170, 1019–1031.

Zhou, H., Yuan, Y., Shi, C., 2009. Object tracking using SIFT features and mean shift. *Computer vision and image understanding* 113, 345–352.